UNIVERSITY OF GENOA

Doctoral School
Sciences and Technologies of Chemistry and Materials

Doctorate Course
Chemical Sciences and Technologies

XXXIII cycle

Nonspecific Interactions of Amphiphilic Nanoparticles and Biomimetic Membranes

Candidate: *Ester Canepa*

Supervisors: *Prof. Annalisa Relini*
Prof. Fabio M. Canepa

Genoa, Italy
2021

How many roads must a man walk down
Before you call him a man?

How many seas must a white dove sail
Before she sleeps in the sand?

Yes, and how many times must the cannonballs fly
Before they're forever banned?

The answer, my friend, is blowin' in the wind
The answer is blowin' in the wind

Abstract

Biomedical research involving synthetic ligand-protected nanoparticles requires robust control over nanoparticle-cell interactions, which are ubiquitous in every in vivo and in vitro application. This requirement is essential to the rational design of tailored nano-bio technologies for bioimaging and advanced drug delivery and to the assessment of the potential adverse impact resulting from undesired nanoparticle-induced perturbation of the biological environment. The controlled behavior of nanoparticles at the cellular interface relies on the fundamental need to elucidate the physicochemical principles that define the interactions between nanoparticles and cell membranes. Despite numerous research efforts, the propensity of surface-modified particles to interfere – or not – with the organization and function of cell membranes is still far from clear due to the inherently complex, heterogeneous, and dynamic nature of these biological barriers. Based on a biomimetic approach, model lipid membranes are extensively exploited for selective and systematic investigations of isolated nanoparticle-membrane interactions in vitro. It is within this bioinspired perspective that the work presented in this thesis was developed.

Here, experimental investigations based on biophysical techniques were undertaken to tackle some aspects of nonspecific nanoparticle-membrane interactions that are still unclear or very poorly addressed. Small gold nanoparticles with a diameter of less than 6 nm and passivated by a mixed ligand monolayer composed of hydrophobic and hydrophilic (ω-charged) alkylthiols were considered. These amphiphilic particles possess high biomedical potential as they are able to enter living cells passively and nondisruptively for diagnostic or therapeutic purposes. Lipid vesicles and supported lipid bilayers with variable structural and morphological complexity were employed to mimic the lipid structure of cell membranes. Particular attention was devoted to the impact that nanoparticle features, such as size and surface charged density, have on membrane integrity and lateral organization during the passive penetration of the lipid bilayer. In turn, the role of membrane fluidity in nanoparticle internalization was also addressed.

The findings of this work have shown that the sign of the nanoparticle surface charge is not responsible for different particle behavior in interacting with neutral membranes. For both negatively and positively charged ligand monolayers, amphiphilic nanoparticles were shown not to induce relevant damage to membrane integrity during passive bilayer penetration. Furthermore, small amphiphilic nanoparticles were revealed to perturb the lateral lipid phase separation of multidomain membranes in a concentration-dependent manner and form peculiar ordered aggregates embedded in the bilayer. Finally, studies on fluid vesicles with progressive membrane stiffening tuned by cholesterol content have allowed us to systematically quantify the impact that reducing membrane fluidity has on the equilibrium amount of particles capable of passive incorporation into the membrane. Overall, these results have provided a novel contribution in elucidating how amphiphilic entities endowed with surface conformational flexibility, such as ligand-protected nanoparticles, can interact with cell membranes.

List of publications

Papers published in peer-reviewed journals

1. E. Canepa, S. Salassi, F. Simonelli, R. Ferrando, R. Rolandi, C. Lambruschini, F. Canepa, S. Dante, A. Relini, and G. Rossi, *Non-disruptive uptake of anionic and cationic gold nanoparticles in neutral zwitterionic membranes*, Scientific Reports, 2021, 11, 1256.

2. E. Canepa, S. Salassi, A. L. de Marco, C. Lambruschini, D. Odino, D. Bochicchio, F. Canepa, C. Canale, S. Dante, R. Brescia, F. Stellacci, G. Rossi, and A. Relini, *Amphiphilic gold nanoparticles perturb phase separation in multidomain lipid membranes*, Nanoscale, 2020, 12 (38), 19746-19759.

3. S. Salassi, E. Canepa, R. Ferrando, and G. Rossi, *Anionic nanoparticle-lipid membrane interactions: the protonation of anionic ligands at the membrane surface reduces membrane disruption*, RSC Advances, 2019, 9 (25), 13992-13997.

4. F. Locardi, E. Canepa, S. Villa, I. Nelli, C. Lambruschini, M. Ferretti, and F. Canepa, *Thermogravimetry and evolved gas analysis for the investigation of ligand-exchange reaction in thiol-functionalized gold nanoparticles*, Journal of Analytical and Applied Pyrolysis, 2018, 132, 11-18.

The candidate and the supervisor Prof. F. Canepa are not relatives.

https://orcid.org/0000-0003-2536-9210

Contents

List of Acronyms

^{1}H-NMR proton nuclear magnetic resonance
AFM atomic force microscopy
AuNP gold nanoparticle
BF-TEM bright-field TEM
$CHCl_3$ chloroform
CH_3OH methanol (or MeOH)
Chol cholesterol
CPP cell-penetrating peptide
COM center of mass
DCCI Dept. of Chemistry and Industrial Chemistry
DCM dichloromethane
DIFI Dept. of Physics
DLS dynamic light scattering
DLiPC 1,2-dilinoleoyl-*sn*-glycero-3-phosphocholine
DOPC 1,2-dioleoyl-*sn*-glycero-3-phosphocholine
DPH 1,6-diphenyl-1,3,5-hexatriene
DPPC 1,2-dipalmitoyl-*sn*-glycero-3-phosphocholine
DNA deoxyribonucleic acid
E Young's modulus
EDTA ethylenediaminetetraacetic acid
EPFL École Polytechnique Fédérale de Lausanne
EtOH ethanol
GM1 ganglioside GM1
HAADF-STEM high-angle annular dark-field scanning TEM
$HAuCl_4 \cdot 3H_2O$ hydrogen tetrachloro-aurate (III) trihydrate
Hyst histidine
IIT Italian Institute of Technology
LSPR localized surface plasmon resonance
MD molecular dynamics
MeOH methanol (or CH_3OH)
MUS 11-mercapto-1-undecanesulfonate
MUS:OT mixed NP monolayer composed of MUS and OT
NP nanoparticle
OT 1-octanethiol
PBS phosphate buffered saline
PC phosphocholine
PEG polyethylene glycol
POPC 1-palmitoyl-2-oleoyl-*sn*-glycero-3-phosphocholine
QCM-D quartz crystal microbalance with dissipation monitoring
QI™ quantitative imaging (by JPK)
RNA ribonucleic acid
RSH alkylthiol
SAM self-assembled monolayer
SM sphingomyelin
TEM transmission electron microscopy
TES 2-[tris(hydroxymethyl)methyl-amino]-1-ethanesulfonic acid
THF tetrahydrofuran
TMA (11-mercaptoundecyl)-N,N,N-trimethylammonium
TMA-DPH 1-(4-(trimethylamino)-phenyl)-6-phenylhexa-1,3,5-triene
TMA:OT mixed NP monolayer composed of TMA and OT
TMSP 3-(trimethylsilyl)propionic-2,2,3,3-d_4 acid
UV-Vis ultraviolet-visible

Aim of the thesis

In recent decades, nanotechnology-derived materials have been widely used in various areas of daily life, including environmental protection, food industry, medicine, and pharmaceutical industry. Cell membranes play a central role when considering the effects triggered by nanometric particles – or nanoparticles (NPs) – after they come into contact, by accident or design, with the biological environment. Indeed, they represent the initial site of interaction between NPs and living cells, which are found everywhere in our organism. Membrane organization and dynamics selectively drive early cell-matter interactions and determine the fate of NPs on the cell surface. A comprehensive understanding of the nano-membrane interface at the fundamental level can assist the design of versatile biomedical NPs with controlled biological behavior. On the other hand, the encounter between synthetic NPs and cell membranes can alter the membrane structure and function, leading to adverse health effects. Membrane damage is one of the potential mechanisms by which exogenous particles can induce cytotoxicity. In recent years, significant effort has been focused on the study of the physicochemical mechanisms of NP interaction with cell membranes, but the progress made to date is still far from an exhaustive and universally accepted interpretation of these phenomena. This thesis aims to give a new contribution to this fundamental research field.

Cell membranes can be described as complex, highly organized, self-assembled structures whose constituent elements are primarily lipids and proteins. These heterogeneous entities represent a key junction for several cellular mechanisms that are difficult to study separately on a molecular scale. Therefore, in this thesis, we used synthetic phospholipid assemblies as simplified membrane models to investigate selected NP-membrane interactions that would be problematic to isolate on living cells. The use of lipid models lacking protein receptors allowed us to focus only on nonspecific NP-lipid interactions. On the NP side, we opted for surface-modified gold NPs for two main reasons: 1) chemical syntheses available to date allow good control over core size and surface composition, and 2) they are currently involved in numerous biomedical technologies (some already included in clinical trials). In particular, we focused on small gold NPs protected by a mixed monolayer of hydrophobic and hydrophilic thiols. Amphiphilic NPs of this type possess high biomedical potential due to their colloidal stability in the biological environment, their ability to load hydrophobic drugs, and their interactions with cell membranes and other biological entities such as viruses and serum proteins.

Projects

The experimental study described in this thesis is divided into three projects that focus on specific aspects of the NP-membrane interaction that are still debated or poorly addressed.

1. Influence of NP surface charge in interacting with neutral lipid membranes. Once NPs have reached the target cells, NP-membrane interactions are governed by numerous features of both sides. The influence of the sign of the NP surface charge is certainly one of the most investigated aspects, but at the same time also one of the most debated. In this project, we compared the effects on membrane integrity of the interaction with either negatively or positively charged amphiphilic gold NPs. In particular, we used membranes composed exclusively of phosphocholines, ubiquitous zwitterionic (neutral) lipids that represent the most abundant class of membrane components.

2. Effects of NP-membrane interactions on the lateral membrane organization. The segregation of lipids into separate lateral phases of different composition and dynamics represents a functional feature of cell membranes. In this project, the use of multicomponent, phase-separated membranes has been an important step towards the exploitation of more complex and biologically relevant biomimetic membrane models. In particular, we selected a lipid mixture aimed at modeling the neuronal cell membrane. Before this study, very little was known about the effect that NP-membrane interactions have on lipid phase separation.

3. Influence of the degree of membrane fluidity in the interaction with NPs. Membrane fluidity is directly related to lipid dynamics. The latter represents a key feature for the proper functioning of the cellular machinery and exhibits considerable biological variability depending on various parameters, including membrane composition. The interaction between NPs and cell membranes is inevitably modulated by the degree of membrane fluidity. While many investigations have examined the effects that NPs have on membrane integrity and fluidity, very few studies have quantitatively and systematically addressed how the intrinsic variability in lipid dynamics affects the interaction with NPs. Notably, for this project, we relied on fluid membranes with progressive stiffening of lipid dynamics induced by increasing cholesterol content.

In a multidisciplinary scenario, the projects presented in this thesis were addressed experimentally by the candidate by developing the following contributions:

- the optimization of the chemical synthesis of monolayer-protected gold NPs and their characterization by dynamic light scattering, ζ-potential analysis, proton nuclear magnetic resonance, and UV-Vis spectroscopy
- the preparation of model lipid membranes (lipid vesicles and planar bilayers) and their characterization by dynamic light scattering, ζ-potential analysis, and atomic force microscopy
- the application of biophysical techniques – atomic force microscopy, quartz crystal microbalance, and fluorescence spectroscopy – to investigate the behavior of NPs interacting with lipid membranes.

When experimental results were acquired thanks to collaborations, it is explicitly indicated.

Gold nanoparticles. The chemical synthesis and characterization of gold NPs were developed in two laboratories located at the *Department of Chemistry and Industrial Chemistry* (DCCI) of the *University of Genova* and at the *École Polytechnique Fédérale de Lausanne* (EPFL, Switzerland), during an internship in the group of Prof. Francesco Stellacci.

Lipid membranes. The preparation and characterization of model membranes were performed at the *Department of Physics* (DIFI) of the *University of Genova*.

Nanoparticle-membrane interaction. The experimental investigation of NP-membrane interaction was carried out at DIFI for projects 1-2-3 (atomic force microscopy and fluorescence spectroscopy experiments). Part of project 3 (atomic force microscopy and quartz crystal microbalance experiments) was carried out at the *Istituto Italiano di Tecnologia* (IIT, Genoa) working in collaboration with Dr. Silvia Dante (*Materials Characterization Facility*, coordinator Dr. Mirko Prato).

Simulations. For projects 1 and 2, the experimental investigation was developed within a continuous dialogue with results obtained *in silico* by means of Molecular Dynamics (MD) simulations. The computational study was carried out by the group of Prof. Giulia Rossi (DIFI) to interpret at the molecular level the nanoscale mechanisms underlying the NP-lipid interactions under investigation.

Structure of the thesis

The thesis is divided into 7 chapters organized as follows:

Chapter 1 introduces the topics of the thesis. It first addresses a general description of functionalized NPs used in biomedicine and their internalization by cell membranes. It then focuses on ligand-protected gold NPs, with particular emphasis on the amphiphilic NPs used in this work. The last part is devoted to the transition from real cell membranes to biomimetic lipid models, focusing on the behavior of membrane lipids.

Chapter 2 provides a general but fundamental description of the techniques used in projects 1-2-3 to study experimentally the NP-membrane interaction. Other techniques used to perform routine characterizations of NPs and model membranes after preparation are not addressed because they are more widely used in experimental laboratories and their operation is assumed to be commonly known.

Chapter 3 discusses the synthetic procedures employed and optimized to obtain small gold NPs passivated by hydrophobic and hydrophilic thiols. A description of NP characterizations is also reported.

Chapters 4, 5, and 6 report and discuss the results of projects 1-2-3, respectively. Chapter 4 is based on the content of the paper Canepa et al., *Scientific Reports* (2021)[1], while Chapter 5 of the paper Canepa et al., *Nanoscale* (2020)[2].

Chapter 7 finally summarizes the outcomes of project 1 (Chapter 4), project 2 (Chapter 5), and project 3 (Chapter 6). This chapter also speculates on how these results may be used for future studies.

Given the valuable contribution of the *in silico* investigation in interpreting and guiding the experiments of projects 1 and 2, Chapters 4 and 5 conclude with a section summarizing the key computational findings developed by collaborators. While projects 1 (Chapter 4) and 2 (Chapter 5) have been completed, project 3 (Chapter 6) is still in progress and comparison with simulations is not yet available for this study.

Full details of materials and methods (synthesis and characterization protocols, experimental set-ups, data analysis, equipment specifications, etc.) are grouped in Appendices A (nanoparticles), B (lipid membranes), C (atomic force microscopy and quartz crystal microbalance), and D (fluorescence spectroscopy).

1. The nanoparticle-cell interface

1.1 Engineered NPs in biomedical research

Over the last decades, biomedical research has witnessed outstanding results in the application in diagnosis and therapy of engineered NPs – i.e. particles with 1÷100 nm size range and peculiar, well defined physicochemical properties. A wide variety of organic and inorganic NPs with different core material, size, shape, and surface functionalization is currently studied to such purpose (Figure 1)[3].

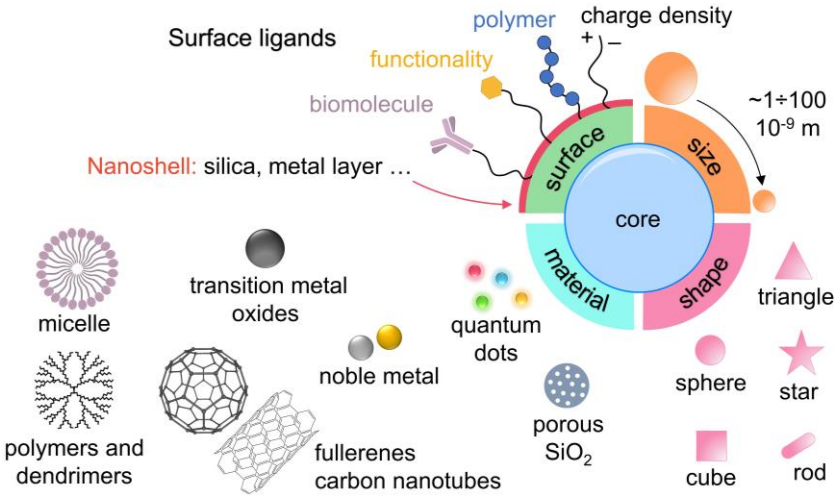

Figure 1. Variability in the rational design of NPs.

The functionalization of NP surface is addressed in the next section.

Functionalized NPs can be used in drug and gene delivery, cancer treatment (e.g. photothermal therapies and magnetic hyperthermia), bioimaging, biosensing (e.g. detection of pathogens and biomolecules), tissue engineering, and so on (Figure 2)[3–5]. For instance, radioactive NPs are exploited in toxicokinetics studies and nuclear nanomedicine[3,6], while magnetic iron oxide NPs are useful for contrast enhancement in magnetic resonance imaging (MRI) and for targeted hyperthermia[3,7]. Currently, plasmonic metal NPs (e.g. gold, silver, and copper) have attracted great interest in a wide range of applications (including biomedicine and environment protection) thanks to their unique optical behavior – i.e. the localized surface plasmon resonance (LSPR) in the UV-Vis/near IR region[8,9]. Noble metal NPs have been extensively studied for biotechnologies based either on their radiative light scattering, such as plasmonic nanoantennas[10] and SERS (Surface Enhanced Raman Scattering) imaging[11], or on their photothermal properties[11,12]. For such applications, the LSPR properties can be accurately tuned by careful selection of surrounding medium conditions (e.g. polarization), NP structural features (e.g. size, shape, and surface chemistry), and NP interaction effects (e.g. controlled interparticle aggregation)[8,9,12].

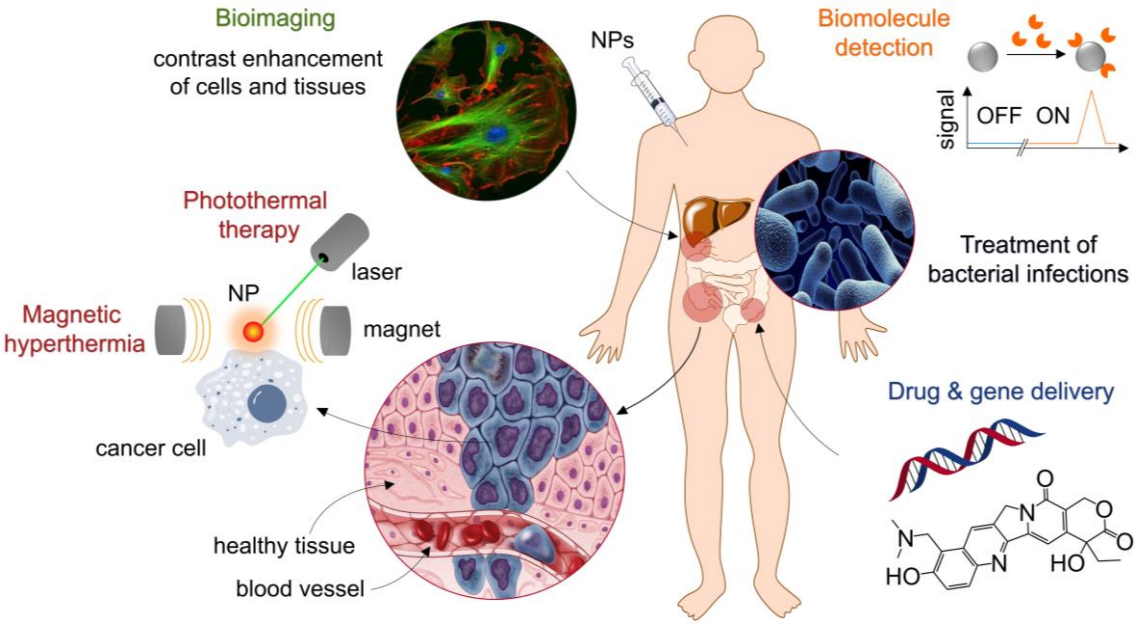

Figure 2. Main applications of NPs in biomedical therapy and diagnosis.

1.1.1 NP surface functionalization

All NPs show a high surface area-to-volume ratio, with surface atoms differing from their bulk counterparts for higher reactivity, free energy, and different electronic state[13,14]. To become stable, the bare surface of NPs spontaneously tends to adsorb organic molecules – defined ligands – that organize into capping layers. Strategies for ligand shell formation onto inorganic NPs are various and flexible, ranging from non-covalent physisorption (e.g. electrostatic adsorption) to chemisorption[14–16]. The latter offers the advantage of stronger NP-ligand binding and thus better stability of ligand shell. Ligands comprise simple or functionalized organic molecules, molecular ions, polymers, and biomolecules (lipids, peptides, carbohydrates, proteins, enzymes, and oligonucleotides such as DNA strands, etc.)[15,17–19]. In general, they significantly alter the interfacial properties of NPs; for instance, charged molecules like citrate ions are usually used to achieve colloidal stability through electrostatic repulsion, while bulky molecules like polyethylene glycol (PEG) chains mainly act as steric stabilizers[19]. Surface functionalization also provides NPs with tailored solubility in water – which is of paramount importance in biomedical technologies – or in organic phase. Depending on ligand nature, ligand shells can be composed of densely packed and highly oriented molecules stabilized by intermolecular forces (e.g. van der Walls interactions) or weakly bound, rather loose, molecules[14,16]. A well-known example of the former case is the formation of self-assembled monolayers (SAMs), i.e. ordered organic assemblies whose molecules exhibit specific affinity for a substrate through terminal chemical functionalities.

Designed manipulation of ligand monolayers has gained remarkable technological interest in nanomedicine[18]. Together with core size and shape, surface functionalization is a key parameter to investigate and control the behavior of NPs in all interactions at the nano-bio interface, which include protein adsorption and cellular uptake[20–26]. In biological media, ligand shells can provide NPs with reliable core protection, long-term colloidal stability, tailored permeation capability, improved biocompatibility and biomimicry, controlled bioaccumulation, reduced immunogenicity, higher blood circulation time, and low toxicity for given applications. Moreover, they are versatile platforms for the bioconjugation of molecular payloads, such as drugs, and targeting ligands, such as antibodies and enzymes[13]. Functionalized NPs show higher efficiency as diagnostic and therapeutic agents, capable of overcoming biological barriers to transport drugs, targeting diseased sites via selective binding to cell membrane receptors, and delivering site-specific therapeutics in the optimal dosage range[27].

1.1.2 Cellular internalization of functionalized NPs

In most biomedical applications, functionalized NPs must be able to enter cells[28–31]. For instance, this is required for NP-assisted intracellular administration of molecules such as oligonucleotides and anticancer drugs[32]. Yet, to reach the intracellular target efficiently, NPs first need to overcome the cell membrane barrier. NP-membrane interactions determine the outcome of NP intracellular transport, thus affecting their biological function. In well-defined experimental conditions, NP uptake by cells only occurs if NP-membrane adhesion is thermodynamically favored[33,34]. Once the NP is adsorbed onto the membrane surface, the highly flexible lipid bilayer elastically deforms to allow for NP internalization[33–36]. The subtle interplay between the energy gain due to attractive adhesion forces and the energy penalty of imposing membrane deformation eventually determines the NP-membrane configuration that minimizes the energy of the system. In particular, the degree of bilayer deformation driving the NP incorporation varies depending on the interactions involved and may result in partial or complete membrane wrapping around NPs[33,34].

In general, the cell membrane employs either passive or active transport mechanisms to exchange substances with the extracellular fluid[28–31]. Passive transport is an energy independent process that requires no energy input, as solutes are able to diffuse freely through the membrane based only on a favorable concentration gradient[37,38]. Simple diffusion across the lipid bilayer is typical of lipophilic molecules (such as many drugs), while some hydrophilic molecules (such as

O_2 and CO_2 gasses) are small enough to passively translocate across specific membrane pores[38]. Since passive diffusion is spontaneous, it cannot be inhibited by cell membranes themselves; this may become toxicologically relevant when cells are exposed to high levels of potentially harmful substances. On the contrary, active transport takes place against the concentration gradient by using energy which is provided by the system. As a further distinction, membrane interactions with foreign substances can be mediated by specific membrane receptors (mainly proteins) or involve direct, nonspecific association with the lipid bilayer.

In eukaryotic cells, endocytosis is an intrinsic fundamental process for active transmembrane transport of exogenous particles, including NPs[39–42]. In this energy-dependent process, particles are wrapped by a small invagination of the cell membrane that finally buds off inside the intracellular space (or cytoplasm) to form a detached vesicle containing the internalized material (Figure 3a-f). According to vesicle size, cargo properties, and mechanism underlying membrane wrapping, endocytosis is divided into phagocytosis and pinocytosis[43]. Phagocytosis (Figure 3a) is a receptor-mediated mechanism exploited only by some specialized cells (macrophages, neutrophils, monocytes, etc.) to engulf and remove very large (≥ 500 nm) particles such as pathogens (bacteria and viruses), cellular debris, or even intact cells. Due to their smaller size, NP internalization via pinocytosis (Figure 3b-f) is way more common. In general, this process is activated by mobile membrane receptors (e.g. clathrin and caveolin) that recognize and selectively interact with NP ligands. Yet, the formation of pinocytotic vesicles can also be nonspecific, i.e. not mediated by ligand-receptor binding (Figure 3f)[44,45]. Some cells such as erythrocytes lack the molecular machinery promoting endocytosis and can only use passive diffusion to internalize NPs; this is also the case of NPs interacting with biomimetic lipid bilayers.

The passive, direct NP translocation across the membrane is regulated by nonspecific NP-bilayer interactions such as van der Waals, electrostatic, hydrophobic interactions, hydration forces, and steric repulsion (Figure 3g)[46]. Within biological systems, nonspecific contributions also comprise thermal and entropic fluctuations[46]. In general, passive NP translocation does not require membrane wrapping to allow for NP internalization[34], and in some cases, it can lead to loss of bilayer integrity by pore formation[47–49]. This behavior prompts a large fluctuation and structural rearrangement of the membrane structure and can represent a direct form of NP cytotoxicity *in vivo* if membrane damage is not transient[50]. In general, passive translocation shows higher delivery efficiency since NPs are free to directly reach the intracellular target without being trapped within endocytic vesicles from which they first have to escape (this step is often preclusive). However, numerous experimental

observations demonstrated that endocytosis is the major entry pathway for functionalized NPs, while passive penetration is generally rarer[51–53]. Several studies have proposed to apply external forces (e.g. electric fields and ultrasounds) to promote direct membrane permeation by biomedical NPs[47].

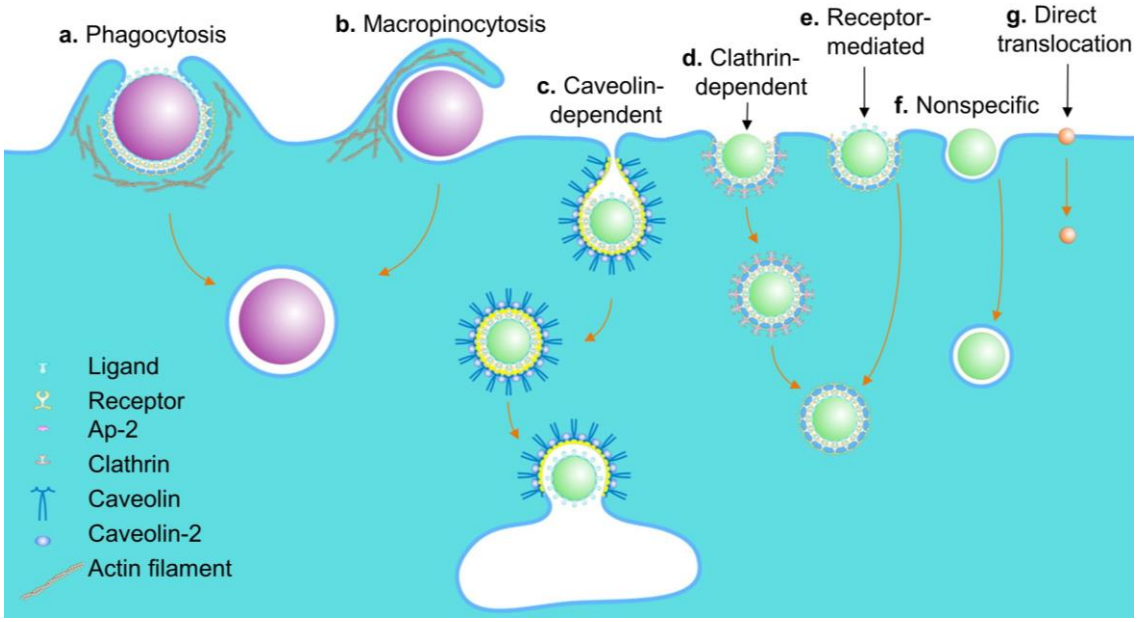

Figure 3. Entry pathways of NPs of variable size within cells; (**b**-**f**) correspond to different types of pinocytosis. Unlike direct, passive translocation illustrated in (**g**), all endocytic mechanisms reported in (**a**-**f**) induce membrane wrapping around NPs and subsequent budding of NP-containing intracellular vesicles. After direct, passive internalization – which is nonspecific (i.e. nonmediated) – free NPs are directly released into the cytoplasm (**g**). Reprinted (adapted) with permission from[45]. Copyright (2015) American Chemical Society.

Cellular mechanisms for NP internalization (and related uptake rate) strongly depend on the interplay of several NP physicochemical properties, such as size, surface charge, hydrophobicity, shape, and surface roughness and stiffness[44,54–56]. Core size is one of the key parameters governing NP cellular uptake[34]. Broadly, NPs with core sizes ranging from tens to hundreds of nm are usually internalized via endocytic processes, while for smaller NPs (usually sub-10 nm) passive translocation becomes more favorable. Thermodynamic calculations demonstrated that the energy cost for membrane wrapping around a single NP increases as the core size diminishes. Thus, endocytosis of very small NPs becomes energetically unfavorable because vesicle formation would induce higher elastic deformation of the membrane[57,58]. Roiter et al.[48,49] reported that extremely small silica NPs (< 1.2 nm) can passively penetrate synthetic lipid bilayers without damaging the membrane, while they form pores when their size increases from 1.2 to 22 nm. Oppositely, the membrane tends to wrap NPs larger than 22 nm, thus hindering direct translocation. In general, the effect of NP size is never isolated and should be considered in combination with other

nanostructural parameters, such as surface charge. Jiang et al.[25] reported that the quantitative cellular uptake of 2-4-6 nm AuNPs strongly depends on the presence of neutral (zwitterionic), anionic, or cationic ligands. In the case of zwitterionic and anionic NPs, the uptake was found to decrease by increasing the NP size, while for cationic NPs the behavior was the opposite. The authors attributed this contrasting tendency to a change in the internalization mechanism (from passive diffusion to multiple endocytic pathways) triggered by the sign of NPs. Another diversification in cell uptake between cationic and anionic NPs was observed by Sokolova et al.[59] using calcium phosphate NPs ten times as large (~120 nm). In other cases, direct NP translocation has been observed for both anionic and cationic NPs regardless of the sign[47], suggesting that surface charge may not be so determinant for such entry pathway. In general, NP surface charge (and charge density) is believed to affect the outcome of NP-cell interactions, especially when the NP sign is opposite to that of membrane bilayer or some membrane components such as protein domains. Electrostatic attraction can promote NP adsorption onto the membrane, and the sign of the NP surface charge can contribute to the potential toxicity of NP-membrane interactions, which usually identifies with destructive NP translocation. Although still debated, some observations seem to suggest that cationic nanomaterials (including AuNPs) induce stronger perturbation on lipid membranes than their anionic counterparts, and thus potentially higher toxicity[60–63]. Moreover, our group recently showed that not only the NP charge affects the NP-membrane interaction, but also it is the other way around. Indeed, Salassi et al.[64] reported that passive NP translocation within the membrane can induce spontaneous protonation of anionic carboxylate groups on the NP surface. The change of NP surface potential is found to be responsible for a faster and less disruptive interaction with the lipid bilayer[64].

Besides electrostatic interaction, the degree of hydrophobicity/hydrophilicity of NPs is another important nonspecific factor governing NP-cell interactions due to the amphiphilic nature of most membrane components[47,53]. Since the membrane core acts as a hydrophobic barrier to the passive diffusion of hydrophilic molecules, water-soluble NPs are typically endocytosed. More generally, NPs with different degrees of hydrophobicity exhibit various interaction mechanisms with the membrane bilayer, ranging from surface adsorption to direct permeation[65,66]. NP shape can also bias the mechanism and efficiency of NP incorporation, with spherical NPs generally favored over their rod or cylindrical-shaped counterparts of the same size[67–69]. Furthermore, even a small variation in the aspect ratio of anisotropic shapes can induce considerable differences in the uptake rates[68]. Even the NP surface roughness and stiffness can modulate NP-cell interactions. In some cases, the presence of a smooth NP surface

was found to increase the membrane wrapping efficiency in active pathways, which on the contrary was hindered by bumpy NPs of the same material and size[49]. Surface softness or rigidity, in turn, have been often found to define the adhesion energy needed for membrane wrapping[57]. Most NP surface properties like charge sign and density, roughness, rigidity, and hydrophobic content can be tuned by designed choice or manipulation of ligand shells (Section 1.1.1). Indeed, surface functionalization is a common and effective strategy to engineer tailored NP-membrane interactions. For instance, numerous ω-functionalized ligands, polymers, and peptides have been found to favor direct NP penetration into cells[47].

Together with NP properties, also membrane features (e.g. surface potential, composition, physical state, elasticity, thickness, surface tension, and lateral heterogeneity) strongly affect the cellular uptake of NPs[26,44,53]. Moreover, membrane electrical and mechanical properties significantly depend on the environmental conditions (e.g. temperature, pH, viscosity, and ionic strength) which in turn can thus modify the internalization ability of cells[47,53]. The latter is also sensitive to the formation of protein corona on NPs exposed to serum[70]. Adsorbed proteins can either trigger receptor-based entry pathways[71] or drastically hinder cell uptake[72]. Over the years, a number of studies probing NP-membrane interactions has assisted the rational design of functionalized NPs with the tailored capability to enter cells via non-harmful, passive or active, mechanisms[40]. Together with experiments, computational techniques such as MD simulations have been extensively exploited to investigate at molecular level the different NP translocation pathways across cell membranes[73,74]. Despite numerous results, the key parameters for driving and controlling these processes are still far from clear and more effort is needed for a better understanding. Within this scenario, this thesis has been focused on the study of nonspecific NP-lipid membrane interactions driving the passive uptake of sub-6 nm amphiphilic – anionic or cationic – gold NPs.

1.2 Gold NPs in the biological environment

Ligand-protected gold NPs (AuNPs) have gained central importance in biomedical research[32,75,76]. The tunable LSPR behavior of the gold (Au) core is used both in diagnostic (*in vitro* sensing and *in vivo* imaging[77,78]) and therapy (delivery applications[79–81] and plasmonic therapies[81–83]). Some of these applications have already entered clinical trials[84,85], while others have been successfully commercialized as new tools for clinical diagnosis and drug discovery[86]. This technological success is supported by the remarkable stability and biocompatibility of the Au core in the

biological environment and by the wide availability of synthetic approaches allowing for good control over Au core formation and surface functionalization.

1.2.1 Ligand-protected gold NPs

Ligand-protected AuNPs are mainly synthesized using bottom-up approaches based on the chemical reduction of Au(III) salts in solution. Freshly generated, metallic Au(0) atoms form atomic clusters that rapidly aggregate into nanosized particles[87] in the presence of stabilizing agents. By passivating the growing Au nuclei, ligands govern the kinetics of NP growth. They inhibit and regulate inter-atom and inter-particle aggregation, thus defining nanostructural features such as core size (and relative polydispersion) and shape. For instance, AuNPs can be generated in the form of spheres, rods, cubes, stars, and cages. Core parameters (and their homogeneity) are also sensitive to reaction conditions such as pH, temperature, solvent, and reducing agent (type, concentration, and addition speed and mode)[88,89]. Both biological and physicochemical behavior of AuNPs (including the LSPR band) strongly depends on the interplay of core size, shape, and surface functionalization. The latter is particularly important to tune NP interfacial features such as solubility, chemical reactivity, surface charge, hydrophobicity, biocompatibility, and binding affinity to biological entities. This explains why bottom-up strategies have witnessed intensive efforts over the years for the development of novel chemical protocols to obtain ligand-protected AuNPs with controlled size, shape, and surface chemistry[88,90–94].

The first chemical synthesis of spherical ligand-protected AuNPs dates back to 1951 when citrate-stabilized AuNPs were reported by Turkevich et al.[95]. Further studies allowed refining this procedure to obtain controlled NP diameter in the 5÷150 nm range by varying the gold-to-citrate feed ratio[88,96]. The stabilization of AuNPs by thiols, introduced with the Brust-Schiffrin method in 1994[97,98], marked a breakthrough in the chemical synthesis of spherical AuNPs with reduced core size (1.5÷5.2 nm). Thiols readily form SAMs on a gold surface by chemisorption through covalent Au-S bonds[14,99]. Fine control of NP diameter is achieved by adjusting the Au(III):thiol ratio and the reduction temperature[100,101]. The original procedure dealt with the synthesis of hydrophobic AuNPs coated by 1-dodecanethiol; later, a wide range of alkyl chain lengths (C3÷C24) and apolar ω-functionalized alkylthiols was successfully tested by minor modifications[101]. Compared to other ligand shells, thiols exhibit peculiar stability due to synergistic contributions of the strong gold-sulfur affinity and the attraction between adjacent alkyl chains (mainly van der Waals and hydrophobic forces). The overall effect of thiol features (e.g. tail functional group and chain length) on final NP properties has been elucidated in numerous studies[101,102].

Since thiol passivation only yields AuNPs smaller than ~6 nm, ligands with a faster desorption rate from the Au core (e.g. citrate ions) are used to obtain larger core sizes. Following the first Brust-Schiffrin syntheses, a plethora of effective ligand place-exchange reactions was developed to broaden the functionalization strategies of small AuNPs[14,101,103,104]. In thiol-for-thiol ligand exchange, original alkylthiols are partially replaced by new thiolated species in a dynamic equilibrium process to obtain mixed monolayer-protected AuNPs for synergistic applications. The exchanging efficiency depends on the interaction time and ligand (molar) feed ratio. Ligand exchange with alkythiols featuring polar (e.g. charged) headgroups proved very useful to obtain sub-6 nm water-soluble AuNPs exploitable in biomedical applications[105,106]. Over the years, both the gold-sulfur interface and the evolution of ligand shell structure in place-exchange reactions have been widely investigated[107–112]. In general, ligand exchange turned simple alkythiolated AuNPs into versatile synthetic platforms with decoupled control over NP core formation and surface manipulation (Figure 4). Since the complete thiol-for-thiol exchange is never achievable due to the strong Au-S affinity, weakly bound stabilizers (e.g. phosphines, amines, and carboxylate ions) are preferred when a totally replaced ligand shell is desired[14].

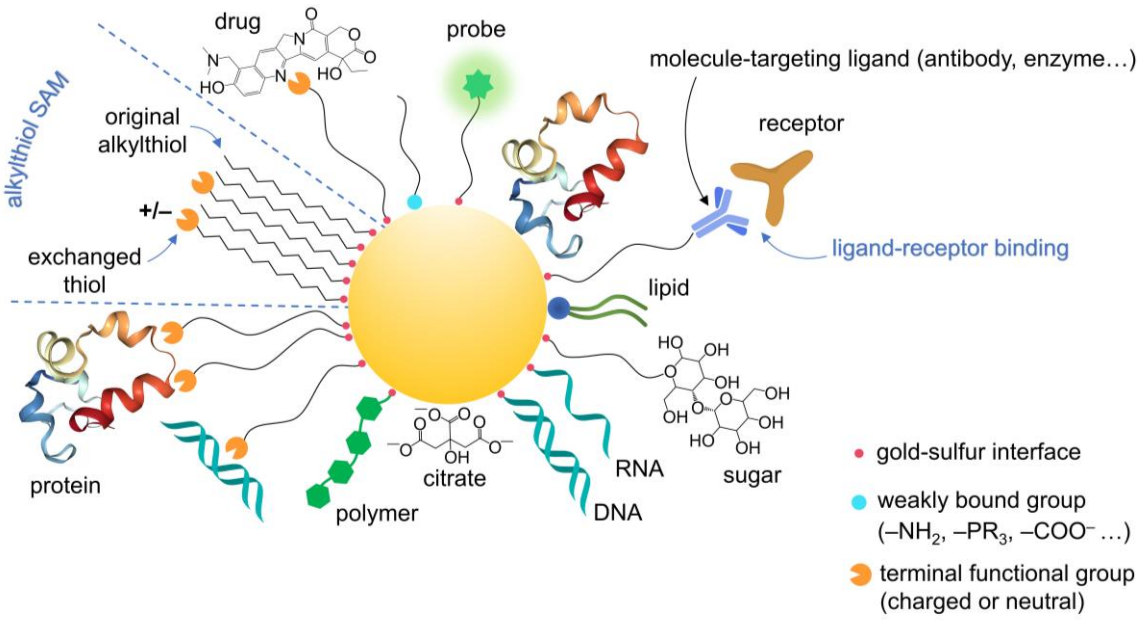

Figure 4. Functionalization possibilities of ligand-protected AuNPs (not to scale). Molecule-targeting ligands are introduced to selectively recognize cell surface receptors. In general, non-covalent conjugation is desirable when facile molecule release (together with process reversibility) is required (e.g. in sensing and delivery technologies). Oppositely, covalent conjugation is preferred when a stable gold-ligand complex is required (e.g. in imaging).

More recently, numerous other organosulfur compounds than alkylthiols have been reported to form homo- or hetero-ligand SAMs on AuNPs[94,113]. These include thiol-modified polymers (e.g. thiol-PEG) and biomolecules such as cysteine and

glutathione. In addition to ligand exchange, other strategies for tailoring the surface of AuNPs include ligand modification via chemical reactions, covalent conjugation of molecule-targeting ligands, and non-covalent adsorption of biomolecules based on specific binding affinity (e.g. electrostatic or hydrophobic interactions)[14,15,94]. As shown in Figure 4, these processes allow combining functionalized AuNPs with drugs, oligonucleotides, proteins, antibodies, enzymes, and fluorescent dyes for imaging applications (to name a few)[15,88,92]. If properly thiol-modified, these molecules – regardless of their steric size – can be directly grafted onto AuNPs without the need for the interposition of other ligands (Figure 4)[15,92,114].

1.2.2 Case study: amphiphilic gold NPs

The wide functionalization versatility of the Au core is precious to tune the behavior of ligand-protected AuNPs in the biological environment[70]. In particular, ligand hydrophobicity and surface charge are both decisive in governing nonspecific NP-bio interactions[23,115–119]. When coupled, the hydrophobic and electrostatic contributions provide the functionalized particle with amphiphilic behavior, as in the case of the thiolated AuNPs used in this thesis. Thiol passivation was chosen to obtain spherical NPs with core diameter ranging between ~2÷6 nm, a size compatible with passive NP translocation within lipid bilayers. Surface amphiphilicity was obtained by variably mixing the apolar alkylthiol *1-octanethiol* (OT) with another thiol featuring both an apolar alkyl chain and a terminal charged headgroup, i.e. the anionic *11-mercapto-1-undecanesulfonate* (MUS) or the cationic *(11-mercaptoundecyl)-N,N,N-trimethylammonium* (TMA) (Figure 5). Hereafter, these NPs will be referred to as MUS:OT and TMA:OT AuNPs.

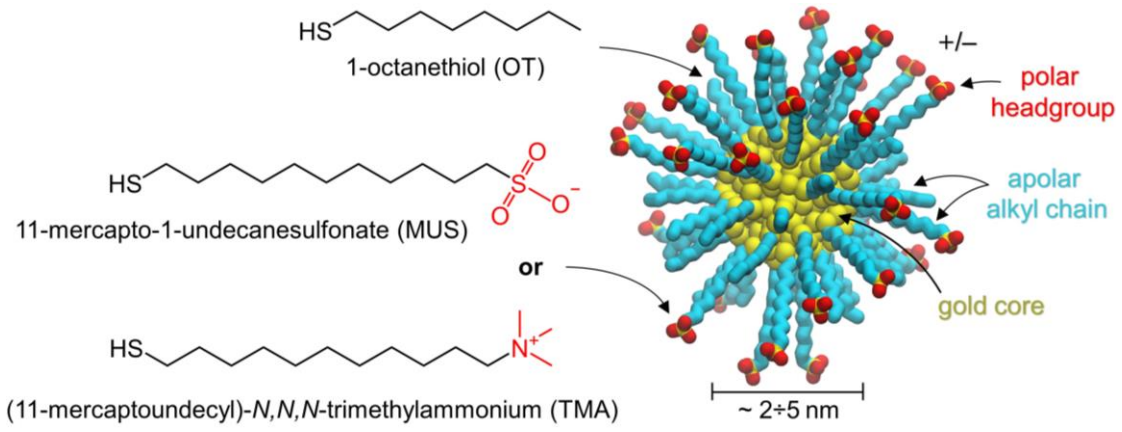

Figure 5. Cartoon of amphiphilic AuNPs used in the experiments described in this thesis. Anionic and cationic AuNPs were functionalized by MUS:OT and TMA:OT mixtures, respectively. Sulfonate ($–SO_3^-$) and trimethylammonium ($–N(CH_3)_3^+$) headgroups were used to impart colloidal stability in water by electrostatic repulsion. NP charge density depends on the number of ω-charged ligands.

MUS and TMA, both comprising a C11 alkyl chain, were selected to disentangle those effects due to charge sign from those due to other physical parameters, such as chain length and flexibility. Notably, even when capped by solely MUS or TMA, AuNPs exhibit amphiphilic features due to the presence of such alkyl moieties. The MUS:OT or TMA:OT stoichiometric ratio defines the NP colloidal stability in aqueous solution[120]. In both MUS:OT and TMA:OT AuNPs used in this thesis, the amount of charged alkylthiol is at least twice as much as OT (i.e. less than 33 mol % OT) to ensure long-term colloidal stability in ultrapure water and saline buffered solutions at pH 7.4[121].

1.2.3 Amphiphilic gold NPs and cell membranes

Numerous amphiphilic proteins stably and nondisruptively reside within cell membranes[122]. Amphiphilicity is also a distinguishing feature of most cell-penetrating peptides (CPPs), i.e. short peptides alternating polar (cationic) and apolar amino acids and capable of efficiently penetrating multiple types of cells to deliver macromolecules (proteins, nucleic acids, etc.)[123]. In some cases, even large NPs can directly translocate into cells when bound to CPPs, thus escaping endocytic pathways[53]. Depending on the peptide, energy-dependent endocytosis and passive translocation have been suggested as the two main mechanisms involved in CPP internalization[123–126]. Direct CPP translocation requires the interplay of nonspecific electrostatic and hydrophobic effects[46,124]. Broadly, CPP cationic residues initially interact with negatively charged membrane components (e.g. the phosphate groups of the lipid bilayer), while the hydrophobic moiety translocates into the hydrocarbon region of lipid tails. Over the years, amphiphilic CPPs and transmembrane proteins have inspired an extensive investigation on the role of electrostatics and hydrophobicity in driving and affecting nonspecific NP-cell membrane interactions. Similar to these biological entities, several synthetic nanomaterials with amphiphilic features were found to spontaneously penetrate lipid membranes, revealing the possibility to be used for intracellular delivery of hydrophobic drugs and imaging technologies[53]. This is the case of the negatively and positively thiolated AuNPs used in this thesis (Section 1.2.2). In particular, the core size distribution (~2÷6 nm) and surface composition of such amphiphilic AuNPs have become a reference for the study of nonspecific NP-membrane interactions[26,61,127–132].

○ Negatively charged MUS:OT AuNPs

Over the last decades, small water-soluble AuNPs coated by MUS and OT ligands have been extensively studied for biomedical applications. Notably, they have

been consistently shown *in vitro*[26,133–138] and *in vivo*[139] to spontaneously and nondisruptively penetrate the cellular membrane of various mammalian cells via energy-independent diffusion. Passive cellular uptake of MUS:OT AuNPs was observed both at physiological temperature and at 4 °C, at which temperature energy-mediated endocytosis is inhibited[133,135]. Even at 37 °C, after treating cells with endocytosis inhibitors, NPs were found to abundantly permeate cell membranes[135]. Proof of direct NP translocation is also given by erythrocytes, which are naturally non-endocytic cells[137]. At physiological temperature, NP incorporation by cell membranes occurs rapidly in a time scale of few minutes or even less[135]. After first observations in cells, passive and nondisruptive permeation of MUS:OT AuNPs was systematically observed also into biomimetic lipid bilayers composed of neutral zwitterionic phosphocholines in the fluid phase (Figure 6)[127,140–142]. Moreover, 1:1 MUS:OT NPs with core size in the 2-3 nm range were reported to induce significant hemifusion between fluid membranes of lipid vesicles[142], while full fusion is achieved upon addition of calcium ions[143]. Recently, 2:1 MUS:OT AuNPs of similar size have been successfully used as a broad-spectrum non-toxic antiviral agents[144]. In all cases, the hydrophobic content, charge density, and the core size of such NPs proved fundamental in determining their nano-bio interactions.

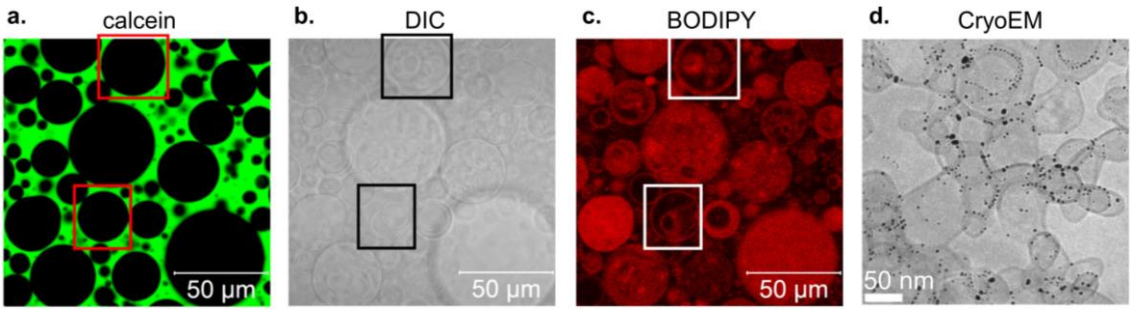

Figure 6. a,**c**) Confocal and **b**) Differential Interface Contrast (DIC) images of BODIPY-labeled (red fluorescence) 1:1 MUS:OT AuNPs (2.2. nm core size) incubated with giant multilamellar vesicles (1,2-dioleoyl-*sn*-glycero-3-phosphocholine) surrounded by the membrane-impermeable dye calcein (green fluorescence). After NP-membrane interaction **a**) calcein emission is recorded only outside vesicles and **c**) BODIPY emission is localized to both interior and exterior membranes of multilamellar vesicles. **d**) CryoEM image of 1:1 MUS:OT AuNPs (2.6 nm core size) incubated with vesicles of the same composition as in (**a**-**c**). This experimental evidence clearly shows that MUS:OT AuNPs do interact with the lipid bilayer in a passive and nondisruptive manner. Reprinted (adapted) with permission from[141] (**a**-**c**) and from[142] (**d**). Copyright (2013) (**a**-**c**) and (2018) (**d**) American Chemical Society.

The molecular mechanism of MUS:OT NP insertion into lipid bilayers has been elucidated by coarse-grained and atomistic MD simulations[129,141,145–147]; similarity has been proposed with the membrane incorporation of amphiphilic transmembrane proteins[145]. Despite this process is favored by the reduction of hydrophobic ligand surface exposed to water upon NP displacement from solvated

to embedded state, in principle, it should be considered energetically unfavorable due to charge insertion into the hydrophobic core of the bilayer. Yet, a key feature of small (sub-10 nm) AuNPs is the large portion of free volume available for each surface ligand, which provides considerable conformational flexibility[148]. This allows ligands to deform when entering the bilayer, favorably shielding apolar alkyl chains of both OT and MUS within the hydrocarbon lipid tail region, while positioning the charged sulfonate moieties at the polar aqueous interface. Such ligand reorganization, commonly referred to as "snorkeling" when observed in transmembrane proteins[149,150], is schematically illustrated in Figure 7a. According to MD simulations, the anchoring mechanism leading to final snorkeling configuration is based on sequential translocation of charged groups across the bilayer (Figure 7b)[129,146,147]. Although the overall NP anchoring within the membrane is highly favorable from a thermodynamic point of view, the flipping of each charged terminal group is limited by the overcoming of an energy barrier[146,147]. The energy cost of ligand translocation has been estimated to be similar[146] or lower[147] than the cost of single monovalent ion translocations, depending on ligand nature and organization on the NP surface, on membrane lipid composition, and on the force field used to perform the free energy calculation[64]. Notably, both *in silico* and experimental evidence suggests that the presence of defects in lipid packing, e.g. hole edges in supported lipid bilayers[127], can greatly reduce the cost of NP anchoring within the bilayer. Besides ligand snorkeling, the NP transmembrane state also benefits from bilayer elastic deformation near the NP interface to match the hydrophobic surface of the anchored NP (Figure 7a).

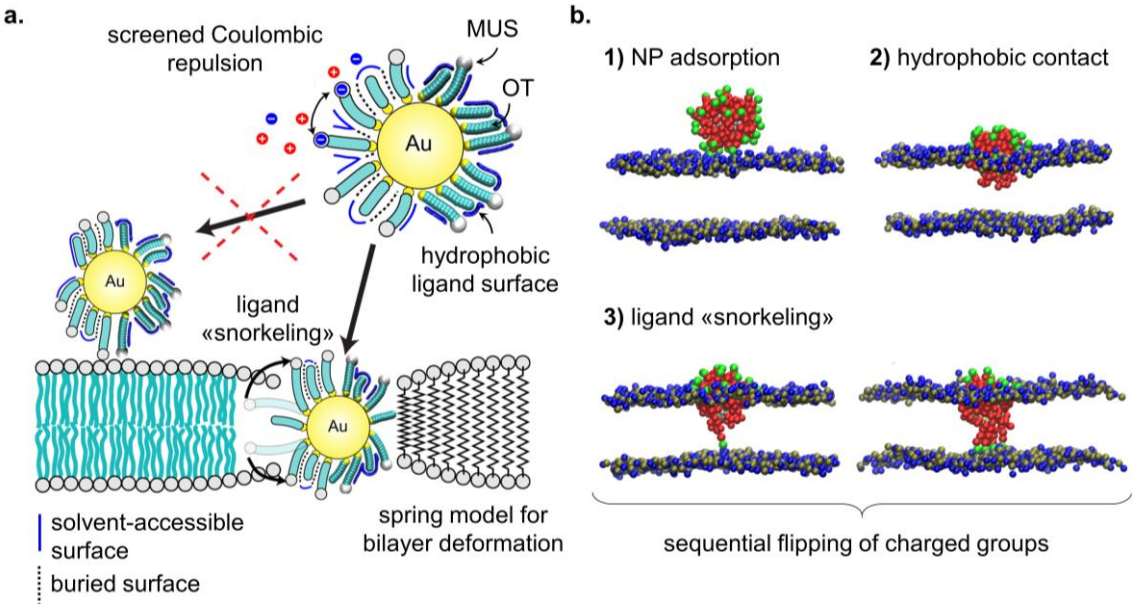

Figure 7. Cartoon and simulation snapshots depicting the nonspecific MUS:OT AuNP-bilayer interaction. **a**) Instead of adopting a surface-adsorbed state stabilized by electrostatic interactions, NP is passively embedded by the bilayer. The final NP transmembrane state, stabilized by ligand

snorkeling, is illustrated. **b**) In detail, regardless of MUS:OT ratio, the NP uptake is a three-steps process: **1.** NP adsorbs onto the bilayer surface, **2.** hydrophobic contact between the hydrophobic ligand surface and the lipid tails triggers partial NP embedding into the membrane core (NP insertion into the entrance leaflet is driven by spontaneous protrusion of a solvent-accessible lipid tail)[127], and **3.** part of charged ligand terminals are translocated one by one to the lipid head region of the opposite leaflet to stabilize the NP-membrane complex in the final snorkeling configuration. NP hydrophobic and charged beads are shown in red and green, respectively; lipid heads in blue (choline) and tan (phosphate) (lipid tails, water, and ions are not illustrated). Reprinted (adapted) with permission from[141] (**a**) and from[129] (**b**). Copyright (2013) (**a**) and (2015) (**b**) American Chemical Society.

Considering this NP insertion pathway, some important considerations follow. Since ligand flexibility decreases as the NP core diameter increases, there is a threshold size above which snorkeling is severely hindered and insertion no longer occurs[141]. Carney et al.[140] demonstrated experimentally that 2:1 MUS:OT AuNPs spontaneously penetrate fluid lipid bilayers only when the core size is less than ~6.5 nm. Oppositely to ligand flexibility, larger core size proportionally increases the NP hydrophobic surface area exposed to water and driving the NP embedding. The competition between ligand snorkeling ability (reduced by larger NP size) and hydrophobic contact (reduced by smaller NP size) is thus compensated at intermediate core sizes at which the tendency of NP passive penetration is maximized. Interestingly, both experiments and simulations show that the NP size thresholds at which direct and stable insertion into lipid bilayers is either maximized or arrested are composition-dependent[141]. In the case of this thesis, two different MUS:OT ratios are considered for NP-membrane experiments: ~80 % and ~68 % MUS (i.e. 4:1 MUS:OT and 2:1 MUS:OT, respectively). Van Lehn et al.[141] accurately demonstrated that 2:1 MUS:OT AuNPs interacting with fluid bilayers report maximized uptake at ~3.5 nm core size and arrested uptake above ~6.5 nm (in agreement with[140]). By reducing the number of charged ligands (e.g. 1:1 MUS:OT ratio), both sizes increase, while by removing OT ligands (i.e. for the all-MUS monolayer) they decrease to ~2 nm and ~3.5 nm, respectively. Basically, the higher the hydrophobic content of the ligand shell exposed to the membrane, the wider the NP size range allowing for passive uptake. This trend allows predicting that the 4:1 MUS:OT composition used in this thesis lies somewhere in between the 2:1 MUS:OT and all-MUS cases, with a ~2÷3 nm core size as the most favorable for NP insertion. Several experimental results on cells match these size thresholds: indeed, abundant passive uptake of 2:1 MUS:OT AuNPs has always been observed in the core range of ~2÷6 nm, while all-MUS AuNPs of ~4.5 nm in diameter were only endocytized[133,135].

○ Positively charged TMA:OT AuNPs

In biomedical research, small positively charged TMA:OT AuNPs do not share the same popularity as anionic MUS:OT AuNPs of similar size. This is mainly

due to previous experimental data *in vitro* suggesting that cationic NPs – mostly assisted by some degree of hydrophobicity – can translocate through cellular membranes inducing permanent or transient loss of bilayer integrity, for example, through nanoscale poration or changes in membrane permeability. This is the case, among others, of polycationic polymeric NPs[151] or positively charged quantum dots coated by amphiphilic thiols[152]. In general, the extent of membrane damage is shown to depend on NP size and charge density[151], and usually, it is not observed using similar amphiphilic NPs bearing anionic charge. For instance, Verma et al.[133] reported that the viability of dendritic cells after incubation with ~6 nm all-TMA AuNPs is remarkably more reduced than with 2:1 MUS:OT AuNPs of similar size due to pore formation in the membrane. Partial membrane disruption by TMA-coated AuNPs (~2÷3 nm core size) was also observed by Montis et al.[153] in eukaryotic macrophages. These results seem to deviate from the behavior of several polycationic amphiphilic CPPs capable of penetrating cell membranes without affecting their structural integrity[154]. Moreover, amphiphilic AuNPs variably coated by TMA and OT mixtures, featuring ~2 nm core size, proved to efficiently transfect mammalian cell cultures without alarming toxic implications[155]. Notably, 2:1 TMA:OT AuNPs – about the same composition used in this thesis – reported the highest transfection efficiency[155].

To provide insight into the interaction between small TMA:OT AuNPs and cell membranes, several studies have focused on biomimetic lipid bilayers composed of neutral zwitterionic phosphocholines. Although NP effects on membrane stability are still debated, there is a general consensus about the favorable passive NP-bilayer interaction. For instance, by means of calcein-leakage assays, Goodman et al.[61] reported that 2:1 TMA:OT AuNPs of ~2 nm core size can induce low dye release upon passive penetration into fluid phase vesicles. Using similar membranes but in the stiffer gel phase, neutron reflectometry experiments by Tatur et al.[130] and Lolicato et al.[132] demonstrated that the same AuNPs spontaneously and stably penetrate into the lipid tail region only when the bilayer fluidity increases by the effect of temperature. Moreover, the authors show that gradual destabilization of membrane integrity occurs only if the temperature is further increased to facilitate the passive embedding of more and more NPs. These results highlight the importance of membrane fluidity in favoring a passive, controlled, and thus safe uptake of small TMA:OT AuNPs. *In silico* simulations have also been performed to investigate the insertion pathway of cationic AuNPs, variably coated by amphiphilic thiol monolayers, within zwitterionic lipid bilayers[132,156–158]. On a molecular level, the formation of an irreversible NP-membrane complex is found to be either spontaneous or modulated by a small free energy barrier. As demonstrated experimentally by ref[130,132], the latter

can be overcome by increasing the temperature. Interestingly, simulations suggest that the incorporation of cationic TMA:OT AuNPs (~2÷6 nm core size) within the lipid bilayer follows the same mechanism previously described for MUS:OT AuNPs (Figure 7)[132]. Therefore, NP-membrane interactions are expected to lead to a final NP transmembrane configuration where ligand alkyl chains are buried within the hydrocarbon core of the bilayer, while cationic trimethylammonium groups – divided between the two membrane leaflets – extend toward the polar aqueous interface.

1.3 Cell membranes: from real systems to bioinspired models

Focusing on the behavior of membrane lipids in the biological environment, this section addresses the transition from real cell membranes to bioinspired synthetic models.

1.3.1 The cell membrane

The cell membrane, or plasma membrane, is a thin barrier separating the cytoplasm from the extracellular fluid. By anchoring the cytoskeleton, it provides the cell with shape and mechanical resistance, thus protecting its integrity. Due to its selective permeability, it contributes to regulating cellular metabolism by controlling the flow of species (e.g. ions, nutrients, breakdown products) entering and exiting the cell. It also plays an important role in endocytosis and exocytosis and facilitates communication and signaling between cells. In 1972, Singer and Nicolson first proposed the theory of the *fluid mosaic model* to explain the complex structure of plasma membranes[159]. Although this model has been improved in terms of structural complexity over the years, it still provides a robust basic description of the organization and dynamics of biological membranes[160]. As shown in Figure 8, the membrane structure is depicted as an ensemble of components embedded in a bulk matrix of phospholipids self-associated into a lipid bilayer with fluid-like properties. This fluidity is vital to the healthy functioning of most membrane processes. In weight, lipids constitute about 50 % of most animal cell membranes, nearly all of the remainder being integral and peripheral membrane proteins (by number, the ratio is ~50 lipids/protein). Plasma membranes also accommodate considerable amounts of cholesterol and minor percentages of carbohydrates bound either to proteins (glycoproteins) or lipids (glycolipids). The exact membrane composition depends on the species and type of cell and is sensitive to changes induced by molecular fluctuations and variations in the surrounding biological environment.

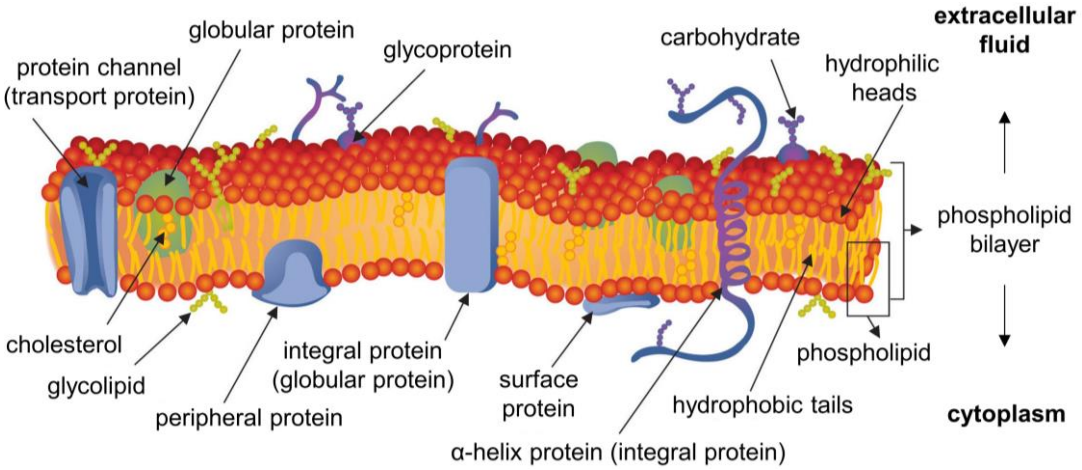

Figure 8. Schematic cartoon of the fluid mosaic model for the structure of cell membranes.

1.3.2 Membrane lipids

Eukaryotic cells invest outstanding resources in synthesizing a complex repertoire of membrane lipids with remarkable chemical and functional diversity[161,162]. As the main membrane building blocks, they are fundamental players in barrier function. Besides, they take part in cell division, gamete fusion, and intracellular membrane trafficking, contribute to aggregation and dispersion mechanisms of some membrane proteins, and participate in signal transduction and molecular recognition processes[161]. Though we understand most functions of membrane lipids, many of their roles have yet to be fully elucidated[161,162]. In mammalian cells, the main membrane lipids are *glycerophospholipids*, *sphingolipids*, and *sterols*. As an example, the lipid composition of erythrocyte membranes of different mammals is shown in Table 1.

Table 1. Lipid composition (weight %) of the plasma membrane of mammalian erythrocytes[163].

Lipids		*Species*					
		human	*pig*	*cat*	*rabbit*	*horse*	*rat*
Glycerophospholipids	phosphatidylcholine	17.5	13.9	18.7	22.3	22.0	31.8
	phosphatidylethanolamine	16.6	17.7	13.6	21.0	12.6	14.4
	phosphatidylserine	7.9	10.6	8.1	8.0	9.4	7.2
	phosphatidylinositol	1.2	1.1	4.5	1.0	< 0.2	2.3
	phosphatidic acid	0.6	< 0.2	0.5	1.0	< 0.2	< 0.2
	lysophosphatidylcholine	0.9	0.5	< 0.2	< 0.2	0.9	2.6
Sphingolipids	sphingomyelin	16.0	15.8	16.0	12.5	7.0	8.6
	glycosphingolipids	11.0	13.4	11.9	5.3	23.5	8.3
Sterols	cholesterol	26.0	26.8	26.8	28.9	24.5	24.7

Glycerophospholipids are the major structural components of plasma membranes. Their chemical structure is composed of a backbone of glycerol esterified to two long-chain fatty acids and to a negatively charged phosphate group, which in turn is

esterified to a terminal alcohol (Figure 9a). Common alcohols of natural glycerophospholipids are reported in Figure 9b; their names define specific subfamilies: phosphatidyl-cholines (PC), phosphatidyl-ethanolamines (PE), phosphatidyl-serines (PS), phosphatidyl-inositols (PI), and phosphatidyl-glycerols (PG). All glycerophospholipid species (PC, PE, etc.) naturally occur in the form of mixtures including dozens of saturated or unsaturated fatty acids, which vary in chain length (normally 14÷24 C atoms), number and type (*cis* or *trans*) of unsaturations, and in bonding position to the glycerol carbons. The predominant mammalian glycerophospholipids are PCs, followed by PEs and PSs (Table 1)[161,164]. Notably, PCs account for more than 50 % of all phospholipids in most eukaryotic membranes[161]. Other membrane glycerophospholipids, far less abundant, show some structural variations. For example, lysophospholipids (e.g. lysophosphatidylcholine) have only one fatty acid. All glycerophospholipids are amphiphilic: the phosphate and the terminal alcohol form the polar head, the hydrocarbon chains of the fatty acids represent the apolar tails, and the glycerol backbone reside at the interface between the hydrophilic and the hydrophobic region (Figure 9). Glycerophospholipids can be either zwitterionic (e.g. PC and PE) or anionic (PS), based on the net charge of the headgroup at physiological conditions (cationic heads do not exist in nature).

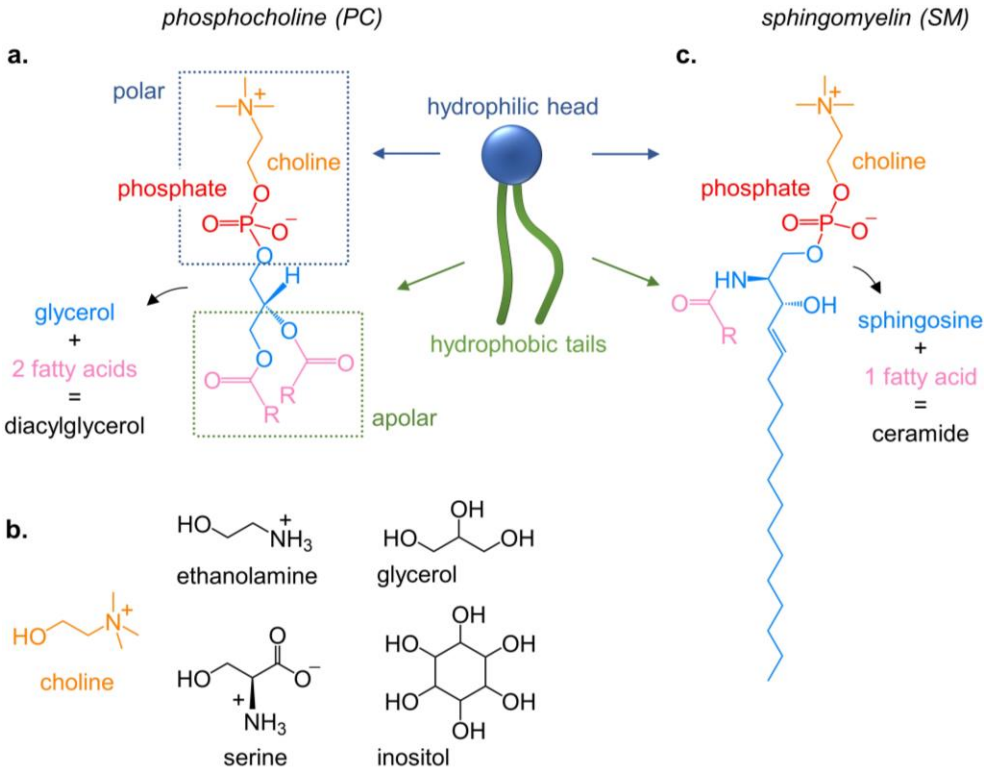

Figure 9. Chemical structures of **a**) a generic glycerophospholipid, **b**) terminal alcohols at physiological pH, and **c**) a generic phosphosphingolipid. In all sphingolipids, the hydrophobic ceramide takes the structural role of diacylglycerol in glycerophospholipids. In the center: a simplified representation of the amphiphilic structure shared by all glycerophospholipids and sphingolipids.

Sphingolipids include 1) *phosphosphingolipids* and 2) *glycosphingolipids*. The backbone of their structure is a sphingoid base, a long-chain aminoalcohol[165,166]. In mammals, the most common sphingoid base is sphingosine, which in turn is amide-linked to a fatty acid to form a ceramide (Figure 9c). The chain length of ceramide fatty acids usually ranges between 14÷30 (or more) C atoms (on average, it is somewhat longer than that of glycerophospholipids). Ceramide fatty acids are predominantly saturated and, in general, polyunsaturation is not found.

1) *Phosphosphingolipids* share the same amphiphilic nature as glycerophospholipids (Figure 9c). As the names suggest, both of these lipid families contain a phosphate group, so they are generally referred to as phospholipids. In phosphosphingolipids, the ceramide is esterified to a phosphate group which in turn is esterified to a terminal alcohol, such as choline, ethanolamine, or serine. The most abundant phosphosphingolipid in mammalian cell membranes is the ubiquitous sphingomyelin (SM)[167], which includes a phosphocholine headgroup (Figure 9c). In humans, SM represents about 85 % of all sphingolipids; it typically makes up 10÷20 mol % of membrane lipids and is particularly abundant in the brain, where it is a key constituent of the myelin sheath. Its concentration is usually lower than that of the major PC, with rare exceptions[168]. Similar to glycerophospholipids, the fatty acid composition of SM also exhibits considerable variability, thus forming SM mixtures.

2) *Glycosphingolipids* are less abundant than phosphosphingolipids but represent the major glycolipids in animal cell membranes[169]. Their structure is considerably more complex since the ceramide is linked, through a glycosidic bond, to one or more saccharide units. The bulky oligosaccharide head is hydrophilic and protrudes from the membrane plane towards the extracellular fluid, acting as a specific receptor on the cell surface. This family includes gangliosides, predominantly found in the nervous system. Besides sugars, the polar head of gangliosides contains one or more sialic acid molecules. We know more than 60 gangliosides, whose "prototype" is the GM1 reported in Figure 10a: according to nomenclature, G states for ganglioside, M (or D, T, etc.) refers to the number of sialic acids (mono, di, tri, etc.), and 1 represents the order of migration on thin-layer chromatography (e.g. GM3 > GM2 > GM1).

Sterols are counted among membrane lipids, although they are technically alcohols. The most common sterol in mammalian plasma membranes is cholesterol[170]. Its structure, mainly hydrophobic and relatively small compared to previous lipids, consists of a rigid steroid nucleus (composed of four fused rings) linked to a branched alkyl chain at one end and an esterifiable hydroxyl group at the other (the latter makes up < 5 % of total mass[171]) (Figure 10b). Most cell membrane cholesterol is unesterified and its content highly depends on cell type[172–174]; a typical

range is 19÷53 mol %[175]. In humans, the highest concentrations reside in the brain, especially in myelin[176]. Its main task consists of regulating membrane fluidity, as detailed in Section 1.3.4.

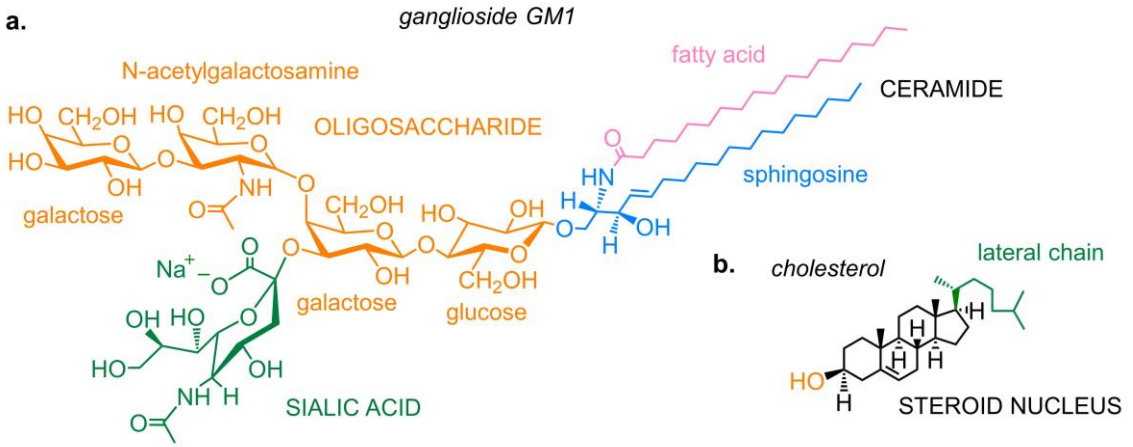

Figure 10. Chemical structures of **a**) GM1 ganglioside with generic chains (sodium salt), and **b**) cholesterol.

1.3.3 Lipid self-assembly

Amphiphilic lipids spontaneously self-assemble into large and well-defined supramolecular aggregates when placed in water at a relevant concentration[177]. This process combines the complex interplay of thermodynamics, intermolecular forces, and the geometry of lipid molecules.

The tetrahedral model for water distribution reported in Figure 11 assumes that each molecule in liquid water at ambient conditions has two donor and two acceptor bonds available with four adjacent molecules[178].

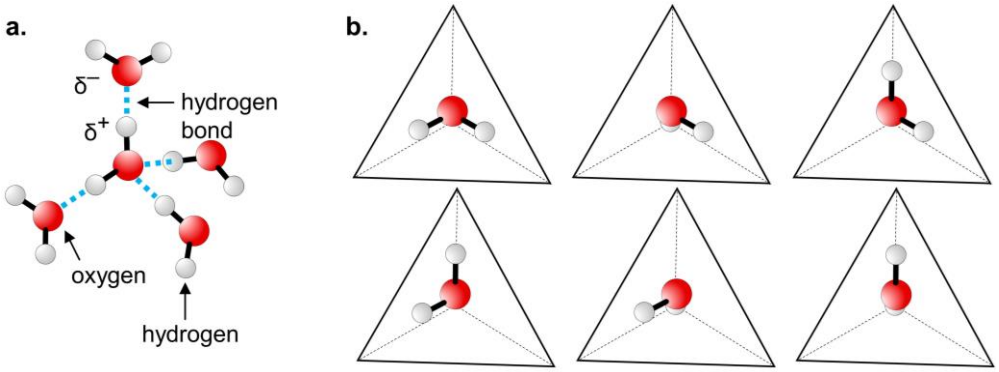

Figure 11. **a**) Tetrahedral hydrogen-bond network in the coordination shell of liquid water; **b**) all water orientations available within this network. Small thermal distortions in the tetrahedral configuration can induce a significant asymmetry in the strength of the interactions involved[178].

The presence of apolar solutes reduces the possible water orientations assured by this configuration. Hence, water entropy remarkably decreases, and the system

becomes entropically unfavorable. This explains why lipid amphiphiles spontaneously self-assemble in aqueous solution to avoid contact between the apolar surface and water. The entropic driving force of this process is known as the *hydrophobic effect*.

Within phospholipid self-assemblies, the apolar chains are segregated from water and induced to closely pack by lipid-lipid hydrophobic attraction. Though mitigated by interchain steric repulsion, this effect is remarkably strong at the hydrocarbon-water interface where polar headgroups reside. Oppositely, the latter are governed by hydrophilic repulsion, which imposes the constraint to maximize the contact with water[179]. These contrasting intermolecular forces tend, on the one hand, to decrease and, on the other, to increase the interfacial area per lipid in contact with water, leading to the optimization of the surface area per headgroup (a_0) at which the total free energy per lipid is minimum. The value of a_0, along with the volume of the hydrocarbon chains (which are assumed to be deformable but incompressible) and the maximum extendible chain length, determines how lipids can associate. Both chain volume and length depend on the presence of branches or unsaturations. Double bonds – in particular in the *cis* conformation – promote kinks in the chains of packed lipids, thus increasing the area per lipid with consequent weaker lipid-lipid association; saturated chains, instead, are more linear and stack tightly, with restricted possibility of bending and deformation. The overall molecular geometry defines the dimensionless packing parameter p:

$$p = \frac{v}{a_0 \cdot l_c} \tag{1}$$

where: a_0 is the optimal headgroup surface area, v is the chain volume, and l_c is the critical chain length. As illustrated in the table of Figure 12, the value of p defines the lipid packing shape, and thus the conformation and curvature of the lipid self-assembly. Such considerations explain why single-chained glycerophospholipids only form micellar aggregates, whereas most common membrane lipids – i.e. diacyl PCs and SM – self-assemble into bilayers (or lamellar phase).

As introduced in Section 1.3.1, the lipid bilayer represents the structural basis of all plasma membranes. Its thickness is very limited compared to the membrane lateral extension and varies depending on lipid composition (chain length and unsaturation degree)[180,181]. Usually, it ranges between 4÷5 nm (~3 and ~1 nm for the apolar and the polar region, respectively)[179–181]. The lipid composition between the two membrane monolayers, or leaflets, shows a remarkable asymmetry whose biological functionality still remains partially unclear[182]. The cytoplasmic leaflet is about twofold more unsaturated than the extracellular one, whose lipids are more tightly packed. The latter is mainly composed of PCs, SM, and a variety of glycolipids

(including GM1, if present)[167], while the former mainly contains PEs, PSs, and PIs.

Lipid	$p = \frac{v}{a_0 \cdot l_c}$	Packing shape	Aggregate structure
Single-chained lipids with large headgroup area e.g. lysophosphatidylcholine	< 1/3	CONE 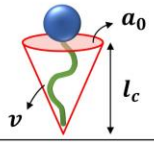	SPHERICAL MICELLE 
Single-chained lipids with small headgroup area	1/3 – 1/2	TRUNCATED CONE 	CYLINDRICAL MICELLE 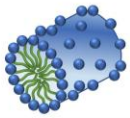
Double-chained lipids with large headgroup area and fluid (saturated and unsaturated) chains e.g. PC, PS, PG, PI, PA, SM	1/2 – 1	TRUNCATED CONE 	FLEXIBLE BILAYER or VESICLE 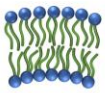 (lamellar phase)
Double-chained lipids with small headgroup area and saturated frozen chains e.g. saturated PE	~ 1	CYLINDER 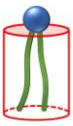	PLANAR BILAYER  (lamellar phase)
Double-chained lipids with small headgroup area and polyunsaturated chains e.g. unsaturated PE	> 1	INVERTED TRUNCATED CONE 	INVERTED MICELLES 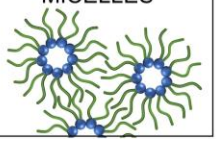

Figure 12. Lipid shape – and corresponding packing parameter p – determining the structure of lipid aggregates. Changes in solution conditions (ionic strength, pH, temperature, surfactant addition, etc.) can alter the effective lipid shape inducing the transformation from one structure to another.

1.3.4 Lipid dynamics

According to the fluid mosaic model, lipid molecules self-assembled into the lamellar phase are involved in collective undulations and are free to laterally diffuse, rotate, bend, or flip from one leaflet to the other (Figure 13a)[179,183]. Since transverse diffusion of lipids is seriously limited by the hydrophobic effect, the lipid bilayer behaves similarly to a two-dimensional fluid, thus forming a liquid-crystalline state. Upon heating, the lipid bilayer can undergo multiple thermotropic phase transitions at well-defined temperatures[161,184]. Lipid phases differ in molecular packing and ordering. Most phospholipids exhibit the transition from the gel ($L_{\beta'}$) – or solid-ordered (S_o) – phase to the liquid-crystalline (L_α) phase shown in Figure 13b, which

occurs at a critical temperature known as gel-to-liquid *melting temperature* (or T_m). The highly disordered L_α phase corresponds to maximum bilayer fluidity, and thus lipid mobility, while hydrocarbon chains in the ordered $L_{\beta'}$ phase are fully extended, closely packed, and exhibit stiffer orientations (lateral diffusion is reduced by at least two orders of magnitude compared to L_α).

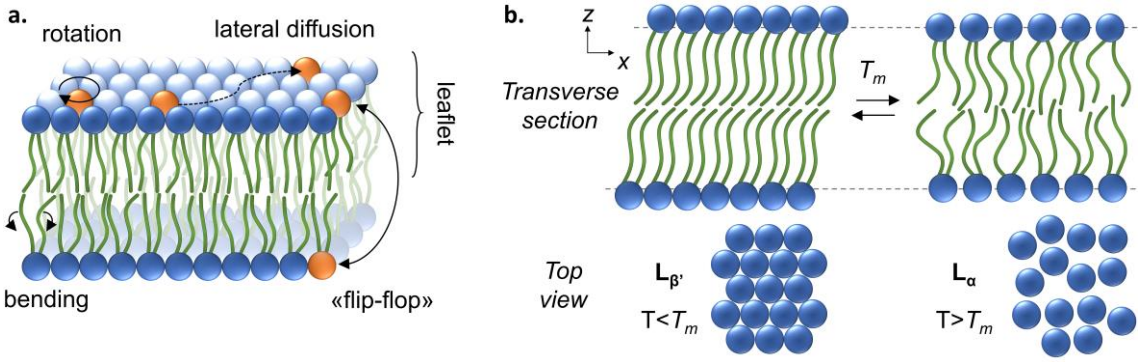

Figure 13. a) Molecular motions in lipid bilayers. Lipids can also protrude out of the leaflet and exchange with lipids in solution. Together with transverse diffusion (or "flip-flop")[185], this exchange is extremely rare (rate of the order of 10^3 s, or even days, compared to 10^{-5}-10^{-6} s of the others; molecular vibrations even occur in about 10^{-14} s). **b**) $L_{\beta'} \rightarrow L_\alpha$ (gel to liquid-crystalline) phase transition. Packing irregularities and extra motional space appear in the disordered L_α phase. The tight packing of fully extended lipids in the ordered $L_{\beta'}$ phase corresponds to a thicker bilayer.

T_m strongly depends on lipid type[181,186,187]. It increases with chain length due to intensified lipid-lipid association limiting lipid mobility. Oppositely, unsaturations hinder lipid close packing reducing T_m. As reported in Table 2, T_m is remarkably sensitive to double bonds. This explains why most membrane phospholipids – mainly unsaturated PCs – already self-assemble into the fluid L_α phase at temperatures significantly lower than the physiological ones. Saturated phospholipids exhibit T_m closer – or much higher – to that of the human body, revealing tighter intermolecular interactions. This is also the case of sphingolipids, including SM.

Table 2. Melting temperatures (T_m) of main membrane diacyl phospholipids at ambient pressure.

Saturated PCs	T_m (°C)	*Saturated PEs*	T_m (°C)	*Other*	T_m (°C)
12:0 (DLPC)	-2	12:0 (DLPE)	29	SMs [a]	~37
14:0 (DMPC)	24	14:0 (DMPE)	50	GM1[b]	19-43
16:0 (DPPC)	41	16:0 (DPPE)	63		
18:0 (DSPC)	55	18:0 (DSPE)	74		
Unsaturated PCs	T_m (°C)	*Unsaturated PEs*	T_m (°C)		
18:1(Δ9) (DOPC)	-17	18:1(Δ9) (DOPE)	-16		
16:0-18:1(Δ9) (POPC)	-2	16:0-18:1(Δ9) (POPE)	25		
18:0-18:1(Δ9) (SOPC)	6				

[a] this value refers to most SMs present in biological membranes[167].
[b] T_m of pure GM1 is not well defined since it strongly depends on its structural arrangement[188].

Cholesterol plays an important role in stabilizing membrane fluidity of mammalian cells. According to the umbrella model[171,189], when this species is incorporated into lipid bilayers, the steroid nucleus is buried in between the phospholipid chains, with the hydroxyl group residing at the hydrocarbon-water interface (Figure 14)[190]. Here, cholesterol spans approximately one membrane leaflet – protected against exposure to water by the phospholipid headgroups – and exhibits discrete possibility of fluctuation (it can either tilt or displace transversely)[190]. In any lipid bilayer, cholesterol incorporation is limited by the elastic stretch exerted on the phospholipid headgroups[171]. Excess cholesterol precipitates out as monohydrate crystals[171] (in PC bilayers, the maximum cholesterol solubility is ~67 mol %[191]). Once incorporated within the bilayer, cholesterol strongly affects the local membrane order, dampening the effects of temperature. It imposes higher conformational order on the chains of lipids in the disordered liquid phase, decreasing the bilayer fluidity but affecting in a minor way the lipid lateral mobility. When considering the cholesterol-induced stiffening of the bilayer, the initial liquid-crystalline state is more commonly referred to as the liquid-disordered phase (L_d). Oppositely, cholesterol separates the chains of lipids in the ordered gel phase, increasing the degree of membrane fluidity without significantly perturbing the lipid conformational order. In both cases, cholesterol leads to the formation of a new hybrid state defined liquid-ordered phase (L_o) (Figure 14). The L_o phase is characterized by solid-like features similar to the gel phase (high conformational order) and by a lateral diffusion only partially slowed down compared to the L_d phase. Thus, cholesterol-induced regulation of membrane fluidity prevents lower or higher temperatures from inducing excessive stiffening or fluidification of the bilayer, respectively. This mechanism preserves the functional fluidity of plasma membranes over a wide range of temperatures.

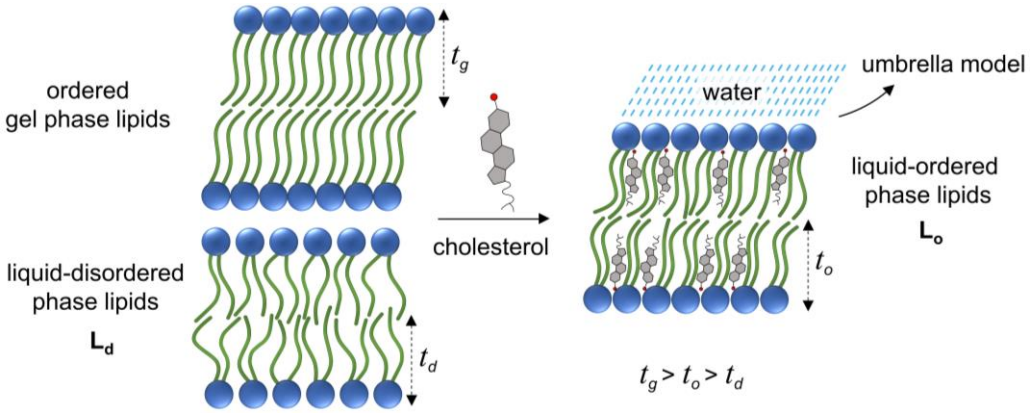

Figure 14. Effect of cholesterol uptake within the hydrophobic region of lipid bilayers. In particular, cholesterol exerts a condensing effect on the liquid-crystalline phase and a fluidizing effect on the gel phase. In the former case, it increases the thickness (*2t*) of the bilayer, while in the latter, it leads to a membrane thinning.

1.3.5 Membrane lateral organization

The main limitation of the fluid mosaic model is to neglect the heterogeneity of lateral lipid organization[192]. In plasma membranes, lipids can separate laterally into highly condensed moving platforms – termed lipid rafts – with distinct composition, dynamics, and physical properties[192–194]. As shown in Figure 15, lipid rafts are self-assembled and specialized nanodomains enriched in cholesterol, relatively saturated lipids, and glycosylated species. They are governed by differential miscibility of lipids[195] and selective lipid-protein interactions that can recruit specific membrane proteins[194]. Moreover, they are highly dynamic in terms of both lateral mobility and association-dissociation. Rafts are functional platforms directly involved in specialized receptor and protein trafficking processes, signal transduction, as well as endocytic and exocytic membrane translocation pathways[196,197]. In living cells, they have long remained ignored because of the lack of direct microscopic detection, ascribable to their tiny size and dynamic, transient nature[198–200]. Initially, indirect proof of raft existence was identified with the evidence that plasma membranes separate into detergent-soluble and insoluble fractions upon detergent extraction with non-ionic detergents at 4 °C[193]. The resistant portion was found to be enriched in cholesterol, SM, and glycosphingolipids[193]. Detergent-resistant domains, initially identified with membrane rafts, were then recognized as artifactual structures that were not present before detergent extraction[201,202]; therefore, it has been argued that they were unlikely to reflect the membrane organization at 37 °C. Only later, experiments on intact cells revealed the existence of lipid microdomains with specialized composition in the plane of the membrane[168,200,203]. After labeling sphingolipids with stable nonperturbative isotopes, secondary ion mass spectrometry was used to quantitatively determine the sphingolipid organization in the plasma membrane. Specifically, sphingolipids were found to segregate into domains with an average diameter of ~200 nm that clustered nonrandomly into sphingolipid-rich membrane micro-patches. Depletion of 30 % cellular cholesterol did not eliminate the sphingolipid domains but moderately decreased their abundance and long-range organization[203].

Evidence for selective lipid segregation has also been provided by model lipid membranes, which are assumed to recreate the same lipid-lipid interactions as real systems (see Section 1.3.6). Indeed, combining a relatively saturated phospholipid with high T_m (e.g. sphingolipids), an unsaturated phospholipid with low T_m (e.g. natural phosphatidylcholines), and cholesterol in a synthetic membrane often results, on the micron scale, in spontaneous L_o–L_d phase separation, where the more ordered L_o phase is reasonably believed to represent a potential physical model of rafts[193,204,205]. Domains with raft-like properties, coexisting with L_d regions, were observed both in

planar supported bilayers[206] and in giant unilamellar vesicles[207,208]. Due to higher degree of lipid packing, both real and model rafts are thicker than the surrounding bilayer[206], resulting in height mismatch at the phase boundary. This imposes the membrane leaflet to elastically deform in the proximity of phase separation to avoid exposure of hydrophobic surfaces to water (Figure 15)[209]. The height mismatch at the domain edge can been investigated experimentally by atomic force microscopy and X-ray scattering measurements[205,210]. Synthetic models for L_o domains differ from lipid rafts by their larger size, simplified composition, and greater difficulty in recruiting raft-associated membrane proteins (Figure 15)[211]. Recently, direct imaging of micro- and nano-domains in giant lipid vesicles obtained from native, protein-rich extracts of plasma membranes has reinforced the belief that the physical forces driving liquid-liquid phase separation in synthetic membranes are the same as those governing the appearance of lipid nanodomains in real plasma membranes[211–215].

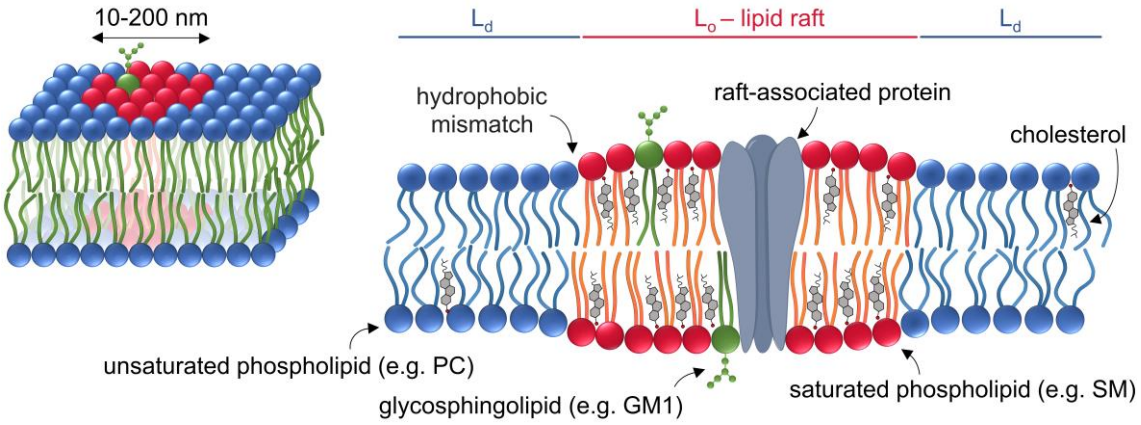

Figure 15. Schematic representation of the liquid-liquid phase separation originating lipid rafts (top view and transverse section). Since the L_o phase is thicker than the surrounding bilayer, the monolayer deforms at domain boundary to compensate the phase hydrophobic mismatch.

1.3.6 Biomimetic membrane models

Due to the complex nature of plasma membranes, elucidating the mechanism of nanoscale interactions occurring at the cell–particle interface is extremely challenging. Thereby, such research primarily relies on simplified models capable of mimicking the natural organization of specific membrane components[216,217]. Synthetic lipid bilayers of growing complexity are robust *in vitro* models to explore how particle physicochemical properties might perturb the basic structure of plasma membranes[33,218,219]. Within this thesis, only *lipid vesicles* – or *liposomes* – and *supported lipid bilayers* – or *SLBs* – prepared via vesicle fusion have been considered, and thus described in this section. Besides basic research, model membranes are widely used in synthetic biology and medical applications[216]. For example, numerous liposome-

based drug formulations have been successfully translated into real-time clinical applications[220].

Liposomes consist of a spherical lipid bilayer containing an aqueous compartment (Figure 16a). The simplest vesicles are unilamellar – i.e. composed of only one bilayer – and their size varies considerably depending on the preparation method. Small unilamellar vesicles (SUVs, ~20÷100 nm diameter) are generally prepared by sonicating or extruding multilamellar vesicle suspensions (MLVs) that spontaneously form upon hydration of dried lipid films (Figure 16a). MLVs consist of several concentric lipid bilayers intercalated by water; most times, their formation is facilitated by mild sonication (Figure 16a). By increasing the pore size of the extruder filters, the same procedure is used to prepare large unilamellar vesicles (LUVs, diameter from ~100 nm to ~1 μm). Giant unilamellar vesicles (GUVs, ~1÷100 μm diameter), instead, are commonly generated using a variety of much more complicated protocols[221] that include electroformation from plasma membrane extracts purified from cells[222,223]. GUV size is the best-suited to mimic the curvature of eukaryotic plasma membranes and GUVs are mainly used for optical microscopy and micromanipulation studies[221,224]. Despite the smaller size of SUV and LUV tends to overestimate the plasma membrane curvature, these vesicles are significantly easier and faster to prepare using highly reproducible and controllable methods. Furthermore, as in this thesis, they are commonly employed for spectroscopy studies and for the efficient preparation of SLBs via deposition and fusion of vesicles on solid substrates.

SLBs are planar model membranes widely used in biomimetic studies[225]. Both planarity and the stability imposed by the rigid support are extremely useful when studying membrane-based molecular processes using surface characterization techniques, such as atomic force microscopy (see Section 2.1)[226]. This technique, for instance, is a useful tool for studying the lateral liquid-liquid phase separation in model membranes[206]. SLBs are generally prepared via the vesicle fusion technique first proposed by McConnell's group[226–228]. After initial adsorption of vesicles onto a hydrophilic solid surface, vesicles tend to deform, flatten, and finally rupture and fuse on the substrate to form a stable SLB, distanced from the support by an ultrathin water layer (Figure 16b)[229]. Despite initial hypotheses, it is now known that this nanometric gap is not sufficient to prevent the substrate from imposing a physical constraint on the membrane, altering – albeit limitedly – the lipid dynamics[218,230]. To facilitate the deposition of defect-free SLBs the system can be heated up to ~60 °C for a few minutes[226]. The substrate has to be flat and clean[229,231], and its constituent material may remarkably affect both vesicle stability and lipid mobility in deposited

SLBs[232]. The most common substrate material is mica[232], a nonconducting mineral that can be easily cleaved by using adhesive tape to obtain an atomically flat surface. Borosilicate glass and silica can be used as well, but their preparation is more laborious. Pathways of SLB deposition strongly depend on several parameters, such as vesicle composition, concentration, surface charge, and osmotic pressure; substrate material (roughness and hydrophilicity); vesicle incubation time and temperature; pH and ionic strength (ions can have screening and charge compensating effects). All these factors may induce remarkable variation in vesicle-support, vesicle-vesicle, and intrabilayer interactions, thus governing the fate of SBL formation[231,233]. Under certain conditions vesicles do not adsorb, while under others they do but remain immobilized as a stable vesicular layer; in some cases, vesicles may slowly form the SLB only after reaching a sufficiently high critical coverage, or their rupture may be instantaneous, leading to direct formation of SLB patches. In the case of mica, for example, in the absence of bivalent cations such as Ca^{2+}, zwitterionic vesicles adsorb but do not merge even at relatively high lipid concentration[233,234].

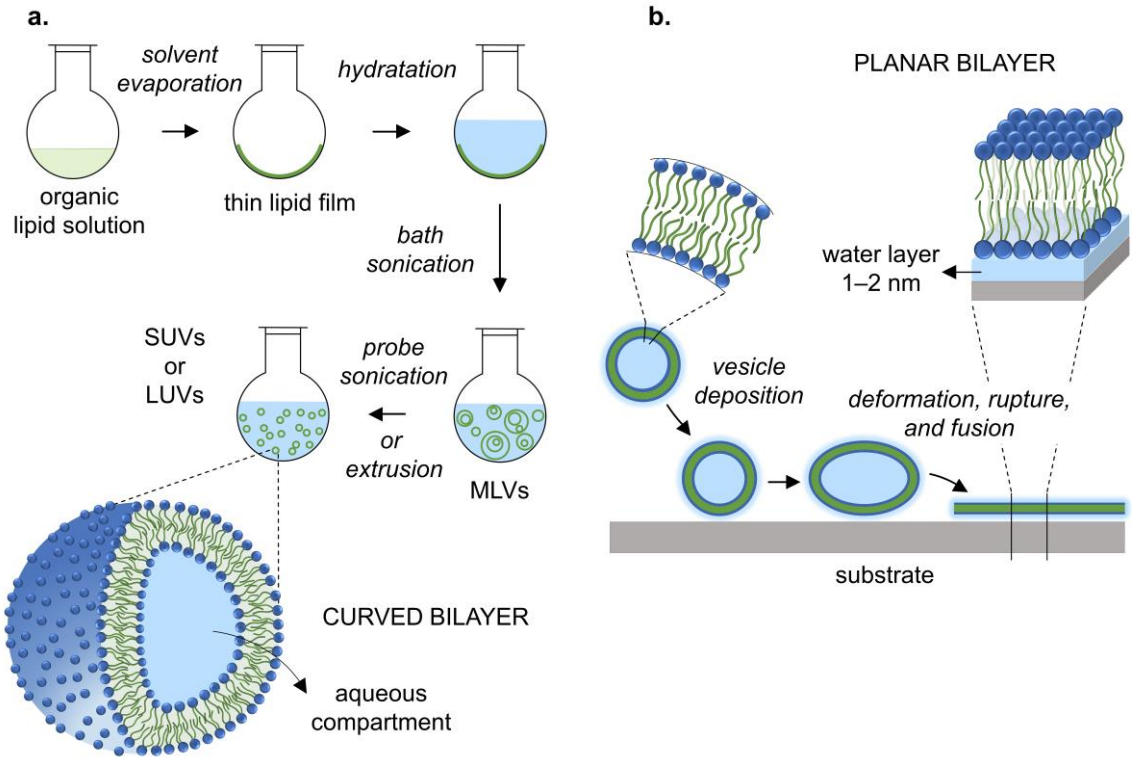

Figure 16. Preparation of **a**) unilamellar lipid vesicles and **b**) SLBs (via vesicle fusion). Vesicle formation starts from stoichiometric lipid mixtures dissolved in a suitable organic solvent; MLV sonication and extrusion lead to homogeneous and remarkably reproducible vesicle suspensions. The scheme of the extruder used in this thesis is reported in Figure 55 (Appendix B1).

Within this thesis, SUVs, LUVs, and SLBs were prepared as detailed in Appendices B1 and C.

2. Experimental techniques

In this thesis, several experimental techniques have been used to thoroughly investigate the NP-membrane interaction and to characterize the mechanical and morphological features of model membranes; these include *atomic force microscopy*, *quartz crystal microbalance with dissipation monitoring*, and fluorescence assays based on *dye-leakage* and *emission anisotropy*. In addition, other techniques (dynamic light scattering, ζ-potential analysis, proton nuclear magnetic resonance, and UV-Vis spectroscopy) have been employed by the candidate to perform routine characterizations of both nanoparticles and model membranes after preparation (see Appendices A and B). This chapter provides a general introduction only to the techniques shown in italics, as they were essential to developing the results discussed in Chapters 4, 5, and 6.

2.1 Atomic Force Microscopy

Atomic Force Microscopy (AFM) is a surface characterization technique belonging to the family of Scanning Probe Microscopies[235,236]. It is best known for high-resolution topographic imaging, but it is also employed for measuring mechanical properties with nanoscale spatial resolution[237]. AFM functioning is based on scanning the sample surface with a sharp mechanical probe. The scanning mechanism can be attached either to the probe base or to the sample stage without changing the operating principle since it is the relative probe-surface distance that needs to be controlled. AFM scanners mainly consist of piezoelectric ceramic tubes designed to undergo – when a specific voltage is applied – tiny but extremely accurate and precise displacements along x-y and z directions (Figure 17a)[238,239]. The probe is a sharp tip attached under the free-swinging end of a micrometric cantilever (Figure 17a). Most cantilevers are made of silicon, silicon nitride, or borosilicate glass and can have different geometries. When the probe is brought very close to the sample surface, the cantilever is deflected by the forces between the atoms of the tip and those of the sample. In this way, it behaves like a spring governed by Hooke's law $F = -kd$, meaning that the tip-surface force F, deflecting the cantilever, depends linearly on d, the cantilever deflection (Figure 17b). Tip-surface interatomic forces depend on the mutual tip-surface distance, as described by the Lennard-Jones potential (Figure 17c). Van der Waals attractive forces and capillary forces prevail in the long-range attraction, while repulsive interatomic forces take over only at short ranges (~few Å). Depending on the operation conditions, the interactions can include water meniscus

forces, dipole-dipole interactions, chemical bonding, electrostatic forces, solvation forces, hydrophobic forces, etc. The most common method to measure the tiny bending of the cantilever is the beam-deflection system illustrated in Figure 17b[240]. Here, a laser beam is first focused on the reflective end of the cantilever, and then reflected and redirected to a photodiode generating an output signal. When the cantilever deflects due to tip-surface forces, the detected laser position shifts accordingly, modulating the output signal. Vertical shifts in the laser spot allow measuring the cantilever deflection – thus calculating the tip-surface interaction (Figure 17b) – while horizontal displacements are induced by cantilever torsion. Output signals recorded during scanning are then reported in a pseudocolor image, in which each pixel corresponds to a specific *x-y* surface position, and its color reflects the signal associated with that position (in a topographic image, the height of surface features). Since the tip-surface interaction depends on their mutual separation, AFM signals can be used to reconstruct the surface topography. Within this thesis, AFM imaging was performed using the constant-signal mode. During scanning, a Z-feedback loop constantly compensates the signal variation caused by modulation in surface height by regulating the tip-surface distance. This adjustment is based on extending or retracting the piezo to keep unchanged the tip-surface interaction and restore the cantilever response to a constant user-defined value defined *setpoint* (Figure 17a).

AFM topographic images can be acquired with different modes, which exploit different tip-surface interaction regimes. In this context, the description will be limited to the two modes used in this thesis: the contact mode and the intermittent contact mode – best known as tapping mode. As shown in Figure 17c,d, the *contact mode* constantly operates in the repulsive regime. The setpoint compensated by the feedback system is the cantilever deflection, which is generally low enough to avoid excessive tip-surface interaction but high enough to ensure stable tip-surface contact. Despite the remarkable high-resolution imaging provided by this mode, the friction force occurring as the tip moves pushing on the surface can induce undesired cantilever torsion[241]. Moreover, it may be not trivial to prevent the probe from sticking to the sample. This is common in the presence of a liquid meniscus layer due, for instance, to air humidity. The dynamic *tapping mode* – constantly moving between attractive and repulsive forces – was developed to bypass this problem (Figure 17c,d)[242]. Here, the cantilever is externally driven to oscillate near the sample surface with a frequency close to the acoustic resonance. The amplitude of cantilever oscillation remains unperturbed as long as no quantifiable damping occurs through short-range repulsive tip-surface interactions. Thus, the amplitude oscillation varies

according to the surface height profile and is used as dynamic setpoint instead of the static cantilever deflection (the lower the setpoint, the higher the tip-sample interaction, and the harsher the imaging conditions). Unlike the contact mode, the tip is not in contact with the surface for most of the oscillation cycle and tip-surface friction is significantly reduced. This explains why tapping mode is preferred with soft samples in liquid, such as the biological ones. Moreover, the phase shift between cantilever excitation and response induced by tip-surface interactions can be recorded and mapped in images discriminating sample areas with similar topography but different mechanics[243].

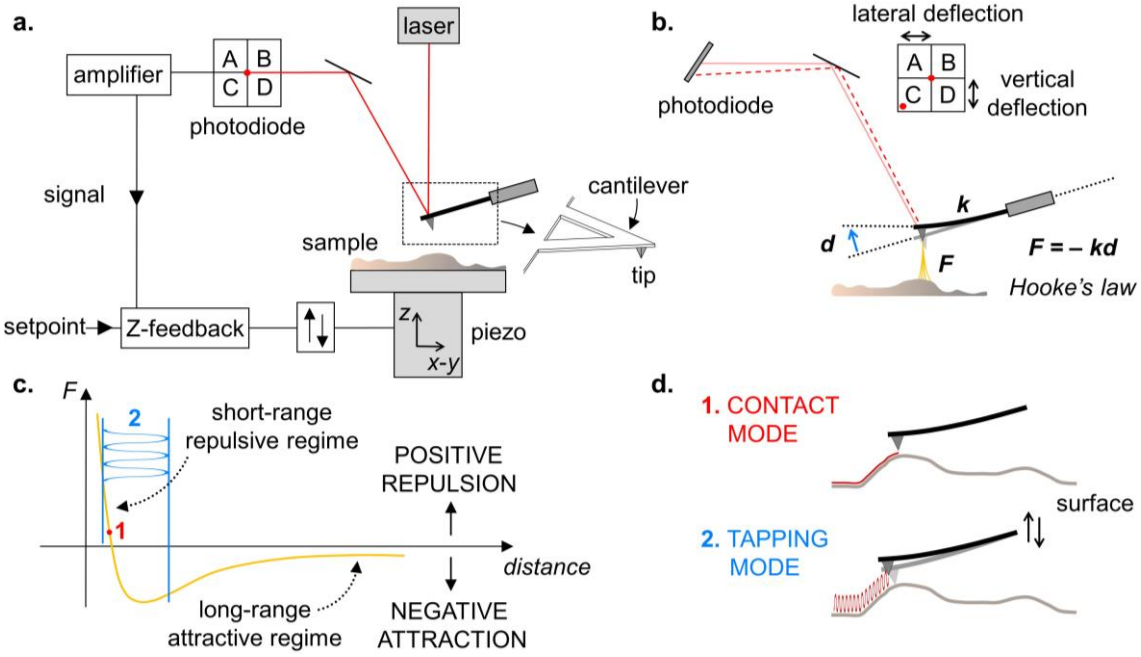

Figure 17. a) AFM instrumental configuration (not to scale); a v-shaped cantilever is taken as an example. **b**) Beam-deflection system. **c**) Lennard-Jones potential curve describing the local tip-surface force *F* as a function of the mutual interatomic distance. This curve is a generally valid approximation since each situation depends on the specific sample, tip geometry, and operation conditions. **d**) AFM modes used in this thesis: **1.** contact mode – operating in the repulsive regime shown in (**c**) – and **2.** tapping mode – involving both repulsive and attractive regimes shown in (**c**).

Besides imaging, AFM can be used for *force spectroscopy* measurements[235,244]. This method consists of approaching, at a fixed *x-y* position, the probe to the sample until a certain deflection setpoint is reached, after which the probe-sample distance is restored to the maximum initial value. The cantilever deflection, and thus interaction force, is monitored during the whole displacement and plotted against the piezo movement. Besides the cantilever deflection recorded in the static contact mode, other parameters can be monitored, but within this thesis, only this specific situation will be considered. Thanks to its nanometric radius, the AFM probe is capable of sensing extremely small interaction areas, providing high sensitivity also to very low

forces. Figure 18a describes in detail the steps of the simplest case of tip-surface interaction, i.e. a hard and incompressible sample analyzed in air in the absence of long-range interactions. During approach, after passing the non-contact region at zero force, attractive forces overcome the spring constant of the cantilever inducing the tip to jump into contact with the surface. As the distance decreases further, the repulsive contact force rises linearly with a slope equal to the cantilever constant *k*. During retraction, the tip often remains in partial contact with the surface due to some adhesion; only after overcoming it, the tip returns to the flat non-contact regime. When analyzing soft (compressible) samples in liquid, as in this thesis, the interpretation of the curves becomes more difficult (Figure 18b)[237]. Here, sample deformability and long-range electrostatic interactions attenuate considerably the clear detection of the jump into contact, and a more gradual force increase in the contact region – often characterized by a non-linear behavior – is more commonly observed. Moreover, due to complex adhesion phenomena inducing viscoelastic losses, it is common to observe hysteresis upon retraction.

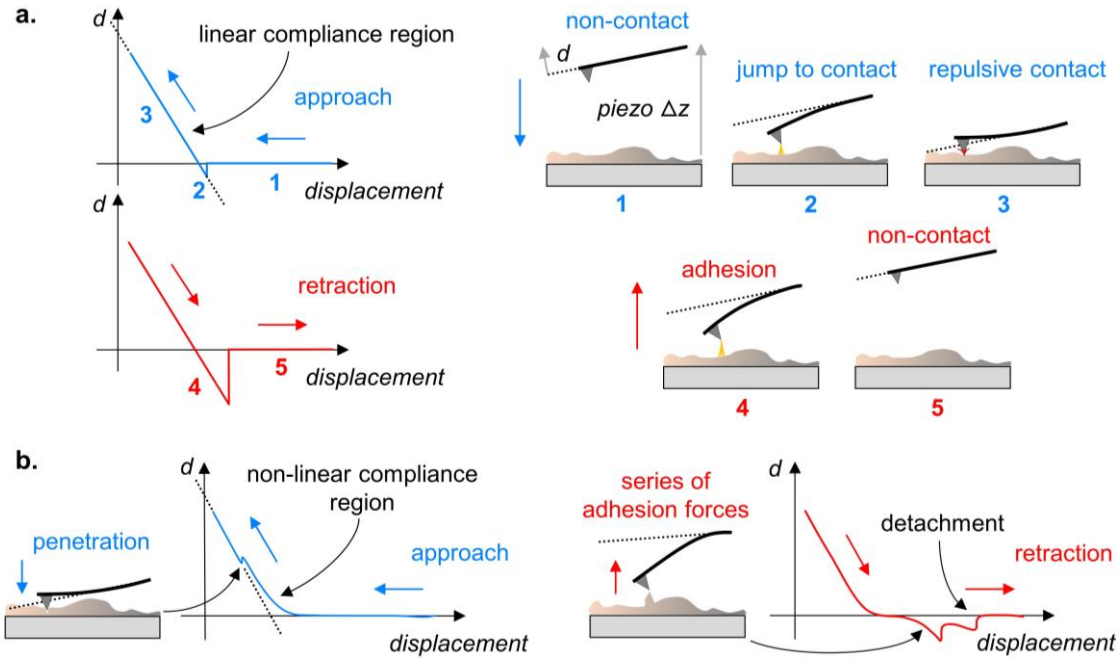

Figure 18. Schematic representation of the cantilever deflection *d vs* the piezo displacement during the contact-based acquisition of force curves in the case of **a**) hard samples analyzed in air in the absence of long-range interactions, and **b**) soft samples in liquid. Approach (blue) and retract (red) curves are reported separately.

For quantitative analysis of tip-surface interactions, the piezo displacement reported in Figure 18 has to be corrected for the nanometric bending of the cantilever to calculate the tip-sample distance. The nanometric distance that the cantilever actually deflects for a certain measured change in photodiode voltage is defined sensitivity and is obtained by calibrating the cantilever. This can be done, for instance,

using the thermal noise method[245,246]. This procedure also allows measuring the exact spring constant k necessary to convert deflection into force values. Only afterward, force *vs* tip-sample separation curves can be fitted with a proper model to calculate the Young's or elastic modulus of the sample – a measure of surface stiffness[237,247].

The capability of the AFM probe of acting as a force sensor can be combined with lateral scanning to reconstruct maps of tip-surface interactions, nanomechanical properties, and topographic images. In this last case, the procedure is known as *Force Volume*[237]: for each scanned *x*-*y* position, a force-distance curve is measured, and the z coordinate is extracted from the curve at the selected setpoint. As in conventional imaging based on contact mode, height information is derived fixing as setpoint the maximum cantilever deflection. The main drawback of this technique is that it is remarkably time-consuming, and the less data is acquired, the more penalized is the image resolution. In the last years, different techniques have been developed by the manufacturers to provide high-speed *Force Volume* with improved resolution imaging, including the *Quantitative Imaging* (QI™) mode by JPK used in this thesis. In QI™ mode, a complete force-distance curve is acquired at each pixel thus allowing mapping the Young's modulus of the sample with the advantage of sampling speed and spatial resolution.

In this thesis, AFM imaging in liquid – tapping mode and QI™ mode – was performed for the projects described in Chapters 5 and 6. All details of equipment specifications and analysis methods are reported in Appendix C1.

2.2 Quartz Crystal Microbalance

The Quartz Crystal Microbalance (QCM) is an ultra-sensitive technique for real-time detection of mass and structural changes involved in surface processes. The sensing unit is a thin disk of piezoelectric quartz crystal sandwiched between a pair of gold electrodes; when applying an alternating voltage, the crystal is excited to oscillate at its acoustic resonance frequency f_0. The piezoelectric performance of quartz disks (including the frequency stability) can be tuned in the production process. The decisive factor is the cutting direction to the main crystallographic axes at which the disk is removed from the source quartz blank. In mass production of oscillator materials, the most widely used angular cut is the AT-cut, which provides quartz crystals with remarkable oscillation stability (0.5÷300 MHz frequency range), thus allowing high accuracy in f_0 registration. In addition to the fundamental mode, QCM device allows replicating the measure at higher harmonics, or overtones. Besides other

variables kept constant during normal operation, the resonance frequency depends on the total mass oscillating on the sensor surface. When a mass is deposited, the quartz oscillation is slowed down due to inertia (Figure 19a). The frequency decrease as the attached mass increases is described by the Sauerbrey equation[248]:

$$\Delta m = -C_f \frac{\Delta f}{n} \quad (2)$$

where: $\Delta f/n$ is the observed frequency shift (Hz) normalized by n, the harmonic number at which the crystal is driven (in the field of acoustic waves, only odd harmonics are measured), Δm is the change in mass per unit area of the piezoelectrically active surface (g/cm^2), and C_f is the linear sensitivity factor of the quartz crystal, i.e. a coefficient that describes the sensitivity of the sensor to mass changes[249,250]. C_f only depends on the acoustoelastic properties of the crystal (f_0, quartz density, and shear modulus). The Sauerbrey model considers the attached mass as a thickness extension of the underlying quartz, and thus only applies to uniform thin-film deposits rigidly coupled to the sensor (in this condition, the foreign film does not experience any shear forces during vibration). For thick films or large mass loads, corrections have been developed[251].

For many years, the QCM was used as a gas-phase mass detector; only recent developments in electrical circuitry allowed the quartz crystal to oscillate stably also under the viscous loading of a liquid environment[252,253]. The Sauerbrey equation can be used also in solution if its conditions are met. When covered by a liquid, the sensor resonance frequency changes proportionally to the square root of the liquid density-viscosity product[254]. Using standard AT-cut disk-typed quartz crystals with f_0 in the 4÷6 MHz range, QCM allows resolution down to 1 Hz in normalized frequency shift, corresponding to ng/cm^2 mass sensitivity[252]. QCM-D in liquid is extremely useful for monitoring the deposition of thin molecular biofilms, such as the SLBs prepared via vesicle fusion[232,233] (see Section 1.3.6 and Figure 19c), and to investigate their interactions with nanoparticles. For example, it provides accurate quantification of the NP mass either tightly adsorbed onto or inserted into the lipid bilayer.

When dissipation monitoring is integrated into the QCM set-up (QCM-D), it is possible to extract simultaneously both the frequency and the energy dissipation response of the oscillator. Dissipation (D) is measured from the time it takes for the oscillation to stop when the driving voltage to the crystal is shut off (Figure 19b). It is directly proportional to the energy dissipated from the oscillating crystal during one oscillation period divided by the total energy stored in the oscillator[255]. The disconnection of the AC voltage can be repeated over 200 times per second, giving

QCM-D remarkable sensitivity and high resolution. While frequency shifts (Δf) can be traced back to changes in the attached mass, variation in energy dissipation (ΔD) measures the damping in the resonator oscillations, thus enabling qualitative analysis of the structural properties of adsorbed layers. By measuring ΔD it is possible to determine if the deposited film is rigid or viscoelastic, since the latter dampens the sensor oscillation, increasing ΔD, as shown in Figure 19b,c. Moreover, Δf and ΔD values can be analyzed to extract quantitative information on layer thickness, density, shear elastic modulus, and viscosity when the Sauerbrey regime is not met, as in the case of viscoelastic samples. The simplest way to determine such properties is to fit the QCM-D data into the Voigt model described in ref[256,257].

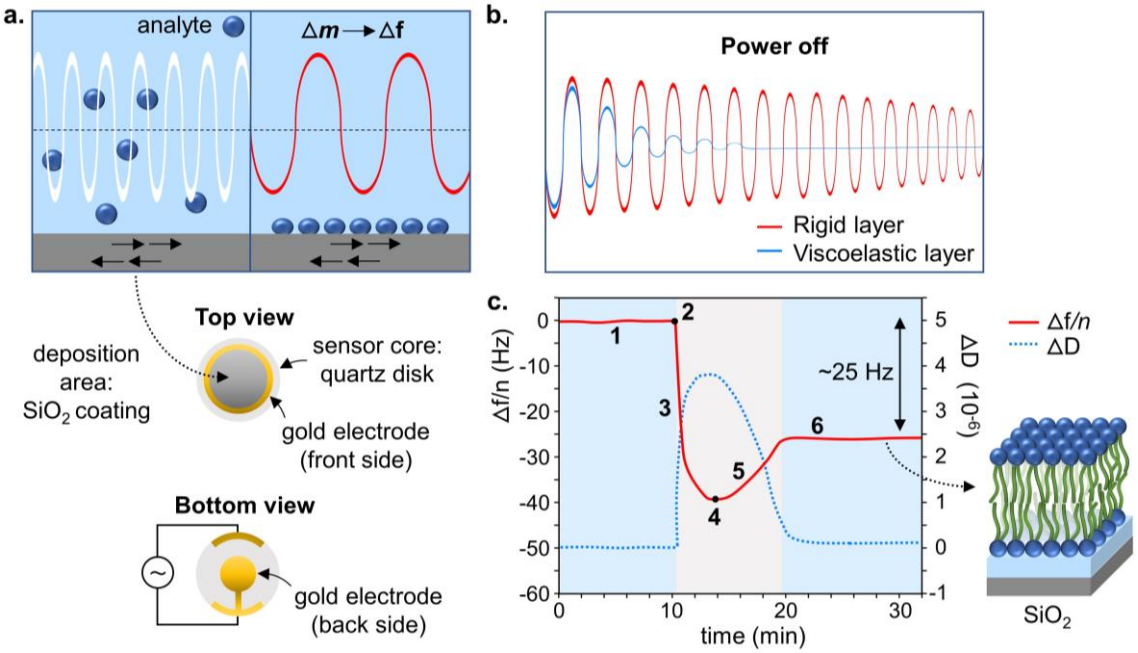

Figure 19. a) Top: mass-induced variation in the resonance frequency of the sensor; bottom: QCM sensing unit (a SiO_2 coated sensor is taken as an example). **b**) Dissipation for rigid and viscoelastic films when the AC voltage is disconnected. **c**) SLB formation via vesicle fusion onto hydrophilic SiO_2 monitored by QCM-D: **1.** sensor oscillating in liquid (Δf=0, ΔD=0), **2.** lipid vesicle injection, **3.** rapid deposition of water-filled lipid vesicles on the sensor (Δf<0, ΔD>0), **4.** critical sensor coverage (Δf min, ΔD max), **5.** water release upon vesicle merging on the sensor (Δf>0, ΔD→0), and **6.** stable SLB (typical normalized Δf_{SLB}~25 Hz, ΔD=0). Vesicle deposition between 2 – 4 leads to the formation of a viscoelastic supported vesicle layer, as revealed by $\Delta D_{2\text{-}4}>0$; as shown in (**b**), viscoelastic deposits dampen the sensor oscillation. The final SLB is rigidly coupled to the sensor; indeed, in 6 the sensor oscillates exactly as it did before vesicle insertion in 1 (during vesicle fusion, between 4 – 6, dissipation returns to the initial value ΔD=0).

In this thesis, QCM-D measurements in liquid were performed for the projects described in Chapters 4, 5, and 6. For data processing, both the Sauerbrey model and the Voigt model were used depending on the nature of the deposited layer. All details of equipment specifications and analysis methods are reported in Appendix C2.

2.3 Fluorescence assays

2.3.1 Dye-leakage

In intact cells, passive intracellular penetration is strictly regulated by the selective permeability of the cell membrane. Some exogenous agents, such as antimicrobial peptides[258,259], proteins[260,261], and toxins[262], can permeabilize plasma membranes compromising their integrity. This can induce transient membrane poration or gradual or all-in-one release of the cellular content, potentially leading to cell lysis. A similar perturbation can be induced by the uptake of nanoparticles. Dye-leakage assays are commonly used for probing the damage extent induced by nanoparticles during passive penetration of synthetic lipid bilayers[61,263,264]. In this thesis, nanoparticle-induced membrane perturbation was investigated with the calcein-leakage assay[265–267]. Calcein is widely exploited in such experiments involving Au nanoparticles[61,263]. The fully deprotonated form of calcein (Figure 20) is commonly used as membrane-impermeant fluorescent dye[267]. For a typical leakage assay, lipid vesicles are loaded with a buffered calcein solution at self-quenching concentrations (above 70 mM). The non-encapsulated dye is removed from the vesicle suspension by gel filtration[268,269]. Filtered vesicles are then placed in a fluorometer cuvette and continuously stirred at constant temperature (Figure 20, step 1). The calcein fluorescence is recorded in real time and nanoparticles are added after a few minutes (Figure 20, step 2). All NP-induced changes in membrane permeability – allowing calcein to leak – involve the external dilution of the probe and thus dequenching (Figure 20, step 3). The concomitant rise in fluorescence emission can be attributed to transient pore formation or vesicle disruption.

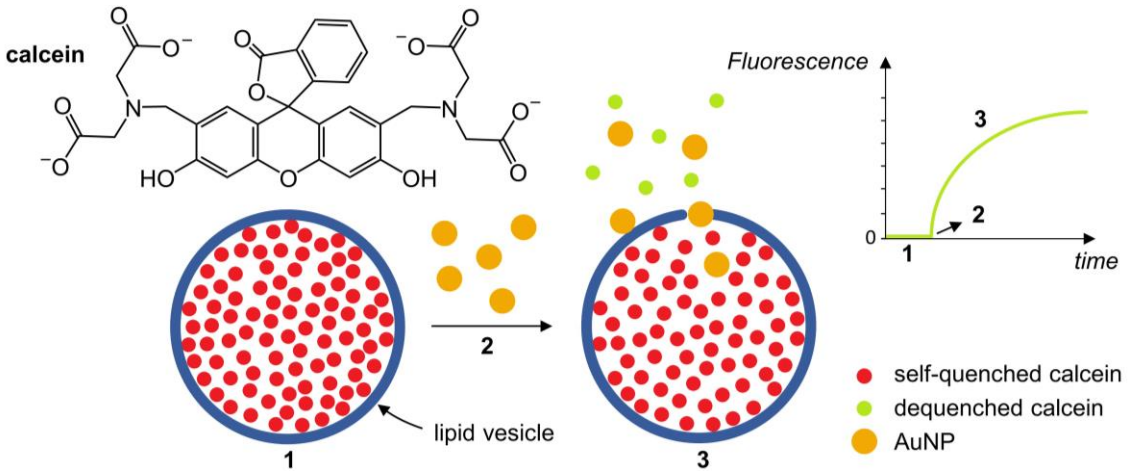

Figure 20. Scheme of the calcein-leakage assay used in this thesis: **1.** liposomes before nanoparticle addition, **2.** nanoparticle injection, and **3.** liposomes after nanoparticle addition. Concentrated calcein solutions are red-brownish and become green upon dilution.

At the end of the experiment, a detergent is added to obtain complete vesicle breakage into micelles with complete calcein release. This step is necessary to calibrate the fluorescence data since the percentage of vesicle leakage is expressed as:

$$leakage\ \%\ (t) = \frac{F(t)-F_0}{F_{max}-F_0}\ \% \quad (3)$$

where: $F(t)$ is the time-dependent fluorescence, F_0 is the fluorescence level immediately before nanoparticle addition, and F_{max} is the fluorescence level obtained with 100 % calcein release.

In this thesis, dye-leakage assays were performed for the project described in Chapter 4. All details of equipment specifications and analysis methods are reported in Appendix D1.

2.3.2 Fluorescence anisotropy

Fluorescence anisotropy assays are based on the principle that the anisotropy of the fluorescence emission of a fluorophore is inversely related to its motional freedom. Such measurements are commonly used to explore the rigidity of several molecular environments, including lipid bilayers. In this case, the probe 1,6-diphenyl-1,3,5-hexatriene, or DPH, and its derivatives are widely used[270–273]. These fluorophores exhibit a strong increase in fluorescence emission when associated with membrane lipids, and their anisotropy response is highly sensitive to dynamical alterations in the physical state of the bilayer caused, for instance, by changes in temperature, pressure, cholesterol content, and phospholipid (or ionic) composition. As shown in Figure 21, DPH is a hydrophobic, rigid, and highly linear molecule. The addition of small amounts of DPH in the liposome preparation results in complete embedding of the fluorophores within the apolar core of the bilayer, where DPH molecules are mostly oriented parallel to lipid tails (Figure 21)[274]. Here, they exhibit diffusional, rotational, and torsional motion[275]. DPH derivatives are chosen to probe the fluidity of other regions of the bilayer. For instance, 1-(4-(trimethylamino)phenyl)-6-phenylhexa-1,3,5-triene, or TMA-DPH, is anchored at the hydrocarbon–water interface and provides information on the polar headgroups (Figure 21). In this position, its dynamics is remarkably more hindered than that of deeper DPH[276].

When irradiated with polarized light, fluorophore molecules emit polarized fluorescence. This is due to the presence of absorption and emission transition moments[277–279] characterized by specific axes along which radiation is absorbed and emitted. In general, determining the actual orientations of the transition moments in a fluorophore is not trivial[280,281]. In the case of DPH (and most derivatives), it is

possible to assume that they lie almost parallel to the elongated axis of the molecule (Figure 21)[278,279,282]. This electronic structure represents a great advantage in anisotropy measurements. Upon excitation, fluorophore molecules with the absorption transition moment parallel to the electric field of the polarized light exhibit the highest probability of excitation (in this description, the polarization direction will be always considered along the z-axis). More precisely, the absorption dipole moments do not need to be exactly aligned to the z-axis to get excited: the absorption probability is proportional to $\cos^2\theta$, where θ is the angle between the axis of the absorption dipole and the z-axis[277] (Figure 21). Hence, when polarized light is applied to an ensemble of mobile fluorophores randomly distributed, there will be some preferential orientation of the excited-state fluorophore population along the z-axis, and very few excited molecules will have their absorption transition moments oriented perpendicularly in the *x-y* plane[277] (Figure 21). This selective excitation process is known as *photoselection* and represents a key concept in fluorescence anisotropy experiments. A typical instrumental configuration used in these measurements is reported in Figure 21. The fluorescence intensity emitted by fluorophores is measured using an emission polarizer whose polarization axis is oriented sequentially parallel and perpendicular to the z-axis. The corresponding intensities $I_{\parallel}$ and $I_{\perp}$ are used to calculating the anisotropy of the fluorescence emission (r)[277,283]:

$$r = \frac{I_{\parallel} - I_{\perp}}{I_{\parallel} + 2I_{\perp}} = \frac{I_{\parallel} - I_{\perp}}{I_{tot}} \tag{4}$$

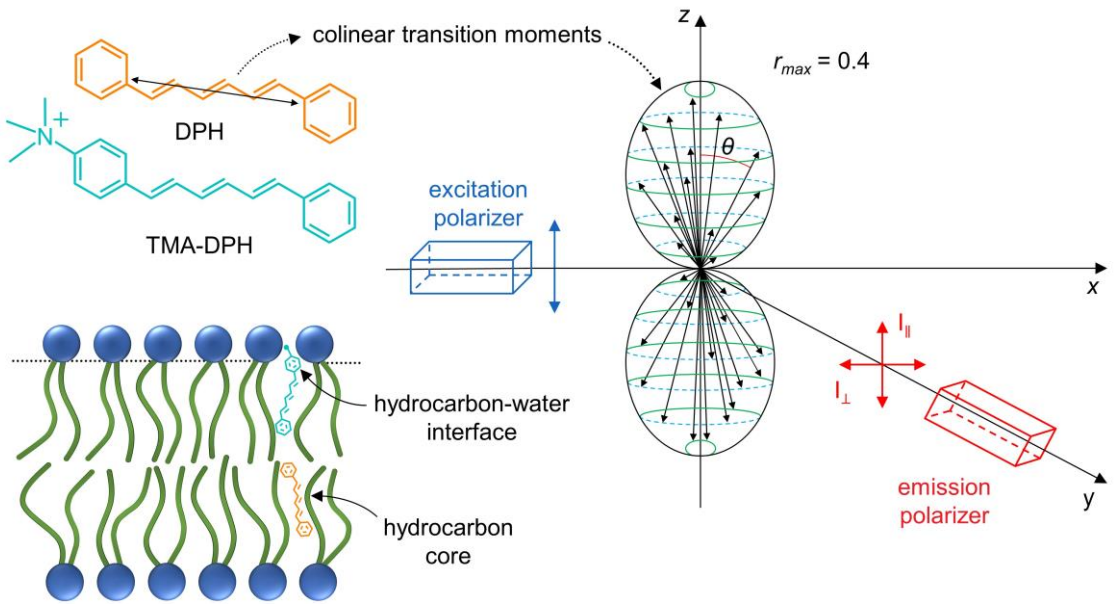

Figure 21. Excited-state distribution for immobilized fluorophores with colinear absorption and emission transition moments – such as DPH and TMA-DPH – irradiated by monochromatic light polarized along the z-axis. In the bilayer cartoon, phospholipids and probes are not to scale.

As shown by Equation 4, r is a dimensionless parameter, normalized by the total fluorescence intensity emitted by the sample (I_{tot}). This means that r does not depend on fluorophore concentration. In the limit case of a single fluorophore aligned to the z-axis, if the fluorescence emission is completely polarized along the transmission direction of the emission polarizer, $I_{\perp}=0$, $I_{\parallel}=I_{tot}$, and $r=1.0$. Thanks to its highly polarizable electronic structure, this is the theoretical case for DPH. However, it is not possible to obtain a perfectly oriented excited-state population of relatively mobile DPH molecules randomly distributed in an isotropic environment. Here, r unavoidably decreases due to the angular dependence of photoselection. Only if the surrounding environment is sufficiently viscous, photoselected DPH molecules do not rotate significantly between absorption and emission events, and the emitted fluorescence will also be highly polarized within a particular range of angles with respect to the polarization direction (i.e. $I_{\parallel} \gg I_{\perp}$). According to geometrical considerations[277], in the case of colinear absorption and emission dipoles, the maximum anisotropy reaches a value of 0.4 ($I_{\perp}=1/3\ I_{\parallel}$) (Figure 21). Instead, if the medium shows fluid-like features, DPH molecules undergo continuous random and fast reorientations with consequent depolarization of emitted fluorescence. When the emission is completely depolarized, $I_{\parallel}$ is statistically equal to $I_{\perp}$ and $r=0.0$. Thus, considering DPH embedded in a lipid bilayer, measuring the change in polarization of radiation between absorption and emission is extremely useful to determine the angular rotation the probe undergoes in between these events and, accordingly, to estimate the order of surrounding lipid acyl chains.

In this thesis, fluorescence anisotropy assays were performed for the project described in Chapter 6. All details of equipment specifications and analysis methods are reported in Appendix D2.

3. Synthesis of amphiphilic gold NPs

Amphiphilic AuNPs with spherical shape and variously functionalized by 1-octanethiol (OT), 11-mercapto-1-undecanesulfonate (MUS), and (11-mercaptoundecyl)-N,N,N-trimethylammonium (TMA) were synthesized using two chemical procedures: 1) a one-phase variant of the Brust-Schiffrin method[97,98], and 2) the thiol-for-oleylamine ligand exchange. The transition from the first to the second synthetic route resulted in a remarkable reduction of the NP size dispersion (i.e. $\frac{standard\ deviation}{mean\ diameter} \cdot 100$). This improvement is important when strict comparability of NP sizes is required in systematic studies involving biological membranes. Under some circumstances, even a small variation in NP size may induce slightly different outcomes of NP-membrane interactions[141].

3.1 One-phase synthesis

As introduced in Section 1.2.1, the synthesis of small spherical AuNPs protected by apolar alkylthiols has been dominated by the Brust-Schiffrin two-phase approach since the early 90's[97]. Subsequently, AuNPs synthesized with this strategy can undergo thiol-for-thiol ligand exchange to obtain mixed monolayers of hydrophobic and ω-functionalized (e.g. hydrophilic) ligands[101,104]. This procedure is easy and only requires ambient conditions, but it comes with some drawbacks: 1) it needs a phase-transfer reagent to displace the Au(III) ions from the water phase, in which they are solubilized, to the organic phase, in which the thiol-assisted reduction takes place; 2) final NPs usually have large dispersion in size, even higher than 50 %; 3) thiol-for-thiol exchange is time consuming and usually requires daylong procedures; 4) since the exchange occurs in the presence of large excess of the incoming thiol and reaches a dynamic equilibrium between the exchanging ligands, fixing (and modulating) the desired amount of alkylthiol to be replaced is not trivial; and finally, 5) because of the strong Au-S association, complete replacement of the original ligand shell is not achievable. More recently, significant effort has been made to develop more reliable and versatile one-phase protocols in which the thiol-assisted reduction of Au(III) ions occurs in a homogeneous phase instead of the two-phase interface of Brust's synthesis[284]. The homogeneity of the reaction mixture is fundamental to obtain colloidal NPs with reduced core size dispersion. Moreover, the one-phase approach allows for quick one-pot preparation of water-soluble AuNPs capped by a mixed thiol monolayer, without the need for further thiol-for-thiol ligand

exchange. This considerably reduces the time of NP synthesis and the number of involved chemicals whose residues are laborious to remove from final NPs. Finally, this synthetic route allows for discrete control over final ligand shell composition and it is commonly used to obtain homoligand hydrophilic shells. Within this thesis, one-phase amphiphilic AuNPs were prepared following a modified, scaled-down, literature procedure[285]; a scheme of the synthesis is reported in Figure 22.

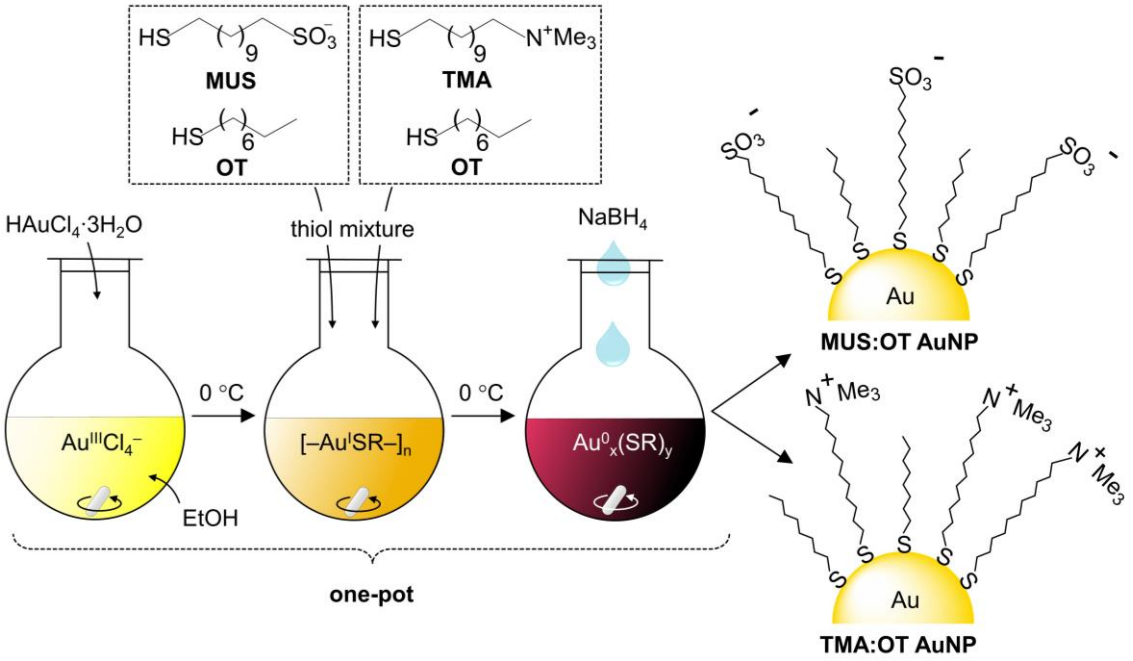

Figure 22. Scheme of the one-phase procedure in EtOH used to obtain small amphiphilic AuNPs. MUS and TMA confer a negative or positive surface charge to the NP ligand shell, respectively. The stoichiometric ratio of the thiol mixture is defined as the ligand feed ratio. Monocomponent thiol solutions can be used to obtain homoligand shells, as in the case of all-MUS and all-TMA AuNPs.

The reaction was performed at 0 °C under continuous magnetic stirring to minimize the effect of any temperature gradients on NP size distribution. The gold precursor, hydrogen tetrachloroaurate (III) trihydrate ($HAuCl_4 \cdot 3H_2O$), was first dissolved in ethanol (EtOH) and then let to stir for a few minutes with an equimolar thiol mixture prepared in a small amount of methanol (MeOH). In this step, the alkylthiols (RSH) pre-reduce Au(III) to Au(I) to form a polymeric Au(I)-thiol complex (Equation 5)[100–102]. This reaction is confirmed by the color change of the gold solution from bright to turbid yellow (Figure 22).

pre-reduction $$Au^{III}Cl_4^- + RSH \rightarrow [-Au^{I}SR-]_n \text{ (polymer)} \quad (5)$$

The 1:1 Au(III):RSH molar ratio is sufficient to obtain a fast and homogeneous NP coverage, while at the same time avoiding excessive unbound thiols. In general, more diluted thiol mixtures lead to larger NP diameters with broader distributions. Au(I)

was then slowly reduced to metallic Au(0) by dropwise addition of a concentrated ethanolic solution of sodium borohydride ($NaBH_4$), an effective reducing agent. This step triggers the formation of Au(0) clusters and concomitant growth into small thiol-protected AuNPs or $Au^0_x(SR)_y$ (Equation 6)[101].

reduction $$[-Au^{I}SR-]_n + BH_4^- \rightarrow Au^0_x(SR)_y \quad (6)$$

After a few hours from the end of reductant addition, the product was isolated from the reaction mixture, repeatedly washed, and finally vacuum dried. Using the same reaction protocol but slightly different washing cycles, amphiphilic AuNPs were prepared with either heteroligand (i.e. MUS:OT and TMA:OT) or homoligand (all-MUS and all-TMA) shells. Unlike the former, the latter have not been tested in experiments with lipid membranes. The detailed protocols followed to synthesize one-phase AuNPs, together with the material list, are reported in Appendix A1.

In the case of mixed monolayers, it was possible to tune with discrete accuracy the ligand shell composition onto the Au core by defining the ligand feed ratio in solution (Figure 22). In particular, for the project described in Chapter 4, MUS:OT and TMA:OT AuNPs with a 2:1 (mol:mol) feed ratio were synthesized. The same MUS:OT AuNPs were also used in the experiments discussed in Chapter 5. In EtOH, ω-charged alkylthiols like MUS and TMA generally show a higher tendency to graft onto the Au core than OT or other hydrophobic alkylthiols[285]. Therefore, to target the preset ligand shell composition, an excess of OT must be used. This behavior may be related to the different solubilities of gold salt, ω-charged ligands and OT in EtOH: while $Au^{III}Cl_4^-$ ions, MUS and TMA are nicely solubilized, the highly hydrophobic OT prefers more apolar solvents (e.g. MeOH, or better, toluene and dichloromethane) and tends to slightly aggregate. Such a tendency may disfavor the readiness of OT to bind to the surface of growing Au(0) nuclei, thus explaining why the grafting yield of better-dispersed ligands is always higher[285]. Within this thesis, the ligand composition of MUS:OT and TMA:OT monolayers was quantified after iodine-mediated etching of the Au core, a procedure that allows to quantitatively release the thiolated ligands as disulfides[286,287]. By proton nuclear magnetic resonance (^1H NMR), the ligand molar ratio can be calculated by comparing the integrals of peaks individually contributed by OT, MUS, and TMA (see Appendix A2). The reliability of this method is well-established and strongly depends on the purity of AuNPs[285]. Therefore, before iodine etching, it is necessary to accurately eliminate any contamination due to unbound ligands or other impurities (e.g. reaction by-products or reagents residues). Moreover, when considering the ligand shell composition, even the purity of reagents and solvents is of paramount importance to obtain reproducible

results. All the chemicals used in this synthetic protocol are commercially available with a high degree of purity, except for MUS. Therefore, MUS was synthesized in house according to a modified literature procedure[144,285]. Notably, we have proposed a protocol to quantify for the first time the organic purity of MUS (i.e. 93 %) by quantitative nuclear magnetic resonance (qNMR). This step provides an important new contribution to the outcome of this synthetic route[285]. All details of MUS synthesis and characterization are reported in Appendix A3.

3.1.1 NP characterization

In general, the experimental characterization of ligand-protected AuNPs is based on a variety of methods, including thermogravimetric analysis (TGA)[100,112], scattering techniques (e.g. dynamic light scattering (DLS) and ζ-potential)[288], microscopy (e.g. transmission electron microscopy (TEM) and AFM[289]), and spectroscopy (e.g. ultraviolet-visible (UV-Vis)[290] and NMR)[291,292]. Combining the weight loss determined by TGA and the mean core size derived by TEM analysis, it is possible to calculate the ligand density onto the Au core approximating the NP shape to a sphere. In general, the ligand density of one-phase AuNPs obtained with this protocol is highly reproducible and well established in the literature, i.e. ~4.8 ligands/nm^2 [145,285].

Within this thesis, amphiphilic AuNPs prepared with the one-phase approach were characterized by TEM, DLS, ζ-potential, ^{1}H NMR, and UV-Vis techniques. TEM analysis was performed to characterize the NP shape and core size distribution, while DLS was used to analyze the overall hydrodynamic NP size. The NP surface potential (ζ-potential) in aqueous solution was also determined. ^{1}H NMR was used before and after iodine etching of the Au core to assess the presence of unbound ligands and the thiol molar ratio within the ligand shell, respectively. Results on NP size analyses are reported in Figure 23 (TEM images) and Table 3. Final AuNPs showed spherical shape and a mean core diameter distributed between ~2÷6 nm; notably, ~20÷30 % core size dispersion was obtained independently of surface functionalization. Table 4 reports the final ligand shell composition and the ζ-potential of MUS:OT and TMA:OT AuNPs used in the experiments with lipid membranes (Chapters 4 and 5). UV-Vis characterization results of MUS:OT and TMA:OT AuNPs are reported in Appendix A2, together with all characterization details not included in this chapter (i.e. sample preparation methods, equipment specifications, and data statistical analyses).

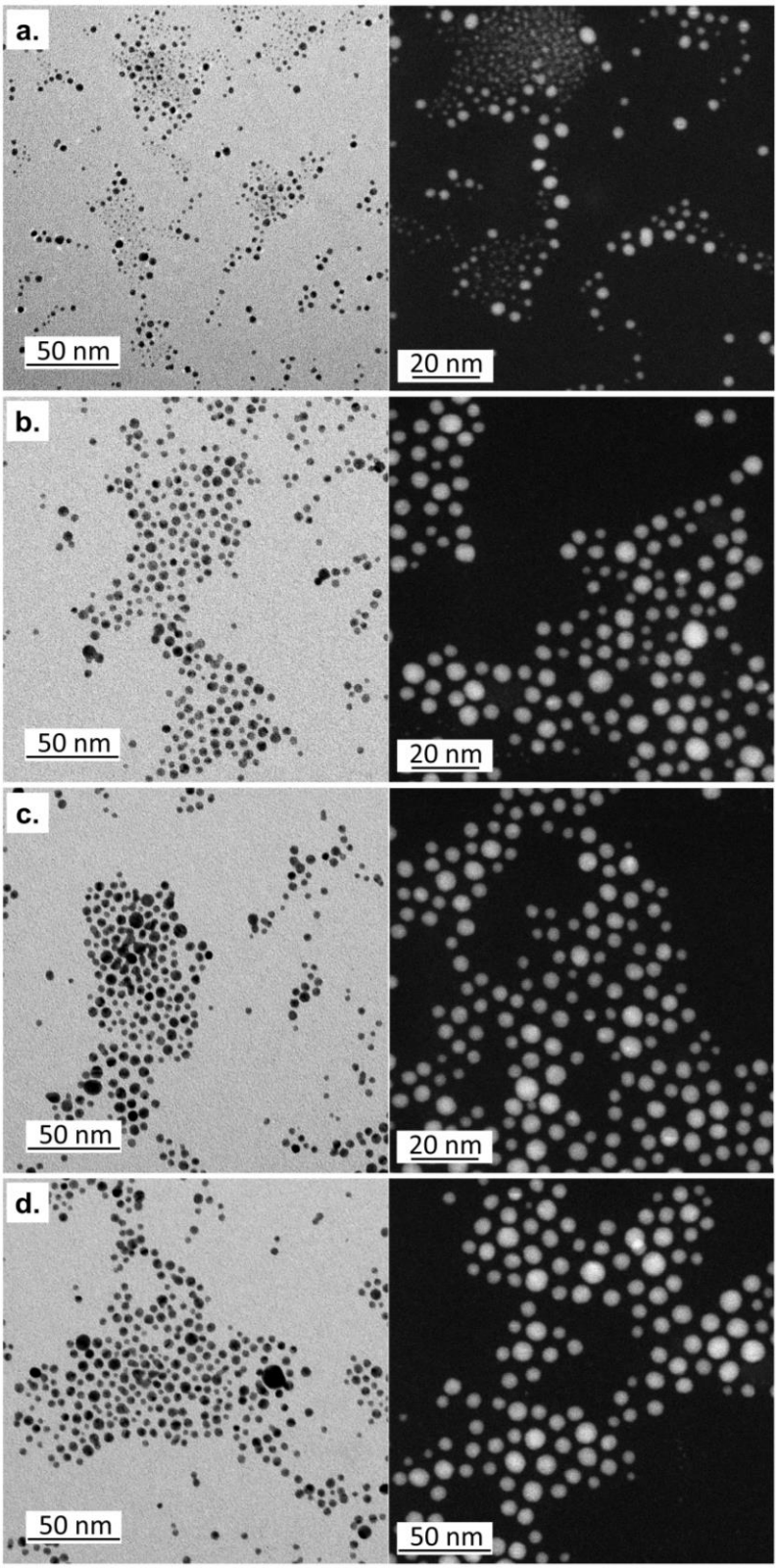

Figure 23. Bright-field TEM (BF-TEM) (left) and high-angle annular dark-field scanning TEM (HAADF-STEM) (right) images of one-phase AuNPs with different surface composition: **a**) 2:1 MUS:OT, **b**) 2:1 TMA:OT, **c**) all-MUS), and **d**) all-TMA. MUS:OT AuNPs in (**a**) and TMA:OT AuNPs in (**b**) were used in the experiments with lipid membranes described in Chapters 4 and 5.

Table 3. Core size and hydrodynamic size of amphiphilic one-phase AuNPs.

Ligand composition	*Ligand feed ratio (mol:mol)*	*TEM*	*DLS*
		core size (nm) [a]	*hydrodynamic size in water (nm)* [b,c]
MUS:OT	2:1	2.7 ± 0.8	6.5 ± 0.2
TMA:OT	2:1	4.5 ± 1.1	7.7 ± 1.4
all-MUS	only MUS	5.2 ± 1.3	5.9 ± 1.2
all-TMA	only TMA	5.4 ± 1.2	8.1 ± 1.4

[a] mean diameter ± one standard deviation.
[b] mean diameter ± error calculated using Student's statistics (95 % confidence level, n=12).
[c] water purified with a Milli-Q ultrapure water system (MilliPore).

Table 4. Ligand shell composition and ζ-potential of one-phase MUS:OT and TMA:OT AuNPs used in the experiments of Chapters 4 and 5.

Ligand composition	*Ligand feed ratio (mol:mol)*	*^{1}H NMR after iodine etching*	*ζ-potential (mV)*	
		% of ω-charged ligand [a]	*in water* [b,c]	*in buffer* [b,d]
MUS:OT	2:1	80 ± 8	−48 ± 4	−31 ± 3
TMA:OT	2:1	72 ± 11	+38 ± 3	+25 ± 2

[a] average (mol %) ± error calculated using Student's statistics (95 % confidence level, n=3).
[b] mean ζ-potential ± error calculated using Student's statistics (95 % confidence level, n=9).
[c] water purified with a Milli-Q ultrapure water system (MilliPore).
[d] experimental buffer used in the project of Chapter 4 and containing 100 mM NaCl (pH 7.4).

3.2 Thiol-for-oleylamine ligand exchange

Even though the one-phase approach has significantly improved the uniformity in size of thiol-protected AuNPs, core size dispersion less than 20 % cannot be achieved by using this synthetic route (unless a subsequent size-fractionation process is adopted[140]). To obtain thiol-protected AuNPs with stricter size control over a wide choice of surface compositions, a viable route is to decouple the controlled growth of the NP core from the subsequent formation of a tailored ligand shell. Within this perspective, intermediate stabilizing agents with labile affinity to gold have attracted remarkable interest to promote fast, complete, and controllable thiol-for-agent ligand exchanges. Among weakly bound capping agents, oleylamine (OAm) is well-known to act as a stabilizer, solvent, and reducing agent[293,294]. When combined with stronger reductants, it allows generating spherical OAm-capped AuNPs (OAm-AuNPs) with remarkably narrow size dispersion, even less than 10 %[293–295]. Moreover, the core size can be finely tuned between 1÷10 nm by varying the reaction temperature at which the reducing agent is injected. Typical reaction temperatures range from 1 to 50 °C and, in general, smaller core sizes are favored by higher temperatures[294,295]. Once OAm-AuNPs with target sizes are generated, OAm can be completely replaced by a wide variety of ligands with higher gold-binding strength, such as alkylthiols and mixtures thereof. Since the structure of the NP core

is not modified during ligand exchange, OAm-AuNPs are an ideal precursor to generate monodisperse thiol-protected AuNPs of identical size but with different ligand shell composition[294]. Such AuNPs are particularly suited for systematic studies in which those effects due to NP size must be disentangled from those attributed to NP surface chemistry. The thiol-for-OAm ligand exchange also allows obtaining NPs with tailored solubility for solvents ranging from polar protic liquids (e.g. water, and EtOH) to highly apolar hydrocarbons.

Within this thesis, thiol-protected AuNPs were prepared following, with minor modification, the two-step approach described by Yang et al.[294] This procedure comprises the synthesis of monodisperse OAm-AuNPs with tunable core size, followed by the complete exchange of the hydrophobic OAm by thiol mixtures to generate water-soluble amphiphilic AuNPs with target surface functionality[296]. This synthesis was performed during an internship in the group of Prof. Francesco Stellacci at the EPFL (Lausanne, Switzerland). As for the previous one-phase method, MUS:OT, TMA:OT, all-MUS, and all-TMA AuNPs were synthesized. Additional AuNPs were prepared by combining MUS with a branched variant of OT, i.e. the 3,7-dimethyl-1-octanethiol (br-OT); these NPs will be referred to as MUS:br-OT AuNPs. Though MUS:OT and MUS:br-OT AuNPs share nearly identical surface composition (in particular, the same degree of hydrophobicity), the former are capable of spontaneous membrane penetration, while the latter fail to enter lipid membranes passively and are mainly endocytosed by cells[133,135,138,141]. Hence, they are usually used in control experiments. Ligand branches are believed to decrease the free volume accessible to each ligand in the monolayer, thus inhibiting the chain deformability necessary to stabilize the NP in the snorkeling configuration (see Section 1.2.3)[145].

***Step 1**: synthesis of OAm-AuNPs.* Monodisperse OAm-AuNPs with tunable core size were synthesized following the scheme illustrated in Figure 24. The gold precursor $HAuCl_4 \cdot 3H_2O$ was dissolved in a mixture of OAm (the capping agent) and a linear hydrocarbon, i.e. the *n*-octane. Linear or planar hydrocarbons (e.g. *n*-octane, *n*-hexane, and toluene) have proven to be the best solvents in optimizing the final size dispersion of OAm-AuNPs[297]. Interestingly, the role of solvent in controlling the NP size dispersion is generally not observed in the previously described one-phase system (Figure 22, Section 3.1). This difference may be due to the weaker binding affinity of amines on the Au core compared to thiols, thus making the OAm protective layer more sensitive to solvent influence[297]. After a few minutes of stirring, an excess of the reducing agent *tert*-butylamine borane complex (tBAB) was rapidly injected into the reaction flask. Stoichiometrically, as shown by Equation 7, for the reduction of Au(III) ions the moles of tBAB must be at least half those of gold[297].

$$2HAu^{III}Cl_4 + (CH_3)_3CNH_2 \cdot BH_3 + 3H_2O \rightarrow 2Au^0 + (CH_3)_3CNH_2 + 8HCl + H_3BO_3 \quad (7)$$

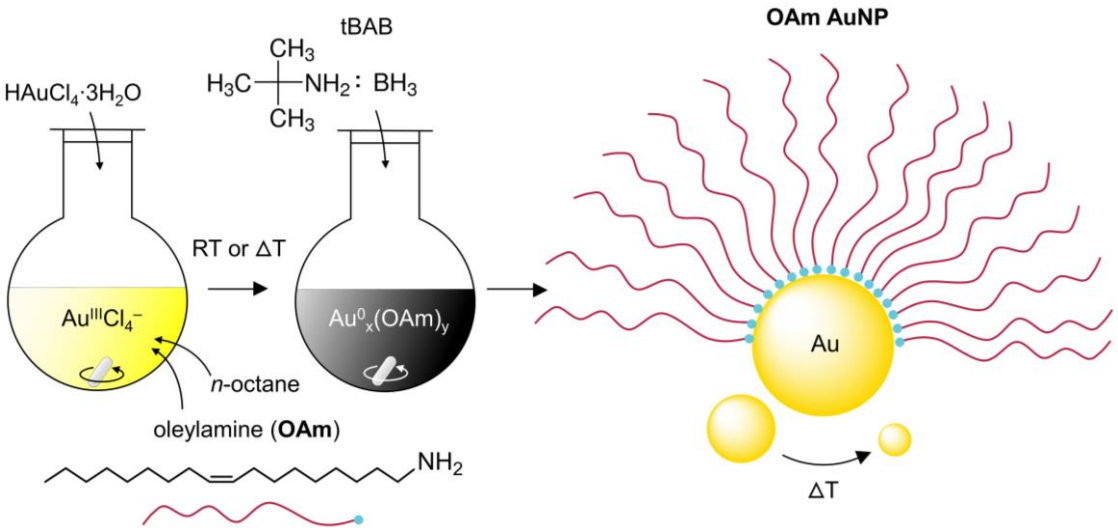

Figure 24. Scheme of the reaction system in *n*-octane used to synthesize monodisperse OAm-AuNPs with tunable size.

The core diameter of OAm-AuNPs was varied in the ~2÷4 nm range by increasing the reduction temperature from room temperature (RT, 22 °C) to ~45 °C, as shown in Figure 25. In line with the literature, an additional temperature increase above 50 °C did not result in a further decrease of NP size[294]. According to the original literature protocol[294], core diameters between 4 and 7 nm can be obtained by reducing the reaction temperature up to 1 °C. Differently, within this thesis, OAm-AuNPs with core diameters between 4÷5 nm were obtained at RT using a scale-up procedure with a decreased OAm-to-Au(III) molar ratio. After intensive washing, all OAm-AuNPs were vacuum dried before following thiol-for-OAm ligand exchange. The detailed protocols followed to synthesize OAm-AuNPs of different sizes, together with the materials list, are reported in Appendix A4.

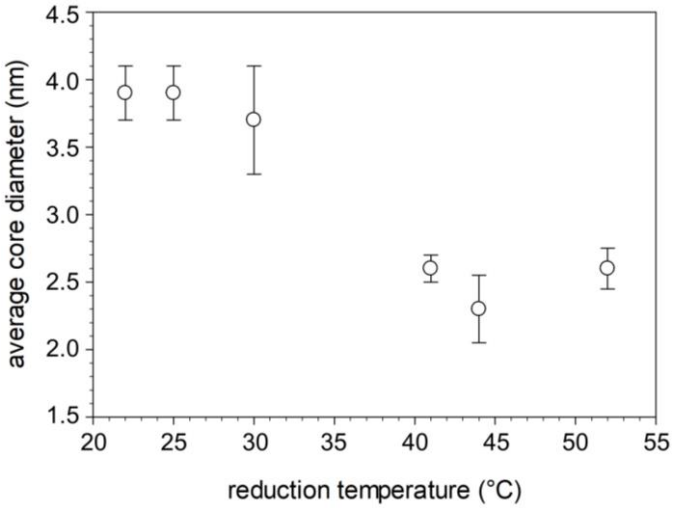

Figure 25. Core size of monodisperse OAm-AuNPs as a function of the reduction temperature (22÷52 °C). Mean diameter ± error (Student's statistics, 95 % confidence level, n=3-10). Size data were acquired by TEM analysis.

Step 2: *thiol-for-OAm ligand exchange.* The exchange procedure was carried out overnight at RT upon continuous stirring (Figure 26)[294,296]. After intensive washing both in organic solvents and water, amphiphilic AuNPs were either vacuum- or freeze-dried. Protocol details are reported in Appendix A4.

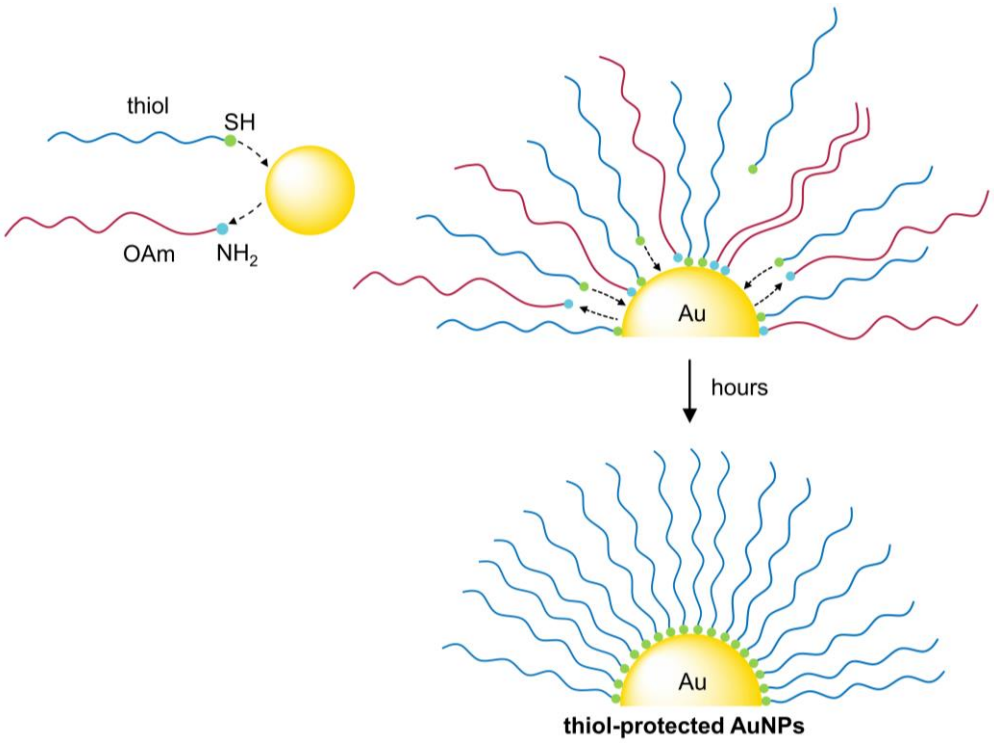

Figure 26. Schematic illustration of the thiol-for-OAm ligand exchange onto the Au core in solution. OAm-AuNPs were vigorously mixed in solution with an excess of thiols. In the case of mixed thiol monolayers, preset ligand feed ratios were used. Due to the strong chemisorption of thiols on Au, OAm is completely replaced in several hours (~12÷15 h). This procedure was used to obtain anionic MUS:OT, MUS:br-OT, and all-MUS AuNPs and cationic TMA:OT and all-TMA AuNPs.

As for the previous one-phase procedure, the thiol yield ratio onto final AuNPs does not match the thiol feed ratio added in solution (Figure 26). In particular, the molar yield (%) of hydrophobic thiols (OT and br-OT) onto the Au core is always way lower than the molar feed (%) mixed with OAm-AuNPs. Within this thesis, the exchange efficiency of OAm by OT and br-OT in combination with either MUS or TMA was extensively investigated to establish an accurate and reliable relationship between the stochiometric ligand ratio stirred in solution and the resulting ligand composition on the surface of AuNPs. In the case of MUS:OT, TMA:OT, and MUS:br-OT coatings, several NP samples with different molar feed (%) of OT or br-OT were prepared and analyzed by ^{1}H NMR after iodine etching of the Au core to determine the corresponding molar yield (%). As reported in Figure 27, NMR data were finally plotted as a function of the NP size in steps of ca. 1 nm. While initially the yield data seemed extremely unreproducible from batch to batch, the systematic

subdivision by NP size revealed diverse trends in the exchange efficiency of OAm by hydrophobic thiols on sub-5 nm AuNPs of different core diameters. Interestingly, OT and br-OT tend to exchange OAm more effectively as the size decreases. On smaller NPs, the exchange process may be facilitated by the larger free volume accessible to each ligand in the surface monolayer (see Section 1.2.3)[148].

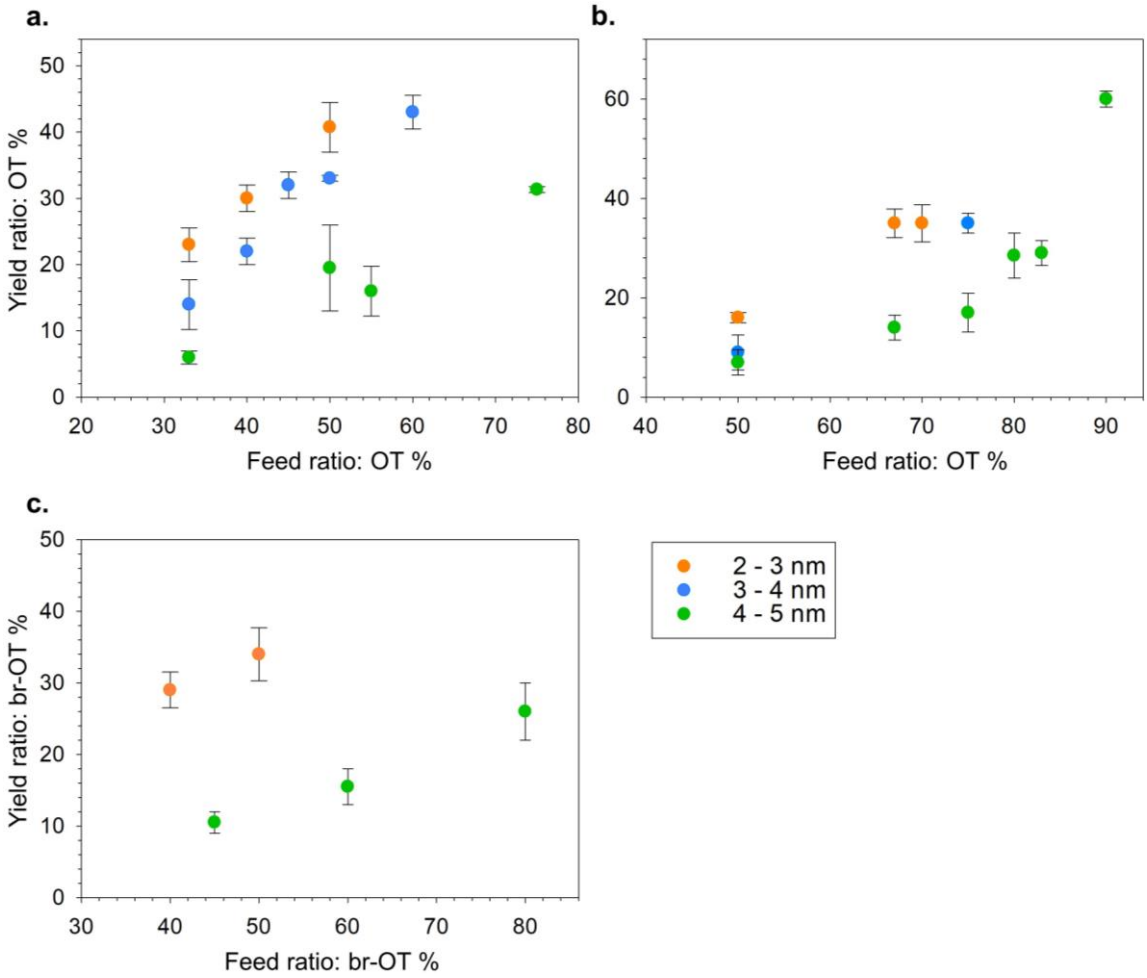

Figure 27. Molar yield (%) of the hydrophobic thiol onto the surface of AuNPs as a function of the molar feed (%) in solution. Ligand shell with **a**) MUS:OT, **b**) TMA:OT, and **c**) MUS:br-OT composition. Average yields (mol %) – determined by ^{1}H NMR after iodine etching of the Au core – were plotted separately for different NP core sizes with steps of ca. 1 nm. Error bars were calculated using Student's statistics and assuming a confidence level of 95 % (n=3-7); in general, uncertainties between 0.5 and 6.5 % were obtained. In all samples, the yield (mol %) of the hydrophobic thiol was always significantly less than the feed (mol %), i.e. the ω-charged ligand (MUS or TMA) was always overexpressed.

Within this synthetic route, these plots have been – and still are – an extremely useful tool to obtain accurate and reliable control over the surface functionalization of monodisperse AuNPs with target ligand shells. Indeed, thanks to their use, it was possible to prepare NP batches that differed by even a few percentage units of the

hydrophobic ligand. Therefore, this result provides an important new contribution to the outcome of this bottom-up synthetic strategy.

3.2.1 NP characterization

All OAm-AuNPs were analyzed by TEM to characterize the NP shape and core size distribution. NP average diameters (2÷4 nm) are plotted in Figure 25 as a function of the reaction temperature (larger values were obtained at RT with the scale-up protocol). In general, spherical AuNPs with 0.3÷0.6 nm standard deviation were obtained regardless of the mean core size; therefore, smaller NPs (2÷3 nm) always result slightly more polydisperse than larger ones. BF-TEM images of OAm-AuNPs of three representative sizes are reported in Figure 28. TEM characterization was also repeated after OAm replacement to confirm that the core diameter did not vary upon the exchange process. Notably, the thiol-protected AuNPs reported in Figure 29 derived from the same OAm-coated precursor. This result clearly shows that this two-step synthetic route is ideal to generate monodisperse amphiphilic AuNPs variously functionalized but with identical core size. Moreover, all thiol-protected AuNPs were characterized by ^{1}H NMR after iodine etching of the Au core. This analysis was performed both to calculate the yield (mol %) of the hydrophobic thiol and to verify the absence of OAm residues in the final ligand shell. As a matter of fact, complete OAm removal is evidenced by the disappearance of its characteristic footprint from the ^{1}H NMR spectrum[294]. NMR results are summarized in Figure 27. The thorough TEM and NMR characterizations carried out on several samples have allowed outlining the experimental conditions necessary to reliably and accurately design the amphiphilic NPs studied in this thesis. Before the experiments with lipid membranes, additional DLS and ζ-potential analyses were performed. Table 5 and Figure 30 report all characterization results of the monodisperse AuNPs used in the project of Chapter 6. These NPs have different sizes but identical 2:1 MUS:OT surface ratio designed using the plot in Figure 27a. All characterization details not included in this chapter (i.e. sample preparation methods, equipment specifications, and data statistical analyses) are reported in Appendix A5.

Table 5. Characterization of monodisperse 2:1 MUS:OT AuNPs of two different sizes. Among all monodisperse NPs prepared in this thesis, only these were selected for the experiments with lipid membranes (Chapter 6).

TEM	*^{1}H NMR after iodine etching*	*DLS - hydrodynamic size (nm)* [c]		*ζ-potential (mV)* [c]	
core size (nm) [a]	*% of OT* [b]	*in water* [d]	*in buffer* [e]	*in water* [d]	*in buffer* [e]
2.4 ± 0.4	32 ± 5	5.6 ± 1.7	11.2 ± 0.4	–46 ± 5	–38 ± 2
4.8 ± 0.5	32 ± 5	13.1 ± 3.8	25.3 ± 1.2	–61 ± 1	–36 ± 1

[a] mean diameter ± one standard deviation.

[b] average (mol %) ± error calculated using Student's statistics (95 % confidence level, n=3).
[c] mean value ± error calculated using Student's statistics (95 % confidence level, n=12-18)
[d] water purified with a Milli-Q ultrapure water system (MilliPore).
[e] experimental buffer: PBS (Phosphate Buffered Saline; 1x, pH 7.4).

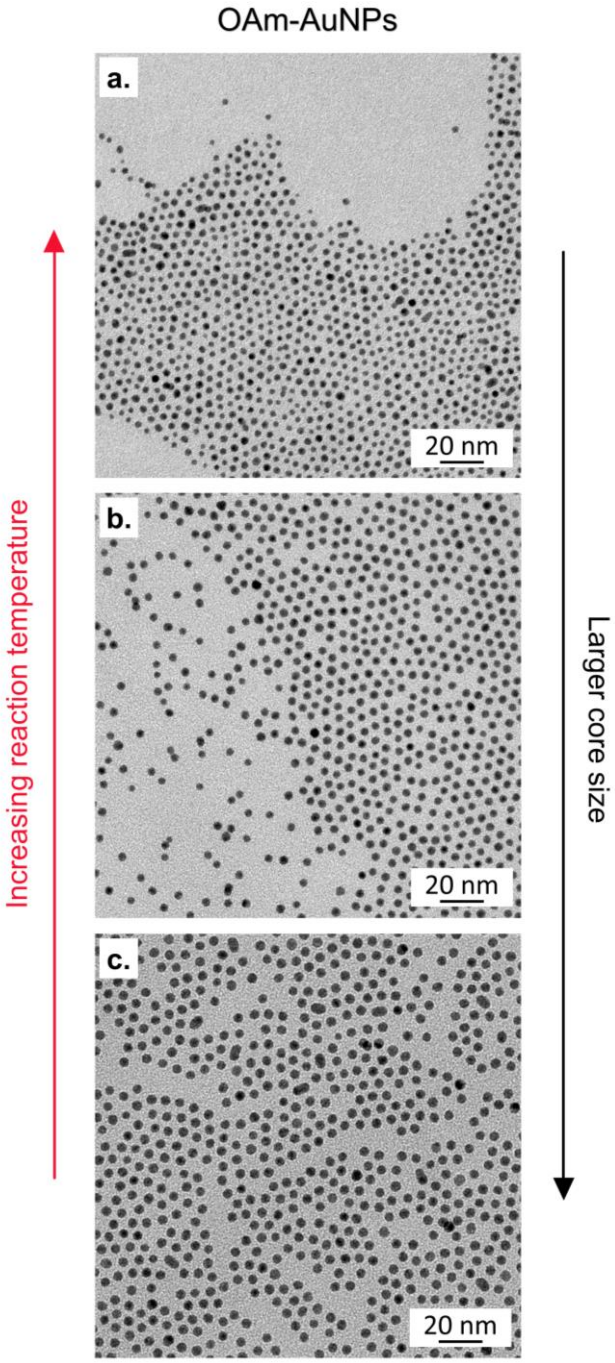

Figure 28. BF-TEM images of OAm-AuNP samples with different core size: **a**) 2.8 ± 0.4 nm, **b**) 3.7 ± 0.3 nm, and **c**) 4.6 ± 0.4 nm (mean core size ± one standard deviation). NPs were synthesized at 41 °C, 30 °C, and 22 °C (scale-up protocol), respectively. See Appendix A5 for full details on TEM characterization.

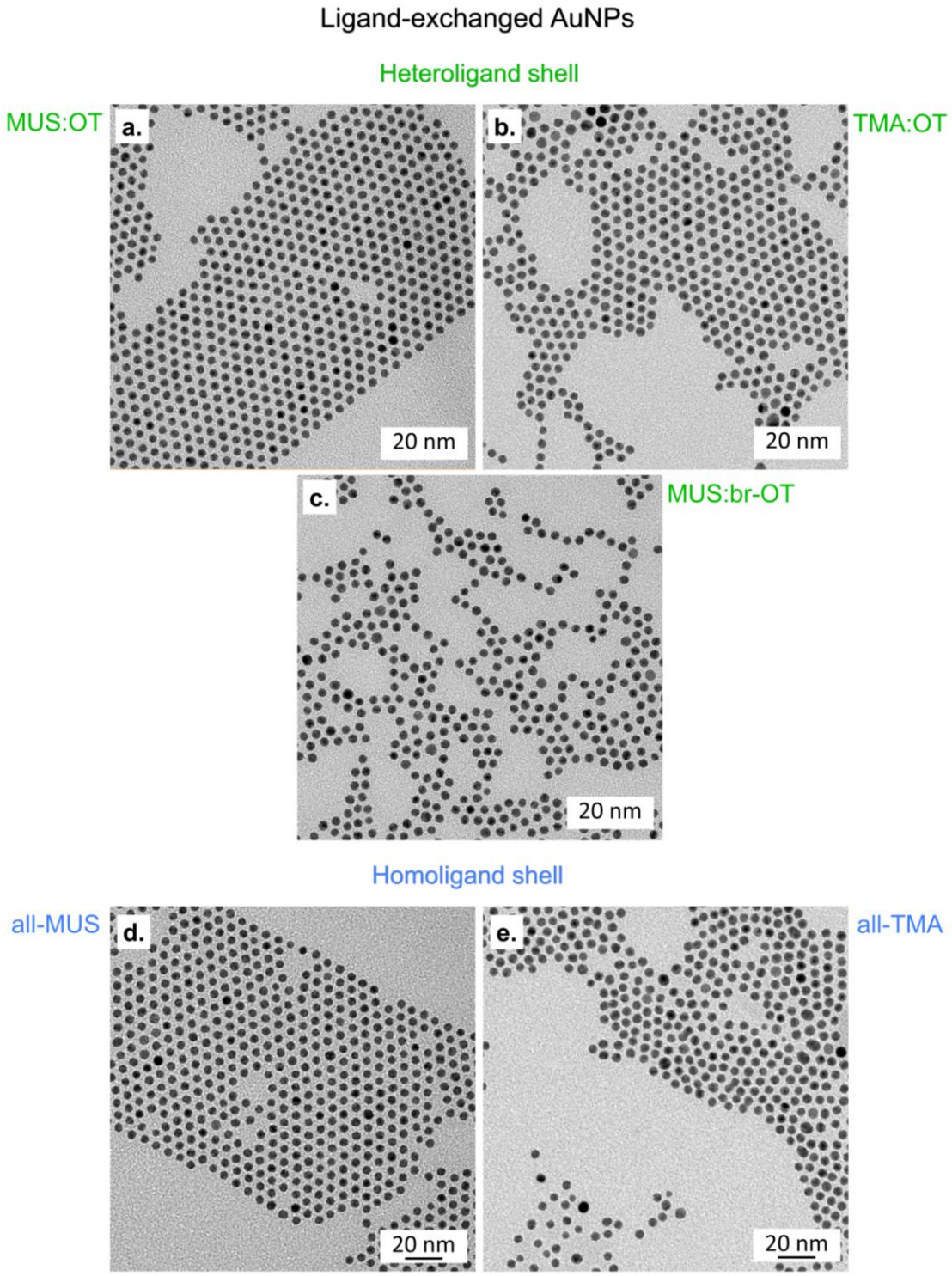

Figure 29. BF-TEM images of monodisperse AuNPs after thiol-for-OAm ligand exchange: **a**) MUS:OT AuNPs (4.9 ± 0.5 nm, 16 % OT yield %), **b**) TMA:OT AuNPs (5.1 ± 0.5 nm, 14 % OT yield %), **c**) MUS:br-OT AuNPs (5.0 ± 0.3 nm, 11 % br-OT yield %), **d**) all-MUS AuNPs (4.7 ± 0.3 nm), and **e**) all-TMA AuNPs (4.7 ± 0.6 nm). For each NP population, mean core size ± one standard deviation is reported. Notably, all these thiol-protected AuNPs derive from the same OAm-AuNP precursor (4.9 ± 0.5 nm); this confirms that the average NP diameter did not change upon ligand exchange. In the case of mixed monolayers (**a**-**c**), AuNPs share a similar yield (mol %) of the hydrophobic thiol.

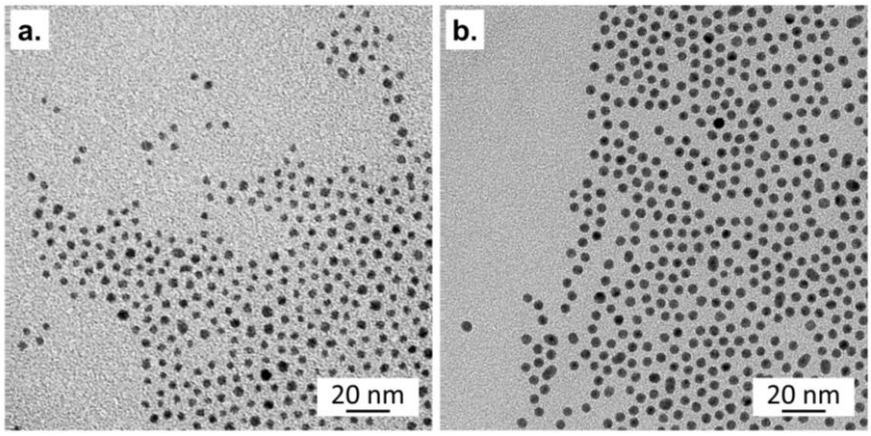

Figure 30. BF-TEM images of monodisperse 2:1 MUS:OT AuNPs used in the experiments reported in Chapter 6. Average core diameter: **a**) 2.4 ± 0.4 nm, and **b**) 4.8 ± 0.5 nm (characterization details are reported in Table 5).

4. Effect of NP surface charge at the NP-membrane interface

4.1 NP surface charge: a debated role in NP-membrane interactions

Among NP surface properties, surface charge is crucial in determining the behavior of ligand-protected NPs interacting with lipid membranes. When looking at the interaction between charged amphiphilic NPs and model lipid membranes, it is tempting to interpret the experimental data by simple electrostatic arguments. Electrostatic attraction between oppositely charged NPs and bilayers certainly favors the formation of stable NP-lipid complexes. This is the case, for example, for positively and negatively charged metal or oxide NPs interacting with charged bilayers[61,298,299]. The interaction between oppositely charged NPs and lipid bilayers can cause transient damage to the membrane, as well. Liposome leakage assays by Goodman et al[61]., for example, reported the disruptive effects of cationic amphiphilic AuNPs on negatively charged bilayers composed by a mixture of 1-stearoyl-2-oleoyl-*sn*-glycero-3-phospho-L-serine (SOPS) and 1-stearoyl-2-oleoyl-*sn*-glycero-3-phosphocholine (SOPC). Recently, combined experimental measurements and computer simulations have reported the favorable adsorption and aggregation, upon interaction, of cationic amphiphilic AuNPs on negatively charged model membranes[131,132]. Furthermore, perturbation of membrane composition and fluidity is shown, since negatively charged lipids cluster around cationic AuNPs[131]. The NP-membrane interaction is also associated with lipid extraction possibly causing membrane perturbation and destabilization[132]. The same reasoning is generally invoked to explain why, *in vitro*, cationic NPs are more toxic than anionic NPs to Gram-negative bacteria[300,301]. Nevertheless, electrostatic attraction is not a necessary ingredient to the formation of stable NP-bilayer complexes, nor to toxicity, which can take place also when the NP and the membrane have a ζ-potential of the same sign[299,300,302].

Even more subtle is the interpretation of the available experimental data on the interaction of charged amphiphilic AuNPs with the surface of membranes exposing neutral (zwitterionic) lipid headgroups, like in the extracellular leaflet of mammalian plasma membranes. As described in Section 1.2.3, thiolated AuNPs capped by negatively or positively charged amphiphilic monolayers – with mean core

diameters in the 2÷6 nm range – can interact passively with mammalian cell membranes and model lipid bilayers[130,132,133,141]. The role played by the sign of the NP charge, though, is still debated. Neutron reflectometry studies by Tatur et al.[130], suggest that anionic AuNPs could adhere to the surface of 1,2-distearoyl-*sn*-glycero-3-phosphocholine (DSPC) bilayer without penetrating it, at variance with cationic AuNPs that would interact with the zwitterionic DSPC membrane in a more disruptive way. According to Goodman et al.[61], in pure zwitterionic SOPC bilayers, the membrane leakage induced by anionic AuNPs is larger than that of cationic AuNPs. On the contrary, Van Lehn et al.[141], showed no membrane translocation of the fluorophore in multilamellar 1,2-dioleoyl-*sn*-glycero-3-phosphocholine (DOPC) vesicles in the presence of anionic AuNPs co-localized with the vesicle bilayers. From computer simulations of NP-membrane interaction, there is a general consensus about the favorable interaction between anionic or cationic amphiphilic AuNPs and model neutral lipid bilayers (Section 1.2.3)[129,132,141,142,146,156–158]. Such interaction can occur spontaneously or require that small free energy barriers are overcome. Though, the role of the NP charge, at the molecular level, is again still unclear and debated.

4.2 Project: objective and methods

This project aimed to clarify the role played by charged ligands during the nonspecific interaction between amphiphilic AuNPs and model zwitterionic lipid membranes. To disentangle the effects due to the NP surface charge from those due to other physical parameters (e.g. core size or ligand length and flexibility), sub-6 nm anionic MUS:OT and cationic TMA:OT AuNPs with a comparable core size distribution and a controlled surface ligand composition (2:1 ligand feed ratio) were used. As shown in Figure 5 (Section 1.2.2), the main difference between these amphiphilic NPs is the opposite charge of the polar headgroup of MUS and TMA ligands. For the sake of compactness, within this project anionic amphiphilic MUS:OT AuNPs and cationic amphiphilic TMA:OT AuNPs will be referred to as NP– and NP+, respectively. As reported in Section 1.2.3, many experimental results indicate the existence of a stable NP-membrane interaction with both ligand types, though a coherent molecular interpretation of the results is still lacking. Model neutral lipid bilayers were prepared using the zwitterionic 1-palmitoyl-2-oleoyl-*sn*-glycero-3-phosphocholine (POPC), one of the predominant mammalian glycerophospholipids The chemical structure of POPC is illustrated in Figure 54 (Appendix B1). The NP-membrane interaction was investigated by means of two experimental techniques: QCM-D in liquid (Section 2.2) and dye-leakage assays (Section 2.3.1). Experiments

were carried out in 100 mM NaCl, 2 mM histidine, 2 mM TES, 0.1 mM EDTA buffered solution adjusted to pH 7.4. QCM-D investigation was performed thanks to the precious contribution of Dr. Silvia Dante (IIT, Genoa). This technique was used to quantify the extent of NP– and NP+ uptake by the membrane, while fluorescence leakage assays allowed probing the resultant damage induced to the integrity of the lipid bilayer.

Thanks to the collaboration with the computational group of Prof. Giulia Rossi (DIFI, University of Genoa), a molecular-level interpretation of the experimental results was offered using coarse-grained MD simulations[303]. This combined experimental and computational approach provided a close match between the experimental investigation and the models *in silico*. Since the nature of this thesis is experimental, and simulations have been elaborated by collaborators, only the main computational results will be described within this chapter (Section 4.3.3). This inclusion is fundamental to provide a comprehensive discussion of the outcomes of this multidisciplinary study. More information on the *in silico* investigation is reported in Canepa et al.[1]

4.3 Results and discussion

4.3.1 NPs and lipid membranes

For convenience of the reader, details on NPs and lipid membranes used in this project are resumed here.

NP– and NP+ were synthesized using the one-phase procedure described in Section 3.1. From TEM measurements, the mean Au core diameter was 2.7 ± 0.8 nm for NP– and 4.5 ± 1.1 nm for NP+ (Figure 23a,b and Table 3, Section 3.1.1). DLS measurements yielded compatible hydrodynamic diameters of 6.5 ± 0.2 nm for NP– and 7.7 ± 1.4 nm for NP+ (Table 3). The fraction of charged ligands was 80 ± 8 % for NP– and 72 ± 11 % for NP+, as determined by ^{1}H NMR measurements after decomposition of the Au core (Table 4, Section 3.1.1). The NP ζ-potential, measured in the experimental buffer in which the NP-membrane interaction took place, was –31 ± 3 mV for NP– and +25 ± 2 mV for NP+ (Table 4). These ζ-potential values show that NP dispersions retained a sufficiently high colloidal stability in the experimental conditions to avoid considerable NP aggregation. Details on NP characterization are reported in Appendix A2. In all experiments, NP– and NP+ were added in the form of filtered aqueous dispersions (see Appendix A1).

Zwitterionic lipid bilayers were prepared in the form of POPC unilamellar vesicles of two different hydrodynamic diameters, i.e. 23 ± 2 nm and 105 ± 6 nm (Table 11, Appendix B2). Smaller vesicles were obtained by sonicating multilamellar vesicle suspensions, whereas larger unilamellar vesicles were prepared by extrusion of multilamellar vesicles. For dye-leakage assays, sonicated and extruded POPC vesicles were loaded with a self-quenched buffered calcein solution (175 mM, pH 7.4). For QCM-D measurements, sonicated calcein-free POPC vesicles were prepared using the experimental buffer instead of the self-quenched calcein solution. The ζ-potential of the POPC bilayer in the experimental buffer was −5.5 ± 0.4 mV. This value, although slightly negative, can still be considered as characteristic of a neutral membrane[304]. All details of vesicle preparation and characterization are reported in Appendix B.

4.3.2 QCM-D and membrane leakage experiments

QCM-D: NP uptake in zwitterionic membranes. Within the experimental time scales considered in this study, extensive NP incorporation in PC-based zwitterionic membranes has already been reported for MUS:OT and TMA:OT AuNPs of similar core size and ligand molar ratio[130,132,140,141]. In this project, to quantify the uptake of NP– and NP+ in the POPC membrane, QCM-D investigations were performed using SiO_2-coated gold-quartz sensors. It is known that POPC vesicles rapidly tend to adsorb and fuse onto SiO_2 to form an essentially defect-free supported lipid bilayer (SLB) completely covering the sensor surface[305]. As shown in Figure 31a, NP– or NP+ were incubated with POPC vesicles in the experimental buffer before insertion into the QCM chamber and SLB deposition. All experimental details on QCM-D set-up, analysis methods, and sample preparation are described in Appendix C2. QCM-D traces for POPC vesicles alone and POPC vesicles incubated with either NP– (POPC/NP–) or NP+ (POPC/NP+) are reported in Figure 31b (frequency shift, Δf) and Figure 31c (dissipation change, ΔD). The frequency traces clearly indicated that the SLB generated via vesicle fusion (Figure 19c, Section 2.2) with different kinetics depending on the charge of the system, as often reported in the literature for anionic and cationic vesicles[233,306]. In particular, SLB formation took place within ~700 s in the case of POPC vesicles alone and POPC/NP–, whereas for POPC/NP+ a direct SLB formation occurred. After SLB deposition, the Δf plateau values were converted into mass values (Δm) using the Sauerbrey equation reported in Section 2.2; indeed, the rigid film approximation can be applied to a thin SLB (4÷5 nm thick) uniformly distributed onto the crystal sensor. The final masses adsorbed onto the sensor surface, Δm, amounted to 343 ± 35

ng/cm² for POPC vesicles alone and very similar values of 479 ± 34 ng/cm² and 445 ± 43 ng/cm² for POPC/NP– and POPC/NP+, respectively. The larger masses found in the experiments with NPs (~136 ng/cm² for NP– and 102 ng/cm² for NP+) clearly confirmed the uptake of NP– and NP+ in the zwitterionic bilayer during incubation. Furthermore, as shown in Figure 31b, Δf did not change after rinsing, indicating that all SLBs were stable and those with NPs stably retained their NP content.

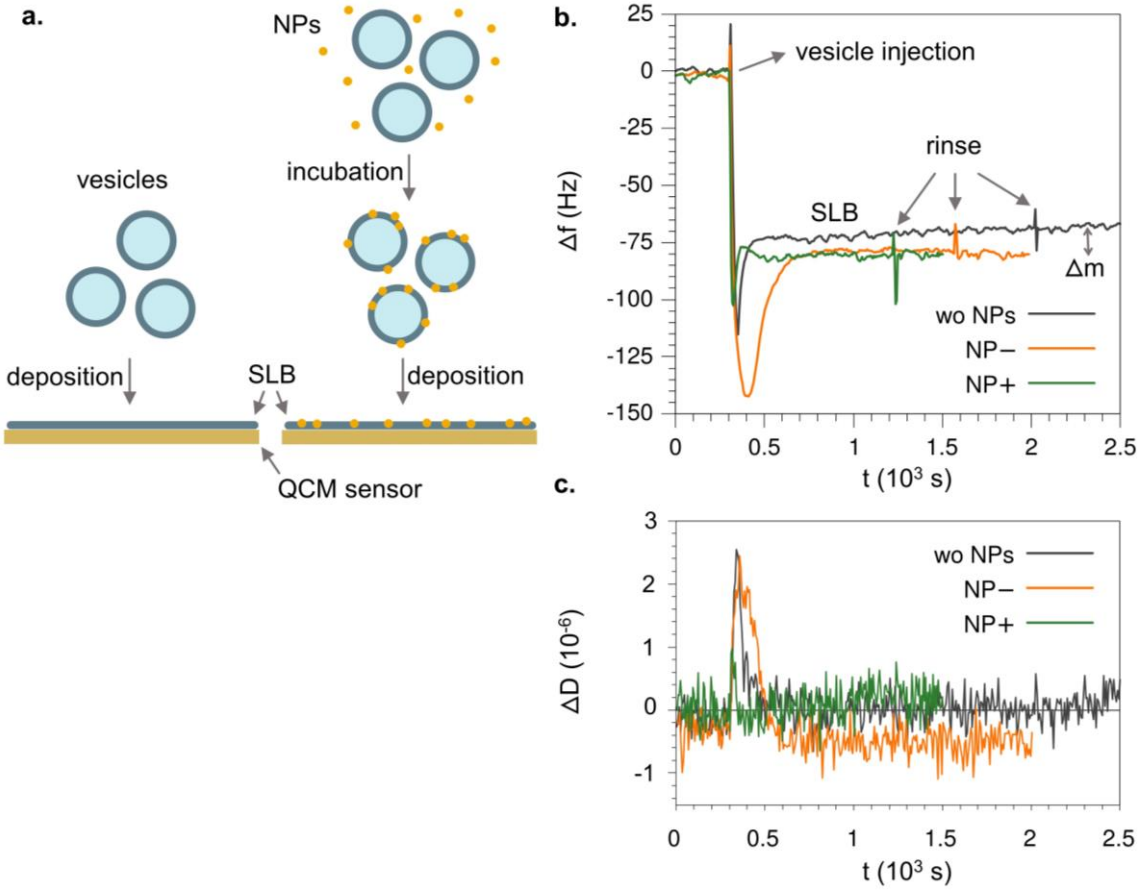

Figure 31. QCM-D quantification of NP uptake into the POPC bilayer. **a**) Schematic drawing of sample preparation: POPC vesicles and NPs (NP– or NP+) were incubated and allowed to interact before vesicle fusion onto the sensor. **b**) Frequency change, Δf, and **c**) dissipation change, ΔD, recorded in real time (3rd overtone) before and after injection in the QCM-D chamber (t=300 s) of POPC vesicles alone and POPC vesicles incubated with either NP– or NP+. Since the traces in (**c**) and (**d**) were recorded simultaneously, ΔD follows the same kinetics of SLB formation shown by Δf (i.e. its maximum corresponds to the Δf minimum). In the case of POPC vesicles alone and POPC/NP–, the dissipation variations are comparable. In the case of POPC/NP+, only a small increase right after NP injection was recorded, followed by the instantaneous formation of the SLB which is evidenced by the ΔD decrease to zero. Images by Canepa et al.[1] licensed under CC BY 4.0.

Membrane leakage: NP effect on zwitterionic membrane integrity. After confirming the uptake of NP– and NP+ in the POPC membrane, the NP ability to destabilize the zwitterionic bilayer was tested by dye-leakage assays on small, sonicated

vesicles (Section 4.3.1) loaded with a self-quenched calcein solution. Full details on the experimental set-up, analysis methods, and sample preparation are provided in Appendix D1. As introduced in Section 2.3.1, dye-leakage assays on lipid vesicles interacting with NPs can be divided into three steps: 1) vesicles before NP addition, 2) NP addition, and 3) vesicles after NP addition (the system is constantly stirred throughout the experiment). A schematic illustration of the assay timeline appears in Figure 32a. Typical membrane leakage curves recorded before and after the addition of NP– and NP+ (NP/lipid mass ratio, $R_m=\frac{m_{NP}}{m_{lip}}=0.03$) are reported in Figure 32b. Calcein fluorescence was monitored as a function of time and the fluorescence level did not change significantly after the injection of both NP– and NP+. The portion of the curve before and immediately after NP addition is enlarged in Figure 32c and compared with a control experiment in which a low amount (250 nM) of the pore-forming peptide gramicidin[307] was added to sonicated vesicles (for the sake of clarity, only the NP– case is reported). The membrane permeabilization induced by gramicidin corresponded to a fast, small but clearly detectable fluorescence increase indicating that POPC vesicles were sensitive to membrane permeability changes. As shown in Figure 32b, the calcein fluorescence intensity remained stable overtime after the injection of NP– and NP+, suggesting that no membrane permeabilization occurred. The addition of detergent (sodium cholate) at the end of the experiment caused a fast vesicle rupture with the complete release of the fluorescent dye. The instantaneous large fluorescence change recorded after the detergent-induced vesicle rupture confirmed that vesicles still retained their contents after NP addition. The final fluorescence level (F_{max}, Figure 32b) was used to normalize the leakage data, as described by Equation 3 of Section 2.3.1. Experiments were repeated increasing the NP concentration to $R_m=0.05$, but no changes were recorded in fluorescence intensity. All leakage results are summarized in Figure 32d, which reports the mean normalized fluorescence intensity of calcein (i.e. mean leakage %) recorded 1 h after the addition of NP– and NP+. Oscillation around zero of the values shown in Figure 32d was attributed to minor fluctuations in fluorescence intensity recorded after NP addition. To understand whether the origin of these fluctuations could be due to the membrane uptake of charged NPs, control experiments were performed adding similar volumes of water aliquots (without NPs). As shown by Figure 32e, the effect of water alone on vesicle suspensions was comparable to that of both NP– and NP+. This confirmed that no minor leakage effect could be attributed to the NP interaction with the zwitterionic bilayer. Further leakage assays were carried out on larger POPC vesicles obtained by extrusion (Section 4.3.1). Even in this case, no membrane leakage was induced by the addition of NP– and NP+ at both $R_m=0.03$ and 0.05 (Figure 32f).

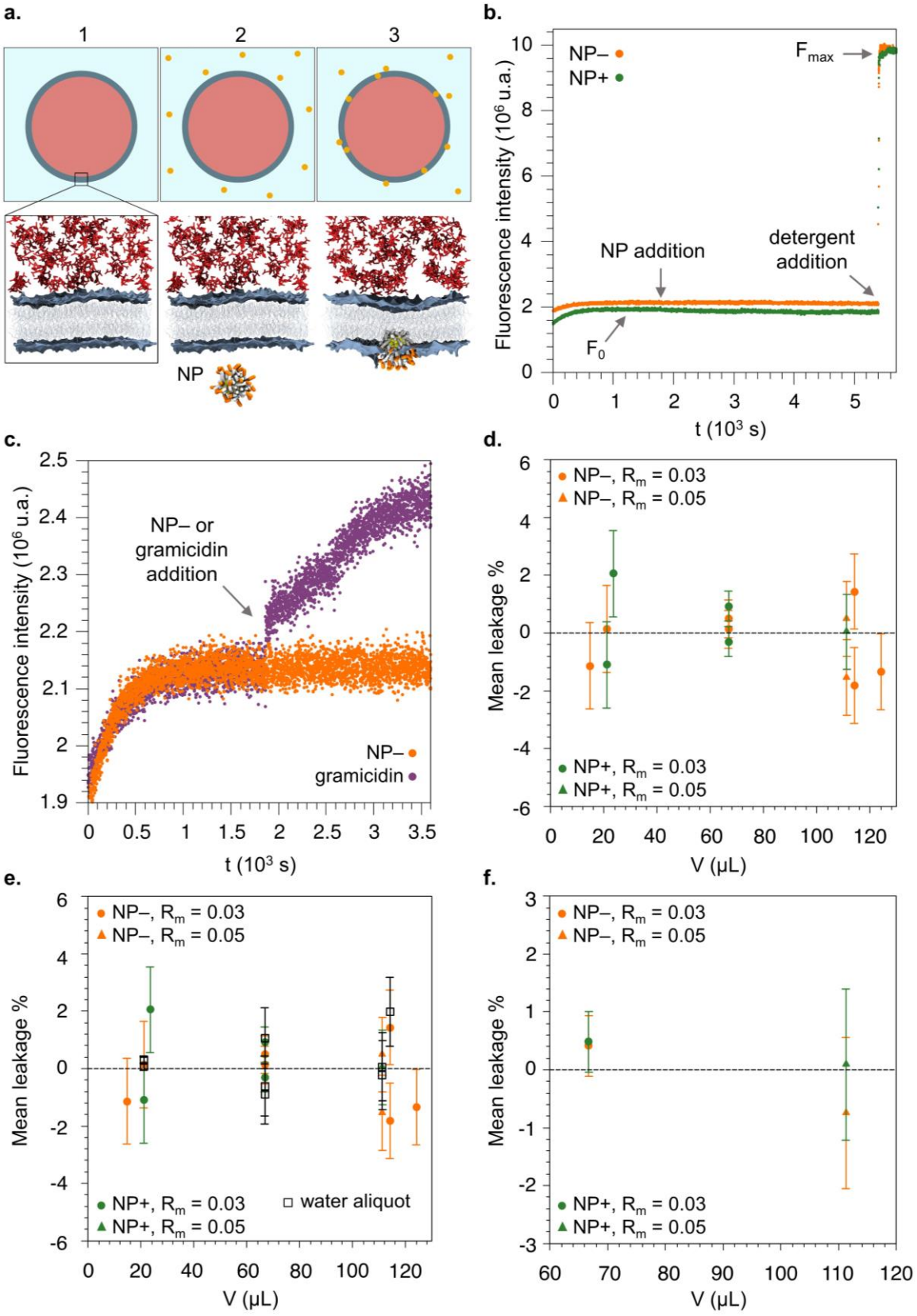

Figure 32. Dye-leakage assays on calcein-loaded POPC vesicles. **a**) Schematic drawing of the assay timeline: **1.** vesicles before NP addition, **2.** NP addition, and **3.** vesicles during the passive NP uptake within the lipid bilayer. Simulation snapshots of a membrane portion are reported in the second row:

lipid heads are shown in blue (surface representation), lipid tails in light-gray, calcein molecules in red, charged terminal groups of NP ligands in orange, hydrophobic moieties of NP ligands in white, and Au atoms in yellow. **b**) Typical leakage traces recorded before and after NP addition (t=1800 s) to sonicated vesicles at R_m=0.03 (V_{NP-}=14.6 μL, V_{NP+}=23.4 μL); F_0: fluorescence level just before NP addition; F_{max}: fluorescence level after the detergent-induced vesicle rupture. In general, for both NPs, no content release (i.e. fluorescence intensity increase) was recorded after NP addition. **c**) First 3600 s of the curve in (**b**) compared to the leakage-inducing effect by a low amount of gramicidin. **d**) Mean leakage % as a function of the added volume of NPs (sonicated vesicles). Comparison of the addition effects of NPs and water aliquots on **e**) sonicated and **f**) extruded vesicles. See Appendix D1 for all assay details. Images by Canepa et al.[1] licensed under CC BY 4.0 (minor changes were made).

Overall, the wide set of leakage results reported in Figure 32 indicates that the destabilization of the zwitterionic membrane following passive incorporation of amphiphilic AuNPs was negligible for both NP– and NP+. This experimental evidence shows that if defects were formed in the lipid bilayer during NP uptake, they were transient and did not allow a significant leakage of the encapsulated dye.

4.3.3 MD simulations

By means of unbiased coarse-grained MD[146,308,309] and biased metadynamics[310] calculations performed by collaborators, the NP-membrane interaction was simulated and the free energy surface of the NP-membrane complex was sampled. Simulation set-ups were prepared with and without the presence of calcein fluorophores used in leakage experiments (175 mM). MUS:OT NP– and TMA:OT NP+ were modeled with a core diameter of 2 nm, identical surface charge density, and a random surface arrangement of ω-charged and hydrophobic ligands.

Previous MD simulations by Simonelli et al.[129] showed that the interaction between charged amphiphilic AuNPs with random ligand distribution and the lipid bilayer is characterized by two metastable energy minima, corresponding to the surface-adsorbed configuration and the snorkeling configuration. The transition between these metastable states requires that part of the ω-charged ligands, initially bound to the polar region of the entrance leaflet, translocate across the apolar core of the membrane to anchor to the opposite leaflet (see Section 1.2.3). Within this study, the ligand anchoring transition, illustrated in Figure 33a, was compared for NP– and NP+. Since this process is associated with a free energy barrier, metadynamics was used to accelerate ligand translocation[310]. In particular, the dynamics of a single charged ligand terminal was biased along the reaction coordinate, i.e. the z component of the distance between the charged terminal and the center of mass (COM) of the membrane.

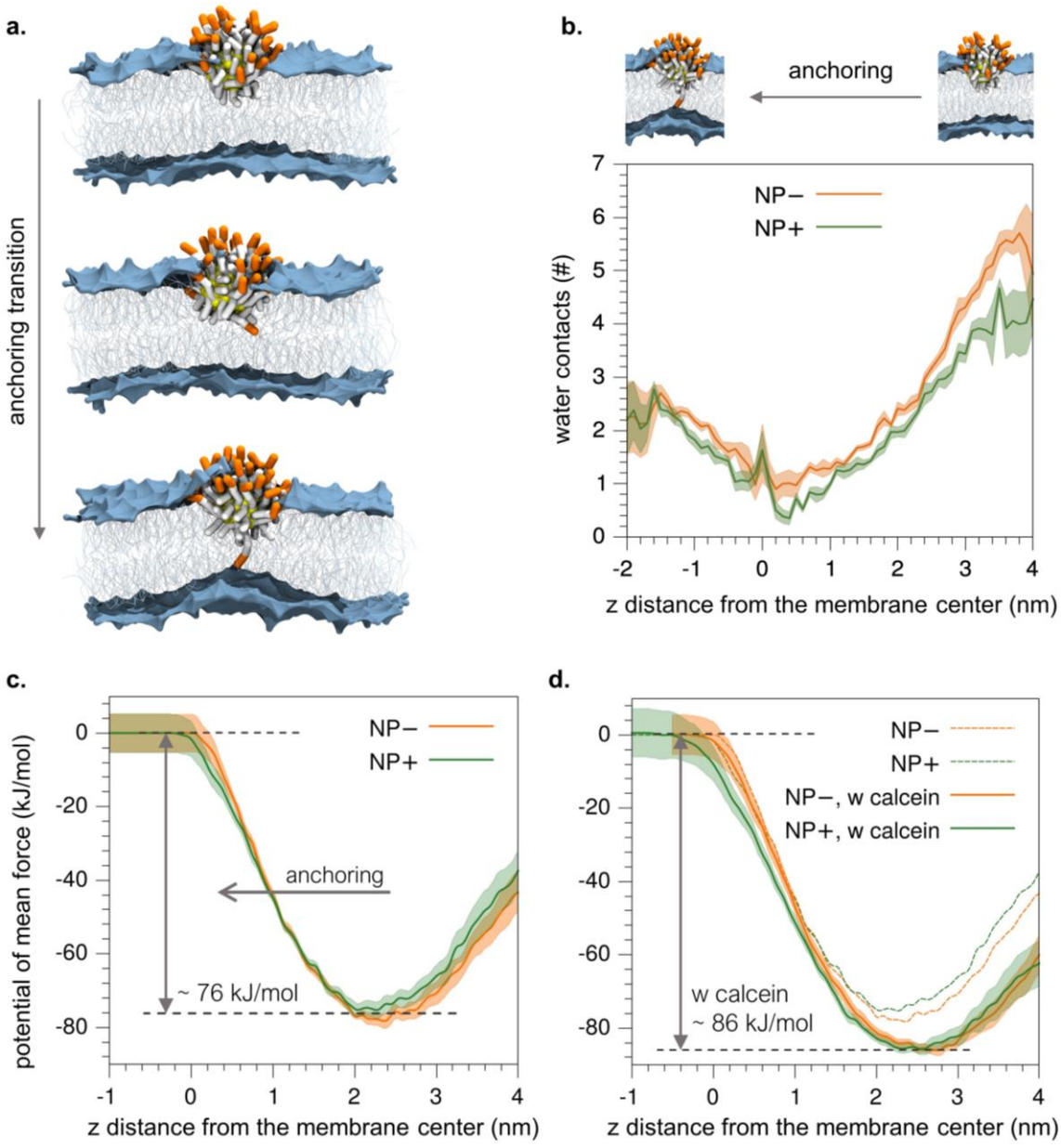

Figure 33. a) Simulation snapshots of the anchoring transition of a single anionic ligand from the entrance to the distal leaflet; color code as in Figure 32a (water beads not shown). The same mechanism of interaction was observed with the cationic ligand. The snapshot at the bottom discloses the bilayer deformation induced by such transition. **b**) Time-average number of contacts between the biased ligand terminal and coarse-grained water beads as a function of the reaction coordinate (shaded areas correspond to standard deviations associated with the time average). Potential of mean force as a function of the reaction coordinate for the anchoring transition of a single charged ligand: **c**) without calcein, and **d**) with and without calcein (shaded areas correspond to standard errors). For the sake of readability, in (**d**), errors are reported only with calcein. See Canepa et al.[1] for all calculation details. Images by Canepa et al.[1] licensed under CC BY 4.0 (minor changes were made).

The anchoring transition of both MUS and TMA ligands was found to induce significant – but transient – membrane deformation, with the translocation of a few water beads across the bilayer (Figure 33a, lower simulation snapshot). As reported

in Figure 33b, when the charged terminals of the ligands approach the COM of the membrane (i.e. z=0), they are hydrated equally in the anionic and cationic case. Despite the NP-induced membrane destabilization[146], no translocation of large calcein molecules was observed in any simulation. Moreover, biased metadynamics calculations[310] were used to quantify the free energy barriers for the anchoring transition of anionic and cationic ligands[146]. As shown in Figure 33c, no significant difference was observed for the anchoring barriers of oppositely charged ligands, which are 76 ± 6 kJ/mol for NP– and 77 ± 5 kJ/mol for NP+. Calcein was found to have a minor effect in slowing down the kinetics of the NP-membrane interaction by increasing the translocation barrier by approximately 10 kJ/mol regardless of the sign of the NP charge. Therefore, the inner dye was not found to induce any preferential interaction with NP– or NP+ (Figure 33d).

5. Effect of NPs on the membrane lipid phase separation

5.1 Lateral lipid heterogeneity: a less in-depth contribution of the NP-membrane interface

On the lipid side of the NP-lipid interface, lipid heterogeneity is a key ingredient of any model system aiming to approach the complexity of real plasma membranes. As described in Section 1.3.5, lipids can separate in the plane of the cell membrane to form highly dynamic, relatively ordered membrane domains, referred to as lipid rafts, which are enriched in cholesterol and sphingolipids[194]. The lateral phase separation originating the liquid-ordered phase of rafts is driven by selective lipid-lipid and lipid-protein interactions and provides different lipid and protein diffusion rates and the possibility of spatial compartmentalization and segregation[194]. Due to the small size and dynamic nature of lipid rafts, their direct microscopic detection is a challenging task which has been fulfilled in few selected cases[311,312], while systematic studies involving interaction of rafts with biological entities are primarily addressed by biomimetic approaches[211]. For instance, multicomponent lipid membranes exhibiting, on the micron scale, spontaneous phase separation into liquid-ordered (L_o) and liquid-disordered (L_d) lipid phases have long been used as synthetic models of raft-forming biological membranes.

Despite the important role played by rafts at the biological level, the study of the effects of ligand-protected metal NPs on the phase separation of model lipid membranes is still at an early stage. Both experimental and computational evidence suggest that the distinct lipid composition and liquid ordering of ordered and disordered regions in the lipid bilayer can influence membrane interactions with NPs. For the smallest NPs (< 4 nm in diameter), the higher fluidity of the liquid-disordered phase has been found to favor stronger, spontaneous NP-membrane interactions[156] and passive NP embedding[137]. Using phase segregated vesicles, Atukorale et al.[142] showed that small amphiphilic MUS:OT AuNPs only bind to fluid phase lipid vesicles and, by contrast, they are excluded from highly ordered gel-phase membranes. Another driving force for the localization of small NPs in the L_o – L_d bilayer is the minimization of the hydrophobic mismatch between the NP size and the hydrophobic thickness of the lipid phase; this behavior may be modulated by tuning the NP size and surface physicochemical properties, such as ligand hydrophobicity,

length, and density[313,314]. Larger metal NPs (up to ~30 nm in diameter), which are expected to adsorb at the surface of model bilayers without being embedded, have also been reported to affect lipid packing and membrane rigidity[315,316]. On the membrane surface, bilayer curvature at the boundary between L_o and L_d domains has been shown to favor the adsorption of small, positively charged amphiphilic AuNPs to phase-segregated bilayers[156,317]. Overall, the picture emerging from these studies shows a subtle dependence of the interaction between NPs and phase-separated bilayers on specific NP features (e.g. size and surface chemistry) and on the lipid bilayer composition, structure, and mechanical properties. Yet, a comprehensive view is still lacking, and – most important – with the available knowledge no prediction on the effect that a specific NP may have on the stability of phase separation can be attempted. Such results point to the need for further investigation on the role of NP on the lipid phase separation of multicomponent lipid membranes.

5.2 Project: objective and methods

This project aimed at investigating the effect of small amphiphilic AuNPs on the stability of the coexistence of ordered and disordered liquid domains in multicomponent lipid membranes. The same negatively charged amphiphilic AuNPs used in Chapter 4 (referred to as NP–) were tested. Model multidomain lipid bilayers were prepared using a lipid mixture of biological relevance composed of the low-melting di-unsaturated DOPC (a naturally abundant phosphocholine in the outer leaflet of animal cell membranes), the high-melting relatively saturated sphingomyelin (SM), cholesterol (chol), and the ganglioside GM1. The chemical structures of these lipids are reported in Figure 54 (Appendix B1). This lipid mixture was selected to model the neuronal plasma membrane, where rafts enriched in SM, cholesterol, and GM1 have been shown to regulate fundamental membrane functions (e.g. signal transduction and membrane elasticity), thus impacting the exocytosis of synaptic vesicles and the release of neurotransmitters[196,318,319]. The NP-membrane interaction was investigated using AFM imaging and QCM-D measurements in aqueous solution (Sections 2.1 and 2.2, respectively). QCM-D investigation was performed thanks to the precious contribution of Dr. Silvia Dante (IIT, Genoa); as in the previous project, this technique allowed quantifying the extent of the passive NP– uptake by the multidomain membrane. AFM images were collected to study the effect of nonspecific NP-bilayer interactions on the morphology of the lipid phase separation.

Even in this case, computational simulations by the group of Prof. Giulia Rossi (DIFI, University of Genoa) allowed interpreting the experimental results at a

molecular level. Interestingly, this multidisciplinary study provided a close match between the experimental investigation and the models *in silico*. Moreover, a general, yet simple thermodynamic model based on simulations was developed to explain the effect of NP– on lipid phase separation. The findings of this project will be addressed as in Chapter 4: the thorough discussion of the experiments will be followed by a more concise description of the main *in silico* results elaborated by collaborators (Section 5.3.3). More information on simulations can be found in Canepa et al.[2]

5.3 Results and discussion

5.3.1 NPs and lipid membranes

As described in Chapter 4, NP– were functionalized by a thiol mixture of the hydrophobic OT and the negatively charged MUS. The NP core and hydrodynamic diameters were 2.7 ± 0.8 nm and 6.5 ± 0.2 nm, respectively (Figure 23a,b and Table 3, Section 3.1.1). The MUS:OT molar ratio in the ligand shell was 4:1 and the NP ζ-potential in water was −48 ± 4 mV, corresponding to high, long-term colloidal stability (Table 4, Section 3.1.1). Details on NP characterization are provided in Appendix A2. Before experiments, NP aqueous dispersions were filtered as shown in Appendix A1.

Multidomain lipid vesicles with three different compositions – referred to as M1, M2, and M3 – were used. The vesicles representative of the neuronal plasma membrane (M1) were composed by DOPC:SM:chol:GM1 63:31:1:5 (molar ratio)[161,320]. M1 vesicles showed a ζ-potential of −64 ± 3 mV, due to the negatively charged GM1. M1 composition spontaneously leads to ordered – disordered lateral phase separation in the bilayer, with ordered domains enriched in SM, cholesterol, and GM1[194,317,321]. Control experiments were performed on other two membrane compositions showing ordered – disordered phase immiscibility: M2 vesicles composed of DOPC:SM:chol 66:33:1 (molar ratio)[320] and M3 vesicles composed of DOPC:DPPC:chol 40:40:20 (molar ratio)[322], where DPPC is the saturated phospholipid 1,2-dipalmitoyl-*sn*-glycero-3-phosphocholine (Figure 54, Appendix B1). All details of vesicle preparation and characterization are reported in Appendix B.

5.3.2 AFM and QCM-D experiments

Membrane phase separation without amphiphilic NPs. After preparation, multidomain vesicles were deposited on mica to form multidomain SLBs for AFM imaging. Figure 34 shows the typical morphology of M1, M2, and M3 SLBs.

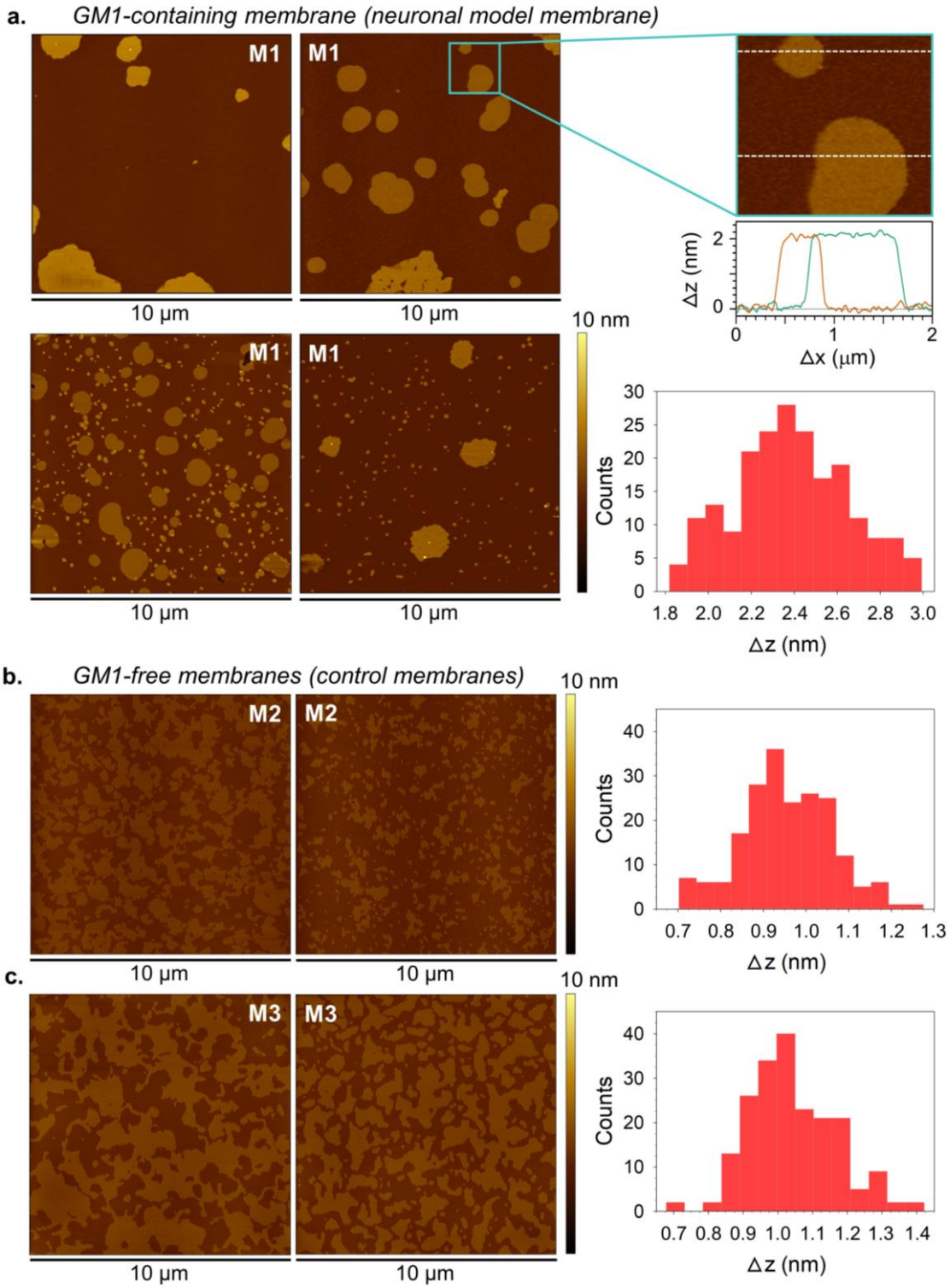

Figure 34. AFM images showing the typical morphology of membrane phase separation in **a**) M1 SLBs mimicking the neuronal membrane composition; **b**) M2 and **c**) M3 SLBs both used in control experiments. Ordered domains of different size and shape are surrounded by the continuous disordered phase; since ordered regions are thicker than disordered ones, they are lighter in color. In (**a**), the height profiles of two ordered domains taken along the lines in the zoomed AFM scan are reported on the right. The distribution of the height difference (Δz) between ordered and disordered domains is shown for each bilayer composition (see Appendix C1 for calculation details). In some

cases, M1 ordered domains exhibited protruding subdomains which can be assigned to regions with higher GM1 concentration. This behavior has already been observed in SLBs formed by mixtures DOPC:SM:chol:GM1[323]. AFM images and height profiles by Canepa et al.[2] (published by The Royal Society of Chemistry) licensed under CC BY-NC 3.0 (minor changes were made).

As typical of the morphology of synthetic phase-separated membranes, the shape and lateral size of ordered domains exhibited an intrinsic degree of variability within M1, M2, and M3 samples (Figure 34). In the case of the M1 bilayer, where ordered domains appear more roundish, the height difference between the two phases (Δz) is 2.4 ± 0.3 nm, whereas for the control M2 and M3 membranes, lower Δz were obtained (Table 6). These values are in good agreement with previous AFM measurements on GM1-containing and GM1-free ordered domains of similar composition[320,324,325]. The phase boundary involves an energy penalty per unit length, which is referred to as *line tension* (γ) [208,326]. To minimize the latter, the domain contour tends to shrink, and a bilayer deformation arises to compensate for the height mismatch between different phases. The line tension has a strong effect on phase separation, including the regulation of the ordered domain morphology[327]: the higher the γ, the greater is the tendency of ordered domains to assume more circular (i.e. less fractal) shape. Based on a theoretical model, Kuzmin et al.[209] have shown that γ depends quadratically on the phase height mismatch. In the present project, a simple geometric evaluation of the shape of M1, M2, and M3 ordered domains was performed by calculating the domain circularity from AFM images; results are reported in Table 6. As expected from AFM images of Figure 34 and other AFM studies[328], the higher Δz of M1 membranes is related to the formation of more circular domains to minimize the higher energetic cost associated with the domain interface length. This behavior may be due to the presence of GM1 ganglioside, which has been previously shown to increase γ at ordered – disordered phase boundary in model membranes[329]. A more in-depth study of the effect of lipid composition on γ, in the context of the membranes used in this project, is under development.

Table 6. Average height difference (Δz) between the ordered and disordered phase and average circularity of ordered domains in the multidomain bilayers used in this study. Data were obtained from the analysis of AFM images acquired at room temperature.

Multidomain bilayer	*Lipid composition*	*Molar ratio*	*Phase height difference or Δz (nm)* [a]	*Ordered domain circularity* [b]
M1	DOPC:SM:chol:GM1	63:31:1:5	2.4 ± 0.3	0.85 ± 0.01
M2	DOPC:SM:chol	66:33:1	1.0 ± 0.1	0.55 ± 0.01
M3	DOPC:DPPC:chol	40:40:20	1.1 ± 0.1	0.60 ± 0.01

[a] average ± one standard deviation.

[b] average ± standard error; domain circularity calculated as $4\pi \cdot \frac{area}{perimeter^2}$ (see Appendix C1). NOTE: for perfectly circular domains, circularity is equal to 1.

All experimental details on the AFM set-up, analysis methods, and sample preparation used in this project are described in Appendix C1.

Amphiphilic NPs weakly adsorb on the SLB disordered phase. To verify whether NP– interact with the model neuronal membrane, different amounts of NP– were deposited on preformed multidomain M1 SLBs and let to interact for different incubation times before AFM imaging. This sample preparation method, based on direct NP-SLB interaction, was the most intuitive at the beginning of this study (see Figure 58a, Appendix C1). The kinetics of NP– interaction with the M1 SLB resulted remarkably slow, without giving any experimental evidence over several minutes (Figure 35a). Only after several hours, regardless of NP– concentration, it was possible to detect large NP– clusters adsorbed on the surface of the disordered phase, often residing at the phase boundary (Figure 35b-f). Presumably, such NP– aggregates slowly formed as a consequence of NP– diffusion on top of the SLB. In general, NP– clusters were often dragged by the AFM tip and most of them could be easily removed from the bilayer upon rinsing, thus suggesting a weak interaction between NP– and preformed M1 SLBs.

The slow kinetics of NP-membrane interaction observed by AFM was confirmed by QCM-D investigation. Even in this case, NP– were injected in the QCM chamber after the formation of the M1 SLB onto the sensor surface. The frequency signal reported in Figure 35g clearly indicates that NP– interacted with the preformed SLB on a time scale of hours. Furthermore, Δf acquisition denoted that the interaction between NP– clusters and the SLB was weak, leading to a slow, transient adsorption of NP– that began to desorb spontaneously from the SLB after a few hours of incubation; finally, the adsorbed mass was completely removed from the sample after a gentle rinse (t=17 h, Figure 35g). After complete NP– removal, the preformed SLB was intact, as indicated by the recovery of the starting frequency (i.e. $\Delta f=0$). The maximum adsorbed mass after NP– injection, calculated from the normalized frequency decrease in the first two hours, corresponded to $\Delta m_{NP}=54$ ng/cm^2. Regarding dissipation monitoring, Figure 35g shows that ΔD acquisition was almost unaffected by NP– addition and subsequent aggregation on the SLB surface. Moreover, after rinsing, the recovery of the initial dissipation value (i.e. $\Delta D=0$) showed that the SLB was as rigid as before the interaction with NP–. This result confirmed that NP– were not incorporated within the bilayer but were only weakly adsorbed on its surface. All experimental details on the QCM-D set-up, analysis methods, and sample preparation used in this project are provided in Appendix C2.

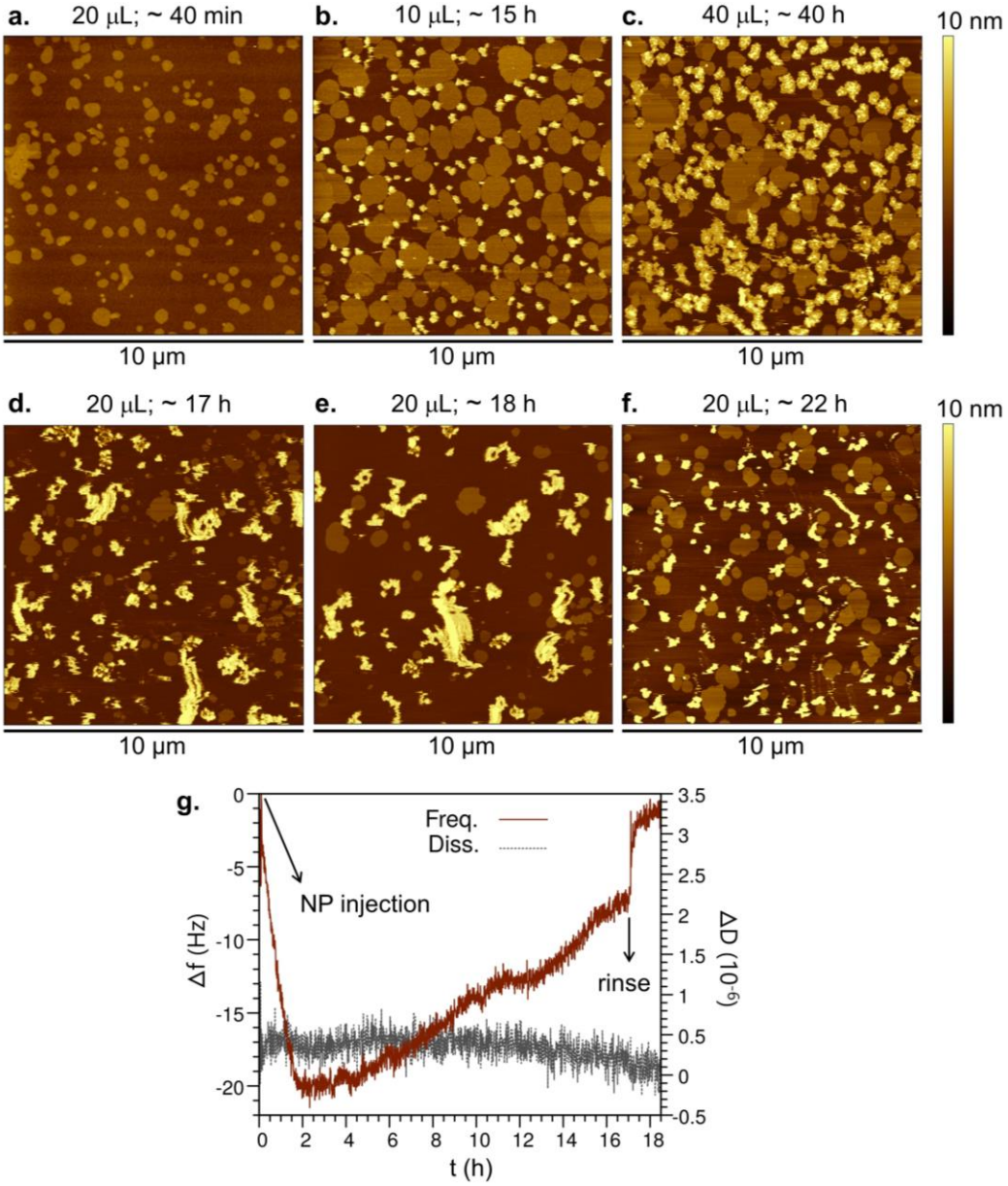

Figure 35. Incubation of NP– on preformed model neuronal SLBs with M1 composition: NP– slowly and weakly adsorb on the disordered phase. **a**-**f**) AFM images acquired after adding different NP– amounts (µL) from the same stock solution and waiting for different NP/SLB incubation times. NP– clusters are higher (i.e. lighter in color) than the ordered domains. **g**) QCM-D curves showing the frequency change (Δf) and dissipation change (ΔD) recorded after NP– injection onto a preformed M1 SLB (7th overtone). All details are reported in Appendix C1 (AFM investigation) and C2 (QCM-D investigation). Images by Canepa et al.[2] (published by The Royal Society of Chemistry) licensed under CC BY-NC 3.0 (minor changes were made).

This weak adsorption of NP– on the surface of the supported lipid bilayer is coherent with the state-of-the-art knowledge about the mechanism of interaction between MUS:OT AuNPs and neutral phosphatidylcholine bilayers. The partial or total embedding of small amphiphilic NPs within the bilayer is characterized by large free energy barriers[146,147], which can be lowered by the presence of membrane

defects[127]. The molecular mechanism allowing for the stabilization of the NP-membrane interaction requires the transient exposure of one or more hydrophobic lipid tails to the NP interface[330,331]. Such lipid tail protrusions are more likely to occur at bilayer edges, such as those forming at the perimeter of hole defects in SLBs[127]. The M1 SLBs prepared in this project, though, are defect-free on a scale of tens of μm (Figure 34 and Figure 35a-f). Furthermore, the physical constraints imposed by the solid support on the planar SLB is likely to suppress lipid dynamics in both in-plane[230] and out-of-plane directions, slowing down the kinetics of NP-bilayer interactions. In particular, the lipid diffusion coefficient in supported bilayers is about two-fold less than that observed in lipid vesicles[332,333].

Membrane fluctuations affect the NP uptake. The slow and relatively loose adsorption of NP– onto the preformed M1 bilayer is consistent with previous experimental observation of little to no adsorption of negatively charged AuNPs (with similar size) injected on GM1-containing multidomain SLBs of slightly different composition[317]. On the other hand, small MUS:OT AuNPs are known to stably interact with the fluid bilayer of DOPC-based vesicles[141,142] and with multicomponent vesicles containing significant percentages of DOPC and SM[137]. Even in the project described in Chapter 4, NP– were shown to stably penetrate within the zwitterionic membrane of POPC vesicles. Moreover, previous computational results published by Rossi and co-authors[64,129,146] also indicated that the spontaneous incorporation of MUS:OT AuNPs in free-standing, liquid-disordered phosphatidylcholine bilayers is possible, though characterized by a slow kinetics. Membrane fluctuations and unrestrained lipid diffusion in the vesicle bilayer allow for the transient defects that stabilize the contact with the amphiphilic NP and, if the NP size permits it, also allow for the incorporation of the NP into the membrane core.

To overcome the motional constraints imposed on the membrane by the solid support, and yet exploit AFM imaging and QCM-D investigation for the characterization of a stable NP-bilayer complex, a second experimental set-up was devised for the preparation of NP-containing samples. NP– were first pre-incubated with the free-standing bilayer of lipid vesicles for a variable lag of time; only then vesicles were let to merge onto the solid substrate to form an SLB with embedded NP– (see Figure 58b, Appendix C1). The NP– uptake by M1 vesicles was checked by QCM-D after 4 h of pre-incubation. The traces reported in Figure 36a clearly indicate the adhesion of a larger mass, during the entire process of SLB formation, in the case of pre-incubated vesicles than without NP–. After rinsing, the difference in frequency shift between pre-incubated vesicles and vesicles without NP– corresponded to a

mass difference of 267 ± 18 ng/cm^2, which was interpreted as the mass of embedded NP– (Δm_{NP}). Such value is considerably higher than that recorded after NP– incubation onto preformed M1 SLBs (Figure 35g); besides, no additional frequency shift was recorded upon rinsing, indicating a stable, strong NP-bilayer association. This result demonstrated that the reduced lipid mobility in the preformed SLB could indeed interfere with the NP-membrane interaction, thus pointing out the effectiveness of the pre-incubation method in obtaining stable NP-lipid complexes.

To further confirm the role of membrane fluctuations in favoring the NP– embedding into the M1 bilayer, the NP– uptake was monitored using a control membrane with a larger mechanical rigidity. M2 bilayers, which differ from M1 membranes only in the removal of the GM1 component (Table 6), have been reported to have a stiffer disordered phase than M1 bilayers[325,334]. After the same pre-incubation time waited for M1 vesicles (i.e. 4 h), QCM-D confirmed that the NP– uptake by M2 vesicles is severely reduced in comparison to the GM1-containing bilayer (Figure 36b). At variance with the M1 case, the frequency shifts were similar both when M2 vesicles attached to the sensors (i.e. in correspondence to the continuous line minima) and when the formation of M2 SLBs was completed (i.e. after reaching the final plateau). In particular, the normalized frequency shifts at the plateau were ~25 Hz; these values are consistent with the formation of an SLB and comparable to the value obtained with GM1-containing vesicles alone (Figure 36a). Since almost no difference in frequency shift was detected before and after vesicle pre-incubation, little or no NP– insertion into the M2 bilayer was expected. However, in contrast to the M1 case, Figure 36b reports a slower kinetics of M2 vesicle adsorption and rupture after pre-incubation with NP–. This phenomenon is consistent with a weak interaction between NPs and the hydrophilic headgroups of the vesicle bilayer. NP– reversibly adsorbed at the surface of the more rigid M2 vesicles, but not fully incorporated into the membrane core, may indeed have affected the vesicle interaction with the sensor. In addition to QCM-D, AFM imaging was performed to characterize the M2 bilayer deposited after 4 h of NP–/vesicle pre-incubation. As expected from QCM-D, NP– did interact with the M2 bilayer but only sparse, relatively little NP– aggregates were observed (Figure 36c); notably, NP– clustered in the stiffer disordered phase or at the edges of ordered domains. The formation of small, rare holes revealed by AFM imaging after deposition of M2 vesicles pre-incubated with NP– (Figure 36d) – if it also occurred on the quartz sensor surface – may have contributed to an underestimation of the frequency shift, and thus the adsorbed mass, during the QCM-D analysis of NP-containing samples (Figure 36b).

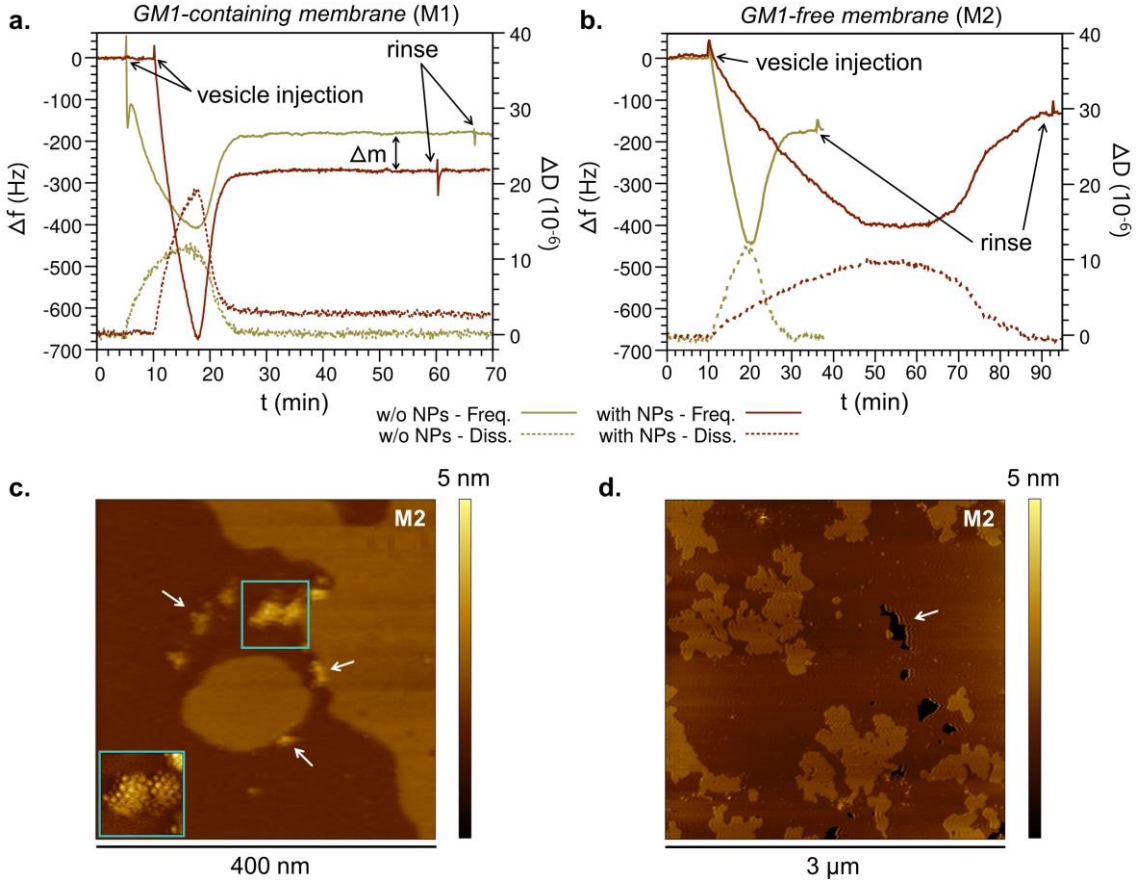

Figure 36. Membrane fluidity favors NP– embedding into the M1 bilayer. Frequency (Δf) and dissipation (ΔD) changes (7th overtone) during the QCM-D deposition of **a**) M1 and **b**) M2 lipid vesicles alone or pre-incubated with NP– for 4 h (see Appendix C2). The traces are typical of SLB formation via vesicle fusion; in both cases, the SLBs were stable after rinsing. **c**,**d**) AFM images of the M2 bilayer after 4h of pre-incubation with NP– (see Appendix C1). In (**c**), the inset shows a zoomed scan of the NP– cluster framed above in the image (other NP– clusters are indicated by arrows). **d**) During AFM imaging of pre-incubated M2 bilayers, small holes (appearing as deeper and thus darker regions, as shown by the arrow) were observed in final SLBs. Images (**a**-**c**) by Canepa et al.[2] (published by The Royal Society of Chemistry) licensed under CC BY-NC 3.0 (minor changes were made).

Effect of amphiphilic NPs on the stability of membrane phase separation. The large NP– uptake within the M1 bilayer recorded by QCM-D and reported in Figure 36a was further confirmed by AFM imaging. This technique proved fundamental in investigating the effects of NP– adsorption on the properties of the multidomain bilayer. Figure 37b,c shows the AFM images of M1 SLBs formed after vesicle pre-incubation with NP– for 10 min and 4 h, respectively. Contrary to what happened when NP– were incubated with preformed M1 SLBs (Figure 35a-f), only 10 min of NP–/vesicle pre-incubation were sufficient to alter the morphology and compactness of ordered domains, which in Figure 37b appear with irregular shapes and ragged boundaries. Such domain morphology is dramatically different

from that observed in the absence of NP– (Figure 37a and Figure 34a). After a few minutes of pre-incubation, the Δz distribution between ordered and disordered domains was way broader than without NP–, shifting from 2.4 ± 0.3 nm (Figure 34a and Table 6) to 1.5 ± 0.5 nm, as shown in Figure 37d. When NP– and M1 vesicles were pre-incubated for longer times (i.e. 4 h), the membrane phase separation was suppressed (Figure 37c). In this case, it was possible by AFM to identify sparse, restricted membrane patches of disordered phase and few NP– clusters, but most of the sample was characterized by a new rough phase containing both lipids and NP–.

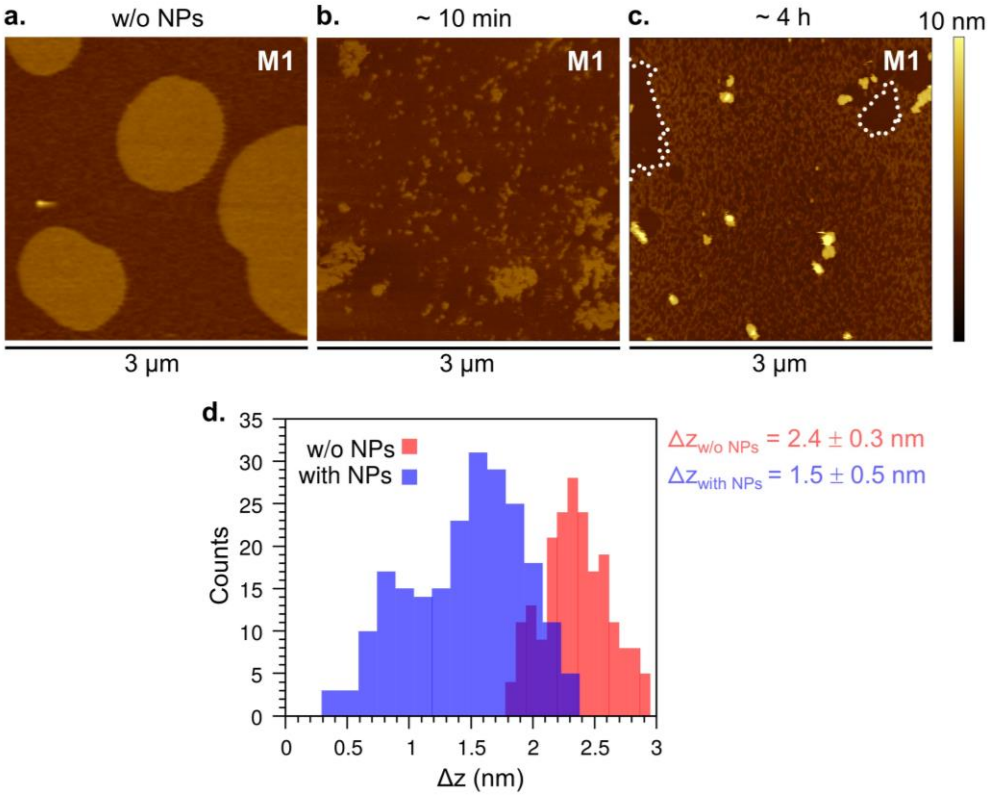

Figure 37. NP-induced perturbation of membrane phase separation in model neuronal bilayers. M1 SLBs imaged by AFM **a**) before and **b**,**c**) after interaction with NP–. Image (**b**) shows the ordered domain fragmentation induced by NP– after only 10 min of pre-incubation, while image (**c**) discloses the suppression of ordered – disordered phase separation induced by the same amount of NP– after 4 h of pre-incubation (see Appendix C1). In (**c**), a new rough phase was homogeneously distributed over almost the entire bilayer surface (the dashed white contours point out some of the sparse disordered patches remained within such phase). In general, when depositing pre-incubated M1 vesicles, no holes were observed in final SLBs. **d**) Comparison of Δz distributions between ordered/disordered domains in M1 SLBs deposited before or after 10 min of pre-incubation with NP– (mean ± one standard deviation). Images (**b**-**d**) by Canepa et al.[2] (published by The Royal Society of Chemistry) licensed under CC BY-NC 3.0 (minor changes were made).

Interestingly, the NP-induced perturbation of phase separation reported above for the model neuronal bilayer was not observed in control membranes with composition M2 (as anticipated in Figure 36c,d) and M3. In these cases, after 4 h of

NP–/vesicle pre-incubation the ordered domains were still clearly distinguishable and only a low NP– uptake was detected by AFM imaging and QCM (Figure 38a-g and Figure 36b, respectively). Moreover, for control M2 and M3 bilayers the average Δz between ordered/disordered domains did not change significantly following vesicle pre-incubation with NP–: as shown in Figure 38h, this behavior is clearly different from that observed for the GM1-containing M1 composition.

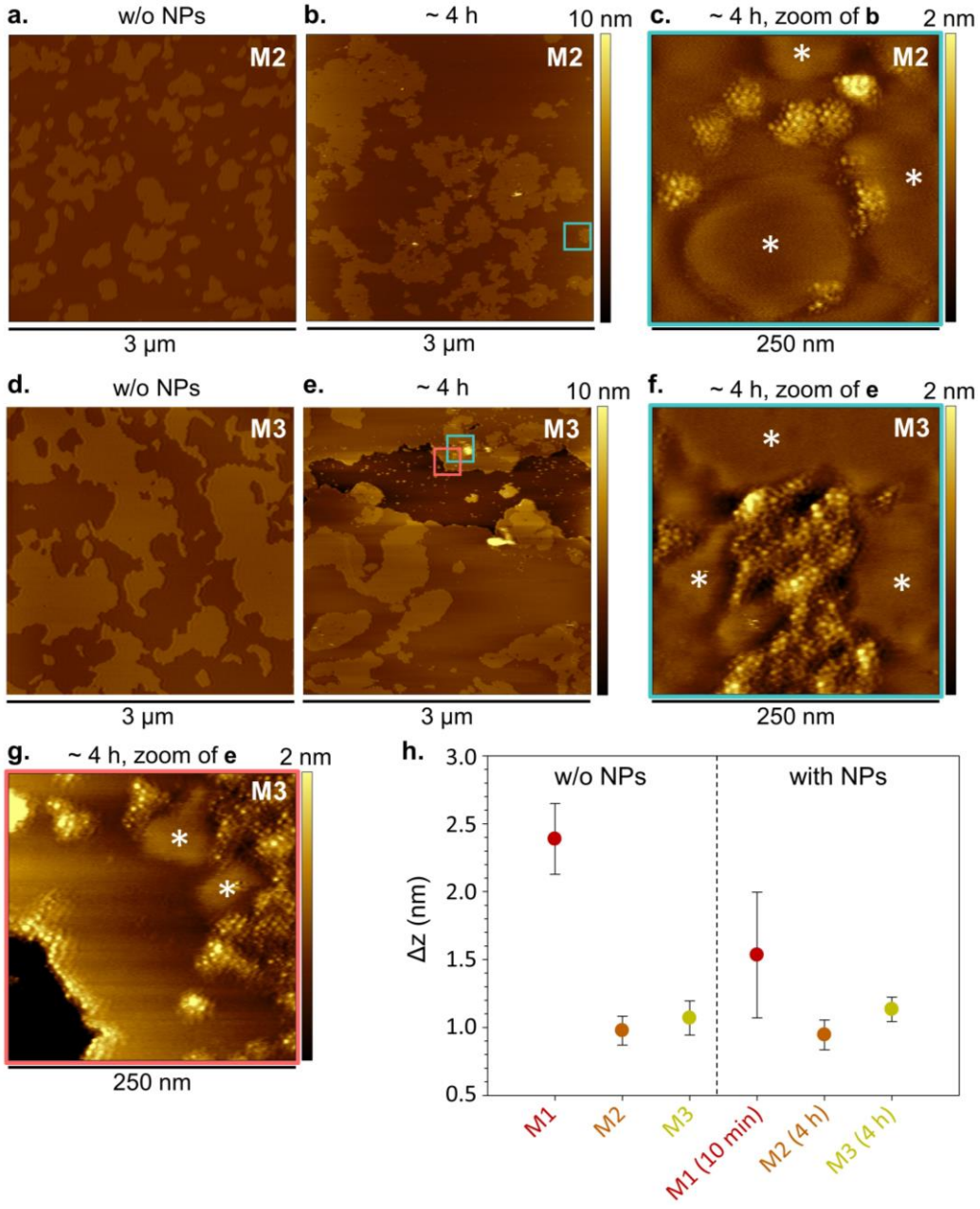

Figure 38. AFM images showing M2 and M3 SLBs deposited before – (**a**) and (**d**), respectively – and after – (**b**,**c**) and (**e**-**g**), respectively – 4 h of NP–/vesicle pre-incubation. NP– were added in the same amount as for the M1 bilayer in Figure 37c (see Appendix C1 for details). White asterisks in the zoomed AFM scans indicate ordered domains. For both control membranes, sparse and relatively little NP– clusters – distributed in the disordered phase, at the phase border, or at hole edges – were

observed. **h**) Comparison of the height difference Δz between the ordered and disordered phase, without and with pre-incubation of M1, M2, and M3 vesicles with NP–; error bars refer to standard deviation. In the case of M1 SLBs, Δz could only be measured after 10 min of pre-incubation, since after 4 h the phase separation was no longer present. Images (**c**,**g**) by Canepa et al.[2] (published by The Royal Society of Chemistry) licensed under CC BY-NC 3.0 (minor changes were made).

Amphiphilic NPs form ordered supramolecular aggregates within the membrane. A more in-depth AFM investigation of the new rough phase observed after pre-incubation of M1 bilayers with NP– for 4 h (Figure 37c) revealed membrane patches containing ordered NP– aggregates. Such aggregates were completely absent after NP– incubation on preformed M1 SLBs on a time scale of hours (Figure 35a-f). Figure 39a shows a representative image of these peculiar patches already after pre-incubation of 10 min. However, after such a limited pre-incubation time, NP– aggregates were scarce, isolated, and with limited size. When NP– were let to interact with M1 vesicles for a few hours before SLB deposition, the NP– lattice became much more evident and uniformly distributed throughout the bilayer. The zoomed AFM scan of Figure 39b discloses the widespread ordered NP– aggregate formed during pre-incubation of 4 h. As shown by the digital zoom of the inset, the NP– aggregate is quite regular, and a periodic lattice is recognizable. The periodicity of the ordered NP– aggregate is also evidenced by the height profile of a NP– row and the Fourier transform reported in Figure 39e,f, respectively. Within the ordered aggregate, the average NP–NP horizontal distance was equal to 7.5 ± 0.1 (standard error) nm (Figure 39c); the corresponding standard deviation, 1.6 nm, is consistent with the core size distribution of one-phase NP– (see Section 5.3.1). In addition, the height difference Δz between the NP– aggregates and the disordered phase was measured by sampling the height step along the contour of disordered patches located within the widespread NP– lattice (e.g., those outlined by dashed white contours in Figure 37c). The Δz distribution reported in Figure 39d reveals that NP– were at least partially embedded within the bilayer, since the average $\Delta z_{\text{NP lattice}}$ was 1.2 ± 0.3 nm (standard deviation), way below the mean NP– diameter. As shown by Figure 36c and Figure 38c for M2 bilayers and Figure 38f,g for M3 bilayers, in the case of control membranes deposited after 4 h of vesicle pre-incubation, NP– exhibited the tendency to form sparse and relatively small aggregates, but never uniformly distributed assemblies over large – i.e. micron-sized – portions of the bilayer.

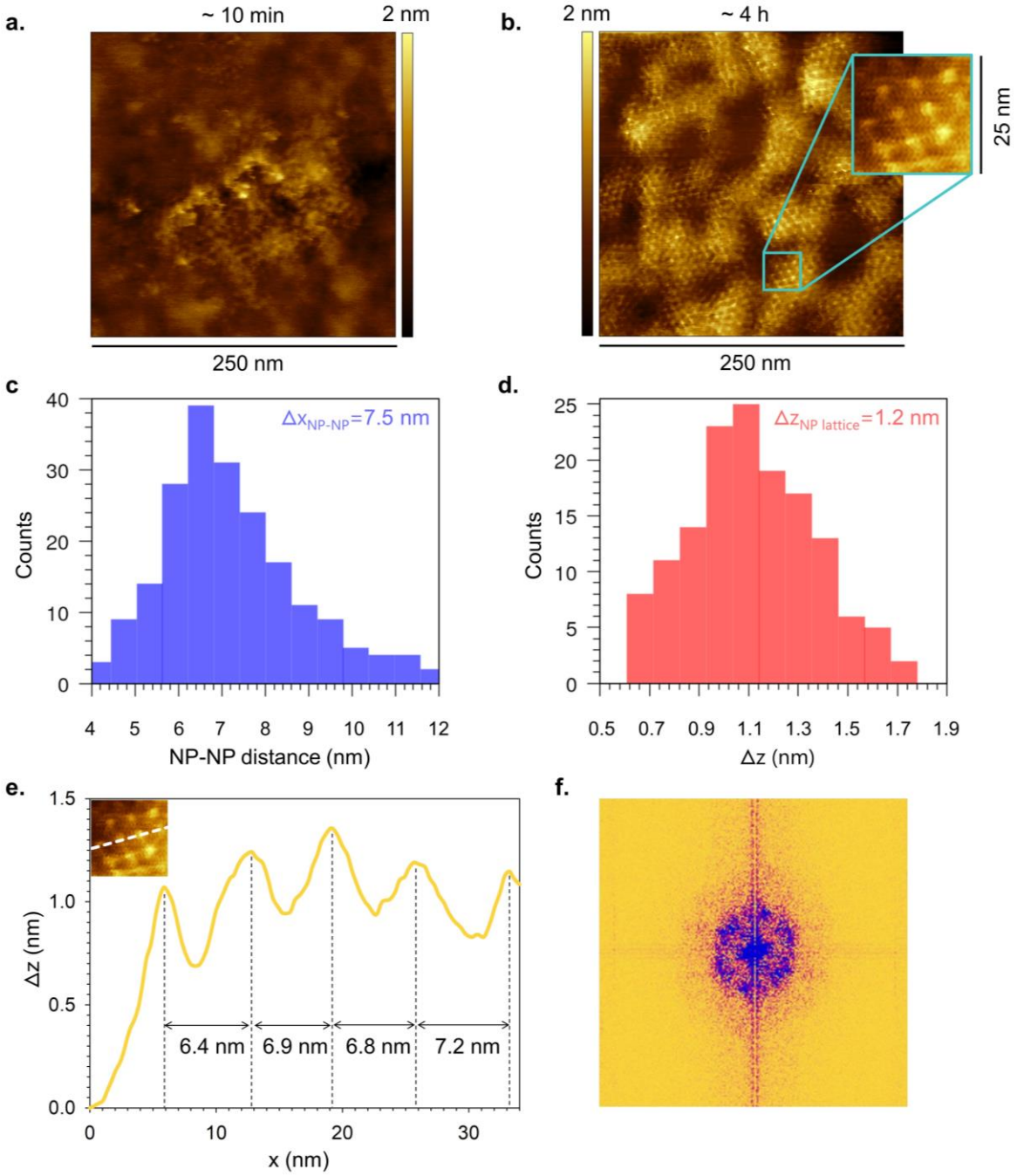

Figure 39. Ordered aggregates formed by NP– after embedding within the M1 bilayer during **a**) 10 min and **b**) 4 h of vesicle pre-incubation. On the right of image (**b**), a digital zoom highlighting the order of the NP– aggregate is shown. The AFM scan region reported in (**b**) is representative of the entire rough phase shown in Figure 37c: the ordered NP lattice spreads over micron-sized portions of the bilayer and the lipid phase separation is no more appreciable. **c**) Distribution of the NP–NP horizontal distance within the ordered NP– aggregate and **d**) distribution of the height of the ordered NP– aggregate (Δz) measured with respect to patches of the disordered phase. **e**) Height profile of a representative NP– row traced along the white dashed line in the inset and showing the regular interparticle distance. **f**) 2D Fourier transform of the image in (**b**) highlighting the periodicity of the bilayer-embedded NP– aggregate. See Appendix C1 for all statistical and experimental details. Images by Canepa et al.[2] (published by The Royal Society of Chemistry) licensed under CC BY-NC 3.0 (minor changes were made).

Quantification of the lipid/NP– ratio in pre-incubated model neuronal membranes. QCM-D results reported in Figure 36a were used to quantify the ratio between lipid molecules and NP– embedded into M1 membranes after pre-incubation of 4 h. The mass of a spherical NP– with a core diameter of 2.7 nm and ligand composition MUS:OT 80:20 is $m_{NP}=1.6\cdot10^{-10}$ ng, considering $MW_{NP}=96279$ g/mol (see the bottom of Appendix C1 for MW_{NP} calculation details). Thus, the number of embedded NP– is $\Delta m/m_{NP}\sim1.7\cdot10^{12}$ NP–/cm², corresponding to 0.017 NP–/nm² (where Δm_{NP} corresponds to 267 ng/cm², Figure 36a). Concerning the lipids, the SLB areal mass calculated from the normalized frequency shift (26 Hz, Figure 36a) was 463 ng/cm²; this mass includes a water layer which has been determined to be ~102 ng/cm² [335,336], which leaves an areal mass for the lipid bilayer of 361 ng/cm². The average molecular weight of the lipid mixture with composition M1 (Table 6) is 813.14 g/mol, corresponding to a molecular mass $1.35\cdot10^{-12}$ ng/molecule. Dividing the areal mass of the SLB by the mass of a single lipid molecule, we estimated that there are 2.67 molecule/nm² on the bilayer or 1.34 molecule/nm² on the lipid monolayer; this value corresponds to a lipid area a_L=0.75 nm²/molecule, in agreement with the structural data in the literature[337]. Therefore, the ratio between the number of lipid molecules and the number of embedded NP– is about 1.34/0.017=79 lipids/NP–. On the other hand, the AFM investigation reported in Figure 39 showed an ordered NP– aggregate with an average NP–NP separation of 7.5 nm. As reported in Section 5.3.3, this horizontal distance was confirmed by simulations (inset of Figure 41d). By assuming a hexagonal unit cell, the unit cell area is 49 nm² which divided by the lipid area a_L gives at least 65 lipids/NP−. This value is not far from, but smaller than the estimation based on the adsorbed mass measured by QCM-D. In fact, the latter estimation considers the total amount of lipid molecules in the SLB, including those within the disordered membrane patches not involved in the ordered NP– aggregate (Figure 37c), thus resulting in a larger lipid/NP– ratio.

5.3.3 MD simulations and thermodynamic model

This project was developed thanks to a continuous comparison between experiments and simulations. The description of the main *in silico* results, therefore, is necessary to complete the discussion of the experimental findings previously presented. MD simulations were performed by collaborators to 1) investigate the molecular mechanisms and energetics of interaction for the NP– adsorption on the L_d phase (as observed by AFM imaging); 2) study the effect of NP– on the lateral lipid phase separation; and 3) characterize, with molecular resolution, the ordered NP aggregation observed within the bilayer after NP/vesicle pre-incubation. The model

used to simulate NP– and multidomain bilayers has a coarse-grained resolution and is compatible with the MARTINI coarse-grained force field for biomolecular simulations[308]. *In silico* NP– have a diameter of 2 or 4 nm, which is representative of the experimental size distribution, and a 70:30 MUS:OT ligand ratio (Figure 40a)[129,146]. The *in silico* M1 bilayer was simulated using a mixture of 1,2-dilinoleoyl-*sn*-glycero-3-phosphocholine (DLiPC), SM, chol, and GM1, in the molar ratio DLiPC:SM:chol:GM1 56:18:17:9 (Figure 40a). This composition, containing DLiPC instead of DOPC and much more cholesterol, was adjusted from the experimental one (Table 6) to obtain a stable L_o – L_d phase separation over a long simulation time scale (Figure 40a,d).

1. Preferential NP interaction with the membrane disordered phase. After initial positioning of 2 or 4 nm NP– in the water phase (not in contact with the bilayer), they either spontaneously adsorbed onto the L_d phase (Figure 40b, top), or transiently adsorbed onto the L_o phase and then quickly (~100 ns later) diffused towards the L_d phase, where they resided for the rest of the simulation time (20 μs). On the L_d phase, NP– were found to adsorb more stably and closer to the membrane midplane than on L_o domains, favored by the higher bilayer disorder allowing for the necessary conformational adjusting of the lipid headgroups in contact with the NP–. The free energy profile of adsorption of a single NP– on top of the L_d and L_o phase of the M1 membrane was then quantified (Figure 40b). Notably, the L_d-NP interaction, with a binding free energy of ~18 kJ/mol, was favored over the L_o-NP interaction (~11 kJ/mol). The thermodynamic advantage of the L_d-NP interaction is in close agreement with the experimental results of Figure 35b-f showing that amphiphilic NPs preferentially (and weakly) adsorb on the disordered phase of preformed SLBs.

2. NPs can suppress membrane phase separation. After spontaneous adsorption on the L_d phase, model NP– showed a remarkable tendency to alter the L_o – L_d phase separation leading to the dissolution of L_o domains within the simulation time scale (Figure 40c,d). Such behavior was observed regardless of NP– size and degree of NP penetration within the membrane core. On the lipid side, the mixing of lipid constituents into the M1 bilayer – following L_o domain destabilization – was quantified by computing the variation of membrane lipid-lipid contacts upon interaction with a single NP– (Figure 40e). At equilibrium, the contacts between the L_d phase lipid (i.e. DLiPC) and the lipids enriching the L_o domains (i.e. SM, cholesterol, and GM1) increased at the expense of all intra-phase contacts. In addition, the adsorption of a single NP– on a bilayer with the simulated M1 composition, but in a melted phase (i.e. deprived of the characteristic phase

immiscibility), was found to be thermodynamically favored over the adsorption on both L_d and L_o phases, as shown by the free energy profile reported in Figure 40b.

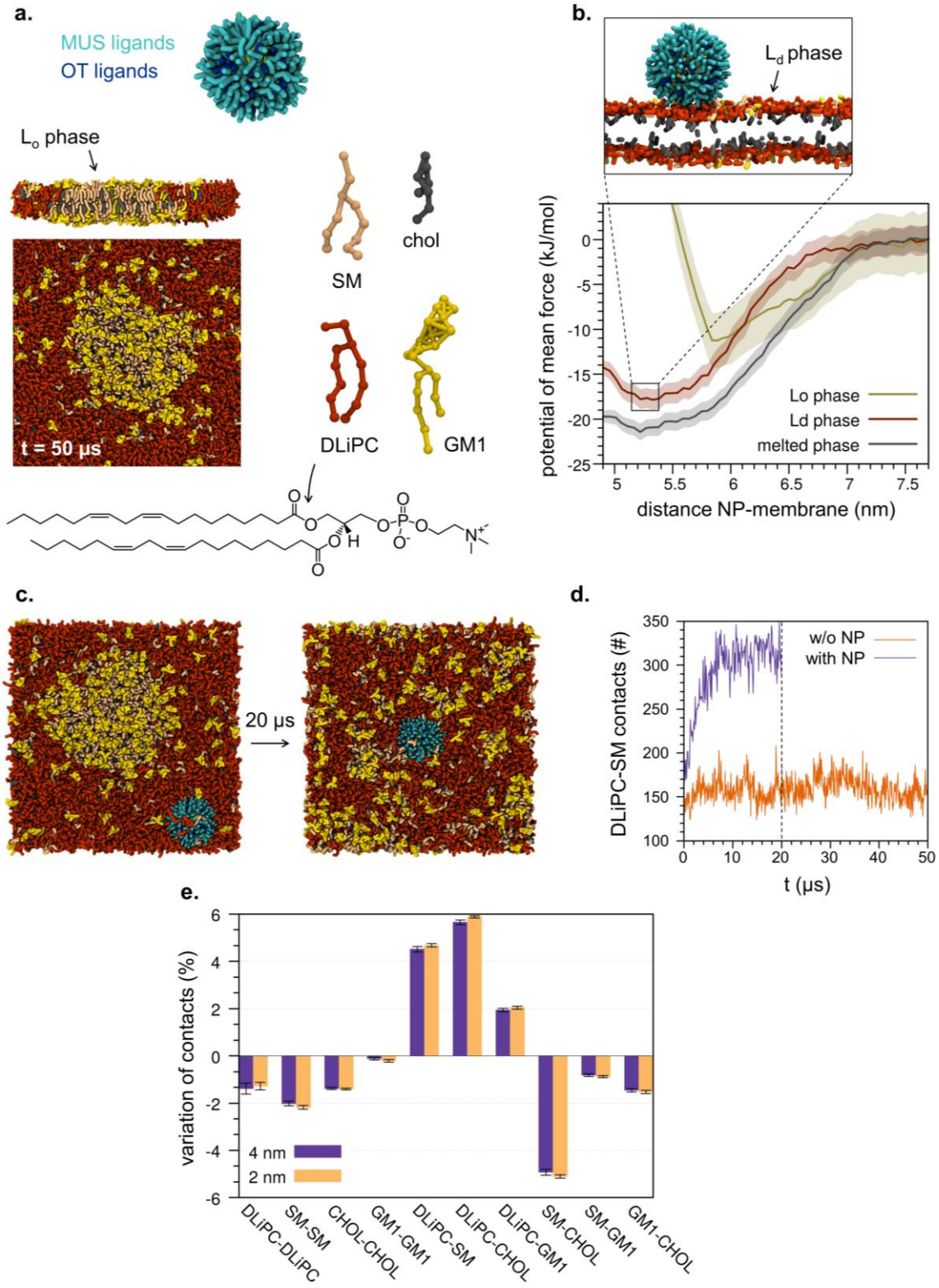

Figure 40. NP– preferentially adsorb on the L_d phase and destabilize L_o – L_d phase separation in multidomain model neuronal membranes. **a**) Coarse-grained models of NP– (MUS ligands in cyan,

OT ligands in blue, and Au atoms in yellow) and lipid species used to simulate a stable M1 membrane. The latter, at equilibrium, is shown below (top and side view). **b**) Top: simulation snapshot of a 4 nm NP– adsorbed onto the L_d phase at ~5.2 nm from the membrane midplane; bottom: potential of mean force profiles for the adsorption of a 4 nm NP– onto the L_d, L_o, and melted phase of M1 membranes. The NP– adsorption on the L_d phase of the phase-separated bilayer has a thermodynamic advantage over the adsorption on L_o domains, but after the NP-induced dissolution of the L_o – L_d phase separation, the NP interaction with the "melted" bilayer becomes even more favored. **c**) Top views of the M1 bilayer before and after the destabilization of phase separation induced by a single 4 nm NP– embedded in the L_d phase. **d**) Number of contacts between DLiPC and SM (as a function of time) before and after NP addition: as shown in (**a**), without NP–, the L_o domain was stable and well defined for all the 50 μs; on the contrary, the inter-phase contacts increased significantly after NP addition, corresponding to almost complete suppression of the lipid phase separation. **e**) Percentual variation of lipid-lipid contacts in the melted phase after L_o domain dissolution, calculated with respect to the stable, NP-free phase-separated bilayer (the lipid-lipid contacts were averaged over time and then normalized by the sum of all lipid-lipid contacts). See Canepa et al.[2] for all calculation details. Images by Canepa et al.[2] (published by The Royal Society of Chemistry) licensed under CC BY-NC 3.0 (minor changes were made).

Both the AFM results reported in Section 5.3.2 and the MD simulations discussed above outlined the NP– tendency to destabilize the lipid phase separation in model neuronal membranes with composition M1. A simple thermodynamic model, based on simulations and supported by experimental results, was developed to interpret this behavior from a general point of view.

In lipid bilayers, the L_o – L_d spontaneous phase separation derives from the minimization of the Gibbs free energy. A lipid mixture that, at equilibrium, exhibits a stable L_o – L_d phase coexistence is such that:

$$\Delta G_{\mathrm{S}\rightarrow\mathrm{M}} = \Delta H_{\mathrm{S}\rightarrow\mathrm{M}} - T\Delta S_{\mathrm{S}\rightarrow\mathrm{M}} > 0 \tag{8}$$

where: S refers to the *phase-separated state* and M to the *mixed state*.

The transition from the phase-separated state to the mixed state ($\mathrm{S}\rightarrow\mathrm{M}$) involves an enthalpic penalty – commonly referred to as *enthalpy of mixing* – and an entropic gain[338]. The entropic contribution comprises both lipid configurational entropy and mixing entropy, the latter being the most significant. Hereafter, the $\mathrm{S}\rightarrow\mathrm{M}$ subscript will be omitted for the sake of notation simplicity (yet, all energy variation reported henceforth will refer to the $\mathrm{S}\rightarrow\mathrm{M}$ transition). In the case of the current study, a certain concentration of NP inclusions has to be inserted within the phase-separated membrane and the distribution of NP inclusions into the membrane hydrophobic core is assumed to be thermodynamically favorable (i.e. NPs spontaneously penetrate the membrane core). The sign of ΔG resulting from the passive NP embedding within the bilayer (ΔG^{NP}) becomes decisive in governing the fate of the lipid phase separation:

$$\Delta G^{\mathrm{NP}} = \Delta H^{\mathrm{NP}} - T\Delta S^{\mathrm{NP}} \quad (9)$$

where: NP superscript indicates the presence of NP inclusions in the bilayer.

When the molar NP concentration is way lower than that of lipids ($C_{NP} \ll C_{lip}$), as in the case of this study, $\Delta S_{NP} \sim \Delta S$. Thus, the change of lipid-lipid enthalpy, i.e the enthalpy of mixing, represents the dominant driving force towards the NP-induced destabilization of membrane phase separation. Two are the possible scenarios that can be further configured:

1. $\Delta H > \Delta H^{\mathrm{NP}}$. In this case, the presence of NPs embedded in the L_d domain of the phase-separated bilayer reduces the stability of the phase-separated state. The term ΔH^{NP} is expected to depend somehow on C_{NP}. There may be a threshold in the NP concentration, or C_{tr}, at which the mixed state becomes equally favorable than the phase-separated state ($\Delta H^{\mathrm{NP}} = \mathrm{T}\Delta \mathrm{S}^{\mathrm{NP}}$). For concentrations higher than C_{tr}, the M state is thermodynamically favored over the S state. This situation seems to fit with the case of NP– interacting with the multidomain M1 bilayer, in which phase separation is no more observed when a large number of NP– penetrate within the bilayer during 4 h of NP–/vesicle pre-incubation (Figure 36a and Figure 37b,c);

2. $\Delta H < \Delta H^{\mathrm{NP}}$. In this case, the presence of NPs increases the stability of the L_o – L_d phase separation. This stabilization may be due to different NP-lipid interactions; for instance, NPs may accumulate at the phase boundary driven by hydrophobic mismatch, thus reducing the line tension between domains in multicomponent membranes[156,317]. Alternatively, NPs may have extremely favorable dispersion interactions with lipids in the L_d phase, as in the case of fullerenes and other small hydrophobic molecules[339,340].

Relatively short equilibrium MD simulations were performed to compare the energetics of the bilayers with composition M1 before and after the embedding of NP–. Additional simulations were acquired using the control composition M3 and control NPs with different surface chemistry, i.e. hydrophobic C_{60} fullerenes[341]. As for the *in silico* M1 bilayer, the M3 composition was simulated by replacing DOPC with DLiPC, while keeping unchanged the experimental molar ratio (DLiPC:DPPC:chol 40:40:20, see Table 6). As reported in Table 7, the enthalpic terms of Equations 8 and 9, $\Delta H_{S\to M}$ and $\Delta H_{S\to M}^{NP}$, were computed for the three combinations: NP– in M1, NP– in M3, and C_{60} in M1. All the analysis details and the

interaction contributions involved in defining these enthalpic terms are detailed in ref[2].

Table 7. Enthalpies of M1 and M3 bilayers before and after the embedding of NP– or C_{60} fullerenes. Simulation results were validated against the experimental data described in Section 5.3.2 (NP– in M1 and NP– in M3) or taken from the literature (C_{60} in M1).

in silico bilayer	$\Delta H_{S\rightarrow M}$ *(kJ/mol)* [a]	*NP type (NP/lipid molar ratio in simulation)*	$\Delta H^{NP}_{S\rightarrow M}$ *(kJ/mol)* [a]	*model prediction*	*experimental validation*
M1 DLiPC:SM:chol:GM1 56:18:17:9	$+9.96\cdot10^{3}$	NP– ($0.35\cdot10^{-3}$) [b]	$-1.2\cdot10^{3}$	destabilize phase separation already at low concentration	AFM images in Figure 37b-d
M3 DLiPC:DPPC:chol 40:40:20	$+4.9\cdot10^{3}$	NP– ($0.28\cdot10^{-3}$) [b]	$+1.9\cdot10^{3}$	destabilize phase separation as concentration increases	AFM images in Figure 38e-g
M1 DLiPC:SM:chol:GM1 56:18:17:9	$+9.96\cdot10^{3}$	C_{60} fullerene ($1.8\cdot10^{-2}$)	$+1.48\cdot10^{4}$	stabilize phase separation	Ha et al.[342] [c]

[a] The overall enthalpy differences were computed by averaging over 200 ns of unbiased MD simulations.
[b] NP– in M1: 1 NP– in 2850 lipids; NP– in M3: 1 NP– in 3520 lipids.
[c] unbiased MD simulations showing the NP-induced stabilization of the lipid phase separation are reported in ref[2].

According to this simple model, $\Delta H > \Delta H^{NP}$ for both NP– in M1 and NP– in M3. In these systems, NP– inclusions are thus expected to destabilize the membrane phase separation by altering the enthalpic gain associated with lipid-lipid interactions within L_d domains (Table 7). This prediction is in good agreement with the experimental case of the M1 bilayer (Figure 37) but seems to contradict what was observed for the M3 bilayer, whose phase separation was not perturbed during NP/vesicle pre-incubation (Figure 38d-h). Interestingly, Table 7 shows that for the NP– in M3 system ΔH^{NP} remains positive at the NP concentration used in the simulations, meaning that the destabilization of phase separation may be achieved only at sufficiently high NP– concentration. Additional simulations reported in ref[2] demonstrated that the stability of the phase separation decreases as the NP– concentration in the simulated M3 bilayer increases. Experimentally, after 4 h of pre-incubation with NP–, M3 bilayers showed only a low uptake of sparse, small NP– aggregates, which was not sufficient to destabilize the membrane phase separation (Figure 38e-g). These results demonstrate that MD can be effectively used as a

predictive tool to assess the propensity of NPs of different compositions to alter or stabilize phase separation in multicomponent lipid bilayers.

3. Molecular-level characterization of ordered NP aggregation within the membrane. Simulations were repeated to investigate the NP behavior after embedding of two or more NP– of 2 or 4 nm in the M1 bilayer. In the case of two NP–, dimerization was found to be much more thermodynamically favored for larger NP–. In unbiased simulations, 4 nm NP– spontaneously formed a stable dimer, with embedded NP– significantly protruding out of the bilayer (Figure 41a,b). On the contrary, 2 nm NP– only formed transient dimers within the simulation time scale (10 μs), with little to no perturbation of the bilayer structure. At the nanoscale, fine size-dependent control of NP-membrane interactions has already been reported in a similar system[142]. Thus, in the current study involving NP–, the transition from the non-aggregation to the aggregation regime is believed to occur within the NP diameter range of 2÷4 nm (an in-depth computational investigation of this effect is under development). The only membrane damage observed upon stable dimerization of 4 nm NP– consisted of the formation, induced by charged MUS ligands, of a small nanopore[343] in between the two NP– (Figure 41a,b). Such pore formation allows the hydrophilic MUS ligands of the two NP– to re-orient within the space between the snorkeled NP– (Figure 41b). Once formed, the pore at NP–NP interface was stable and did not expand. After investigating the spontaneous tendency to stably dimerize, the aggregation of 4 nm NP– was tested using several NP– embedded in the bilayer. By combining seven NP– not in contact with each other and let to diffuse freely in the bilayer, the spontaneous formation of a stable hexagonal aggregate was observed (Figure 41c), in which the NP–NP distance (Figure 41d) nicely matched that measured by AFM imaging after NP–/vesicle pre-incubation (Figure 39c). Even in the case of the hexagonal aggregate, the spontaneous formation of nanopores was observed in between neighboring NP–. On the microsecond scale, such pores opened and closed several times at the interface between different pairs of adjacent NP–. As for experiments, simulations reported that the average height of the NP– aggregate over the bilayer (Δz) is way below the mean NP– diameter (Figure 41e for simulations *vs* Figure 39d for experiments). These results consistently suggest that NP– were partially embedded into the bilayer. The slight Δz difference between experiments and simulations could be ascribed to the experimental NP– size dispersion (0.8 nm standard deviation). The movie reported in ref.[2] illustrates the spontaneous formation of the stable NP– hexagonal aggregate within this system.

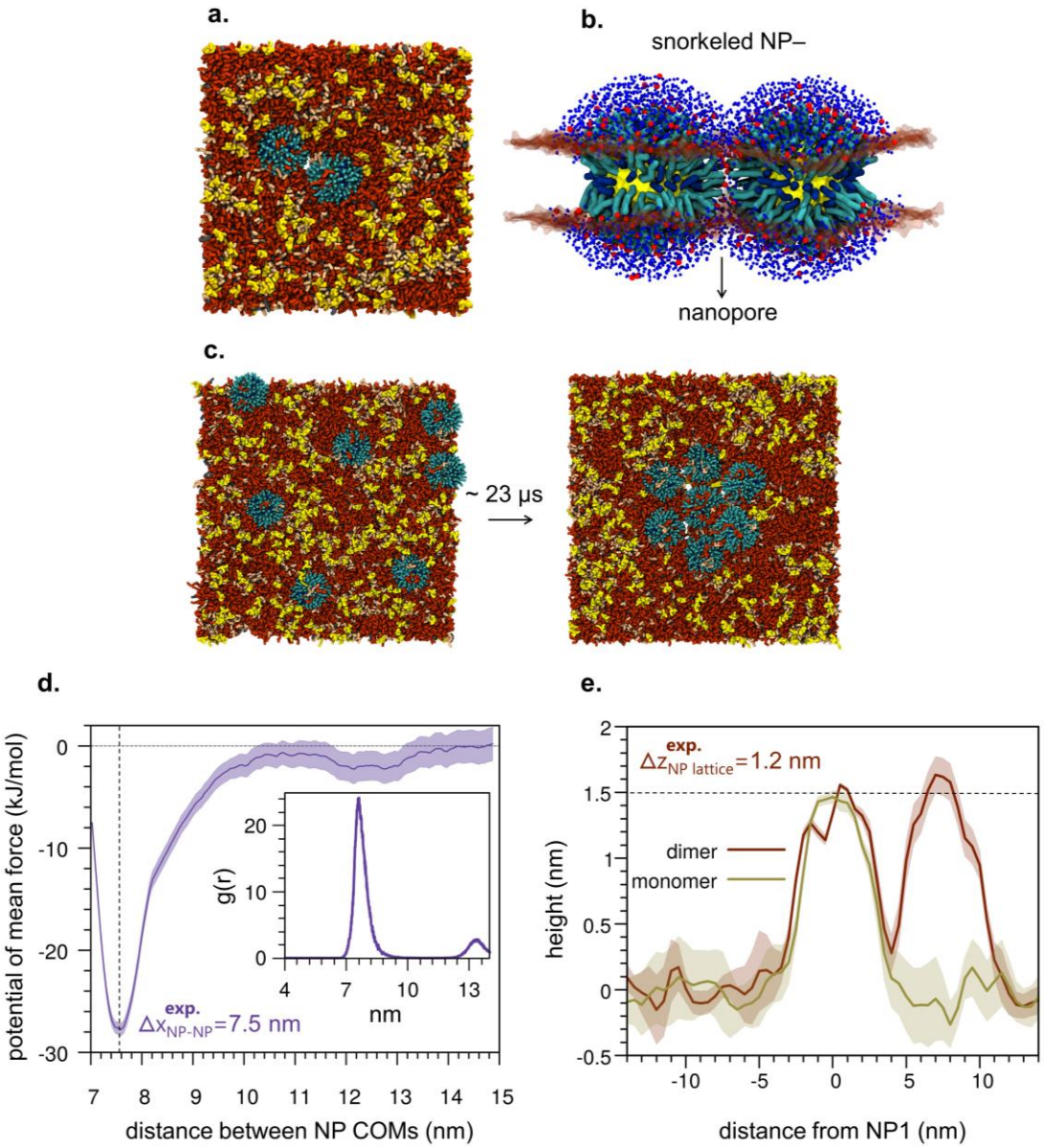

Figure 41. *In silico* structural investigation of the ordered aggregates formed by 4 nm NP–. **a**) Top view of the stable, spontaneous NP– dimerization. **b**) Lateral view showing both the protrusion of NP– dimer on top of the bilayer and the nanopore formation in between the two NP– (lipid headgroups are shown as semi-transparent surface, lipid tails are not shown for clarity, Na+ ions are shown in red, while water in blue). **c**) Top views of the initial and final configuration showing the spontaneous formation of a stable hexagonal NP– aggregate. **d**) Potential of mean force for the NP–dimerization. The inset reports the NP–NP radial distribution function, g(r), obtained during the unbiased run with 7 NP–: the first neighbor peak, at 7.5 nm, matches the experimental result. **e**) Height profile (averaged along the simulation time) of the protrusion of a single NP– and a NP–dimer with respect to the bilayer surface (mean protrusion of 1.5 nm in the simulations *vs* 1.2 nm in the experiments). See Canepa et al.[2] for all calculation details. Images by Canepa et al.[2] (published by The Royal Society of Chemistry) licensed under CC BY-NC 3.0 (minor changes were made).

6. Influence of membrane stiffening in passive NP uptake

6.1 Membrane fluidity and NP uptake: a reciprocal influence

The variable fluidity of plasma membranes plays a critical role in providing the appropriate environment for the operation of metabolic enzymes, membrane-bound transporters, ion channels, and other cellular machinery. Several enzymatic functions require that membrane components diffuse freely within the lateral plane of the lipid bilayer, whereas other processes rely on motional constraints imposed on structural elements. Even in phase-separated membranes, which are discussed in Chapter 5, the discontinuity in membrane fluidity resulting from lateral lipid segregation is crucial for various cellular processes[344,345]. As explained in Section 1.3.4, cholesterol plays a key role in preserving and regulating functional membrane fluidity over a wide range of temperatures. Mammalian plasma membranes contain ~40÷90 % of total cellular cholesterol[346], which in turn constitutes ~20÷50 mol % of all membrane lipids [161,175,347,348]. The cholesterol content varies by cell type and species; for instance, high levels of cholesterol have been found in cells of some cancer tissues[349]. Cholesterol also contributes to maintaining membrane integrity and modulating lateral phase separation resulting from preferential lipid-lipid interactions[350,351]. Cholesterol depletion by exogenous entities, such as certain cyclodextrins, has a major impact on membrane mechanics and permeability[211,352]. These alterations can be detrimental to membrane structure, even resulting in cytotoxic effects[352,353].

To date, the impact of membrane fluidity on NP uptake – and vice versa – has been assessed using model systems primarily composed of phospholipids, in the absence of cholesterol. At room temperature, small amphiphilic AuNPs have been reported to penetrate exclusively within fluid phases of phase-separated lipid vesicles[142], as also confirmed by the results described in Chapter 5[2]. Consistently, the temperature-induced increase in membrane fluidity has been shown to dramatically boost the incorporation of both negatively[142] and positively[132] charged amphiphilic AuNPs (~2÷3 nm) into gel-phase bilayers. These experiments indicate that membrane fluidity dramatically affects both the uptake kinetics and equilibrium amount of small amphiphilic AuNPs within the lipid bilayer[132,142]. On the other hand, the broader literature on the effects of NP adsorption on membrane fluidity appears

controversial and a general consensus is still lacking. In various model systems, NP adsorption has been shown to alter the phase behavior of the lipid bilayer. For instance, experiments by Bothum[354] reported that hydrophobic silver NPs (~6 nm) induce an appreciable decrease in the melting temperature of DPPC bilayers. Furthermore, Park et al.[355,356] showed that the uptake of slightly smaller hydrophobic silver (and gold) NPs further fluidizes the DPPC membrane even above the melting temperature. Slight softening of the bilayer has been also described for negatively charged silica NPs (~8 nm) adhered to fluid DOPC vesicles[357]. In contrast, Montis et al.[358] observed that adsorption of citrate-capped anionic AuNPs (15 nm) onto POPC vesicles induces local membrane restructuring into stiffened lipid domains. In addition to AuNPs, NP-induced membrane stiffening has also been reported experimentally for charged polystyrene[359] and silica[360] NPs of similar size. Specifically, Granick et al.[359] showed that nonspecific adsorption of negatively charged NPs onto single-component PC bilayers induce localized gelation around NPs in liquid-crystalline phases, whereas positively charged NPs were observed to promote local fluidization in gel phases[359]. This charge dependence of the influence of NP uptake on membrane fluidity has also been supported by coarse-grained MD simulations involving smaller NPs (~6 nm) with different surface charge densities[361].

Although cholesterol-tuned bilayer fluidity represents an intrinsic aspect of cell membrane complexity, no experimental study has systematically addressed the effect of cholesterol concentration in nonspecific NP-membrane interactions. Recently, flow cytometry analysis by Atukorale et al.[142] revealed no difference in the uptake of 2÷3 nm MUS:OT AuNPs by fluid DOPC bilayers with or without only 25 % chol. Over a wider composition range, unbiased MD simulations by Gkeka et al[362] showed that penetration of small MUS:OT AuNPs (~4 nm) into DPPC bilayers with 0÷50 mol % chol induces, in all systems studied, local disorder and cholesterol depletion in the lipid bilayer. As a consequence of cholesterol expulsion around NPs, the authors observed no definite effect of cholesterol concentration in hindering the NP translocation within the bilayer. Evidently, the impact of cholesterol content on the passive uptake of NPs in fluid bilayers composed of disordered phospholipids requires further experimental and computational investigation.

6.2 Project: objective and methods

The aim of this project – which is still under development – is to investigate, by adopting a systematic and comparative approach, the influence of cholesterol-induced membrane stiffening on the passive uptake of amphiphilic NPs. In particular,

sub-5 nm monodisperse AuNPs with MUS:OT ligand shell have been considered. On the membrane side, lipid vesicles with a progressive decrease in bilayer fluidity have been prepared by mixing the di-unsaturated DOPC with increasing amounts of cholesterol. First of all, variation in membrane fluidity before interaction with NPs was characterized by AFM nanomechanical measurements (contact-based QI™ mode by JPK, Section 2.1) and fluorescence anisotropy spectroscopy (Section 2.3.2). While former experiments allowed measuring Young's modulus of DOPC/chol SLBs, the latter technique was used to reveal any constraints to the motion of bilayer-embedded fluorophores as a function of the composition of the surrounding lipid environment. In general, fluorescence anisotropy assays are commonly used to detect structural perturbations increasing or decreasing the lipid packing in model systems, such as the incorporation of cholesterol in between disordered phospholipids considered in this project. In turn, membrane fluidity is directly related to the structural arrangement of lipid molecules. Even the NP-membrane interaction was investigated using fluorescence anisotropy to propose further considerations on the influence of NP uptake on membrane fluidity. However, the systematic study of NP uptake has been developed primarily by means of QCM measurements (Sections 2.2). As in previous projects, QCM-D provided a sensitive and accurate quantification of the amount of NP passively incorporated within the bilayer; yet, in this case, experiments have relied on a different NP-lipid system. Instead of analyzing the formation of SLBs on the crystal sensor after NP/vesicle pre-incubation, the NP-membrane interaction was monitored in real time by incubating NPs onto a supported vesicle layer (SVL). QCM-D investigation, together with AFM measurements, were performed at the Materials Characterization Facility – IIT, Genoa – working in collaboration with Dr. Silvia Dante.

6.3 Results and discussion

6.3.1 NPs and lipid membranes

Amphiphilic MUS:OT AuNPs with remarkably low core size dispersion were synthesized using the thiol-for-OAm ligand exchange procedure described in Section 3.2. For QCM-D and fluorescence anisotropy measurements, small NPs with 2.4 ± 0.4 nm core diameter (Figure 30a and Table 5, Section 3.2.1) were employed. Additional fluorescence experiments were performed using larger NPs with 4.8 ± 0.5 nm core diameter (Figure 30b and Table 5). The ζ-potential in the experimental buffer (PBS, 1x, pH 7.4) was –38 ± 2 and –36 ± 1 mV (Table 5) for small and large NPs,

respectively. These values ensured good stability against aggregation within the experimental time scales considered in this study (i.e. several hours). The stability of colloidal NP dispersions is also confirmed by comparing the hydrodynamic diameters in water and PBS reported in Table 5. For all NPs, the MUS:OT molar ratio in the ligand shell was 2:1 (32 % OT), as determined after decomposition of the Au core (Table 5). See Appendices A4 and A5 for all details of NP synthesis and characterization.

Unilamellar DOPC vesicles with cholesterol content varying in the biological range (0, 15, 26, 29, 35, 43, and 52 mol %) were extruded in PBS with a 100 nm pore size filter. To avoid repetition, henceforth all percent cholesterol concentrations will refer to the molar content. For fluorescence anisotropy assays, small amounts of DPH or TMA-DPH (Section 2.3.2) were incorporated within the vesicle bilayer. All details of vesicle preparation and characterization are provided in Appendix B.

Although DOPC-rich lipid mixtures are widely used to prepare model membranes with or without lateral phase separation, the characterization of DOPC phase behavior in combination with cholesterol is less studied than expected. Most phase studies focus on ternary systems from which the behavior of the DOPC/chol boundary mixture in the cholesterol solubility range (0÷67 % chol[191]) can only be inferred based on a few isolated experimental points, mostly concentrated at low cholesterol content. At room temperature, these studies consistently reveal a uniform phase for the DOPC/chol mixture between 0÷20 % chol[363]. Although cholesterol is universally accepted to inhibit the membrane dynamics and decrease membrane fluidity in liquid-crystalline bilayers, the DOPC/chol phase behavior above 20 % chol is still assumed to be a delicate issue. While confocal images of dye-labeled GUVs show uniform fluorescence that is consistent with a single phase[363], some spectroscopy results show the occurrence, at ~30 % chol, of nanosized L_o domains within the L_d bilayer, followed by a uniform $L_d \rightarrow L_o$ phase transition at higher cholesterol content[364]. If real, nanoscopic L_o domains are extremely likely to evade direct microscopic detection; at the same time, bilayer-embedded probes may represent impurities that interfere with the lipid phase behavior, inducing the formation of localized artifactual structures. Recently, Chakraborty et al.[365] reported a comprehensive structural characterization of the physical state of DOPC membranes upon progressive cholesterol addition (0÷50 %). According to experiments and simulations, DOPC bilayers undergo a cholesterol-induced increase in membrane thickness and viscosity and a reduction in local fluctuation dynamics. More important, cholesterol has been shown to locally increase the bilayer bending stiffness, similar to saturated membranes, by increasing the lipid packing density[365].

6.3.2 AFM, fluorescence anisotropy, and QCM-D experiments

Characterization of fluid bilayers with progressive membrane stiffening. After extrusion in PBS, fluid DOPC vesicles with increasing cholesterol content were deposited on silicon at 60 °C to promote SLB formation. AFM imaging of the planar bilayers was performed in tapping mode and QI mode to investigate the surface topography and measure the Young's modulus of the samples, respectively. Unlike the DOPC-based multicomponent membranes studied in Chapter 5, no lateral lipid phase separation was observed for each cholesterol content, and the SLB surface was uniformly flat on a scale of tens of microns. Topographic tapping-mode images of SLBs with three representative compositions are shown in Figure 42a; the white dashed line marks the location of the height profiles (Δz) reported in Figure 42b. In general, the surface roughness of the samples was very similar regardless of the cholesterol content; moreover, the ~4 nm hole in the sample at 29 % chol confirms the presence of a lipid bilayer. Compared to the AFM images reported in Chapter 5, here the DOPC-based SLBs always reported a slightly increased surface roughness (even at 0 % chol). This difference may be due to either the different microscope model or the different substrate for SLB deposition (mica *vs* silicon); in general, each substrate shows a peculiar surface roughness and slightly different chemical properties[233].

AFM imaging was then shifted to contact-based QI mode to acquire force *vs* tip-sample separation curves within 5 × 5 μm^2 lateral scans (a schematic of a typical force spectroscopy experiment is illustrated in Figure 57 of Appendix C1). Force curves were then processed to map the bilayer Young's modulus (E) distribution. As expected, the results plotted in Figure 42c indicated a clear linear increase in the mean E value with increasing cholesterol content up to ~40 %; this is consistent with a progressive stiffening of the fluid DOPC/chol bilayer. Surprisingly, at 52 % chol, the E value did not increase further; this result may be due to an overestimation of the actual cholesterol content in the bilayer (Appendix B1) or to reaching the maximum membrane stiffness within the cholesterol solubility range. The E values shown in Figure 42c, on the order of several tens of MPa, are similar to those reported for other DOPC-based liquid bilayers at similar loading force[366]. For the 0 % and 35 % chol bilayers, maps of the Young's modulus are shown in Figure 42d. In general, the E distribution was homogeneous on a scale of several microns, indicating lateral uniformity in membrane stiffness. Figure 42e reports the respective E distributions obtained from multiple maps. Full experimental details on the AFM set-up, analysis parameters, and sample preparation are described in Appendix C1.

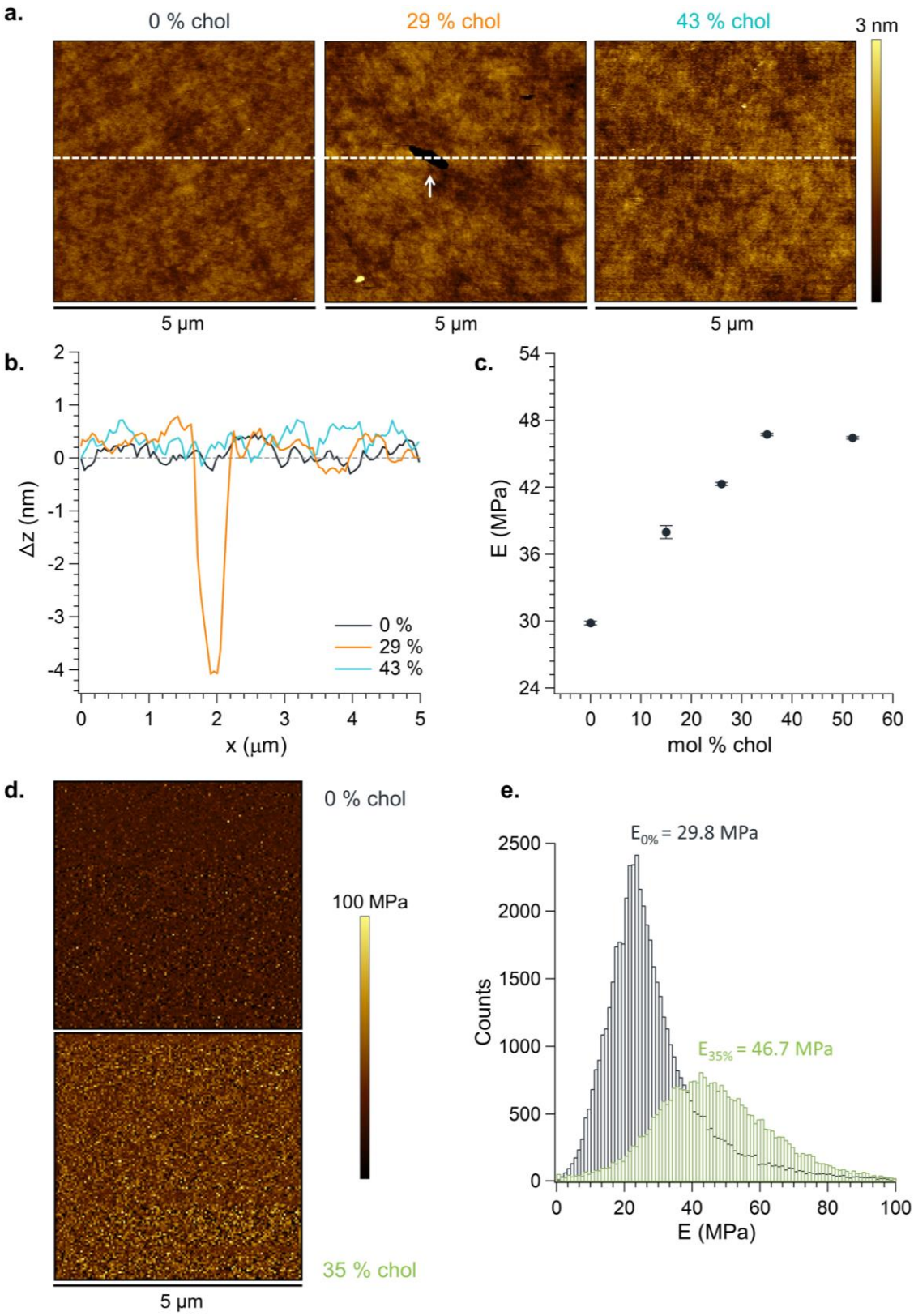

Figure 42. AFM characterization of fluid DOPC SLBs with progressive chol-induced membrane stiffening (deposited on silicon). For all samples in the 0÷52 % chol range, no microscopic phase-separation was observed. **a**) Representative topographic images (tapping mode) in the absence of cholesterol and in the case of medium or high cholesterol content (29 % and 43 %, respectively). **b**)

Height profiles of the SLBs taken along the white dashed lines in the images shown in (**a**); the peak in the orange curve at 29 % chol corresponds to the bilayer hole (~4 nm) indicated by the white arrow in the corresponding image. **c**) Young's modulus (*E*) *vs* chol %. **d**) Two representative *E* maps, acquired in contact-based QI mode, at 0 % and 35 % chol. **e**) *E* distributions at the same percentages reported in (**d**); histograms were elaborated from a different number of counts: ~31000 at 35 % chol and ~53000 at 0 % chol. See Appendix C1 for full details on data analysis.

Cholesterol-induced membrane stiffening was further investigated by fluorescence anisotropy assays. As described in Section 2.3.2, the anisotropy emission of DPH and TMA-DPH molecules embedded in the phospholipid bilayer is widely used to obtain information on the lipid ordering at different depths of the bilayer: while the highly apolar DPH is buried within the hydrophobic core of the membrane, in between the phospholipid tails, TMA-DPH is firmly anchored to the polar region of PC heads due to its terminal cationic group. Anisotropy results as a function of cholesterol concentration (0÷52 %) are shown in Figure 43.

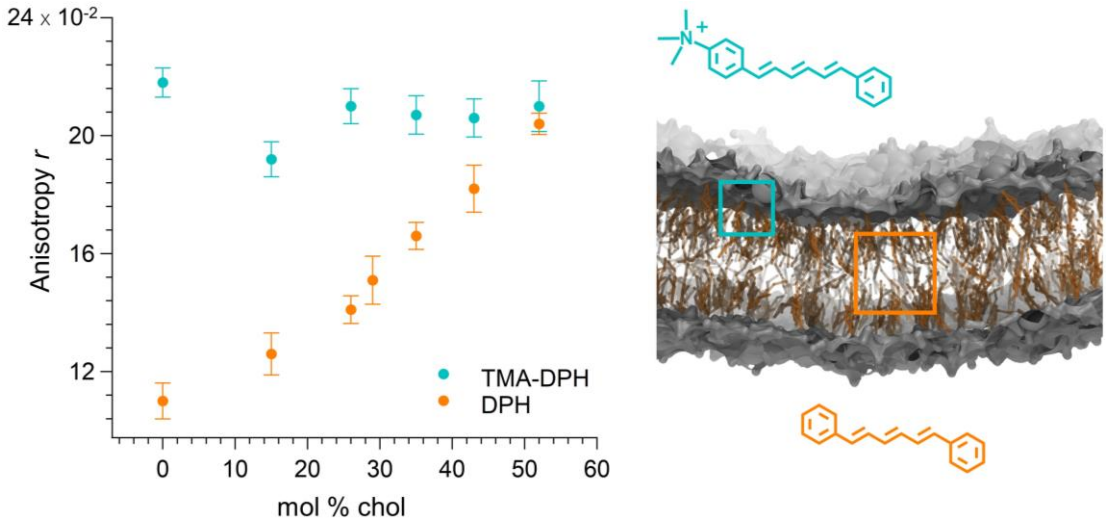

Figure 43. Fluorescence anisotropy of DPH and TMA-DPH in DOPC vesicles with increasing cholesterol content (0÷52 %; 20 °C). Right: simulation snapshot of the DOPC/chol bilayer with 30 % chol; lipid heads in gray (surface representation), lipid tails in light-gray sticks, and cholesterol in tan sticks (lipid tails are made transparent to make tan cholesterol visible). DPH and TMA-DPH tend to reside within the separate bilayer regions framed in the snapshot (i.e. the hydrocarbon core and the hydrocarbon-water interface, respectively). Their rotation is not isotropic as they exhibit preferred orientations[276]. Their anisotropy emission (*r*) increases as their translational and orientational freedom within the bilayer decreases (r_{max}=0.4, see Section 2.3.2).

In the absence of cholesterol, the behavior of the two membrane-embedded molecular probes differs significantly. While DPH tends to occupy a larger portion of the bilayer with a discrete translational and rotational freedom, which thus corresponds to a reduced anisotropy emission (r=0.110), the motional order of TMA-DPH at the hydrocarbon-water interface is much more constrained, and therefore its emission is more anisotropic (r=0.218). When cholesterol is added, the anisotropy of DPH increases linearly, whereas the emission of TMA-DPH is almost unaffected and

settles around the maximum value reached by DPH at 52 % chol. The trend shown by DPH suggests that the lipid environment in which the probe is inserted undergoes a progressive stiffening as cholesterol increases. In the case of cationic TMA-DPH, the anisotropy is maintained at higher constant values, indicating that the constraints on probe motion due to the anchoring of the cationic group at the hydrocarbon-water interface are likely to overcome those induced by the presence of cholesterol. Full details of the fluorescence anisotropy assays carried out for this project (including data analysis) are described in Appendix D2.

NP uptake by fluid bilayers with progressive membrane stiffening. Freshly extruded lipid vesicles with increasing membrane rigidity were deposited on gold-coated crystal sensors to form stable SVLs which were then incubated with MUS:OT AuNPs (2.4 nm). SVLs have already been tested on other systems to study NP-membrane interactions[367,368]. Unlike SLBs, SVLs are viscoelastic films with non-negligible energy dissipation (i.e. $\Delta D_{sensor} < \Delta D_{sensor+SVL}$). Throughout the experiment – which is schematized in Figure 59 (Appendix C2) – changes in frequency and dissipation were recorded in real time by QCM-D to monitor vesicle integrity and quantify NP uptake. For this project, this NP-lipid system has the following advantages: 1) unlike SLBs, the motional constraints imposed by the substrate on the supported vesicles can be considered negligible (see Chapter 5); 2) using viscoelastic modeling, Δf and ΔD data can be quantitatively interpreted to extract information about SVL properties, such as layer density (g/cm^3) and thickness (nm)[257]; and 3) by adding NPs onto preformed SVLs – instead of vesicles pre-incubated with NPs as in Chapter 5 – the kinetics of NP uptake can be monitored in real time. All details of QCM-D set-up are thoroughly described in Appendix C2.

Figure 44a shows the frequency shifts for SVL formation as cholesterol concentration varied in the 0÷52 % range. The time required for homogeneous coverage of the sensor surface by vesicles – corresponding to a plateau in the frequency curve (Δf_{SVL}) – was significantly longer than for SLB formation (hours *vs* minutes, see Chapters 4 and 5). Moreover, the vesicle layer formed more rapidly and caused higher Δf_{SVL} as the cholesterol content increased. Since a decrease in resonance frequency is commonly interpreted as an increase in the mass adsorbed onto the sensor (as in the case of rigid films), it is tempting to directly correlate different Δf_{SVL} values to different surface coverages by the vesicles (i.e. different number of vesicles per unit area). However, the interpretation of QCM data should include potential variations in viscoelastic properties of the SVL (e.g. density and thickness) due to differences in experimental conditions (e.g. vesicle concentration in solution) or in

vesicle characteristics (e.g. size and lipid composition)[257]. In all experiments, vesicle size after extrusion (Figure 56, Appendix B2) did not vary significantly and vesicles were injected in the QCM chamber at the same concentration. Application of the Voigt model (whose details are described in ref[256]) to QCM-D data after SVL formation showed that, as the cholesterol content increased, the layer density increased, whereas the layer thickness remained unchanged (Figure 44b).

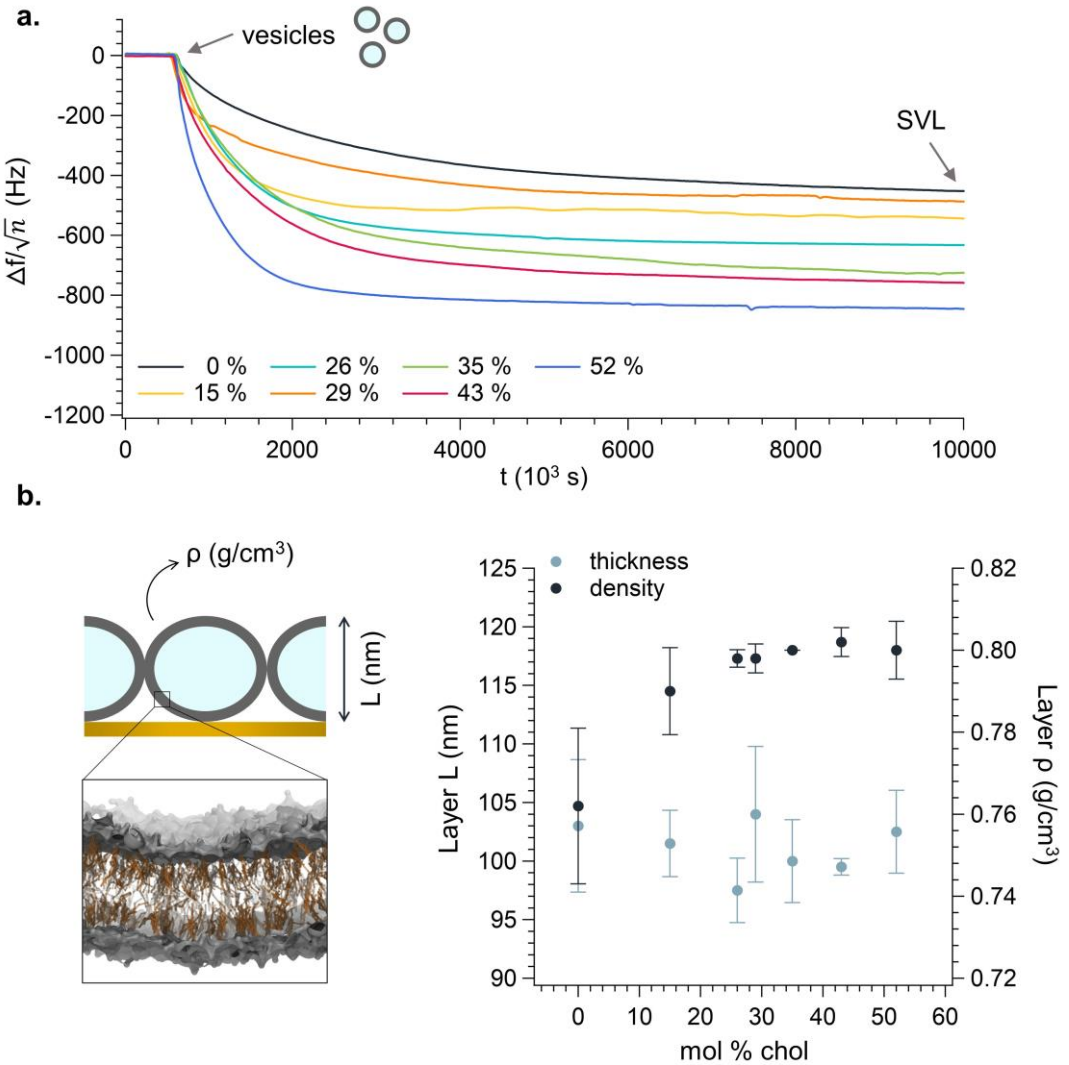

Figure 44. SVL formation onto gold-coated QCM sensors at pH 7.4 and 22 °C. **a**) Asymptotic frequency variation, Δf, recorded in real time (5th overtone) after the injection in the QCM-D chamber (t=600 s) of fluid DOPC/chol vesicles with varying cholesterol content (vesicle concentration in solution is the same for all experiments). Unlike the frequency traces reported in Chapters 4 and 5, the frequency shifts were normalized by $\sqrt{n}$, which is typical for viscoelastic films. The time required for Δf_{SVL} to stabilize at a plateau – corresponding to complete coverage of the sensor surface by vesicles – was different for each vesicle composition, e.g. ~6000 s at 52 % chol and ~18500 min at 0 % chol (intermediate times were recorded for intermediate cholesterol concentrations). **b**) Left: SVL cartoon and simulation snapshot of the DOPC/chol membrane (same color code as in Figure 43). Right: layer density (ϱ) and thickness (L) as a function of cholesterol

content. In (**b**), data analysis was performed by fitting the Δf and ΔD data from multiple overtones to the model described in ref.[256] and using the layer density and thickness as fitting parameters. The layer mass can be obtained as thickness × density[257]. See Appendix C2 for more details on data analysis.

Since both SVL thickness and vesicle diameter can be assumed to be constant from one bilayer composition to another, it can be concluded that the number of vesicles per unit area of the sensor was the same among all SVLs under investigation. Moreover, no increase in frequency shift was recorded after complete SVL formation, indicating no significant loss of vesicles from the sensor. These assumptions allow considering the same overall aqueous content for all SVLs (same number of vesicles with the same volume). Thus, the mass (gross of water content) contained in the SLV at each cholesterol content can be derived from the density and thickness data in Figure 44b. In light of all these considerations, the increase in Δf_{SVL} can be explained by the increase in layer density and thus, for the same aqueous content, in lipid bilayer packing. This result is consistent with structural measurements indicating a cholesterol-induced increase in the lipid packing of DOPC/chol membranes[365,369,370]. Interestingly, in the case of pure DOPC vesicles, the layer density reported in Figure 44b (0.762 ± 0.019 g/cm^3) is in excellent agreement with QCM-D data of ref[257] (0.776 ± 0.024 g/cm^3). Furthermore, the comparison of the average SVL thickness reported in Figure 44b (~101 nm) with the average vesicle diameter reported in Figure 56 (~135 nm, Appendix B2) strongly suggests that SVLs were composed of vesicles deformed to the same extent[257].

After SVL rinsing, NPs and SVLs were incubated for at least 20 h at 22 °C and pH 7.4. As an example for all experiments, the frequency and dissipation traces for the DOPC SVL before and after interaction with NPs are shown in Figure 45a. Figure 45b compares the NP uptake in the first four and a half hours between membranes with the highest (0 % chol) and lowest (52 % chol) bilayer fluidity, respectively. At 0 % chol, NP uptake started immediately after vesicle injection and reached a plateau after ~4 h, whereas at 52 % chol, NP uptake was significantly slowed down (however, an asymptotic value was reached at similar times). The flattening of the frequency signals was interpreted as the achievement of membrane saturation by embedding NPs. This assumption was confirmed by control experiments at low cholesterol content, and thus high membrane fluidity: after a second addition of NPs, no further uptake was recorded within the supported vesicles. Furthermore, the times recorded for bilayer saturation are consistent with the NP/vesicle pre-incubation measurements reported in Chapter 5, which involved DOPC-rich multicomponent membranes and similar amounts of NPs. Indeed, after 4 h of NP/vesicle preincubation, AFM imaging revealed the presence of numerous, uniformly

distributed NPs embedded within the bilayer in the form of ordered aggregates (Figure 39b). In general, NPs did not show significant destructive behavior during passive uptake within zwitterionic SVLs, which is consistent with the results discussed in Chapter 4[1]. Only in a few experiments, at intermediate cholesterol content, a slight and slow increase in frequency shift (corresponding to a limited mass loss at the sensor surface) was recorded after several hours of NP/SVL incubation under continuous sensor oscillation. However, this event always occurred after Δf stabilized at a minimum value. Figure 45c reports the percentage change in the mass of the SVL at membrane saturation by NPs, i.e. $\frac{\Delta m_{NP}}{\Delta m_{SVL}} \cdot 100$, where Δm_{NP} is the net mass change due to maximum NP uptake and Δm_{SVL} is the mass of the SVL before NP addition. Δm_{NP} and Δm_{SVL} values were calculated separately using two different models: a modified Sauerbrey model based on frequency shifts normalized by $\sqrt{n}$, and the Voigt model[256,257] used to extract the SVL density and thickness before NP addition (Figure 44b); more details on data processing are described in Appendix C2. In general, the frequency and dissipation shifts after NP uptake were always sampled at the plateau and before any bilayer destabilizations. Thus, NP quantification always assumed that the SVL was unaffected in terms of vesicle number and water content after NP uptake. In the case of the Voigt model, Δf and ΔD data at NP saturation were analyzed to obtain post-uptake SVL thickness and density values from which the net mass of adsorbed NPs was deduced. As shown by Figure 45c, both models provided very similar NP uptake efficiencies: as membrane stiffness increases, the amount of NP penetrating the bilayer decreases linearly up to approximately 35 % chol; from this percentage onwards, the NP incorporation remained stable at very low values. The higher uptake observed at 52 % may be attributable to dynamic inhomogeneities in the distribution of the high cholesterol content within the bilayer. The mechanical measurements shown in Figure 42c also disclosed an anomalous behavior at this cholesterol concentration, revealing lower than expected bilayer stiffness comparable to that measured at 35 % cholesterol (an underestimation of the cholesterol content incorporated into the bilayer was suggested as a possible cause).

As shown in Figure 45c, increasing membrane cholesterol from 0 % to ~40 % dramatically decreases the NP uptake efficiency by about 90 %, whereas an addition limited to 15 % is sufficient to reduce the uptake by 30 %. Interestingly, the Δm_{NP} values used to calculate the percent mass change of the SVL shown in Figure 45c were normalized by the total mass of the SVL, when in fact only the overlying portion of the vesicle layer was available for NP uptake. Given the geometry of the system, the actual mass changes in free-standing fluid vesicles due to NP uptake is expected

to be higher. To date, this is the first NP/membrane study in which the Voigt model has been used to quantify the NP uptake in SVLs, as the previously cited studies[367,368] have relied predominantly on the classical Sauerbrey method. However, the modified Sauerbrey equation proposed in this project has been shown to be suitable for interpreting mass changes in the viscoelastic vesicle layer due to NP adsorption.

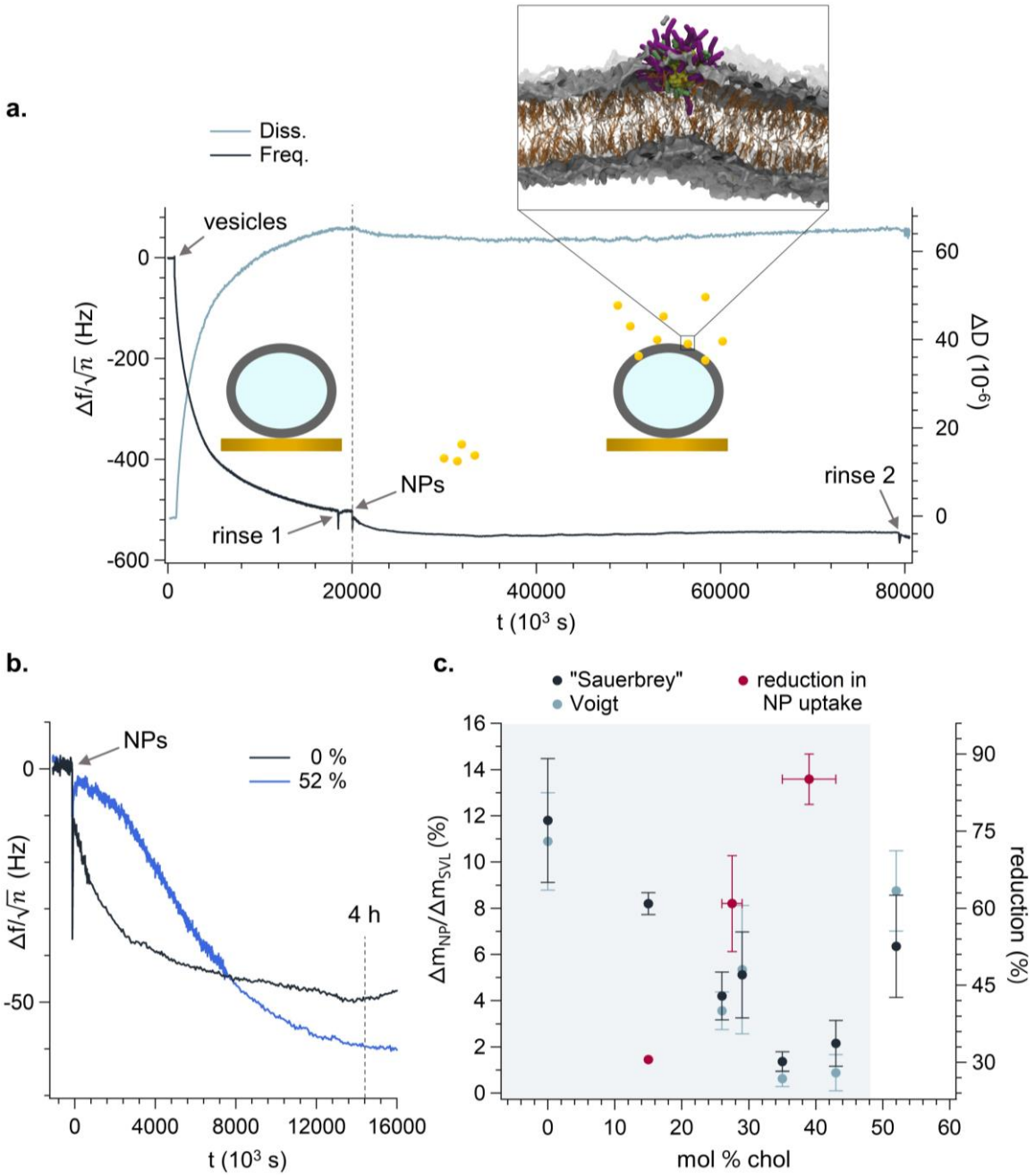

Figure 45. NP-SVL interaction monitored by QCM-D. **a**) Frequency (Δf) and dissipation (ΔD) traces of a representative experiment (0 % chol) before and after NP addition (t=20000 s). The continuous increase in energy dissipation after vesicle injection is consistent with the formation of a viscoelastic vesicle layer. The SVL was rinsed twice: before NP injection and at the end of the recording; in general, no SVL destabilization was observed in either event. In the absence of

cholesterol, NP uptake began immediately after NP addition. Simulation snapshot: bilayer color code as in Figure 43, while for the embedding NP Au atoms are in yellow, OT ligand in green, and MUS ligand in purple. **b**) Comparison of NP uptake kinetics at 0 % and 52 % chol, which is the highest cholesterol concentration considered in this study (the thicker trace corresponds to 1 s sampling rate; a point average every 10 s was then recorded overnight). **c**) Percent mass changes of the SVL at membrane saturation by NPs (i.e. at Δf plateau after NP addition) calculated using both the modified Sauerbrey equation and the Voigt model. The reduction (%) in NP uptake was normalized with respect to the maximum uptake efficiency at 0 % chol; vertical error bars at ~30 % and ~40 % chol refer to the Student's error (95 % confidence level, n=18) calculated by averaging the data at 26-29 % chol and 35-43 % chol, respectively.

After quantifying the change in NP uptake as a function of membrane stiffness, fluorescence anisotropy spectroscopy was used to investigate the influence of MUS:OT AuNPs on membrane fluidity. Figure 46a reports the anisotropy of DPH emission after vesicle incubation with NPs of both 2.4 nm and 4.8 nm diameter, while Figure 46b reports the anisotropy of TMA-DPH emission after vesicle incubation with 2.4 nm NPs.

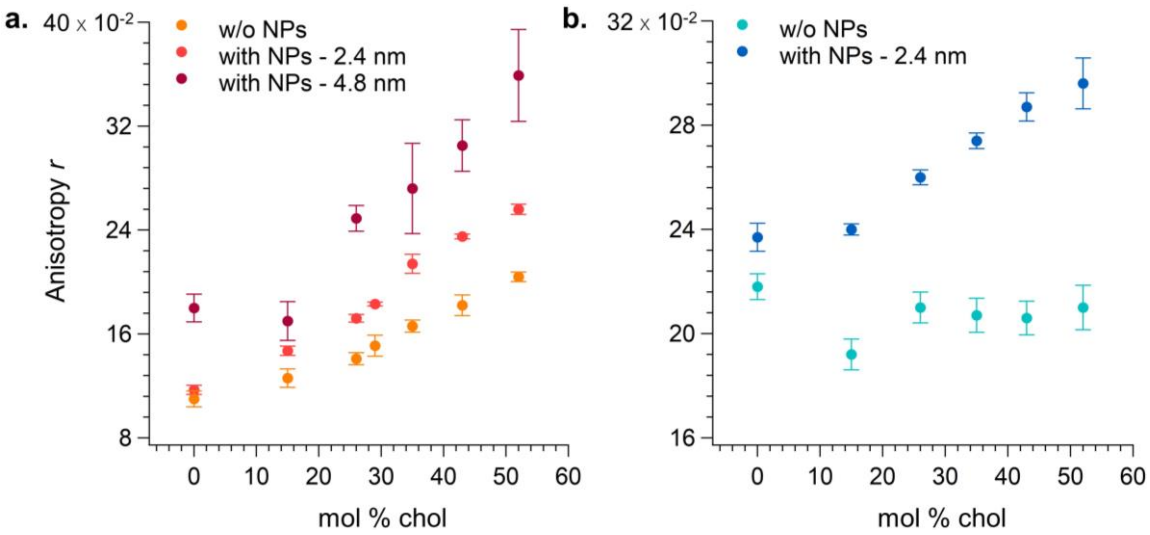

Figure 46. Fluorescence anisotropy emission (*r*) of **a**) DPH and **b**) TMA-DPH before and after vesicle incubation for ~3 h with 2.4 nm NPs and ~4 days with 4.8 nm NPs. See Appendix D2 for details on experimental set-up and data analysis.

In the case of 2.4 nm NPs, the same as used in QCM-D experiments, fluorescence measurements indicated that passive NP uptake within the fluid bilayer limited the motional freedom of the fluorophores both in the hydrophobic tail region (Figure 46a) and at the hydrocarbon-water interface (Figure 46b). This evidence suggests diffuse membrane stiffening, additional to that attributed to cholesterol, induced by NP incorporation (and proportional to NP size). However, this conclusion seems not to hold in the case of the DPH-labeled DOPC bilayer (0 % chol) after incubation with 2.4 nm NPs (Figure 46a). Here, the anisotropy emission did not vary after NP/vesicle incubation. A preliminary hypothesis that would explain

this behavior is related to the lower lipid packing of the di-unsaturated DOPC bilayer[365,369,370]: indeed, the larger area available for each phospholipid could promote abundant penetration of NPs into the membrane (Figure 45c) without significantly limiting the rotational and translational motion of DPH molecules. On the other hand, at 0 % chol, a shift in TMA-DPH emission was recorded before and after incubation with NPs (Figure 46b). Interestingly, among all vesicles tested with 2.4 nm NPs, 100 % DOPC vesicles labeled with TMA-DPH were the only ones to be incubated for ~4 h (instead of ~3 h). As observed by QCM measurements, NP uptake by 100 % DOPC membranes reached the plateau after at least 4 h of NP/SVL incubation (Figure 45b). Therefore, in the case of TMA-DPH, the difference in anisotropy recorded at 0 % chol can be attributed not to increased bilayer stiffening at the hydrocarbon-water interface but to more NPs penetrating the membrane. At the same time, a direct interaction between the cationic head of the probe and the negatively charged NPs cannot be ruled out. Finally, the increase in anisotropy induced by bilayer-embedded NPs was found to be sensitive to NP concentration during incubation. Indeed, by reducing the amount of 2.4 nm NPs by 75 % during incubation with vesicles containing the highest cholesterol content (52 %), the anisotropy shift before and after NP-membrane interaction decreases slightly, but clearly, by ~10 % for DPH (from r=0.256 to r=0.235) and ~5 % for TMA-DPH (from r=0.296 to r=0.280).

Unfortunately, the trends in fluoresce anisotropy observed in the presence of NPs are not easily understood with previous information obtained from QCM-D. Experiments on SVLs showed that NPs enter the membrane at all bilayer compositions, from 0 % to 52 % chol, and that NP uptake is severely reduced by the cholesterol-induced membrane stiffening. On the other hand, the anisotropy results after NP/vesicle incubation suggest a general increase in the anisotropy emission by bilayer-embedded fluorophores, which is compatible with a decrease in the fluidity of the vesicle membrane upon NP incorporation. This could be due to structural changes and specific interactions between lipid molecules (DOPC and cholesterol) and NPs within the bilayer. The probe itself may interfere with these interactions, albeit present in very limited amounts. Furthermore, the increase in fluorescence anisotropy for both DPH and TMA-DPH may also be consistent with the results shown by Gkeka et al.[362] on DPPC:chol membranes, which report the formation of cholesterol-depleted membrane regions between the bilayer-embedded NPs. However, this hypothesis would only be justified if the probes are also displaced into stiffer, cholesterol-enriched membrane patches. Definitely, more information needs to be obtained at the molecular level to fully elucidate the results shown in Figure 46.

7. Conclusions

In this thesis, an ensemble of biophysical techniques was employed to investigate experimentally the interaction occurring between small amphiphilic AuNPs and model lipid membranes with variable structural and morphological complexity. This work has provided original contributions in the interpretation of three specific aspects of NP-membrane interaction, as detailed below.

o Effect of NP surface charge at the NP-membrane interface

The first project discussed in this thesis concerns the comparative study of the interaction between charged amphiphilic AuNPs and neutral (zwitterionic) lipid membranes. To date, the effect of NP surface charge at the membrane interface is one of the most controversial aspects of NP-membrane interaction mechanisms. In this project, the influence of the NP surface charge, negative or positive, was compared using particles of similar size distribution, ligand shell compositions, and ζ-potentials. For both NP– and NP+, the average core diameter is ~3÷4 nm, a size that is known to allow passive NP penetration within fluid membranes[130,132,141]. By QCM-D investigation, the incorporation of NP– and NP+ into the lipid bilayer of POPC vesicles was confirmed and quantified at very similar adsorbed mass values. Furthermore, NP uptake was found to be stable and irreversible on a time scale of several hours. After checking the embedding of NPs into the zwitterionic bilayer, leakage assays performed on calcein-loaded vesicles incubated with NP– or NP+ revealed that NP-membrane interaction did not induce significant release of the inner dye. This evidence strongly suggests that membrane integrity is not disrupted during penetration of anionic and cationic amphiphilic NPs within zwitterionic membranes. These results are in good agreement with previous experiments by Liu et al.[371], reporting that AuNPs functionalized by chemisorbed thiols (in their case mercaptopropionic acid and glutathione) do not cause calcein release from PC vesicles during passive incorporation into the bilayer.

Leakage and QCM results discussed in this project were corroborated by coarse-grained MD simulations. On the one hand, the computational investigation revealed, at the molecular level, that the anchoring of charged ligands to the distal leaflet induces transient membrane deformations regardless of the charge sign. However, this partial destabilization has never been found to promote the permeation of calcein molecules through the bilayer. On the other hand, simulations have clearly

indicated that, at fixed surface charge density, anionic and cationic amphiphilic NPs share the same molecular mechanisms and energetics of interaction with the zwitterionic PC bilayer. This result is particularly significant for the cationic case, as a large body of literature (Section 1.2.3) supports that translocation of positively charged NPs across cell membranes induces a permanent or transient loss of bilayer integrity.

These results are in line with the growing number of studies addressing the interaction between neutral lipid bilayers and charged molecules[372–375]. Here, the incorporation of both charged NPs within the core of the lipid bilayer was observed to only transiently perturb membrane integrity, an interaction mechanism similar to charged amino acids[376] and positive and negative atomic ions (i.e. Na^+ and Cl^-)[377]. Moreover, the calculated free energy barriers for the translocation of anionic or cationic NP ligands across the PC bilayer are also in reasonable agreement with those calculated, by all-atom simulations, for charged amino acids[376] and Na^+ and Cl^-[377].

In general, the experiments and simulations discussed in this project clearly show that the opposite sign of the NP surface charge does not lead to a different outcome of the interaction between anionic or cationic amphiphilic NPs and zwitterionic bilayers. Notably, both charged amphiphilic NPs are observed to passively and nondisruptively penetrate fluid PC membranes. These results suggest that, when considering the interaction between neutral lipid membranes and small amphiphilic NPs that share similar core size distribution and charged ligand content, the sign of the NP surface charge does not differentiate their behavior at the membrane interface. Other intrinsic characteristics of NPs, such as core size or shape, and the design of the surface monolayer in terms of ligand length, surface density, and patterning, likely have a greater impact on the mechanisms of nonspecific NP-membrane interactions.

○ Effect of NPs on the membrane lipid phase separation

The second project discussed in this thesis concerns the behavior of small, amphiphilic, and negatively charged AuNPs interacting with phase-separated model membranes. This study is one of the very first aimed at elucidating experimentally the influence of nonspecific NP-membrane interaction on the membrane phase separation. By means of AFM imaging and QCM-D experiments, the same anionic AuNPs used in project 1 (NP–) were observed to significantly perturb the lateral lipid organization of neuronal model plasma membranes enriched in zwitterionic

phospholipids and containing gangliosides. Indeed, NP–, which have been previously shown to passively and nondisruptively enter zwitterionic lipid bilayers[1], reported a sharp tendency to alter the stability of ordered membrane domains, leading to their suppression. Also, experiments revealed that NP– form stable, diffuse, and partially embedded aggregates in the lipid bilayer. Within these NP-lipid aggregates, NP– are organized into peculiar, highly ordered two-dimensional lattices.

Further experiments on control membranes revealed that the ability of NP– to destabilize the lipid phase separation depends on their concentration in the membrane: when NP uptake is very abundant, as in model neuronal membranes, the ordered – disordered phase separation disappears. An effective thermodynamic model based on MD simulations, but validated by experiments, was developed to elucidate the driving force behind the effect of NPs on lateral lipid segregation. This model shows that the change in lipid-lipid enthalpy between the phase-separated and the mixed (domain-lean) lipid state, with and without NPs, is the dominant physicochemical indicator of the influence that NP-membrane interaction will have on lipid phase separation. The model is simple, yet of general application: after successful testing on control systems (three different NP-bilayer compositions), its applicability is strongly believed to be extendible with equal validity to any bilayer-embedded NP with nanometric dimensions comparable to the bilayer thickness.

The thermodynamic model developed in this study can be used as an effective tool to predict whether a specific NP will tend to stabilize or destabilize the phase separation of multidomain lipid membranes. The same approach may be used to study the influence on lateral lipid heterogeneity by other inclusions embedded in the bilayer, such as membrane-bound peptides and proteins[378,379]. Indeed, it is now known that some transmembrane proteins can stabilize lipid rafts[380,381], while others can induce their destabilization[382]. In some cases, these opposing tendencies may even distinguish the behavior of the same protein in slightly different lipid membranes. For instance, the hydrophobic helical peptide gramicidin-A has been reported to partition in the disordered phase of DOPC/DSPC/chol bilayers and then, depending on the lipid ratio, to stabilize or destabilize the lipid phase separation[382].

In addition to the NP effect on the lipid phase separation, the formation of ordered NP– aggregates within the bilayer has been addressed. The ligand snorkeling ability that characterizes small amphiphilic AuNPs during penetration and stabilization within lipid bilayers closely resembles the snorkeling effect adopted by some transmembrane peptides or protein segments[150]. Indeed, there is a close analogy between the configuration assumed by many transmembrane proteins and that of

NPs snorkeled in the bilayer. Moreover, even the physicochemical factors governing protein-protein aggregation in lipid membranes exhibit strong similarities to the behavior of bilayer-embedded amphiphilic AuNPs. For instance, the presence of a hydrophobic mismatch between the protein, or NP, and the host lipid phase can induce proteins, or NPs, to aggregate[381,383]. Protein- or NP-induced membrane curvature can also induce aggregation to minimize membrane deformation. In the case of amphiphilic NP– used in this project, MD simulations revealed that the conformational flexibility of surface ligands, which is greater than that of proteins, contributes to stabilizing NP– aggregates: after interparticle aggregation has occurred, the ligands all reorient around the NP– and ion-stabilized transient water nanopores form within the interstitial space between adjacent NP–. However, a comprehensive analysis of the different driving forces governing NP aggregation in PC-based bilayers is still lacking and further investigation is needed. Given the need for a molecular-level interpretation of this phenomenon at the nanoscale, simulations will play a crucial role in this investigation.

○ Influence of membrane stiffening in passive NP uptake

This study, which is still in progress, has primarily focused on the effects of membrane fluidity changes on the passive incorporation of amphiphilic NPs. To date, several studies have addressed this aspect of NP-membrane interaction focusing mainly on the impact of temperature in promoting NP penetration within bilayers composed of saturated phospholipids, such as DPPC[142] and DSPC[132]. However, when mammalian plasma membranes are considered, other factors, far more neglected than temperature variation in studies involving NPs, contribute to modulate lipid bilayer fluidity. Among these, the variable membrane cholesterol content considered in this study plays a key role. The amphiphilic AuNPs employed in this project share the same negatively charged coating as those used in the first two projects; however, they exhibit much narrower core size dispersion and thus a more uniform behavior in spontaneous penetration into lipid bilayers[141]. By means of a comparative QCM-D investigation, the ability of fluid membranes with increasing cholesterol content in internalizing NPs was systematically quantified. The experiments revealed that the peculiar ability of these small amphiphilic AuNPs to passively and nondisruptively translocate within lipid bilayers is not arrested in the considered cholesterol concentration range, i.e. 15÷52 mol %, which is representative of the cholesterol content in mammalian plasma membranes. More importantly, the progressive cholesterol-induced increase in bilayer stiffness was revealed to have a

strong impact on the equilibrium amount of embedding NPs: indeed, NP uptake was severely reduced by the increasing cholesterol content. For the first time, an experimental quantification of cholesterol-tuned variation in NP uptake has been provided. Furthermore, some additional experiments were performed to understand how, in turn, the NP uptake affects the physical state of the bilayer. This aspect, more extensively studied and widely debated in the literature, is still under development. Further investigation will certainly need interpretation at the molecular level to determine the changes in the energetics of NP-bilayer interaction and to elucidate the interaction mechanisms occurring between NPs, cholesterol, and phospholipids.

Overall, this study presents an important applicative perspective. Indeed, quantitative characterization of the ability of amphiphilic NPs to passively penetrate multiple types of cell membranes, with different degrees of fluidity, is crucial to develop biomedical technologies that rely on NP-assisted intracellular administration of site-specific therapies in the optimal dosage ranges. Furthermore, variability in membrane cholesterol concentration can be exploited in the selective targeting of cancer cells by amphiphilic NPs for advanced drug delivery applications.

Future perspectives

The results obtained in this work provide further evidence that the specific physicochemical features of both NPs (e.g. size and surface functionalization) and lipid bilayers (e.g. composition, morphology, and structure) play a crucial role in shaping the nano-membrane interaction. More efforts, however, need to be devoted to elucidating further aspects of this interaction necessary for the design of amphiphilic NPs as safe, versatile drug carriers or imaging probes. Future developments should include a structural investigation of the effects that embedded amphiphilic AuNPs have on the nanoscale organization, and thus phase behavior, of the surrounding bilayer. This study is particularly relevant to the project involving cholesterol-containing membranes described in Chapter 6. Indeed, such a structural analysis could clarify, along with a molecular-level interpretation provided by simulations, the fluorescence anisotropy results observed after NP/vesicle incubation. Finally, the work of this thesis can further develop into a mechanical characterization of lipid membranes upon interaction with NPs. The potential NP-induced alteration of bilayer mechanical properties, such as bilayer compressibility, stiffness, and bending modulus, may represent a biologically relevant consequence of the impact that NPs have, directly or indirectly, on the functioning of several membrane components, including transmembrane proteins.

Appendix A – Nanoparticles

When used, water was always purified with a Milli-Q ultrapure water system (18.2 MΩ·cm resistivity at 25 °C; MilliPore).

A1) One-phase synthesis of AuNPs

Materials. Hydrogen tetrachloroaurate (III) trihydrate ($HAuCl_4 \cdot 3H_2O$, 99.999 % trace metal basis), 1-octanethiol (OT, ≥ 98.5 %), (11-mercaptoundecyl)-N,N,N-trimethylammonium bromide (TMA, 98 %), sodium borohydride ($NaBH_4$, fine granular, ≥ 96 %), ethanol absolute (EtOH, > 99.8 %), anhydrous methanol (MeOH, 99.8 %), methanol (≥ 99.9 %), acetone (≥ 99.9 %), and 2-propanol (≥ 99.5 %) were purchased from Sigma Aldrich and used without further purification unless otherwise stated. The anionic ligand 11-mercapto-1-undecanesulfonate (MUS, 93 %) was prepared in house as detailed in Appendix A3.

Synthesis protocol. Before adding all chemicals, the solvent ethanol was purged in argon (Ar) for nearly 30 min. All the steps thereafter were performed in the presence of a gentle flow of Ar. Gold precursor $HAuCl_4 \cdot 3H_2O$ (0.225 mmol) was dissolved in ethanol (45 mL) at 0 °C in a 250 ml 2-neck round-bottomed glass flask. The solution was stirred with a magnetic bar (600-800 rpm) till complete dissolution of the salt. A thiol mixture (0.225 mol), composed of 1-octanethiol (OT, 0.075 mmol) and the ω-charged thiol (0.15 mmol, twice the amount of OT), was prepared in anhydrous methanol (5 mL, 0 °C). After mild sonication to ensure complete ligand dispersion, the thiol mixture was added to the gold solution and they were stirred together for 15 min before the addition of the reducing agent. During this time, the color and turbidity of the gold mixture changed from transparent yellow to turbid yellowish, indicating the formation of the polymeric gold-thiolate complex (Equation 5, Section 3.1). $NaBH_4$ (2.5 mmol, large excess) was dissolved in ethanol (50 mL, 0 °C) and slowly added dropwise by using a syringe needle (optimized flux speed: 1.25 mL/min). Upon reduction, the gold-thiol solution slowly darkened to reddish-black. After the complete addition of $NaBH_4$, the solution was stirred for 3 h.

NOTE: in the case of all-MUS and all-TMA AuNPs, 0.225 mmol of MUS and TMA were used, respectively. Amphiphilic NPs coated by homoligand shells were not used in experiments with lipid membranes.

NP washing. The reaction mixture was then placed in the refrigerator (-21 °C) to precipitate the NPs overnight. Different optimized washing protocols were adopted to wash cationic and anionic AuNPs, consisting of repeated overnight precipitations at -21 °C in EtOH, MeOH, and acetone for anionic AuNPs (MUS:OT and all-MUS monolayers), and in EtOH, MeOH, and 2-propanol for cationic AuNPs (TMA:OT and all-TMA monolayers). Two cleaning cycles per solvent were performed on each NP batch. Before each precipitation, NP dispersions were sonicated in an ultrasonic bath for ca. 5 min to promote the separation of NPs from unbound molecules, thus increasing the washing efficiency. Purified AuNPs were finally dried under high vacuum to obtain shiny dark powders stable in air. Before characterization and experiments with biomimetic membranes, amphiphilic AuNPs were suspended in water and diluted in buffer solution when specified.

NP treatment before characterization and experiments with lipid membranes. Cationic TMA:OT AuNPs dispersed in water showed slightly less long-term colloidal stability than anionic MUS:OT AuNPs (the former were used in the project of Chapter 4, while the latter were used in the projects of Chapters 4 and 5). Thus, TMA:OT NP dispersions were centrifuged (10 min at 11900 g) to remove the minority of unstable NPs and only the stable colored supernatant was kept for further use (DLS, ζ-potential, and NMR characterizations and experiments). All NP dispersions were finally filtered using a 20 nm pore size filter (Anotop® 10, Whatman) before interaction with lipid membranes. This step was particularly important for the fluorescence spectroscopy experiments reported in Chapter 4, where the potential presence of large entities such as dust and NP aggregates can give rise to undesired scattering phenomena. The concentration of filtered NP dispersions was accurately determined by UV-Vis absorption measurements (4 replicates), using a Jasco V-530 spectrophotometer. Calibration curves were previously obtained with NP aqueous dispersions of known concentration prepared from dried powders (Figure 47).

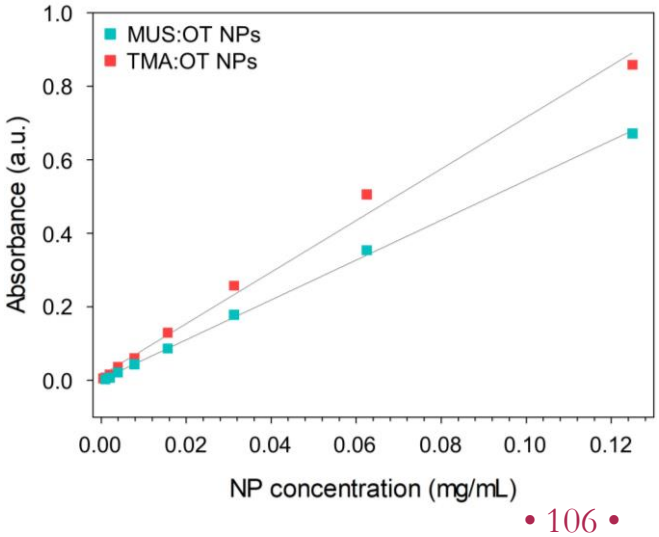

Figure 47. Calibration curves for one-phase MUS:OT and TMA:OT AuNPs (2:1 molar feed ratio) used in the experiments of Chapters 4 and 5. These curves were elaborated by preparing NP aqueous dispersions of varying concentration and measuring their UV-Vis absorption (λ=550 nm). UV-Vis spectra of MUS:OT and TMA:OT AuNPs are reported in Appendix A2.

A2) Characterization of one-phase AuNPs

One-phase AuNPs were characterized by TEM, DLS, ζ-potential, ^{1}H NMR, and UV-Vis analyses.

TEM. Bright-field transmission electron microscopy (BF-TEM) and high-angle annular dark-field scanning TEM (HAADF-STEM) analyses were performed to characterize the NP core morphology and size distribution. TEM images were collected by Dr. Rosaria Brescia (IIT, Genoa) using a Tecnai G2 F20 TWIN TMP TEM, operated at 200 kV. NP samples were prepared by suspending a small amount of NP powders in water; after sonication in a bath-type sonicator, few drops of diluted dispersions were deposited onto an ultrathin carbon-coated Cu grid. TEM results of one-phase AuNPs synthesized in this thesis are shown in Figure 23 and Table 3 (Section 3.1.1). The NP mean diameter and standard deviation were calculated by assuming spherical morphology and by counting at least 300 particles with ImageJ software.

DLS and ζ-potential. The NP hydrodynamic size after dispersion in water was measured by DLS. Average diameters were obtained from number distributions. DLS characterization was performed on all NPs prepared with the one-phase method; size results are reported in Table 3 (Section 3.1.1). NP ζ-potentials were evaluated from electrophoretic mobility measurements to assess the colloidal stability of NP dispersions before interaction with lipid membranes. For this reason, the ζ-potential analysis was performed on MUS:OT and TMA:OT AuNPs used in the experiments of Chapters 4 and 5. ζ-potential measurements were carried out in water and in the experimental buffer (pH 7.4) used in the project of Chapter 4; results are summarized in Table 4 (Section 3.1.1). For NP size analysis, measurements were acquired at $2 \cdot 10^{-2}$ mg/mL since lower NP concentrations did not provide a good quality report; ζ-potential acquisitions were carried out at $1 \cdot 10^{-2}$ mg/mL. In all cases, NP dispersions were filtered and sonicated in an ultrasonic bath before analysis; in the case of TMA:OT AuNPs, before filtration NP dispersions were also centrifuged (see above). Uncertainties on average values were obtained using Student's statistics, assuming a confidence level of 95 %. Both DLS and ζ-potential measurements were performed at room temperature using a Malvern Zetasizer Nano ZS instrument with a 173° detection angle (Malvern Instruments).

^{1}H NMR. NMR characterization of one-phase AuNPs was performed in collaboration with Dr. Chiara Lambruschini (DCCI, University of Genoa). In particular, NMR spectra of MUS:OT and TMA:OT AuNPs used in the projects of

Chapters 4 and 5 were recorded with a Varian Mercury Plus 300 (300 MHz for ^{1}H) spectrometer equipped with ATB (USA) broadband probe at 27 °C using as internal standard tetramethylsilane (TMS, 0.00 ppm). All deuterated solvents were purchased from Sigma Aldrich and used without further purification. ^{1}H NMR analysis was first used to confirm the purity of washed NPs (i.e. to verify the absence of unbound ligands). When ligands are grafted onto the NP surface, they only generate broad signals due to the complex gold core effect; although this is a demonstration of the effective bond between gold and thiols, it prevents an accurate and quantitative interpretation of integrated peaks[384,385]. For this control, NPs (ca. 5 mg) were dispersed in MeOH-d_4 (600 µL), the sample was sonicated for 30 min and the ^{1}H NMR spectrum was acquired. The absence of clear and sharp peaks indicated that no unbound ligands were present for both MUS:OT and TMA:OT AuNPs. Subsequently, the Au core was etched with a large iodine excess to quantify the ligand shell composition. This procedure induces the decomposition of the NP core by releasing all thiolated ligands as free disulfides[286,287]. MUS:OT AuNPs (ca. 5 mg) were dispersed in the etching solution (I_2 in MeOH-d_4, 0.5 mg/mL, 600 µL) and the mixture was sonicated for 30 min. Minor modifications were applied to the preparation of TMA:OT samples. As reported above, aqueous dispersions of cationic AuNPs (ca. 5 mg in 2 mL water) were centrifuged before NMR characterization to remove unstable NPs. The stable supernatant was kept and evaporated to dryness. The residue was taken up in DMSO-d_6 (600 µL), I_2 (1.6 mg) was added, and the mixture was sonicated for 30 min to etch the gold core. In both cases, a black precipitate (Au aggregates) was formed and only the clear orange solution was transferred into 5 mm NMR tubes and analyzed. ^{1}H NMR spectra were then acquired (delay: 60 s, acquisition time: 4 s, number of scans: 1024). Post-acquisition processing was performed with MestReNova (Mestrelab research v. 11.0): manual phase correction, 264 k zero filling, 3rd order polynomial baseline correction, apodization LB=0.1 Hz, and manual integration. Representative NMR spectra of iodine-etched MUS:OT and TMA:OT AuNPs are reported in Figure 48. After normalization on the number of nuclei and correction due to each contribution, the integral values were used to calculate the ratio between OT and the ω-charged ligand. Three spectra were repeated on separately weighed NP samples; uncertainties on average values were obtained using Student's statistics, assuming a confidence level of 95 % (Table 4, Section 3.1.1). All details of ligand ratio calculation are thoroughly described in Appendix A5.

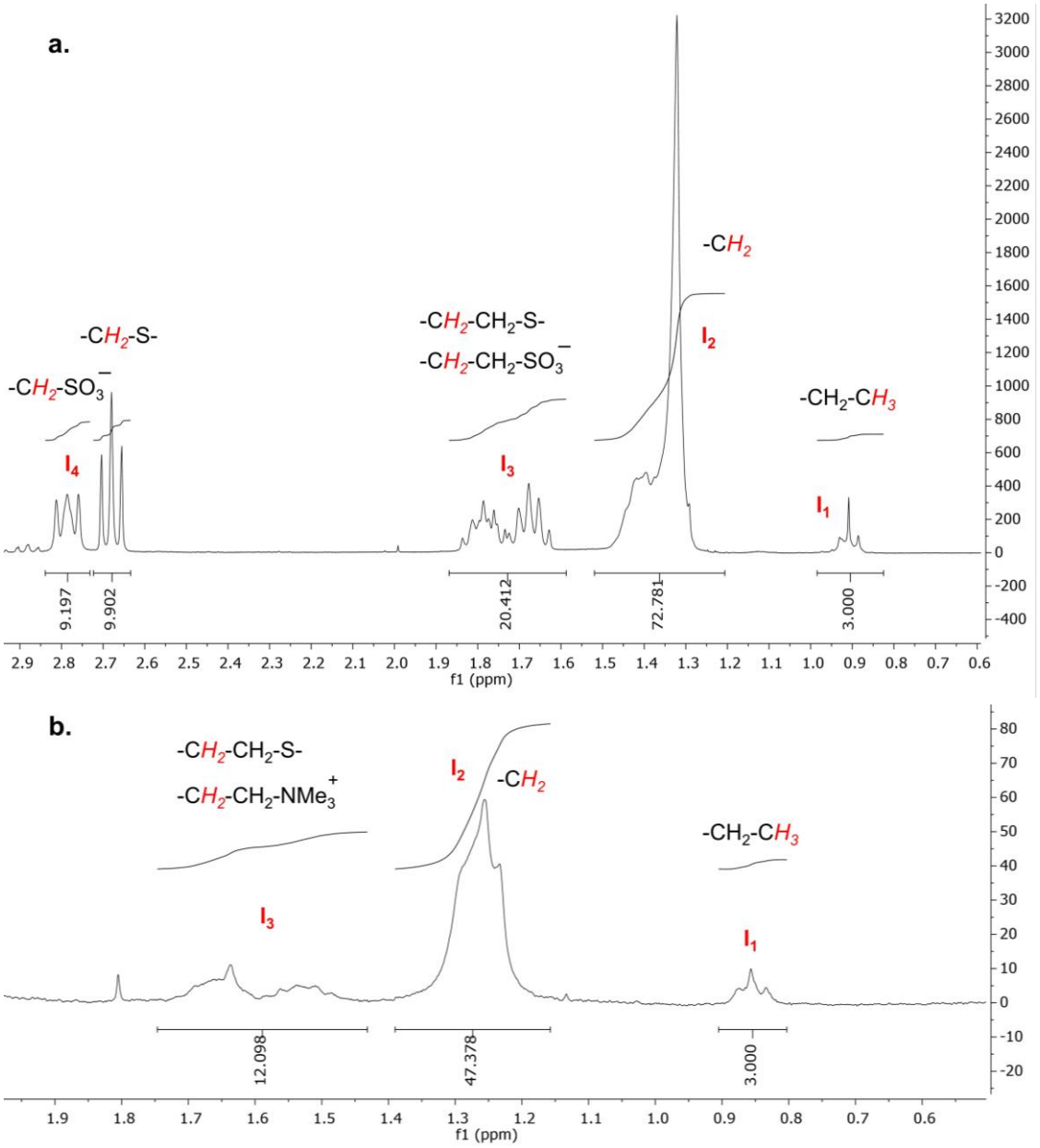

Figure 48. Expansion of ^{1}H NMR spectra (with corresponding peak assignment) of iodine-etched **a**) MUS:OT and **b**) TMA:OT one-phase AuNPs (f1 stands for the chemical shift). Monolayers contain an average of 80 % and 72 % (mol %) of MUS and TMA, respectively. In solution, a 2:1 MUS (or TMA):OT stochiometric feed ratio was used. Image (**a**) by Canepa et al.[2] (published by The Royal Society of Chemistry) licensed under CC BY-NC 3.0 and image (**b**) by Canepa et al.[1] licensed under CC BY 4.0; minor changes were made in both cases.

UV-Vis. The LSPR absorptions of one-phase MUS:OT and TMA:OT AuNPs employed in Chapters 4 and 5 were characterized by UV-Vis spectroscopy using a Jasco V-530 spectrophotometer. NP powders were first dispersed in water (0.125 mg/mL), mildly sonicated in an ultrasonic bath, and finally transferred into a quartz cuvette for analysis. UV-Vis spectra reported in Figure 49 show the characteristic LSPR peak of sub-6 nm AuNPs at around 550 nm.

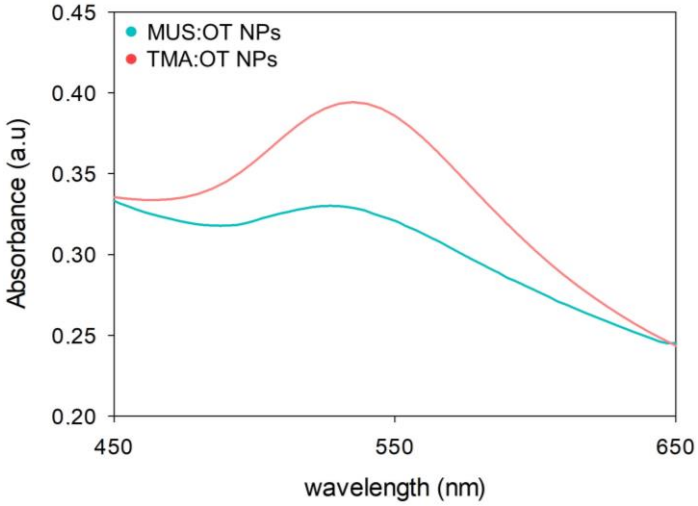

Figure 49. Expansion of the UV-Vis spectra of one-phase MUS:OT and TMA:OT AuNPs (2:1 molar feed ratio) used in the experiments of Chapters 4 and 5. MUS:OT AuNPs have a mean core diameter of 2.7 nm, while TMA:OT AuNPs of 4.5 nm (Table 3, Section 3.1.1).

A3) Synthesis and characterization of MUS ligand

Materials. All the chemicals indicated in the following protocols were purchased from Sigma Aldrich and used without further purification unless otherwise stated.

Synthesis protocol. The anionic ligand 11-mercapto-1-undecanesulfonate (MUS) used in the one-phase synthesis described in Appendix A1 was home synthesized with the precious contribution of Dr. Chiara Lambruschini (DCCI, University of Genoa). A modified literature procedure was used (Figure 50)[144,285]. In particular, we optimized the thiol-ene reaction (step 2) and calculated the purity of MUS by quantitative NMR (qNMR).

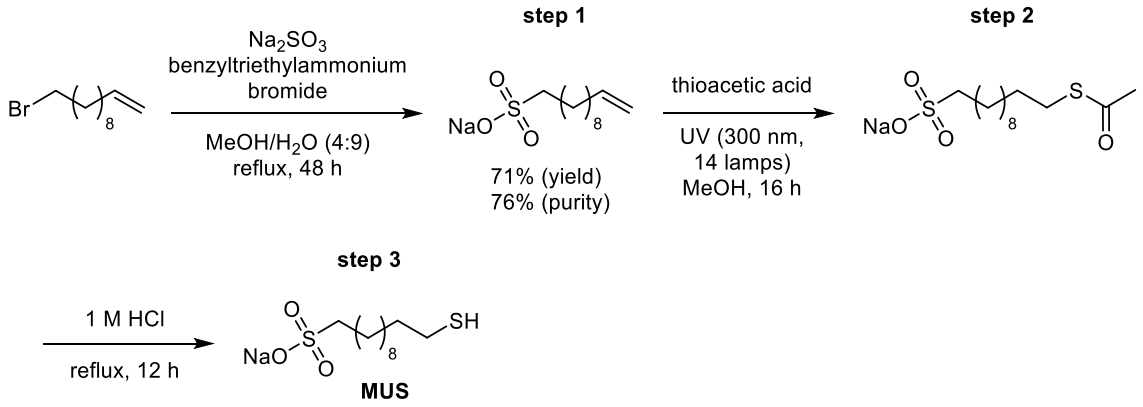

Figure 50. Reaction scheme of the MUS synthesis. This procedure is divided into three steps, which are detailed below. Image by Canepa et al.[2] (published by The Royal Society of Chemistry) licensed under CC BY-NC 3.0.

1) Synthesis of sodium undec-10-ene-1-sulfonate

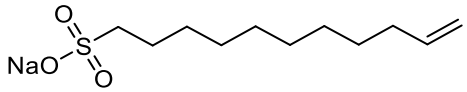

To a solution of sodium sulphite (5.77 g, 184.5 mmol) in a mixture of MeOH (40 mL) and water (90 mL), benzyltriethylammonium bromide (13 mg, 0.05 mmol) and 11-bromo-1-undecene (5 mL, 22.8 mmol) were added. The resulting solution was stirred for 48 h under reflux, then it was extracted with Et_2O (80 mL × 5), the aqueous layer was evaporated, and the resulting white solid was further dried under high vacuum. To remove inorganic salts, the solid was suspended in MeOH (150 mL) and the solution collected after filtration was evaporated. This step was repeated twice, and the desired product was obtained as white solid (4.176 g, yield 71 %, purity qNMR 76 %) and directly used in the next step. ^{1}H NMR (300 MHz, D_2O) chemical shift (δ) characterization: δ 5.79 (ddt, *J*=17.0, 10.2, 6.7 Hz, 1H, C<u>H</u>=CH$_{cis}$H$_{trans}$), δ 4.92 (ddt, *J*=17.3, 2.2, 1.6 Hz, 1H, CH=CH$_{cis}$<u>H$_{trans}$</u>), δ 4.84 (ddt, *J*=10.2, 2.4, 1.1 Hz, 1H, CH=C<u>H$_{cis}$</u>H$_{trans}$), δ 2.83–2.67 (m, 2H, CH$_2$C<u>H$_2$</u>SO$_3$Na), δ 1.98–1.83 (m, 2H, C<u>H$_2$</u>CH=CH$_2$), δ 1.68–1.50 (m, 2H, C<u>H$_2$</u>CH$_2$SO$_3$Na), and δ 1.36–1.08 (m, 12H, 6×CH$_2$).

2) Synthesis of sodium 11-(acetylthio)undecane-1-sulfonate

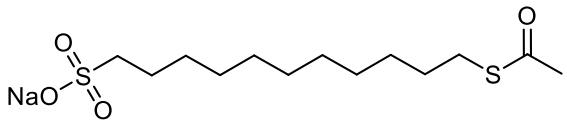

To a solution of sodium undec-10-ene-1-sulfonate (4.176 g, 16.28 mmol) in dry MeOH (75 mL, previously degassed with nitrogen) in a Pyrex tube under N_2 atmosphere, thioacetic acid (4.03 mL, 56.4 mmol) was added. The tube was placed into the Rayonet apparatus and irradiated under stirring at 300 nm for 16 h (14 lamps, 8 W each) (see Table 8 for the optimization of this step). Then the solvent was evaporated and the excess of thioacetic acid was removed with *n*-heptane (5 mL × 4). The resulting beige solid was washed with Et_2O (30 mL × 4) obtaining a white solid that was dried under high vacuum. The product was dissolved in MeOH (40 mL) by sonication in an ultrasonic bath and was further purified by adding active charcoal (600 mg). After stirring for 2 h, the charcoal was removed by filtration through a Celite plug and the solvent was evaporated. The desired product was obtained as white solid (6.588 g) and used directly in the next step. ^{1}H NMR (300 MHz, D_2O) chemical shift (δ) characterization: δ 3.00–2.81 (m, 4H, 2×CH$_2$C<u>H$_2$</u>S), δ 2.38 (s, 3H, C<u>H$_3$</u>CO), δ 1.84–1.67 (m, 2H, C<u>H$_2$</u>CH$_2$S), δ 1.60 (p, *J*=7.1 Hz, 2H, C<u>H$_2$</u>CH$_2$S), and δ 1.51–1.22 (m, 14H, 7×CH$_2$).

Table 8. Optimization of the reaction time and the number of lamps for the thiol-ene reaction. For this step, a Rayonet apparatus was used. The optimized combination is reported in bold.

Entry	*Number of lamps* (300 nm)	*Time*	*Conversion* (^{1}H NMR)
1	8	14 h	60 %
2	15	20 h	100 %
3	**14**	**16 h**	**100 %**

3) Synthesis of sodium 11-mercapto-1-undecanesulfonate (MUS)

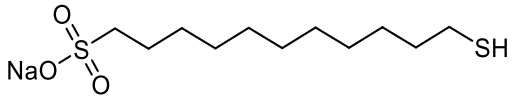

A solution of sodium 11-(acetylthio)undecane-1-sulfonate (6.588 g, 19.8 mmol) in 1 M HCl (75 mL) was stirred under reflux for 12 h. The mixture was cooled at 0 °C, then water (75 mL) and 1 M NaOH (35 mL) were added. The mixture was kept at 4 °C overnight and the product crystallized as a viscous precipitate. After decantation of the clear supernatant, the resulting suspension was centrifuged (6500 rpm, 45 min) to favor the separation of the product. A white solid was collected and dried under high vacuum in the presence of P_2O_5, while the supernatant was subjected to three subsequent crystallizations and more product was obtained. The purity was checked for each batch (Table 9) and the purest one was used for the synthesis of one-phase MUS:OT and all-MUS AuNPs (purity qNMR 93 %). The qNMR protocol is reported in the next section. ^{1}H NMR (300 MHz, D_2O) chemical shift (δ) characterization: δ 2.84–2.67 (m, 2H, $CH_2C\underline{H_2}S$), δ 2.41 (t, J=7.1 Hz, 2H, $CH_2C\underline{H_2}S$), δ 1.69–1.54 (m, 2H, $C\underline{H_2}CH_2S$), δ 1.48 (p, J=7.1 Hz, 2H, $C\underline{H_2}CH_2S$), and δ 1.36–1.08 (m, 14H, 7×CH_2).

Table 9. Purities of final MUS batches. The batch used for the one-phase synthesis of 2:1 MUS:OT and all-MUS AuNPs (Section 3.1) is reported in bold; anionic 2:1 MUS:OT AuNPs were used in the projects of Chapters 4 and 5.

Batch	*Purity* (qNMR)
1	82 %
2	**93 %**
3	84 %
4	87 %

Characterization of MUS purity: qNMR protocol. The sample MUS (ca. 10 mg) and the internal standard 3-(trimethylsilyl)propionic-2,2,3,3-d$_4$ acid sodium salt (TMSP, ca. 10 mg) were precisely weighed into a vial, then D_2O (600 µL) was added and the mixture was sonicated in an ultrasonic bath for 10 min. The clear solution was transferred into a 5 mm NMR tube and the ^{1}H NMR spectrum was acquired (delay: 60 s, acquisition time: 4 s, number of scans: 64). Post-acquisition processing was performed with MestReNova (Mestrelab research v. 11.0): manual

phase correction, 264 k zero filling, 3rd order polynomial baseline correction, apodization LB=0.1 Hz, and manual integration. The purity was calculated by applying the following equation:

$$P\,\% = \frac{n_{ISTD} \cdot Int_t \cdot MW_t \cdot m_{ISTD}}{n_t \cdot Int_{ISTD} \cdot MW_{ISTD} \cdot m_S} \cdot P_{ISTD} \qquad (10)$$

where: *n* is the number of protons that give rise to the integrated signal, *Int* is the integral value of the signal used for the quantification, *MW* is the molecular weight, *m* is the weight (mass) and *P* is the purity of the internal standard. The subscript notations are *ISTD* for the internal standard, *t* for the target analyte, and *S* for the analyzed sample.

A4) Synthesis of monodisperse AuNPs

Materials. Hydrogen tetrachloroaurate (III) trihydrate ($HAuCl_4 \cdot 3H_2O$, 0.2 % max. alkalis and other metals), oleylamine (C18-content 80-90 %), and *n*-octane (97 %) were purchased from Acros Organics (Fisher Scientific). *Tert*-butylamine borane complex (tBAB, powder, 97 %), 1-octanethiol (OT, ≥ 98.5 %), (11-mercaptoundecyl)-N,N,N-trimethylammonium bromide (TMA, 98 %), ethanol absolute (EtOH, > 99.8 %), dichloromethane (DCM, ≥ 99.8 %), acetone (≥ 99.9 %), and tetrahydrofuran (THF, ≥ 99.9 %) were purchased from Sigma Aldrich. All chemicals were used without further purification unless otherwise stated. The anionic MUS ligand[285] and the branched form of OT, i.e. the 3,7-dimethyl-1-octanethiol (br-OT)[133], were prepared in house at EPFL by other members of Prof. Stellacci's group.

Step 1: OAm-AuNP synthesis. All glassware was washed in *aqua regia* (3 moles hydrochloric acid to 1 mole nitric acid) before use. The reaction mixture was continuously stirred (and heated, when needed) using a magnetic hotplate stirrer equipped with temperature control. Magnetic stirring was finely regulated at 300 rpm and the occurrence of temperature gradients was avoided by immersing the reaction flask in a thermostated water bath. $HAuCl_4 \cdot 3H_2O$ (0.5 mmol) was first dissolved in a solvent mixture of 16 mL OAm and 20 mL *n*-octane within a 100 ml 3-neck round-bottomed glass flask. The flask was then sealed with rubber septums, abundantly flushed with Ar to exchange all air, and then placed in a sonicator bath for ca. 1 min before stirring at designed temperature. In particular, to obtain monodisperse OAm-AuNPs with ~2÷4 nm mean core diameter, the reaction temperature was varied within the 22÷52 °C range (Figure 25, Section 3.2). A static Ar atmosphere was maintained throughout the NP synthesis. After ca. 10 min, a tBAB reducing solution

(0.5 mmol in 4 mL of OAm) was quickly added to the gold-OAm mixture. The immediate gold reduction was evidenced by the rapid color change of the reaction mixture from transparent yellow to black. One hour after tBAB addition, ca. 40 mL of EtOH was added to quench the reaction and facilitate NP precipitation. The flask content was equally divided into (at least two) centrifuge tubes (50 mL capacity, polypropylene, conical bottom) and final OAm-AuNPs were collected by centrifugation at 5000 g for 10 min.

NOTE: OAm-AuNPs of ~5 nm mean core diameter were obtained at RT (22 °C) by following a slightly modified scale-up version of this protocol. The reaction was carried out in a 500 mL 3-neck round-bottomed glass flask and the magnetic stirring was increased to 700-800 rpm. $HAuCl_4 \cdot 3H_2O$ (2 mmol) was dissolved in a solvent mixture of 34 mL OAm and 50 mL *n*-octane, while tBAB (2 mmol) was solubilized in 16 mL OAm. In this case, ca. 100 mL of EtOH was added to separate final AuNPs from the reaction solution.

Hydrophobic NP washing. Three more washing cycles in EtOH were performed to purify OAm-AuNPs. Before each centrifugation (5000 g, 10 min), NPs were redispersed in a small volume of DCM (~5 mL) and diluted in fresh EtOH. Both after DCM and EtOH addition, NP dispersions were vortexed and sonicated in an ultrasonic bath to promote the removal of unbound ligands. Final OAm-AuNPs were dried under high vacuum to obtain shiny dark powders. Despite OAm-AuNPs are stable in air for several months, the following thiol-for-OAm ligand exchange was always performed within a few days of storage.

Step 2: thiol-for-OAm ligand exchange. Thiol-for-OAm ligand exchange was performed at RT. A concentrated NP dispersion was prepared by dispersing ca. 30 mg of hydrophobic OAm-AuNPs in 5 mL of DCM. In a separate glass vial (40 mL capacity), a large excess (0.1 mmol) of the thiol mixture was dissolved in 20 mL of DCM. In the case of heteroligand mixtures, preset ligand feed ratios (mol %) were used. While OT and br-OT are nicely soluble in DCM, ω-charged thiols (especially MUS) tend to form small aggregates that loosely dissolve to form turbid solutions. In all cases, an ultrasonic bath for several minutes of sonication was adopted before NP injection into the thiol vial under vigorous magnetic stirring (600 rpm). During the first 2 h of ligand exchange, the exchange mixture was mildly sonicated for ca. 30 s every half hour; the stirring was then left overnight. The same sonication procedure was repeated 2 h before NP washing. Successful replacing of OAm with amphiphilic (water-soluble) thiol shells was indicated by the different solubility in DCM of final AuNPs, which tend to slowly precipitate upon stirring removal.

NOTE: in the case of ligand exchange with only MUS (i.e. all-MUS AuNPs), a two-phase system water:DCM (1:1 v/v) was used instead of DCM alone. While the concentrated OAm-NPs dispersion was prepared in DCM, MUS was nicely solubilized in water. The MUS-for-OAm ligand exchange was confirmed by NP displacement from the lower organic phase (DCM) to the upper aqueous phase, which separates upon stirring removal.

Amphiphilic NP washing. After ~12-15 h, the exchange mixture was diluted in acetone (ca. 15 mL) and centrifugated (5000 g, 4 min) to speed up NP separation. Collected AuNPs were then redispersed in ca. 5 mL of fresh DCM, diluted in fresh acetone, and recentrifuged. Both after DCM and acetone addition, NP dispersions were vortexed and sonicated in an ultrasonic bath to promote the removal of unbound ligands (OAm and excess thiols). In total, 6 washing cycles in organic solvent were performed before vacuum drying to remove all DCM and acetone traces. After a few hours, dried AuNPs were dispersed in water (ca. 15-20 mL) and transferred into a hydrated AMICON® ultra centrifugal tube (regenerated cellulose membrane, 10 kDa cutoff molecular weight). NP dispersions were then centrifuged (4000 g, 6 min) to filter off the excess of water-soluble ω-charged thiol. This cleaning process was repeated at least 10x; in between each cycle, NP concentrated dispersions were rediluted in fresh water, vortexed, and sonicated.

NOTE: using AMICON® tubes, the absence of foaming when agitating the aqueous waste of final centrifugation is a good indication of complete removal of amphiphilic molecules such as MUS and TMA.

To turn final AuNPs into a manageable powder, concentrated NP aqueous dispersions were transferred into a 15 mL centrifuge tube, diluted in THF, and ultracentrifuged at 14500 g for 10 min. Alternatively, to avoid THF addition, NP aqueous dispersions were freeze-dried. In all cases, at least two days of vacuum drying were waited before storing NP powders in air. Before characterization, monodisperse amphiphilic AuNPs were suspended in water and diluted in buffer solution when specified.

NP treatment before characterization and experiments with lipid membranes. Unlike the previous case, water dispersions of monodisperse amphiphilic AuNPs were not filtered before characterization and interaction with lipid membranes. In particular, only 2:1 MUS:OT AuNPs were used in the experiments described in Chapter 6. These NPs showed remarkable long-term colloidal stability in water and their dispersions did not require further manipulation before use. To confirm the absence of aggregates or dust in the fluorescence

spectroscopy measurements reported in Chapter 6, DLS characterization was performed prior to all experiments.

A5) Characterization of monodisperse AuNPs

Monodisperse AuNPs, before and after thiol-for-OAm ligand exchange, were variably characterized by TEM, DLS, ζ-potential, and ^{1}H NMR analyses.

TEM. BF-TEM images were collected with the precious contribution of Matteo Gasbarri (EPFL, Prof. Stellacci's group) by using a FEI Tecnai Osiris operated at 200 kV. TEM characterization was performed on all NP batches before and after thiol-for-OAm ligand exchange. NP samples were prepared by suspending a tiny amount of NP powders in DCM and water, respectively. After sonication in an ultrasonic bath, few drops of diluted dispersions were deposited onto an ultrathin carbon-coated Cu grid. Representative TEM images of hydrophobic OAm-AuNPs and amphiphilic thiol-protected AuNPs are shown in Figure 28 and Figure 29 (Section 3.2.1), respectively. Table 5 (Section 3.2.1) reports the average TEM core size of 2:1 MUS:OT AuNPs used in the project of Chapter 6 (corresponding TEM images are reported in Figure 30, Section 3.2.1). In all cases, the core mean diameter and standard deviation were calculated by assuming spherical morphology and by automatically counting a few thousand (at least 1000) particles with ImageJ software.

DLS and ζ-potential. As for one-phase AuNPs, both DLS and ζ-potential analyses were performed at room temperature using a Malvern Zetasizer Nano ZS instrument (Malvern Instruments, UK). Average hydrodynamic diameters (from number distributions) and ζ-potentials were characterized only for anionic 2:1 MUS:OT AuNPs used in the experiments with lipid membranes (Chapter 6). Measurements were performed in water and the experimental buffer (PBS, 1x, pH 7.4); results are reported in Table 5 (Section 3.2.1). NP concentrations of $3 \cdot 10^{-1}$ mg/mL and $2 \cdot 10^{-1}$ mg/mL were used for size analysis in water and in buffer, respectively. ζ-potential acquisitions were performed at $7 \cdot 10^{-2}$ mg/mL in water and $1 \cdot 10^{-1}$ mg/mL in buffer. In all cases, NP dispersions were sonicated in an ultrasonic bath before analysis. Uncertainties on average values were obtained using Student's statistics, assuming a confidence level of 95 %.

^{1}H NMR. NMR spectra of amphiphilic AuNPs were acquired in a Bruker AVIII400 UltraShield Plus (400 MHz for ^{1}H) spectrometer. All deuterated solvents were purchased from Sigma Aldrich and used without further purification. NMR characterization was systematically performed only after thiol-for-OAm ligand

exchange. As for one-phase AuNPs, ^{1}H NMR analysis was first used to confirm the absence of unbound ligands (OAm and thiols). For this control, NPs (4-5 mg) were dispersed in D_2O (800 μL), sonicated for ca. 20 min, transferred into a 5 mm NMR tube, and the ^{1}H NMR spectrum was acquired. The absence of sharp peaks demonstrated the effectiveness of the adopted washing protocol in removing all unbound ligands. A representative spectrum of amphiphilic AuNPs before iodine etching is reported in Figure 51.

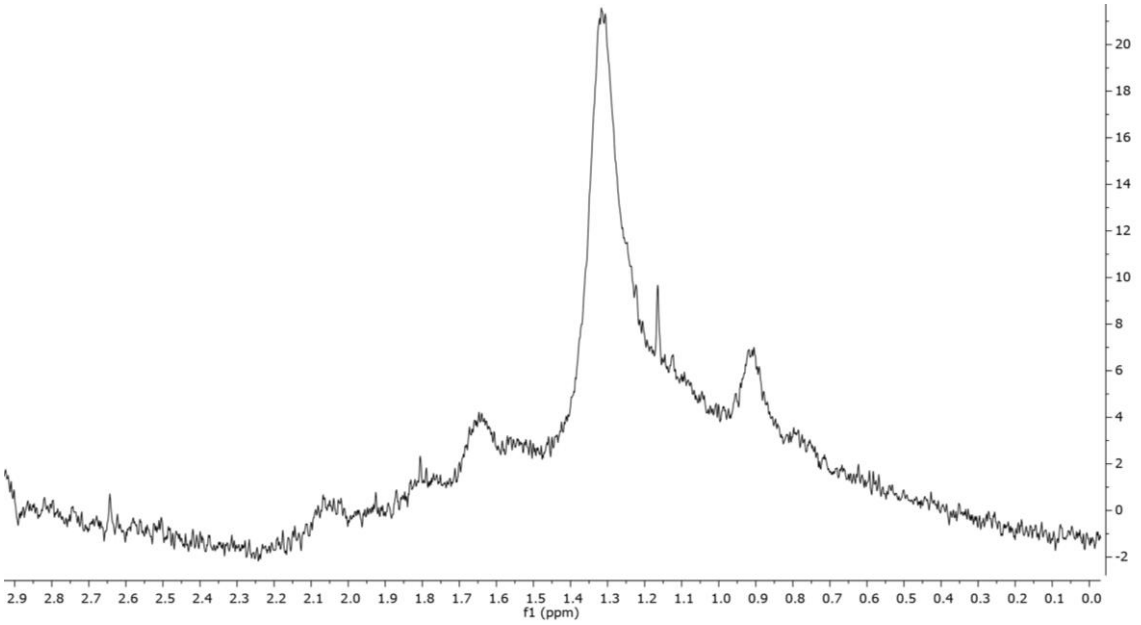

Figure 51. Representative NMR spectrum of MUS:OT AuNPs before decomposition of the Au core (f1 stands for the chemical shift). This spectrum clearly shows the peak-broadening effect of ligands owing to the complex chemical environment on the Au surface.

Subsequently, the Au core was decomposed with a large excess of iodine to quantify the amount of hydrophobic thiol (OT or br-OT) in MUS:OT, TMA:OT, and MUS:br-OT mixed monolayers. A concentrated iodine solution was prepared by dissolving 15-20 mg of iodine in 800 μL CD_3OD. After ca. 20 min of sonication to favor the complete solubilization of iodine, 800 μL of the etchant solution was added to 4-5 mg of NPs. The NP-iodine mixture was sonicated in an ultrasonic bath for ca. 30 min before transferring the clear orange supernatant into a 5 mm NMR tube. ^{1}H NMR spectra were then acquired with 32 scans; post-acquisition processing was performed with MestReNova (Mestrelab research v. 11.0): automatic phase correction, full auto (polynomial fit) baseline correction, and manual integration. Representative NMR spectra of iodine-etched MUS:OT, TMA:OT, and MUS:br-OT AuNPs are reported in Figure 52. In general, no residual trace of OAm was recorded in all spectra, thus confirming that the thiol-for-OAm ligand exchange has always

been complete. Full details on ligand ratio calculation are reported right after the NMR spectra.

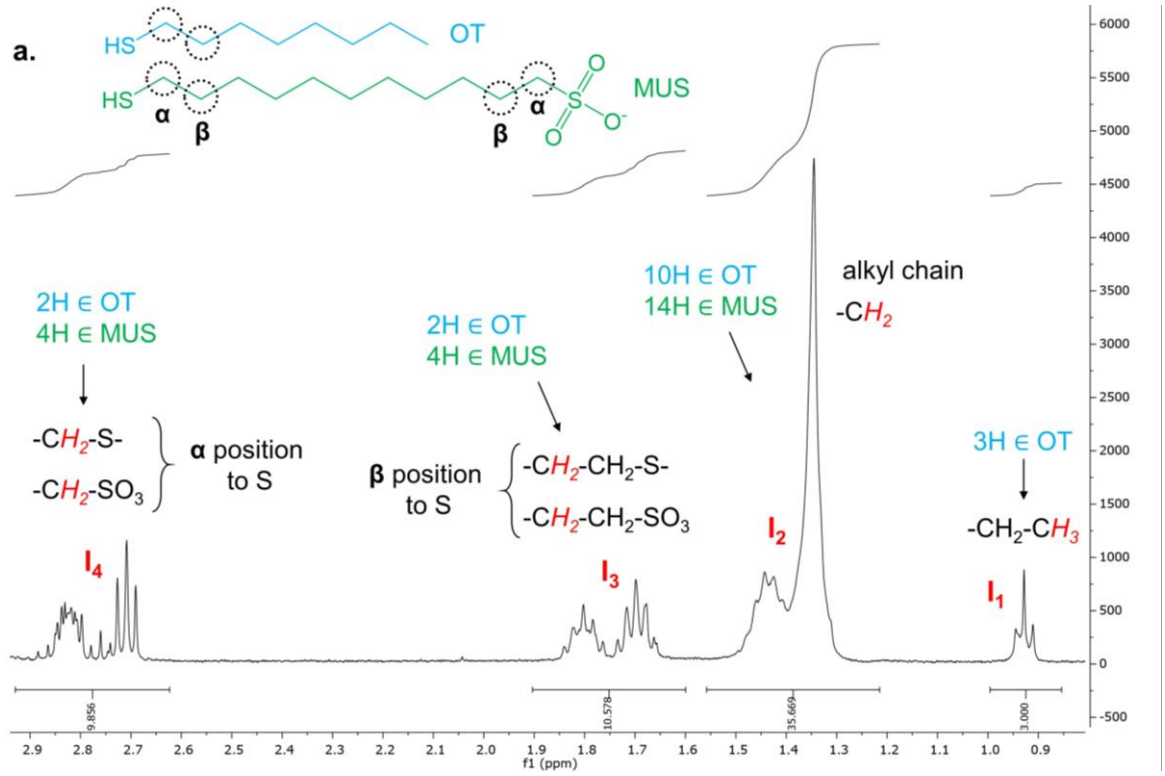

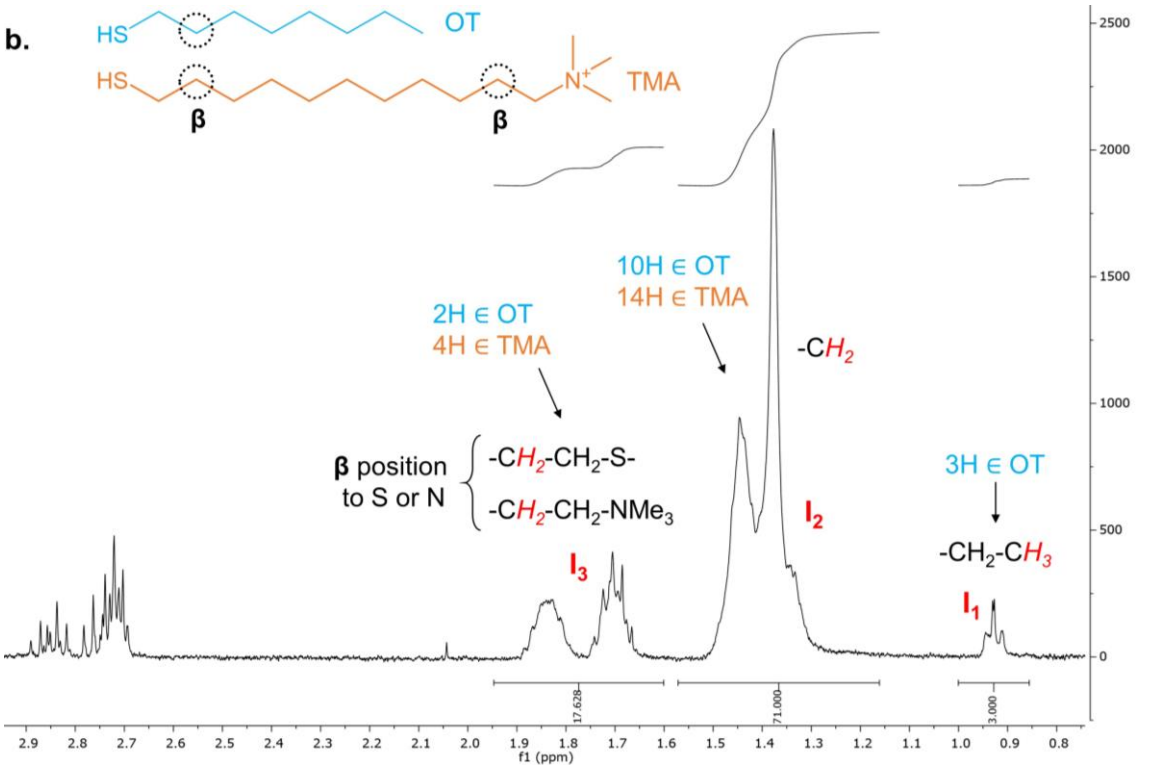

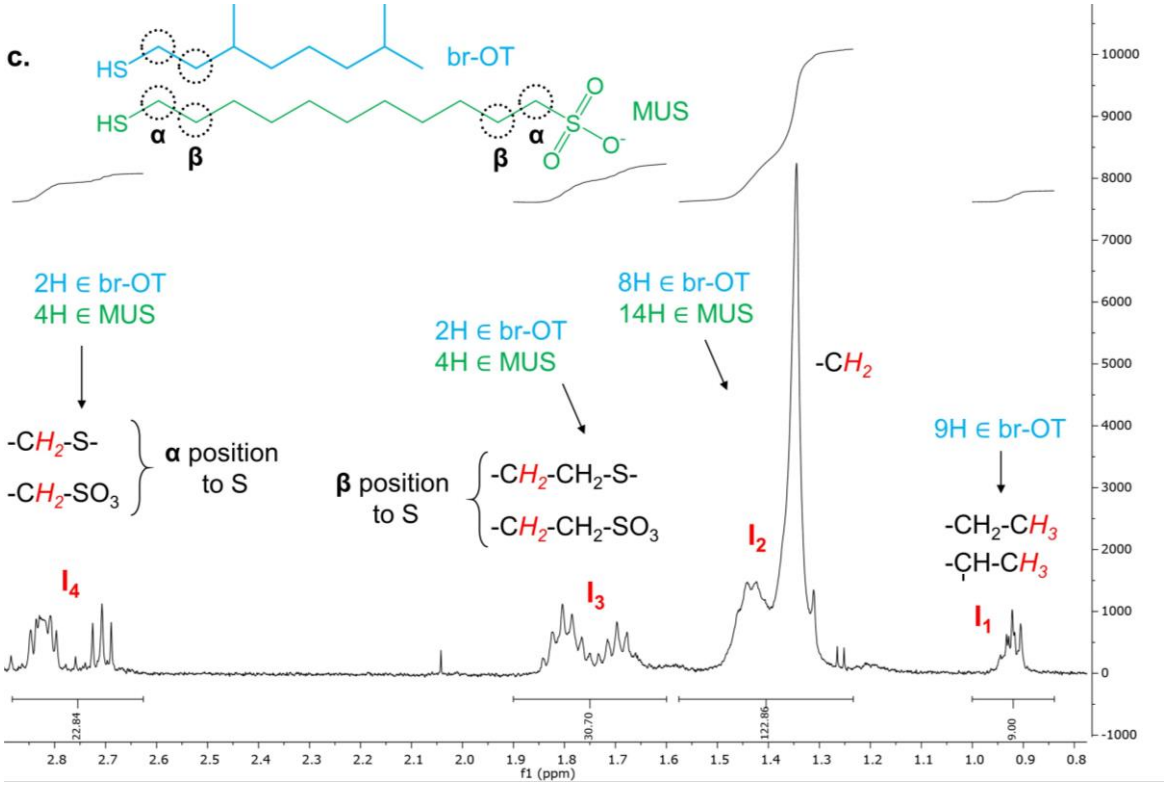

Figure 52. Expansion of ^{1}H NMR spectra (with corresponding peak assignment) of iodine-etched **a**) MUS:OT, **b**) TMA:OT, and **c**) MUS:br-OT AuNPs obtained via thiol-for-OAm ligand exchange. Mixed monolayers contain, respectively, 34 % OT % (I_2: 35.3 %, I_3: 31.8 %, I_4: 33.7 %), 20 % OT % (I_2: 18.7 %, I_3: 20.4 %), and 13 % br-OT % (I_2: 10.9 %, I_3: 12.2 %, I_4: 16.1 %). In solution, the corresponding feed % of the hydrophobic thiol (mol %) was 45 %, 75 %, and 45 %, respectively.

Details on ligand ratio calculation. All peaks assignments were made on the basis of chemical shifts (ppm). In the case of OT-containing NPs, 3 is the number of protons giving rise to the peak at ~0.9 ppm, since it corresponds to the terminal methyl group (–CH_3) of OT. The integral value of this signal is referred to as I_1. When br-OT takes the place of OT, this peak corresponds to 9 protons (3 methyl groups due to two additional branches). As reported in each spectrum, the other peaks (with overall integral values I_2, I_3, and I_4) are assigned to protons of either the hydrophobic or the ω-charged thiol. To calculate the relative OT (or br-OT) mol % in the amphiphilic monolayer, it is necessary to normalize I_1 to 3 (or 9) and apply the following equations[285,287]:

$$OT\ \% = \frac{1}{\frac{I_2 - 10}{14} + 1} \cdot 100 \qquad (11)$$

$$br\text{-}OT\ \% = \frac{1}{\frac{I_2 - 8}{14} + 1} \cdot 100 \qquad (12)$$

$$OT\ \% \text{ or } br\text{-}OT\ \% = \frac{1}{\frac{I_3\ (or\ I_4) - 2}{4} + 1} \cdot 100 \qquad (13)$$

These calculations assume that there is one arbitrary unit of OT (or br-OT) in the system. At least two of the previous equations were applied to each spectrum and the

molar yield (%) of the hydrophobic thiol was calculated as the average of the results. When uncertainties on average values are reported (Table 5, Section 3.2.1), NMR analysis was repeated on separately weighed NP samples; Student's statistics was then applied assuming a confidence level of 95 %.

Finally, NMR characterization was also performed on iodine-etched all-MUS and all-TMA AuNPs (Figure 53).

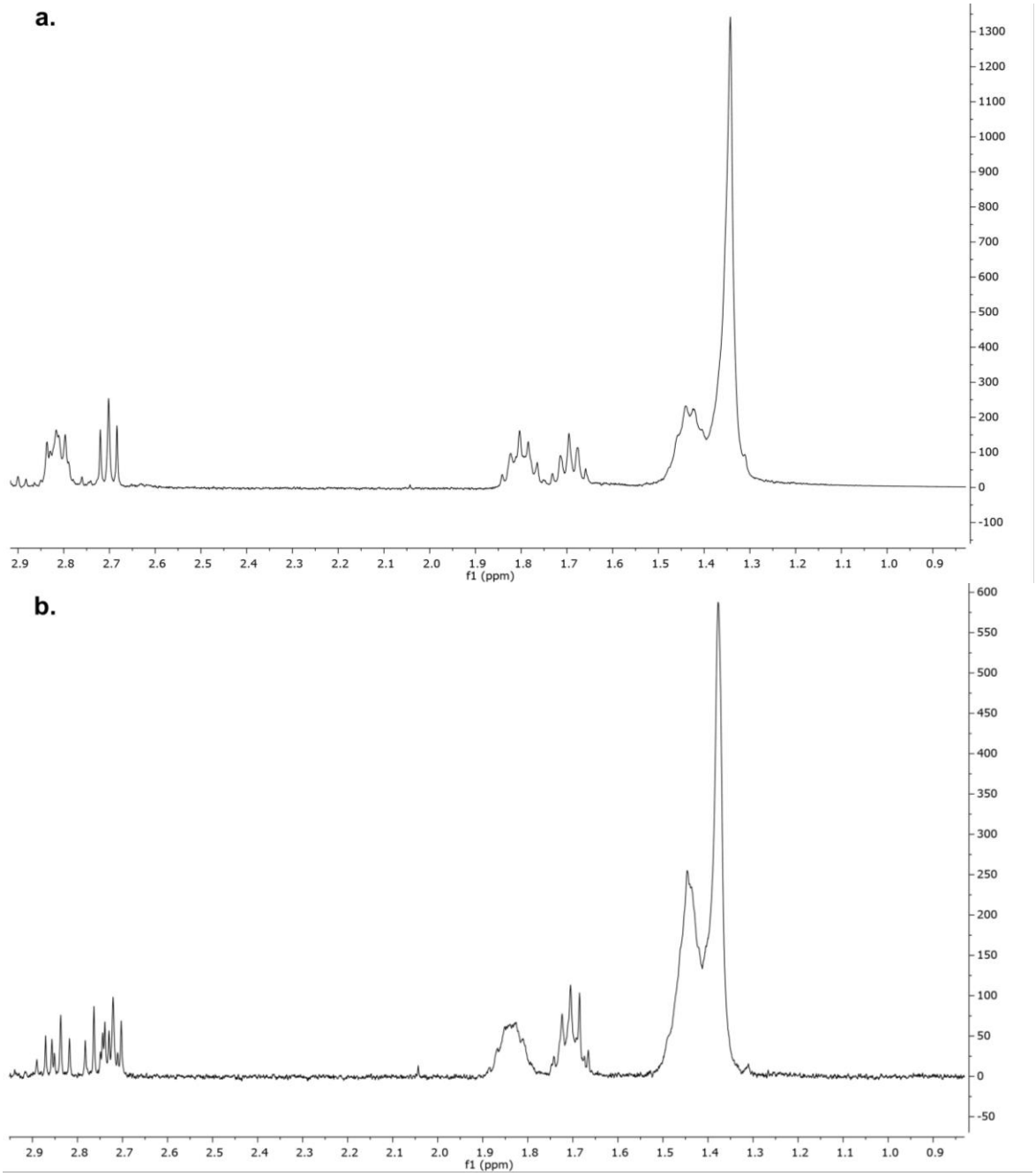

Figure 53. Expansion of ^{1}H NMR spectra of iodine-etched **a**) all-MUS, and **b**) all-TMA AuNPs obtained via thiol-for-OAm ligand exchange of the same OAm-capped precursor. As expected, no methyl ($–CH_3$) peak at ~0.9 ppm was detected in both cases indicating the presence of the hydrophobic thiol. Peak assignments of MUS and TMA ligands are the same as in Figure 52.

Appendix B – Model membranes

Within this thesis, two types of model membranes have been considered, i.e. lipid vesicles and supported lipid bilayers (SLBs). The latter were obtained via vesicle fusion onto a hydrophilic solid substrate, i.e. mica or silicon for AFM measurements and silica (SiO_2) for QCM experiments (Figure 16b, Section 1.3.6). Appendix B contains all protocols used for vesicle preparation and characterization. In general, vesicle preparation was based on the thin-film hydration method illustrated in Figure 16a. Protocols used for SLB formation are included in the description of AFM and QCM-D sample preparation, which is addressed in Appendices C1 and C2.

As for NP synthesis and characterization (Appendix A), when used, water was always purified with a Milli-Q ultrapure water system.

B1) Preparation of unilamellar lipid vesicles

Materials. Figure 54 illustrates the chemical structure of the membrane lipids used to prepare model lipid membranes.

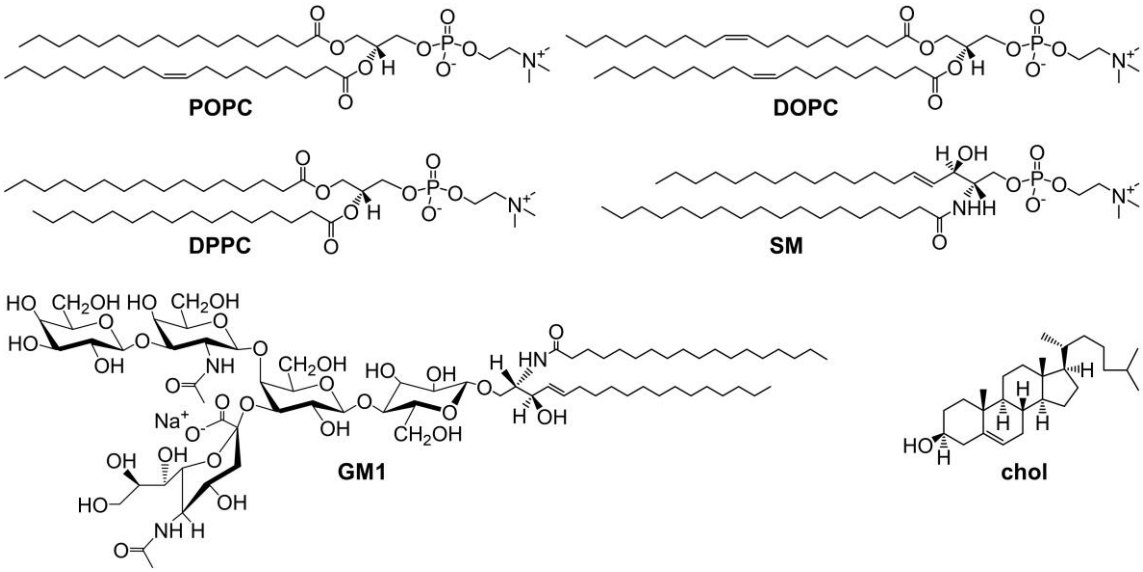

Figure 54. Chemical structures of the lipids used to prepare biomimetic membrane models.

1-palmitoyl-2-oleoyl-*sn*-glycero-3-phosphocholine (POPC, 16:0-18:1 PC, > 99 %), 1,2-dioleoyl-*sn*-glycero-3-phosphocholine (DOPC, 18:1(Δ9-Cis) PC, > 99 %), 1,2-dipalmitoyl-*sn*-glycero-3-phosphocholine (DPPC, 16:0 PC, > 99 %), sphingomyelin (SM, porcine brain, > 99 %), and ganglioside GM1 (ovine brain, sodium salt, > 99 %)

were purchased as lyophilized powders from Avanti Polar Lipids. Cholesterol (chol, ≥ 99 %, lyophilized powder), 2-[tris(hydroxymethyl)methylamino]-1-ethanesulfonic acid (TES, ≥ 99 %), L-histidine (≥ 99 %), ethylenediaminetetraacetic acid disodium salt (EDTA, 99 %), sodium chloride (≥ 99.5 %), 1,6-diphenyl-1,3,5-hexatriene (DPH, 98 %), (1-(4-trimethylammoniumphenyl)-6-phenyl-1,3,5-hexatriene (TMA-DPH, ≥ 96.0 %), chloroform ($CHCl_3$, ≥ 99.5 %), methanol (CH_3OH, ≥ 99.9 %), Sephadex® G-50 (fine powder), 3-(trimethylsilyl)propionic-2,2,3,3-d_4 acid sodium salt (TMSP, 99 %), phosphate buffered saline (PBS, 1x, pH 7.4), and deuterated solvents were purchased from Sigma Aldrich. Calcein (Merck, ≥ 96 %) was purchased from VWR International PBI. All chemicals were used without further purification.

Zwitterionic lipid vesicles. Monocomponent zwitterionic lipid vesicles were prepared from POPC (Figure 54) and used in the fluorescence assays and QCM-D measurements described in Chapter 4. Lyophilized POPC was weighed in a glass vial, dissolved in $CHCl_3$, and divided into aliquots. Lipid solutions were gently dried under a stream of nitrogen (N_2) to form homogeneous thin films, which were put under vacuum in a desiccator for ca. 24 h to remove residual solvent. For membrane leakage assays, POPC films were hydrated at a lipid concentration of 1 mg/mL in a 175 mM calcein, 2 mM histidine, 2 mM TES buffer solution (adjusted to pH 7.4 using NaOH and HCl). This calcein concentration is self-quenched. Hydration was made easier by employing a bath-type sonicator for 10 min to form multilamellar lipid vesicles. Sonication is also helpful to promote the incorporation of all the lipid within the membrane. The multilamellar dispersion was then sonicated with a probe-type sonicator under N_2 at room temperature for 15 min to obtain small unilamellar vesicles. To remove large lipid aggregates and titanium impurities (the latter derived from the sonicator probe), the vesicle preparation was centrifuged for 10 min at 11500 g. Additional unilamellar calcein-loaded vesicles with larger diameter were prepared using the Avanti Mini-Extruder (Avanti Polar Lipids) illustrated in Figure 55a-b. In this case, after the hydration step in the ultrasonic bath, the lipid suspension was passed through a polycarbonate membrane (100 nm pore diameter) 11 times at room temperature (Figure 55b-c). Sonicated and extruded calcein-loaded vesicles were separated from the non-encapsulated dye by gel filtration using the minicolumn centrifugation technique[268,269]. Minicolumns (1.0 cm × 10 cm; Pierce) were filled with Sephadex® G-50 swollen in a 2 mM histidine, 2 mM TES, 100 mM NaCl, 1.0 mM EDTA buffer solution (adjusted to pH 7.4) and centrifuged twice for 1 min at 3000 g to remove the excess buffer from the gel filtration medium. The vesicle preparation was then divided into aliquots of 100 µL per column and filtered by centrifugation at 3500 g for 1 min. The lipid concentration after vesicle filtration was determined by

^{1}H NMR, as described in the following section. For QCM-D measurements reported in Chapter 4, sonicated calcein-free POPC vesicles (3 mg/mL) were prepared using the 2 mM histidine, 2 mM TES, 100 mM NaCl, 0.1 mM EDTA buffer instead of the self-quenched calcein solution. All vesicle suspensions were stored at 4 °C and used within a few days; in the presence of calcein, vesicle batches were protected from light before use.

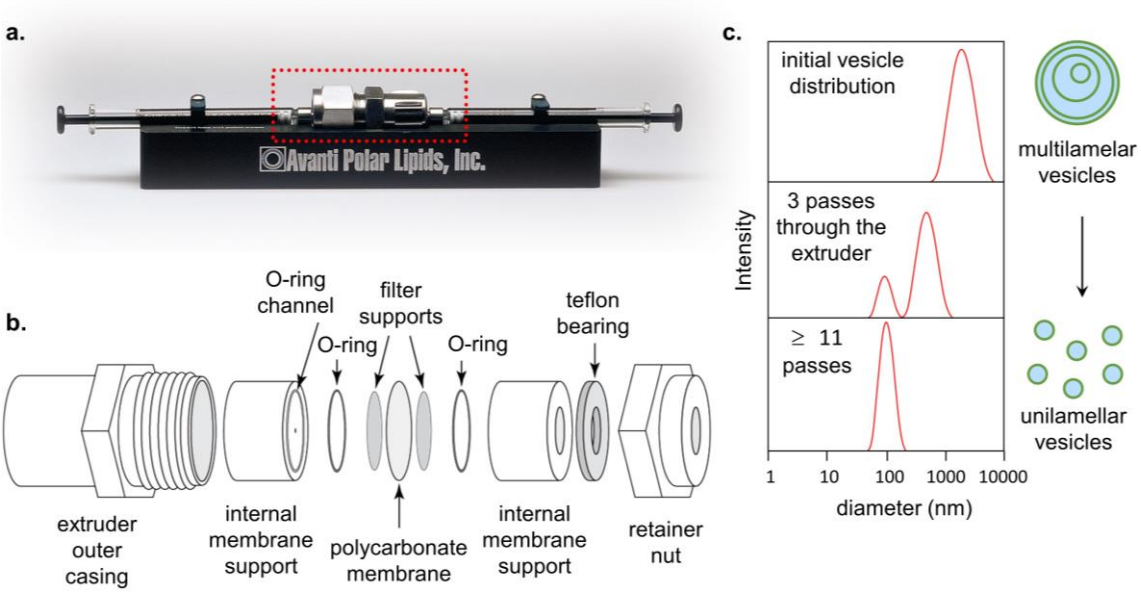

Figure 55. a) Avanti Mini-Extruder kit commercialized by Avanti Polar Lipids; **b**) central extruder unit framed in (**a**) shown in its single components. Within this thesis, 100 nm pore size polycarbonate membranes (Nuclepore filters, Whatman) were used for all extrusions. **c**) Using this preparation technique, the size distribution of final vesicles depends on the number of passes through the extruder membrane. In general, at least 11 passes are performed to obtain homogeneous suspensions of monodisperse unilamellar vesicles. Images (**a**) and (**b**) are taken from *avantilipids.com*.

Lipid concentration after gel filtration of zwitterionic vesicles. The phospholipid content in vesicle samples after the minicolumn filtration (see the previous section) was quantified by ^{1}H NMR following with minor modifications the procedure reported by Hein et al.[386]. This analysis was performed with the contribution of Dr. Chiara Lambruschini (DCCI, University of Genoa). TMSP (0.00 ppm) was used as internal standard. 200 μL of vesicle solution was directly mixed with 430 μL CD_3OD, 100 μL $CDCl_3$, and 15 μL 5.9 mM TMSP in D_2O in a 5 mm NMR tube. After mixing, a clear and homogeneous solution was obtained and directly analyzed. After integration, the concentration of phospholipid was calculated and resulted to be 1.15 mM (0.9 mg/ml) of POPC. This concentration was diluted before the following leakage assays (Appendix D1).

Details on concentration calculation. (H)PRESAT parameters: from –2.0 to 14.0 ppm spectral window, presaturation of H_2O peak (δ 4.6 ppm), 256 scans, 3.0 s

relaxation delay. Post-acquisition processing was performed with MestReNova (Mestrelab research v. 11.0): manual phase correction, 264 k zero filling, 3rd order polynomial baseline correction, apodization LB=1.0 Hz, and manual integration. Peak assignments were made on the basis of chemical shifts. The following equation was employed to calculate the concentration of phospholipid:

$$C_{PL} = \frac{3 \cdot C_{Std} \cdot V_{Std} \cdot I_{PL}}{2 \cdot V_{PL} \cdot I_{Std}} \quad (14)$$

where: C_{PL} is the final concentration of phospholipid (mM), C_{Std} is the concentration of TMSP (mM), V_{PL} is the volume of phospholipid (µL), V_{Std} is the volume of TMSP (µL), I_{PL} is the integral value of terminal CH_3 of phospholipid (δ 0.90 ppm) and I_{Std} is the integral value of TMSP (δ 0.00 ppm).

Multidomain lipid vesicles. Vesicles showing lateral lipid phase separation – commonly referred to as multidomain vesicles – were used in the AFM and QCM-D measurements described in Chapter 5. Multidomain vesicles were prepared from three lipid mixtures spontaneously exhibiting ordered – disordered phase immiscibility: DOPC:SM:chol:GM1 63:31:1:5[320], DOPC:SM:chol 66:33:1[320], and DOPC:DPPC:chol 40:40:20[322] (Figure 54). All compositions are reported as molar ratios and are referred to as M1, M2, and M3, respectively. Briefly, stoichiometric quantities of the lipid components – previously dissolved in $CHCl_3$:CH_3OH (2:1, v/v) – were mixed, gently stirred for a few minutes to promote homogenization, and then dried under a gentle N_2 flux. The solvent evaporation was performed at 60 °C, above the transition temperature of all the lipids in the mixture. The dried lipid film was stored one day under vacuum and resuspended in water at a lipid concentration of 0.5 mg/mL. For QCM-D measurements, the film was hydrated to a lipid concentration of 1 mg/mL in PBS to help the merging of the vesicles on the sensor of the QCM-D chamber (Appendix C2)[387]. All lipid suspensions were first sonicated in an ultrasonic bath for 15 min at 60 °C and thereafter extruded 11 times at the same temperature to form unilamellar vesicles. Extrusion was performed using the Avanti Mini-Extruder reported in Figure 55. All vesicle suspensions were stored at 4 °C and used within a few days. The morphology of the lipid phase separation in multidomain membranes was characterized by AFM imaging after SLB deposition; results are reported in Figure 34 (Section 5.3.2).

Lipid vesicles with progressive bilayer stiffening. Lipid vesicles with varying membrane fluidity were used in the fluorescence assays and AFM and QCM-D measurements described in Chapter 6. Samples were prepared at room temperature by adding increasing amounts of cholesterol to fluid membranes composed of DOPC

(Figure 54). As described in Section 1.3.4, the incorporation of cholesterol within lipid bilayers consisting of unsaturated lipids reduces membrane fluidity. Briefly, lyophilized DOPC was weighed in a glass vial, dissolved in $CHCl_3$:CH_3OH (2:1, v/v), and divided into aliquots. Stochiometric amounts of cholesterol – previously dissolved in the same solvent mixture – were added to DOPC aliquots to set the chol mol % to 17, 30, 33, 40, 50, 60 %. After gently mixing for a few minutes to homogenize each sample, the solvent was evaporated under a stream of N_2. Residual $CHCl_3$:CH_3OH traces were removed under vacuum for ca. 24 h. The lipid films were then hydrated at a lipid concentration of 2 mg/mL in PBS. To ensure that all the lipid was incorporated within the membrane and to promote the formation of multilamellar vesicles, hydrated samples were subjected to a brief period (ca. 15 min) of sonication at room temperature in an ultrasonic bath. Subsequently, each lipid suspension was extruded 19 times at room temperature (Figure 55). In the case of fluorescence anisotropy assays, the fluorescent labeling of the bilayer was obtained by adding small aliquots of DPH and TMA-DPH probes to DOPC/chol organic mixtures. The probe-to-lipid molar ratio was set to 1:1000[388] and 1:500[389], respectively. Highly concentrated stock solutions of the probes were previously prepared in $CHCl_3$:CH_3OH (2:1, v/v). Such relatively low DPH and TMA-DPH molar fractions were chosen to yield adequate signal to noise ratio and avoid any probe-induced perturbation of the bilayer structure. Upon hydration of labeled lipid films, both fluorophores are known to readily separate from aqueous dispersions to intercalate into the lipid bilayer, accompanied by strong fluorescence enhancement[390]. The amount of probe partitioning in water solution was considered negligible due to the high lipid-water partition coefficient (K_p) of DPH and TMA-DPH ($K_p=1.3\cdot10^6$ and $2.4\cdot10^5$, respectively[391]) and to the low probe-to-lipid molar ratio used in vesicle preparation. All vesicle suspensions were stored at 4 °C and used within a few days; batches containing fluorescent probes were also protected from light till further use.

Estimated cholesterol content into the extruded DOPC bilayer. The vesicle phospholipid:chol composition is not equal to the lipid ratio before film hydration. Indeed, the actual cholesterol content in the vesicle bilayer is always lower than the nominal content added in solution, and in general, the gap between the two values increases with increasing cholesterol. A robust and accurate determination of the *de facto* cholesterol content in DOPC/chol vesicles extruded as in this thesis was reported by Goñi et al.[392] Based on the incorporation efficiency derived from data of ref.[392] – determined in the 0÷67 mol % chol range – the cholesterol content of vesicles used in Chapter 6 was estimated as reported in Table 10. These estimated cholesterol

mol % are reported in Chapter 6 and in Appendix B2 instead of the nominal values used in vesicle synthesis.

Table 10. Average estimated cholesterol content in DOPC/chol vesicles extruded using Nuclepore filters (0.1 μm pore diameter) at room temperature and pH 7.4. According to ref.[392], the standard deviation relative to estimated concentrations is within 15 % of the mean value.

Nominal mol % chol	*Estimated mol % chol*
17	15
30	26
33	29
40	35
50	43
60	52

B2) Characterization of unilamellar lipid vesicles

DLS and ζ-potential. DLS and ζ-potential measurements were performed at room temperature using a Malvern Zetasizer Nano ZS instrument with a 173° detection angle (Malvern Instruments). All measurements were carried out right after extrusion or probe-type sonication, without diluting final vesicle suspensions (Appendix B1). The vesicle hydrodynamic diameter was assessed by DLS from number distributions; size results are reported in Table 11 and Figure 56. In the case of zwitterionic POPC vesicles and M1 multidomain vesicles, additional ζ-potential measurements were performed to characterize the vesicle surface potential before experiments with NPs. The ζ-potential was −5.5 ± 0.4 mV (experimental buffer, pH 7.4) and −64 ± 3 mV (water) for POPC and M1 vesicles, respectively; uncertainties on average values were obtained using Student's statistics, assuming a confidence level of 95 % (n=9).

Table 11. Hydrodynamic diameters (nm) of freshly prepared unilamellar lipid vesicles measured by DLS. Uncertainties on average values were obtained using Student's statistics, assuming a confidence level of 95 % (n=12).

Model		*Lipid composition (molar ratio)*	*Probe-type sonicated vesicles*	*Extruded vesicles*
Zwitterionic vesicles [a]		POPC	23 ± 2 nm	105 ± 6
Multidomain vesicles [b]	M1	DOPC:SM:chol:GM1 63:31:1:5	only extruded	108.7 ± 1.4
	M2	DOPC:SM:chol 66:33:1	only extruded	102.8 ± 0.7
	M3	DOPC:DPPC:chol 40:40:20	only extruded	101.8 ± 0.5
Vesicles with progressive bilayer stiffening [c]		DOPC:chol 100:0÷48:52	only extruded	Figure 56

[a] in the experimental buffer (pH 7.4) after gel filtration (Appendix B1).
[b] in water.
[c] in PBS (1x, pH 7.4).

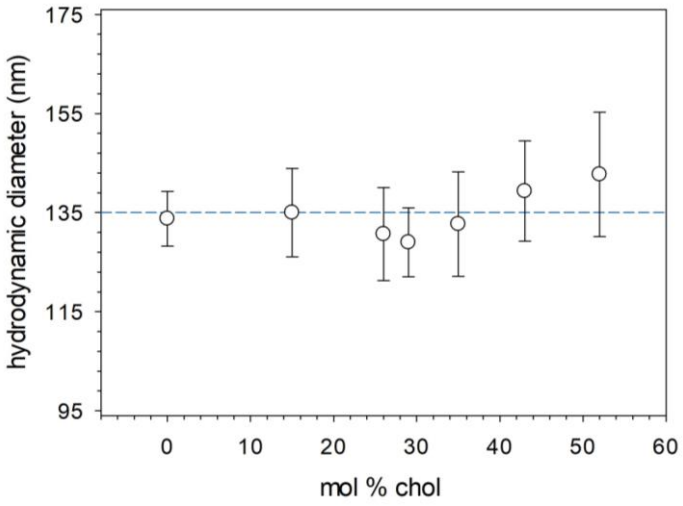

Figure 56. Hydrodynamic diameters (nm) of lipid vesicles composed of DOPC and increasing amounts of cholesterol (final size range: 129÷142 nm). Single diameters were averaged over all vesicle preparations in PBS used for fluorescence and QCM measurements (Chapter 6). Given the copious amount of prep and data, error bars refer to the standard errors.

Appendix C – AFM and QCM-D

AFM and QCM-D investigations of the NP-membrane interaction were performed for the projects described in Chapters 5 and 6, in which multidomain bilayers and bilayers with progressive membrane stiffening were studied, respectively. QCM-D measurements were also carried out for the project reported in Chapter 4, where zwitterionic POPC membranes were employed.

When indicated, phosphate buffered saline (PBS) 1x at pH 7.4 and water purified with a Milli-Q ultrapure water system (see Appendix A) were used.

C1) AFM: sample preparation and measurements

AFM analysis. AFM investigation was performed in liquid using two microscopes: 1) a Multimode SPM equipped with "E" scanning head (maximum scan size 15 μm) and driven by a Nanoscope V controller (Digital Instruments-Bruker), and 2) a Nanowizard III AFM (JPK Instruments) mounted on an Axio Observer D1 inverted optical microscope (Carl Zeiss). In these microscopes, the scanning mechanism is attached to the sample stage and the probe holder, respectively (Section 2.1). In all experiments, V-shaped silicon nitride cantilevers (DNP-10, cantilever C, Bruker) were used (nominal spring constant: 0.24 N/m; drive frequency in liquid: 12-14 kHz; 0.5-1.5 Hz scan rate). All AFM measurements were performed at room temperature.

- In *Chapter 5*, AFM imaging in liquid (tapping mode, Bruker Multimode) was performed to study both the morphology of multidomain SLBs and the effect of amphiphilic NPs on the membrane lateral phase separation.

- In *Chapter 6*, contact-based QI™ in liquid (Nanowizard, JPK) was exploited to map the Young's modulus of SLBs with progressive membrane stiffening. Additional imaging (Nanowizard, JPK) was performed in tapping mode to obtain topographic images at higher resolution. All AFM measurements reported in this chapter were performed in the absence of NPs.

For the QI characterization of model membranes discussed in Chapter 6, QI images (5 × 5 μm^2 scan size) based on 128 × 128 force curves were collected after cantilever calibration with the thermal noise method (Section 2.1)[245,393]. Very short force curves, with low tip-sample interaction, were acquired for each scan point to obtain small

bilayer indentations (setpoint or loading force: 0.6 nN; Z length: 50 nm; speed 10 µm/s; data acquisition rate: 200 kHz; extend/retract time: 2 ms). These parameters are also recommended to minimize tip contamination by the lipid and preserve the tip and the sample from damage. A typical force spectroscopy experiment is illustrated in Figure 57. The Young's modulus of SLBs was determined by fitting the force *vs* tip-sample separation curves (one for each pixel) with the well-known Hertz model described in ref[247] (JPK application note) (Equations 15-18 and Figure 57). The Hertz model is valid only for small indentations that do not exceed ~20 % of the sample thickness; it is commonly used in the case of spherical indenters and biological samples[394].

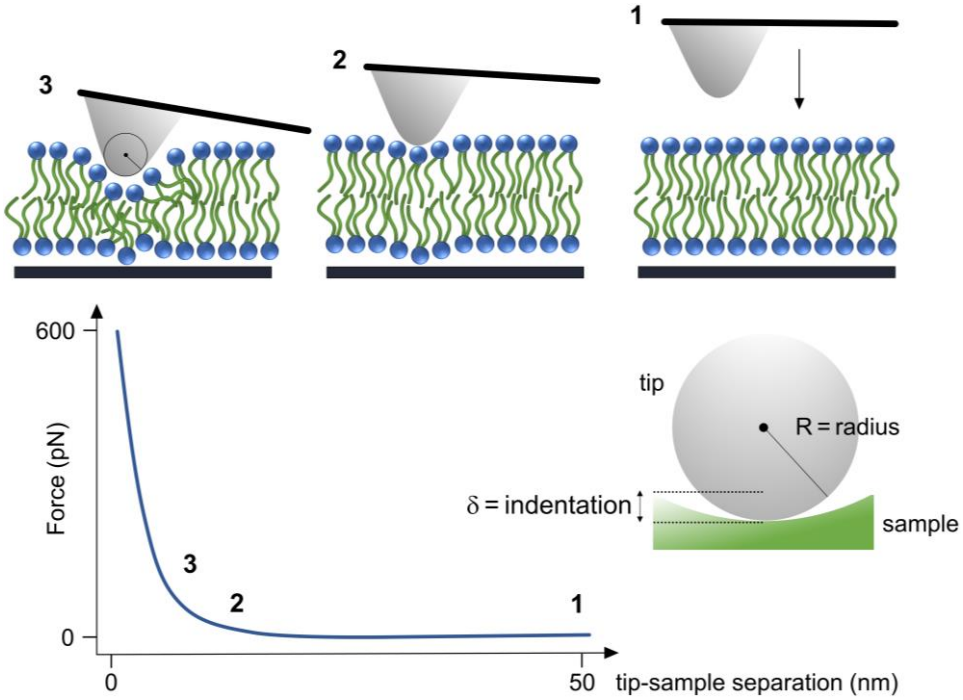

Figure 57. Cartoon (not to scale) illustrating a typical force spectroscopy experiment used in this thesis on SLBs: **1.** the tip and the SLB are not interacting, **2.** the bilayer is elastically deformed by the AFM tip until **3.** the loading force (i.e. the setpoint) is reached. After step 3, the tip is retracted to the initial position 1 for the next curve acquisition (in contact-based QI imaging, this experiment is repeated for each scanned point). Since the Young's modulus describes the linearity between stress and strain in the elastic regime, the setpoint is kept much lower than the breakthrough force (which is typically of several nN). During the breakthrough event, the tip indents the bilayer and comes into contact with the substrate; such event marks the onset of the bilayer plastic deformation regime[395].

$$F = \frac{E}{1-\nu^2}\left[\frac{(a^2+R^2)}{2}\, ln\left(\frac{R+a}{R-a}\right) - aR\right] \quad (15)$$

$$\delta = \frac{a}{2} ln\left(\frac{R+a}{R-a}\right) \quad (16)$$

$$a = \sqrt{R\delta} \quad (17)$$

$$\delta = -d(t) \text{ for } d \leq 0 \quad (18)$$

where: F is the indenting force, E is the Young's modulus, ν is the Poisson ratio (0.5 in this case), a is the contact radius, R is the probe radius, δ is the indentation, and $d(t)$ is the instantaneous tip-sample separation.

AFM data analysis was performed as follows:

- *Chapter 5*. All mean height differences (Δz) were calculated counting at least 200 values on 5 different AFM images using NanoScope 7.30 software; a similar analysis was applied for the NP–NP horizontal distance (Δx_{NP-NP}) shown in Figure 39c. Average domain circularity reported in Table 6 was calculated by counting with ImageJ software a few hundred area and perimeter values of ordered domains from AFM images[328].

- *Chapter 6*. The Young's modulus of lipid bilayers was calculated using the JPK Data Processing software. At least 3 QI images were collected for each lipid composition. The AFM tip was approximated to a sphere with a curvature radius of 20 nm (Figure 57); results were averaged on at least 30000 curves (Figure 42c,e).

NOTE: in general, AFM data are reported as mean value ± standard error. It is specified if standard deviation is used instead of standard error.

AFM samples without amphiphilic NPs. SLBs without NPs were deposited either on mica (Chapter 5) or silicon (Chapter 6) via fusion of lipid vesicles prepared in water and in PBS, respectively (Appendix B1).

Chapter 5. For each bilayer, a diluted suspension of multidomain lipid vesicles (40 μL, 0.1 mg/mL) and a fresh $CaCl_2$ solution (10 μL, 10 mM) were deposited onto an approximately 1.0 × 1.0 cm^2 freshly cleaved mica foil glued on metal support (the latter is required to magnetically fix the sample to the Bruker Multimode sample stage).

Chapter 6. Vesicles with varying cholesterol content (40 μL, 0.1 mg/mL) were deposited onto plates of silicon wafer of similar size (in this case attached to a glass slide) in the absence of Ca^{2+}. In the presence of PBS, vesicle fusion onto silicon occurs without the need for bivalent ions.

In all cases, after vesicle deposition samples were first stored for 10 min at room temperature and then incubated for 15 min at 60 °C in a close chamber at 100 % relative humidity. During this time, vesicles merge on the hydrophilic substrate to

form a homogeneous and defect-free SLB. SLBs were then let to cool down at room temperature and finally gently rinsed with water. This step was necessary to remove non-deposited vesicles from the liquid that may interfere with AFM measurements. AFM imaging usually started at least two hours after rinsing to let the system to equilibrate.

AFM samples with amphiphilic NPs. The NP-membrane interaction was studied by AFM only in the case of multidomain bilayers deposited on mica (Chapter 5). All AFM samples containing amphiphilic NPs were prepared using a 0.12 mg/mL (1.2 μM) filtered stock solution of one-phase MUS:OT AuNPs (Appendix A1). As illustrated in Figure 58, NPs were let to interact with the multidomain bilayer following two different procedures: the incubation and the pre-incubation method.

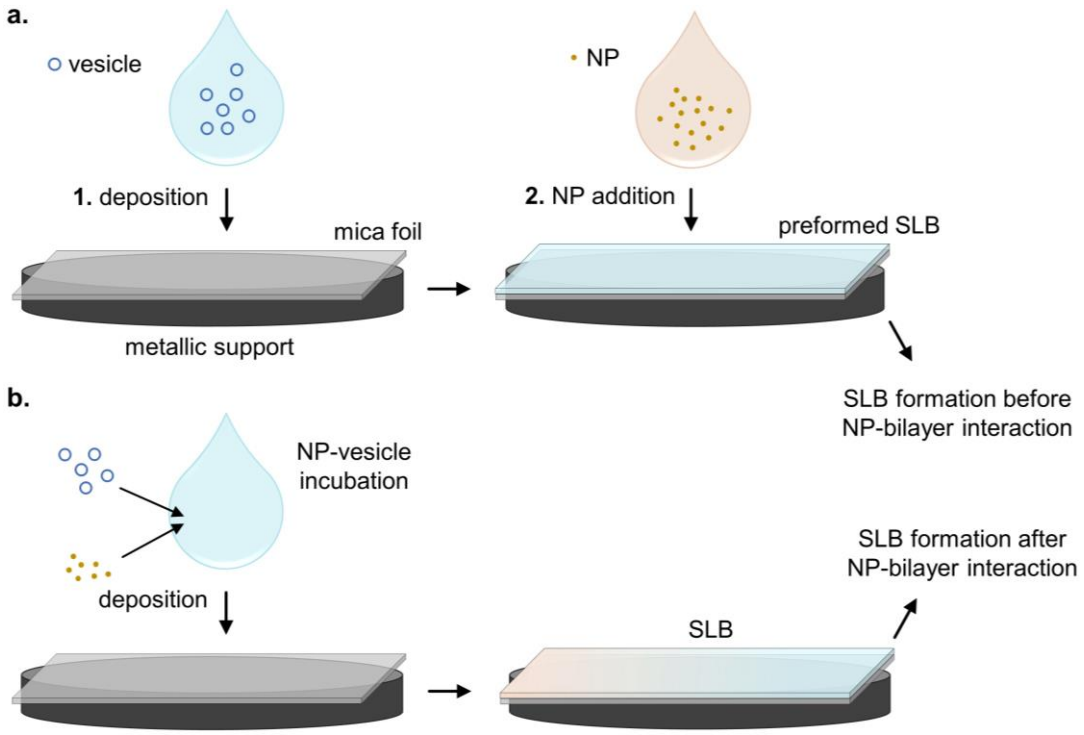

Figure 58. AFM samples containing NPs were prepared in water following two protocols: **a**) the incubation and **b**) the pre-incubation method. In (**a**), NPs were incubated on a preformed multidomain SLB deposited onto a freshly cleaved mica foil. In (**b**), NPs were pre-incubated with multidomain lipid vesicles before their deposition on mica and subsequent SLB formation. NP-vesicle pre-incubation always occurred at room temperature and in the absence of stirring. Image by Canepa et al.[2] (published by The Royal Society of Chemistry) licensed under CC BY-NC 3.0 (changes were made).

- In the *incubation method* (Figure 58a), the first used, a drop of NP dispersion was cast onto a preformed multidomain SLB obtained as described above. The bilayer was rinsed with water immediately before NP addition and no second rinse was carried out before AFM investigation. Different NP volumes were

tested (10-20-40 μL). Each bilayer was observed either shortly after the addition of NPs or after several hours.

- In the *pre-incubation method* (Figure 58b), which was developed later, multidomain vesicles (40 μL, 0.1 mg/mL) and NPs (20 μL) were pre-incubated for different times (10 min and 4 h) before their deposition on mica and $CaCl_2$ addition. Each SLB sample prepared with this protocol was rinsed a few hours before AFM investigation.

With both methods, NPs were let to interact with the multidomain membrane before AFM imaging. In the first method, NPs interact directly with a supported planar membrane, whereas in the second case the interaction takes place in the presence of the curved and free-standing membrane of the vesicle, without any constraints from the substrate[218].

NOTE: the same methods shown in Figure 58 were variably applied to prepare NP-containing samples for the QCM-D investigations reported in Chapters 4 and 5.

Details on NP molecular weight calculation. To calculate the lipid/NP ratio reported in Section 5.3.2, the mean NP molecular weight (MW) was estimated considering an Au density of 34.377 atoms/nm^3 and a ligand density of 4.775 molecules/nm^2. These values derive from the NP model reported by Lopez-Acevedo et al.[396], which considers a NP with a 2 nm diameter, a core of 144 Au atoms in icosahedral symmetry, and 60 S atoms bonded on its surface – i.e. $Au_{144}(SR)_{60}$. In the case of one-phase MUS:OT AuNPs used in Chapter 5 – 2.7 nm mean core diameter and 4:1 ligand molar ratio – the MW_{NP} is 96279 g/mol.

C2) QCM-D: sample preparation and measurements

QCM-D analysis. QCM-D measurements were carried out in liquid using a QCM-Z500 microbalance (KSV Finland LLC) equipped with a thermostated flow chamber to characterize the NP uptake by model membranes. QCM-D investigation was based on two different lipid systems:

- in *Chapters 4 and 5*, vesicles were deposited onto the surface of a SiO_2-coated crystal sensor where they rapidly merge to form a homogeneous SLB[305,397];

- in *Chapter 6*, vesicles were deposited onto the surface of a gold-coated crystal sensor where they accumulate but do not rupture. In this way, a supported

vesicle layer (SVL) was formed[257]. Vesicular monolayers can form on gold surfaces, but not on SiO_2[398].

Both sensor types contain a AT-cut disk-typed quartz crystal with standard resonance frequency of 5 MHz, a sensitivity coefficient (C_f) of 17.7 ng/(cm²·Hz) (Sauerbrey equation, Section 2.2), and a piezoelectrically active surface of 78.5 mm². Before usage, the sensors were subjected to UV/Ozone for at least 10 min. For all experiments, the monitoring of higher (3rd-11th) overtones was carried out at a sampling rate of 1 s; when overnight acquisitions were performed, a point average every 10 s was recorded. For all QCM-D results shown within this thesis, frequency and dissipation traces are reported only for one overtone, which is specified in the caption of each figure (the most stable among overtones was considered).

QCM-D data analysis was performed as follows:

- *Chapters 4 and 5 (SLB formation)*. QCM-D results based on SLB formation were interpreted in the assumption of acoustically rigid film formation (see Figure 19c, Section 2.2) and the Sauerbrey equation (Equation 2, Section 2.2) was used to calculate the mass per unit area adsorbed onto the sensor surface after normalization of the frequency shifts (i.e. $\Delta f/n$, where n is the overtone number)[399].

- *Chapter 6 (SVL formation)*. QCM-D results based on SVL formation were processed in the assumption of a modified Sauerbrey model to include the viscoelasticity of the deposited layer. In particular, frequency shifts entered in the Sauerbrey equation (Equation 2, Section 2.2) were not normalized by n, which is typical for rigid films, but by $\sqrt{n}$, which is typical for viscoelastic films. Overall, this model assumes that the shift in resonant frequency (Δf) during the NP-membrane interaction is attributed solely to changes in mass on the sensor surface. Such data processing, which only considers Δf, was validated by comparing the results with a more complicated viscoelastic modeling. As explained in Section 2.2, information on membrane viscoelastic properties can be derived considering also the variation in energy dissipation (ΔD)[400]. In particular, the thickness (nm) and density (kg/m³) of SVLs before and after interaction with NPs were determined by fitting experimental Δf and ΔD data (from at least 2 harmonics) to the Voigt model included in the KSV QCM Impedance Analyzer Software. A thorough describtion of the Voigt theory is provided in ref[256]. The mass per unit area adsorbed onto the sensor surface

after SVL formation and after NP addition was then derived from thickness and density data.

The KSV QCM-Z500 measurement principle is based on the impedance analysis of the quartz crystal. In turn, the model included in the software of this instrument (used to obtain the thickness and density of SVLs) is based on the concept that, with a viscoelastic film of finite thickness, the surface mechanical impedance associated to the QCM-D circuit is given by the following equation:

$$Z_s = \sqrt{G\rho_f}\tanh(\gamma h_f) \tag{19}$$

$$\gamma = \sqrt{\frac{j\omega\rho_f}{G}} \tag{20}$$

where: G is the complex shear modulus (G=G'+jG", with G'=storage modulus and G"=loss modulus), ρ_f is the film density, γ is the complex wave propagation constant, h_f is the film thickness, and ω=2πf where f is the frequency. Details on the software elaboration to fit ρ_f and h_f data are reported in the QCM-Z500 operation manual.

In general, for each QCM-D experiment reported in this thesis at least two replicates were performed. All uncertainties on mass values (Δm) were processed by averaging the overtones of different replicates and by applying the Student's statistics (95 % confidence level). Only for the SVL thickness and density values shown in Figure 44b (Chapter 6), error bars correspond to standard deviation.

QCM-D samples on SiO_2 (SLBs) without amphiphilic NPs. SLBs alone, in the absence of NPs, were prepared for the projects of Chapters 4 and 5.

Chapter 4. Before the deposition of POPC SLBs, the chamber and the access tubing to the chamber (pre-chamber) were filled with the experimental buffer (100 mM NaCl, 2 mM histidine, 2 mM TES, 0.1 mM EDTA, adjusted to pH 7.4) and let to equilibrate at 22 °C until the frequencies of all overtones were stable.

Chapter 5. In the case of multidomain SLBs, the same procedure was performed in PBS at 40 °C. This temperature was kept during the entire sample preparation to promote the formation of a homogeneous fluid-state SLB.

For both projects, a freshly extruded vesicle suspension was diluted in the corresponding buffer to a final concentration of 0.25 mg/mL. The vesicle suspension (2 mL) was then injected into the thermostated pre-chamber and let to equilibrate at

either 22 °C for 10 min (POPC vesicles, Chapter 4) or at 40 °C for 30 min (multidomain vesicles, Chapter 5). When all overtones were stable, the recording was started and the frequencies and dissipations of all overtones were set as baselines (i.e. frequency, f, and dissipation, D, zero values). After 300 s or 600 s, the diluted vesicle suspensions were injected in the chamber, carefully avoiding microbubble formation; in all cases, SLB formation began immediately after vesicle insertion (Figure 31b,c of Chapter 4 and Figure 36a,b of Chapter 5). Final SLBs were rinsed with fresh buffer thermostated at either 22 °C (for POPC bilayers) or 40 °C (for multidomain bilayers) to remove the excess of undeposited vesicles. In general, all SLBs deposited on SiO_2 showed high stability upon rinsing.

Only in the case of multidomain SLBs (Chapter 5), PBS was subsequently exchanged with water (thermostated at 40 °C) and the experimental temperature was finally set to 22 °C. These additional steps were applied to mimic the experimental conditions used for AFM analysis (Appendix C1).

QCM-D samples on SiO_2 (SLBs) with amphiphilic NPs. SLBs in the presence of amphiphilic NPs were studied by QCM-D in the projects of Chapters 4 and 5. In both cases, one-phase MUS:OT AuNPs were tested, while only in Chapter 4 also one-phase TMA:OT AuNPs were used (Appendix A1).

Chapter 4. QCM-D samples containing NPs were prepared following the pre-incubation method described in Figure 58b. Filtered NP dispersions were added to a POPC vesicle suspension (0.25 mg/mL) diluted in 100 mM NaCl, 2 mM histidine, 2 mM TES, 0.1 mM EDTA (pH 7.4) to reach a NP/lipid mass ratio, $R_m=\frac{m_{NP}}{m_{lip}}$, of 0.05. POPC/NP dispersions (2 mL) were then pre-incubated for ca. 4 h at room temperature without stirring. In the case of cationic TMA:OT AuNPs, the ionic strength of the buffer was changed after POPC/NP incubation to 200 mM NaCl, to allow vesicle fusion on the sensor[397]. As in the case of SLB preparation without NPs, before each measurement, the chamber and the pre-chamber were filled with the experimental buffer and let to equilibrate at 22 °C until the frequencies of all overtones were stable. After 10 min equilibration at 22 °C in the pre-chamber, each POPC/NP dispersion was injected into the QCM chamber and the SLB was rapidly formed (Figure 31). As for SLB formation in the absence of NPs, the buffer was then exchanged to remove vesicle excess from the chamber. No difference in the frequency signal was recorded before and after rinsing (Figure 31).

Chapter 5. One-phase MUS:OT AuNPs were added to the bilayer using both procedures described in Figure 58. The same 0.12 mg/mL filtered NP stock solution used for AFM investigation was employed for all QCM experiments (Appendix C1).

- *Incubation method.* After SLB formation and rinsing as described in the previous paragraph, a diluted NP water dispersion (2 mL, 0.03 mg/mL) was injected in the pre-chamber, let to equilibrate at 22 °C for 20 min, and then inserted in the QCM chamber. The NP-membrane interaction was then monitored for more than 18 h at 22 °C, at a sampling rate of 10 s; the solution containing excess NP was finally exchanged with fresh water to rinse the SLB (Figure 35g).

- *Pre-incubation method.* Before each measurement, the chamber and the pre-chamber were filled with PBS and let to equilibrate at 40 °C until the frequencies of all overtones were stable. Vesicles (500 μL, 1 mg/mL) and NPs (500 μL) were added to PBS (1 mL) to obtain final concentrations of 0.25 mg/mL and 0.03 mg/mL, respectively. Vesicles were pre-incubated with NPs for 4 h at room temperature before injection into the QCM pre-chamber. After equilibration for 30 min at 40 °C, the measurement was started, and vesicles were introduced into the QCM chamber. After vesicle fusion and SLB formation, PBS was exchanged with fresh buffer. No difference in the frequency signal was recorded before and after rinsing (Figure 36a,b).

QCM-D samples on gold (SVLs) without amphiphilic NPs. For lipid vesicles with varying cholesterol content (Chapter 6), the homogeneous SLB formation used in Chapters 4 and 5 proved unsuccessful because vesicles containing more than 20 mol % chol partially (and variably) remained intact on the SiO_2[401]. This behavior generated remarkable irreproducibility between measurements, with final $\Delta f/n$ values considerably higher than those expected for a typical SLB formation (i.e. ~25 Hz). Therefore, a new experimental set-up was adopted: lipid vesicles were deposited at 22 °C on Au to form a stable SVL which was then let to interact with amphiphilic AuNPs. For SVL formation, freshly extruded vesicle suspensions were diluted in PBS (0.25 mg/mL) and then inserted into the pre-chamber. After 10 min of equilibration at 22 °C, vesicle suspensions were injected into the QCM chamber. In general, SVL deposition was much slower than SLB formation and occurred with different kinetics depending on the cholesterol content (Figure 44a). Before NP addition, each SVL was gently rinsed with fresh PBS (thermostated at 22 °C) to remove the excess of undeposited vesicles as well as any vesicle loosely attached to the SVL surface (Figure 45a). In general, SVLs were highly stable after deposition and rinse.

QCM-D samples on gold (SVLs) with amphiphilic NPs. Monodisperse MUS:OT AuNPs (Appendix A4) were added to preformed SVLs and let to interact for several hours under QCM monitoring (Chapter 6). A scheme of the experimental set-up is illustrated in Figure 59. Before each experiment, a fixed NP volume was taken from a stock solution in water (0.6 mg/mL) and diluted in PBS (2 mL) to achieve a lipid/NP molar ratio of ~1600 with respect to the vesicle concentration previously injected to form the SVL (0.25 mg/mL). This ratio is nominal since excess vesicles were rinsed away before NP addition (Figure 59, step 2); the real lipid/NP value during SVL-NP incubation is therefore lower. Each NP dispersion in PBS was then sonicated for a few minutes in an ultrasonic bath and finally inserted into the pre-chamber. After 10 min of equilibration at 22 °C, NPs were injected into the chamber and let to interact with the preformed SVL for at least 20 h at 22 °C (Figure 45a). After a few hours with a sampling rate of 1 s, a point average every 10 s was selected. The following day, the NP-SVL complex was gently rinsed with PBS before the end of the recording. In all cases, no mass losses were recorded after buffer exchange (Figure 45a).

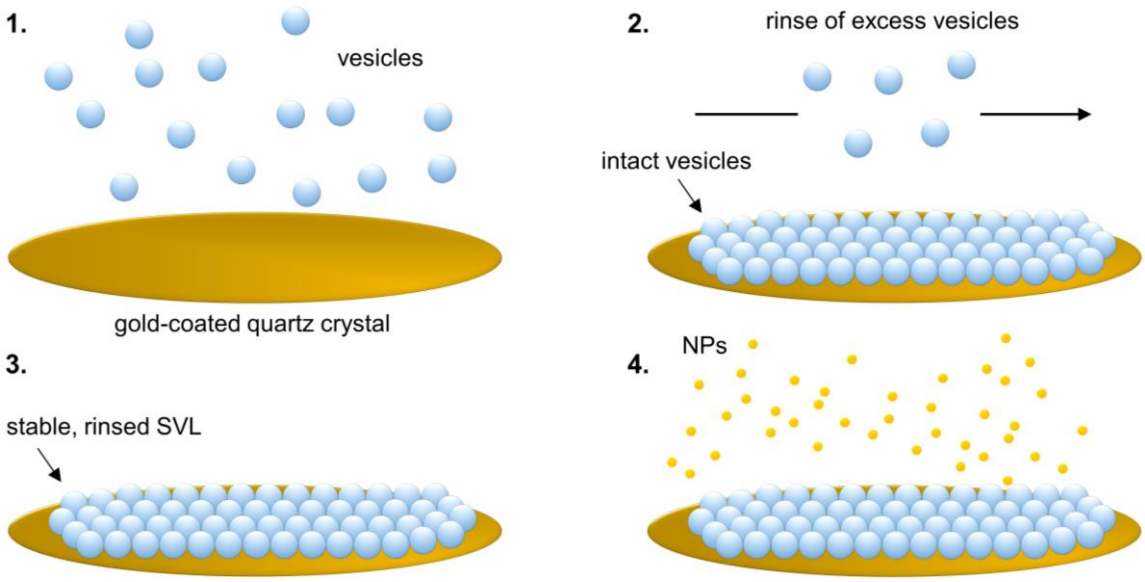

Figure 59. Schematic drawing (not to scale) illustrating the QCM-D experiments with NPs of Chapter 6. Vesicles (0.25 mg/mL) were first injected into the QCM chamber (**1**) and allowed to deposit on the surface of a gold-coated quartz sensor, where they accumulated but did not merge. After rinsing away the excess of undeposited vesicles (**2**), the stable SVL (**3**) was let to interact with NPs for several hours (at least 20) (**4**). At the end of the experiment, the NP-SVL complex was rinsed with fresh PBS to flush out the excess NPs.

NOTE: to calculate the lipid/NP molar ratio, the MW_{NP} was estimated as indicated in the bottom of Appendix C1 for one-phase MUS:OT AuNPs. In the case of monodisperse MUS:OT AuNPs let to interact with SVLs – 2.4 nm mean core diameter and 2:1 ligand molar ratio – the MW_{NP} is 68689 g/mol.

Appendix D – Fluorescence assays

Within this thesis, all fluorescence spectroscopy measurements were performed using a Fluorolog-3 spectrofluorometer (Horiba Jobin-Ivon) equipped with polarizers and temperature control of the cell holder.

D1) Dye-leakage assays

In the project of Chapter 4, NP-induced vesicle leakage was tested by means of calcein release[265–267] (Section 2.3.1). This technique is commonly used for leakage assays involving AuNPs to probe the bilayer integrity during NP-membrane interactions[61,263]. Measurements were performed at 25 °C in quartz cuvette (Hellma, optical path length 10 mm × 10 mm) using a sample volume of 2.4 mL. After filtration, calcein-loaded vesicles suspensions (175 mM calcein, Appendix B1) were diluted in 100 mM NaCl, 2 mM histidine, 2 mM TES, 0.1 mM EDTA (adjusted to pH 7.4) to a lipid concentration of 0.035 mM (i.e. 0.03 mg/mL). Throughout the whole experiment, calcein fluorescence (λ_{ex}=490 nm, λ_{em}=520 nm) was monitored as a function of time with a sampling rate of 1 s. To ensure the homogeneity of the system before and after NP addition, the sample was continuously stirred with a magnetic bar. As shown in Figure 32b, the introduction of the stirring bar in the cuvette was found to cause a transient, reproducible fluorescence increase that reached a plateau after 30 min. This behavior was absent if fluorescence was recorded for the same length of time in the absence of the magnetic bar. This phenomenon was thus interpreted as due to the adsorption of lipids by the hydrophobic Teflon surface of the magnetic bar and by the hydrophilic walls of the quartz cuvette, facilitated by stirring, and resulting in the disruption of some vesicles with subsequent calcein release. Similar behavior has already been observed for vesicles of different compositions and the extent of release was shown to depend on the lipid mixture and the cuvette material[402]. Therefore, to avoid artifacts, NPs were always added to the POPC vesicle suspension 30 min after introducing the stirrer in the cuvette. In particular, filtered NP dispersions (one-phase MUS:OT and TMA:OT AuNPs, Appendix A1) were added to POPC vesicles at a NP/lipid mass ratio, R_m, of 0.03 and 0.05. Such mass ratios (excluding higher values) were chosen to limit as much as possible NP aggregation before interaction with lipid vesicles. These NP/lipid mass ratios are slightly higher than those used in the literature for similar experiments with Au NPs[264]. Besides, they correspond to a sufficiently high NP uptake by the POPC bilayer, as demonstrated by QCM-D results reported in Figure 31b (Section 4.3.2).

Therefore, these R_m values represent a good compromise to study the effect of NP uptake on the bilayer integrity of calcein-loaded vesicles and to limit undesired NP aggregation in solution. As shown in Figure 32d-f (Section 4.3.2), the NP volumes added to POPC vesicles were in the range between 14.6 and 124 μL, depending on the concentration of NP aqueous dispersions after filtration (Figure 47, Appendix A1). At the end of each experiment, the complete leakage of the inner dye was induced by the detergent addition, i.e. 0.5 % (w/v) sodium cholate.

Statistical analysis of leakage data. The mean leakage % reported in Figure 32d-f were processed averaging the results of Equation 3 (Section 2.3.1) calculated over the last 10 min before the addition of the detergent. The minimum and the maximum fluorescence levels – i.e. F_0 and F_{max} – were calculated as the mean fluorescence intensity immediately before NP injection (F_0) and immediately after detergent addition (F_{max}) (data averaged over 10 minutes). Error bars were calculated using Student's statistics (n=3).

D2) Fluorescence anisotropy assays

In the project of Chapter 6, steady-state fluorescence anisotropy measurements were performed on lipid vesicles labeled with either DPH or TMA-DPH fluorophores (Appendix B1). These assays were used to investigate the changes in membrane fluidity of DOPC vesicles due to the incorporation of increasing amounts of cholesterol. Measurements were also performed after membrane interaction with NPs. In particular, monodisperse 2:1 MUS:OT AuNPs with core diameter of 2.4 nm or 4.8 nm (Table 5, Section 3.2.1) were incubated with lipid vesicles for ~3 h and ~4 days (respectively) in the dark and at room temperature (passive penetration of large NPs is usually slower than small NPs). Measurements were carried out at constant temperature (20 °C), under continuous magnetic stirring, using a quartz cuvette (Hellma, optical path length 10 mm × 4 mm) with sample volume of 850 μL. For each experiment, freshly extruded vesicle suspensions were diluted in PBS (1x, pH 7.4) to a lipid concentration of 500 μM[403]. When NPs were incubated with vesicles, a fixed NP volume was added from a stock solution in water (6 mg/mL) to obtain a final NP concentration of 3.2 μM. Thus, the lipid/NP molar ratio was ~160. Notably, this value is similar to that of NP/vesicle pre-incubated samples used in AFM experiments of Chapter 5 (see Appendix C1). Before all acquisitions, polarizers were appropriately set on the excitation and the emission beams. The fluorescence intensity emitted by the fluorophores was detected after passing through the emission polarizer held vertical or horizontal to the direction of

the electric vector of the polarized excitation (Figure 21, Section 2.3.2). All experiments were performed using excitation and emission slits with a bandpass of 4.5 nm; $\lambda_{ex}/\lambda_{em}$ were set as 358/428 nm for DPH and 360/428 nm for TMA-DPH.

NOTE: in the case of monodisperse 2:1 MUS:OT AuNPs with mean core diameter of 4.8 nm, the MW_{NP} is 470836 g/mol (see bottom of Appendix C1 for calculation details). As indicated in Appendix C2 for QCM-D measurements involving SVLs, the MW_{NP} of 2.4 nm NPs is 68689 g/mol.

Statistical analysis of anisotropy data. The fluorescence anisotropy (r) of DPH and TMA-DPH reported in Figure 43 and Figure 46 (Chapter 6) was calculated using Equation 4 reported in Section 2.3.2. Four replicates were acquired in the case of vesicles alone and vesicles incubated with 2.4 nm NPs, while 8 replicates were carried out when 4.8 nm NPs were tested. Indeed, with larger NPs, on average the measurements were noisier due to higher light scattering caused by NPs that remained in solution. Uncertainties on mean values were calculated using Student's statistics assuming a 95 % confidence level.

References

(1) Canepa, E.; Salassi, S.; Simonelli, F.; Ferrando, R.; Rolandi, R.; Lambruschini, C.; Canepa, F.; Dante, S.; Relini, A.; Rossi, G. Non-Disruptive Uptake of Anionic and Cationic Gold Nanoparticles in Neutral Zwitterionic Membranes. *Scientific Reports* **2021**, *11* (1), 1256.

(2) Canepa, E.; Salassi, S.; de Marco, A. L.; Lambruschini, C.; Odino, D.; Bochicchio, D.; Canepa, F.; Canale, C.; Dante, S.; Brescia, R.; Stellacci, F.; Rossi, G.; Relini, A. Amphiphilic Gold Nanoparticles Perturb Phase Separation in Multidomain Lipid Membranes. *Nanoscale* **2020**, *12* (38), 19746–19759.

(3) Giner-Casares, J. J.; Henriksen-Lacey, M.; Coronado-Puchau, M.; Liz-Marzán, L. M. Inorganic Nanoparticles for Biomedicine: Where Materials Scientists Meet Medical Research. *Materials Today* **2016**, *19* (1), 19–28.

(4) De, M.; Ghosh, P. S.; Rotello, V. M. Applications of Nanoparticles in Biology. *Advanced Materials* **2008**, *20* (22), 4225–4241.

(5) Salata, O. V. Applications of Nanoparticles in Biology and Medicine. *Journal of Nanobiotechnology* **2004**, *2* (3), 1–6.

(6) Lewis, M. R.; Kannan, R. Development and Applications of Radioactive Nanoparticles for Imaging of Biological Systems. *Wiley Interdisciplinary Reviews: Nanomedicine and Nanobiotechnology* **2014**, *6* (6), 628–640.

(7) Revia, R. A.; Zhang, M. Magnetite Nanoparticles for Cancer Diagnosis, Treatment, and Treatment Monitoring: Recent Advances. *Materials Today* **2016**, *19* (3), 157–168.

(8) Garcia, M. A. Erratum: Surface Plasmons in Metallic Nanoparticles: Fundamentals and Applications (Journal of Physics D: Applied Physics (2011) 44 (283001)). *Journal of Physics D: Applied Physics* **2012**, *45* (38).

(9) Amendola, V.; Pilot, R.; Frasconi, M.; Maragò, O. M.; Iatì, M. A. Surface Plasmon Resonance in Gold Nanoparticles: A Review. *Journal of Physics Condensed Matter* **2017**, *29* (20).

(10) Habib, A.; Zhu, X.; Fong, S.; Yanik, A. A. Active Plasmonic Nanoantenna: An Emerging Toolbox from Photonics to Neuroscience. *Nanophotonics* **2020**, *9* (12), 3805–3829.

(11) Hernández, Y.; Galarreta, B. C. Noble Metal-Based Plasmonic Nanoparticles for SERS Imaging and Photothermal Therapy. In *Nanomaterials for Magnetic and Optical Hyperthermia Applications*; Elsevier, 2019; pp 83–109.

(12) Kim, M.; Lee, J. H.; Nam, J. M. Plasmonic Photothermal Nanoparticles for Biomedical Applications. *Advanced Science* **2019**, *6* (17).

(13) Altavilla, C.; Ciliberto, E. *Inorganic Nanoparticles: Synthesis Application and Perspectives*; CRC Press, 2010.

(14) Love, J. C.; Estroff, L. A.; Kriebel, J. K.; Nuzzo, R. G.; Whitesides, G. M. *Self-Assembled Monolayers of Thiolates on Metals as a Form of Nanotechnology*; 2005; Vol. 105.

(15) Sperling, R. A.; Parak, W. J. Surface Modification, Functionalization and Bioconjugation of Colloidal Inorganic Nanoparticles. *Philosophical Transactions of*

the Royal Society A: Mathematical, Physical and Engineering Sciences **2010**, *368* (1915), 1333–1383.

(16) Ulman, A. Formation and Structure of Self-Assembled Monolayers. *Chemical Reviews* **1996**, *96* (4), 1533–1554.

(17) Avvakumova, S.; Colombo, M.; Tortora, P.; Prosperi, D. Biotechnological Approaches toward Nanoparticle Biofunctionalization. *Trends in Biotechnology* **2014**, *32* (1), 11–20.

(18) Mout, R.; Moyano, D. F.; Rana, S.; Rotello, V. M. Surface Functionalization of Nanoparticles for Nanomedicine. *Chemical Society Reviews* **2012**, *41* (7), 2539.

(19) Sapsford, K. E.; Algar, W. R.; Berti, L.; Gemmill, K. B.; Casey, B. J.; Oh, E.; Stewart, M. H.; Medintz, I. L. Functionalizing Nanoparticles with Biological Molecules: Developing Chemistries That Facilitate Nanotechnology. *Chemical Reviews* **2013**, *113* (3), 1904–2074.

(20) Huang, R.; Carney, R. P.; Stellacci, F.; Lau, B. L. T. Protein–Nanoparticle Interactions: The Effects of Surface Compositional and Structural Heterogeneity Are Scale Dependent. *Nanoscale* **2013**, *5* (15), 6928.

(21) Hung, A.; Mwenifumbo, S.; Mager, M.; Kuna, J. J.; Stellacci, F.; Yarovsky, I.; Stevens, M. M. Ordering Surfaces on the Nanoscale: Implications for Protein Adsorption. *Journal of the American Chemical Society* **2011**, *133* (5), 1438–1450.

(22) Abdelkhaliq, A.; van der Zande, M.; Punt, A.; Helsdingen, R.; Boeren, S.; Vervoort, J. J. M.; Rietjens, I. M. C. M.; Bouwmeester, H. Impact of Nanoparticle Surface Functionalization on the Protein Corona and Cellular Adhesion, Uptake and Transport. *Journal of Nanobiotechnology* **2018**, *16* (1), 70.

(23) Moyano, D. F.; Saha, K.; Prakash, G.; Yan, B.; Kong, H.; Yazdani, M.; Rotello, V. M. Fabrication of Corona-Free Nanoparticles with Tunable Hydrophobicity. *ACS nano* **2014**, *8* (7), 6748–6755.

(24) Simonelli, F.; Rossi, G.; Monticelli, L. Role of Ligand Conformation on Nanoparticle-Protein Interactions. *Journal of Physical Chemistry B* **2019**, *123* (8), 1764–1769.

(25) Jiang, Y.; Huo, S.; Mizuhara, T.; Das, R.; Lee, Y. W.; Hou, S.; Moyano, D. F.; Duncan, B.; Liang, X. J.; Rotello, V. M. The Interplay of Size and Surface Functionality on the Cellular Uptake of Sub-10 Nm Gold Nanoparticles. *ACS Nano* **2015**, *9* (10), 9986–9993.

(26) Verma, A.; Stellacci, F. Effect of Surface Properties on Nanoparticle – Cell Interactions. *Small* **2010**, *6* (1), 12–21.

(27) Blanco, E.; Shen, H.; Ferrari, M. Principles of Nanoparticle Design for Overcoming Biological Barriers to Drug Delivery. *Nature Biotechnology* **2015**, *33* (9), 941–951.

(28) Zhao, F.; Zhao, Y.; Liu, Y.; Chang, X.; Chen, C.; Zhao, Y. Cellular Uptake, Intracellular Trafficking, and Cytotoxicity of Nanomaterials. *Small* **2011**, *7* (10), 1322–1337.

(29) Shang, L.; Nienhaus, K.; Nienhaus, G. Engineered Nanoparticles Interacting with Cells: Size Matters. *Journal of Nanobiotechnology* **2014**, *12* (1), 5.

(30) Chou, L. Y. T.; Ming, K.; Chan, W. C. W. Strategies for the Intracellular Delivery of Nanoparticles. *Chem. Soc. Rev.* **2011**, *40* (1), 233–245.

(31) Chithrani, D. B. Intracellular Uptake, Transport, and Processing of Gold Nanostructures. *Molecular Membrane Biology* **2010**, *27* (7), 299–311.
(32) Giljohann, D. A.; Seferos, D. S.; Daniel, W. L.; Massich, M. D.; Patel, P. C.; Mirkin, C. A. Gold Nanoparticles for Biology and Medicine. *Angewandte Chemie International Edition* **2010**, *49* (19), 3280–3294.
(33) Contini, C.; Schneemilch, M.; Gaisford, S.; Quirke, N. Nanoparticle–Membrane Interactions. *Journal of Experimental Nanoscience* **2018**, *13* (1), 62–81.
(34) Mendozza, M.; Caselli, L.; Salvatore, A.; Montis, C.; Berti, D. Nanoparticles and Organized Lipid Assemblies: From Interaction to Design of Hybrid Soft Devices. *Soft Matter* **2019**, *15* (44), 8951–8970.
(35) Helfrich, W. Elastic Properties of Lipid Bilayers: Theory and Possible Experiments. *Zeitschrift für Naturforschung C* **1973**, *28* (11–12), 693–703.
(36) Deserno, M. Elastic Deformation of a Fluid Membrane upon Colloid Binding. *Physical Review E* **2004**, *69* (3), 031903.
(37) Backes, W. L. Passive Diffusion of Drugs Across Membranes. In *Reference Module in Biomedical Sciences*; Elsevier, 2015.
(38) Feher, J. Passive Transport and Facilitated Diffusion. In *Quantitative Human Physiology*; Elsevier, 2017; pp 161–169.
(39) Iversen, T.-G.; Skotland, T.; Sandvig, K. Endocytosis and Intracellular Transport of Nanoparticles: Present Knowledge and Need for Future Studies. *Nano Today* **2011**, *6* (2), 176–185.
(40) Canton, I.; Battaglia, G. Endocytosis at the Nanoscale. *Chemical Society Reviews* **2012**, *41* (7), 2718.
(41) Park, J. H.; Oh, N. Endocytosis and Exocytosis of Nanoparticles in Mammalian Cells. *International Journal of Nanomedicine* **2014**, 51.
(42) Behzadi, S.; Serpooshan, V.; Tao, W.; Hamaly, M. A.; Alkawareek, M. Y.; Dreaden, E. C.; Brown, D.; Alkilany, A. M.; Farokhzad, O. C.; Mahmoudi, M. Cellular Uptake of Nanoparticles: Journey inside the Cell. *Chemical Society Reviews* **2017**, *46* (14), 4218–4244.
(43) Pratten, M. K.; Lloyd, J. B. Pinocytosis and Phagocytosis: The Effect of Size of a Particulate Substrate on Its Mode of Capture by Rat Peritoneal Macrophages Cultured in Vitro. *Biochimica et Biophysica Acta (BBA) - General Subjects* **1986**, *881* (3), 307–313.
(44) Kettler, K.; Veltman, K.; van de Meent, D.; van Wezel, A.; Hendriks, A. J. Cellular Uptake of Nanoparticles as Determined by Particle Properties, Experimental Conditions, and Cell Type. *Environmental Toxicology and Chemistry* **2014**, *33* (3), 481–492.
(45) Zhang, S.; Gao, H.; Bao, G. Physical Principles of Nanoparticle Cellular Endocytosis. *ACS Nano* **2015**, *9* (9), 8655–8671.
(46) Adibnia, V.; Mirbagheri, M.; Salimi, S.; De Crescenzo, G.; Banquy, X. Nonspecific Interactions in Biomedical Applications. *Current Opinion in Colloid & Interface Science* **2020**, *47*, 70–83.
(47) Nakamura, H.; Watano, S. Direct Permeation of Nanoparticles across Cell Membrane: A Review. *KONA Powder and Particle Journal* **2018**, *35*, 49–65.
(48) Roiter, Y.; Ornatska, M.; Rammohan, A. R.; Balakrishnan, J.; Heine, D. R.;

Minko, S. Interaction of Nanoparticles with Lipid Membrane. *Nano Letters* **2008**, *8* (3), 941–944.

(49) Roiter, Y.; Ornatska, M.; Rammohan, A. R.; Balakrishnan, J.; Heine, D. R.; Minko, S. Interaction of Lipid Membrane with Nanostructured Surfaces. *Langmuir* **2009**, *25* (11), 6287–6299.

(50) Kashchiev, D.; Exerowa, D. Bilayer Lipid Membrane Permeation and Rupture Due to Hole Formation. *Biochimica et Biophysica Acta (BBA) - Biomembranes* **1983**, *732* (1), 133–145.

(51) Beddoes, C. M.; Case, C. P.; Briscoe, W. H. Understanding Nanoparticle Cellular Entry: A Physicochemical Perspective. *Advances in Colloid and Interface Science* **2015**, *218*, 48–68.

(52) Zhu, M.; Nie, G.; Meng, H.; Xia, T.; Nel, A.; Zhao, Y. Physicochemical Properties Determine Nanomaterial Cellular Uptake, Transport, and Fate. *Accounts of Chemical Research* **2013**, *46* (3), 622–631.

(53) Qu, Z. G.; He, X. C.; Lin, M.; Sha, B. Y.; Shi, X. H.; Lu, T. J.; Xu, F. Advances in the Understanding of Nanomaterial–Biomembrane Interactions and Their Mathematical and Numerical Modeling. *Nanomedicine* **2013**, *8* (6), 995–1011.

(54) Zhao, J.; Stenzel, M. H. Entry of Nanoparticles into Cells: The Importance of Nanoparticle Properties. *Polymer Chemistry* **2018**, *9* (3), 259–272.

(55) Saha, K.; Kim, S. T.; Yan, B.; Miranda, O. R.; Alfonso, F. S.; Shlosman, D.; Rotello, V. M. Surface Functionality of Nanoparticles Determines Cellular Uptake Mechanisms in Mammalian Cells. *Small* **2013**, *9* (2), 300–305.

(56) Zhang, S.; Li, J.; Lykotrafitis, G.; Bao, G.; Suresh, S. Size-Dependent Endocytosis of Nanoparticles. *Advanced Materials* **2009**, *21* (4), 419–424.

(57) Yi, X.; Shi, X.; Gao, H. Cellular Uptake of Elastic Nanoparticles. *Physical Review Letters* **2011**, *107* (9), 098101.

(58) Ding, H.; Ma, Y. Theoretical and Computational Investigations of Nanoparticle-Biomembrane Interactions in Cellular Delivery. *Small* **2015**, *11* (9–10), 1055–1071.

(59) Sokolova, V.; Kozlova, D.; Knuschke, T.; Buer, J.; Westendorf, A. M.; Epple, M. Mechanism of the Uptake of Cationic and Anionic Calcium Phosphate Nanoparticles by Cells. *Acta Biomaterialia* **2013**, *9* (7), 7527–7535.

(60) Leroueil, P. R.; Berry, S. A.; Duthie, K.; Han, G.; Rotello, V. M.; McNerny, D. Q.; Baker, J. R.; Orr, B. G.; Banaszak Holl, M. M. Wide Varieties of Cationic Nanoparticles Induce Defects in Supported Lipid Bilayers. *Nano Letters* **2008**, *8* (2), 420–424.

(61) Goodman, C. M.; McCusker, C. D.; Yilmaz, T.; Rotello, V. M. Toxicity of Gold Nanoparticles Functionalized with Cationic and Anionic Side Chains. *Bioconjugate Chemistry* **2004**, *15* (4), 897–900.

(62) Feng, Z. V.; Gunsolus, I. L.; Qiu, T. A.; Hurley, K. R.; Nyberg, L. H.; Frew, H.; Johnson, K. P.; Vartanian, A. M.; Jacob, L. M.; Lohse, S. E.; Torelli, M. D.; Hamers, R. J.; Murphy, C. J.; Haynes, C. L. Impacts of Gold Nanoparticle Charge and Ligand Type on Surface Binding and Toxicity to Gram-Negative and Gram-Positive Bacteria. *Chemical Science* **2015**, *6* (9), 5186–5196.

(63) Lin, J.; Zhang, H.; Chen, Z.; Zheng, Y. Penetration of Lipid Membranes by

Gold Nanoparticles: Insights into Cellular Uptake, Cytotoxicity, and Their Relationship. *ACS Nano* **2010**, *4* (9), 5421–5429.

(64) Salassi, S.; Canepa, E.; Ferrando, R.; Rossi, G. Anionic Nanoparticle-Lipid Membrane Interactions: The Protonation of Anionic Ligands at the Membrane Surface Reduces Membrane Disruption. *RSC Advances* **2019**, *9* (25), 13992–13997.

(65) Li, Y.; Chen, X.; Gu, N. Computational Investigation of Interaction between Nanoparticles and Membranes: Hydrophobic/Hydrophilic Effect. *The Journal of Physical Chemistry B* **2008**, *112* (51), 16647–16653.

(66) Wong-Ekkabut, J.; Baoukina, S.; Triampo, W.; Tang, I.-M.; Tieleman, D. P.; Monticelli, L. Computer Simulation Study of Fullerene Translocation through Lipid Membranes. *Nature Nanotechnology* **2008**, *3* (6), 363–368.

(67) Nel, A. E.; Mädler, L.; Velegol, D.; Xia, T.; Hoek, E. M. V.; Somasundaran, P.; Klaessig, F.; Castranova, V.; Thompson, M. Understanding Biophysicochemical Interactions at the Nano–Bio Interface. *Nature Materials* **2009**, *8* (7), 543–557.

(68) Chithrani, B. D.; Ghazani, A. A.; Chan, W. C. W. Determining the Size and Shape Dependence of Gold Nanoparticle Uptake into Mammalian Cells. *Nano Letters* **2006**, *6* (4), 662–668.

(69) Yang, K.; Ma, Y.-Q. Computer Simulation of the Translocation of Nanoparticles with Different Shapes across a Lipid Bilayer. *Nature Nanotechnology* **2010**, *5* (8), 579–583.

(70) Nel, A. E.; Mädler, L.; Velegol, D.; Xia, T.; Hoek, E. M. V.; Somasundaran, P.; Klaessig, F.; Castranova, V.; Thompson, M. Understanding Biophysicochemical Interactions at the Nano–Bio Interface. *Nature Materials* **2009**, *8* (7), 543–557.

(71) Prapainop, K.; Witter, D. P.; Wentworth, P. A Chemical Approach for Cell-Specific Targeting of Nanomaterials: Small-Molecule-Initiated Misfolding of Nanoparticle Corona Proteins. *Journal of the American Chemical Society* **2012**, *134* (9), 4100–4103.

(72) Zhu, Y.; Li, W.; Li, Q.; Li, Y.; Li, Y.; Zhang, X.; Huang, Q. Effects of Serum Proteins on Intracellular Uptake and Cytotoxicity of Carbon Nanoparticles. *Carbon* **2009**, *47* (5), 1351–1358.

(73) Angioletti-Uberti, S. Theory, Simulations and the Design of Functionalized Nanoparticles for Biomedical Applications: A Soft Matter Perspective. *npj Computational Materials* **2017**, *3* (1), 48.

(74) Gao, H.; Shi, W.; Freund, L. B. From The Cover: Mechanics of Receptor-Mediated Endocytosis. *Proceedings of the National Academy of Sciences* **2005**, *102* (27), 9469–9474.

(75) Dreaden, E. C.; Alkilany, A. M.; Huang, X.; Murphy, C. J.; El-Sayed, M. A. The Golden Age: Gold Nanoparticles for Biomedicine. *Chemical Society Reviews* **2012**, *41* (7), 2740–2779.

(76) Dykman, L.; Khlebtsov, N. Gold Nanoparticles in Biomedical Applications: Recent Advances and Perspectives. *Chemical Society Reviews* **2012**, *41* (6), 2256–2282.

(77) Mieszawska, A. J.; Mulder, W. J. M.; Fayad, Z. A.; Cormode, D. P. Multifunctional Gold Nanoparticles for Diagnosis and Therapy of Disease. *Molecular Pharmaceutics* **2013**, *10*, 831–847.
(78) Huang, X.; Xu, Z.; Mao, Y.; Ji, Y.; Xu, H.; Xiong, Y.; Li, Y. Gold Nanoparticle-Based Dynamic Light Scattering Immunoassay for Ultrasensitive Detection of Listeria Monocytogenes in Lettuces. *Biosensors and Bioelectronics* **2015**, *66*, 184–190.
(79) Dreaden, E. C.; Mackey, M. A.; Huang, X.; Kang, B.; El-Sayed, M. A. Beating Cancer in Multiple Ways Using Nanogold. *Chemical Society Reviews* **2011**, *40* (7), 3391.
(80) Ghosh, P.; Han, G.; De, M.; Kim, C. K.; Rotello, V. M. Gold Nanoparticles in Delivery Applications. *Advanced Drug Delivery Reviews* **2008**, *60* (11), 1307–1315.
(81) Lee, S.-M.; Kim, H. J.; Kim, S. Y.; Kwon, M.-K.; Kim, S.; Cho, A.; Yun, M.; Shin, J.-S.; Yoo, K.-H. Drug-Loaded Gold Plasmonic Nanoparticles for Treatment of Multidrug Resistance in Cancer. *Biomaterials* **2014**, *35* (7), 2272–2282.
(82) Riley, R. S.; Day, E. S. Gold Nanoparticle-Mediated Photothermal Therapy: Applications and Opportunities for Multimodal Cancer Treatment. *Wiley Interdisciplinary Reviews: Nanomedicine and Nanobiotechnology* **2017**, *9* (4), e1449.
(83) Xiong, R.; Raemdonck, K.; Peynshaert, K.; Lentacker, I.; De Cock, I.; Demeester, J.; De Smedt, S. C.; Skirtach, A. G.; Braeckmans, K. Comparison of Gold Nanoparticle Mediated Photoporation: Vapor Nanobubbles Outperform Direct Heating for Delivering Macromolecules in Live Cells. *ACS nano* **2014**, *8* (6), 6288–6296.
(84) Bobo, D.; Robinson, K. J.; Islam, J.; Thurecht, K. J.; Corrie, S. R. Nanoparticle-Based Medicines: A Review of FDA-Approved Materials and Clinical Trials to Date. *Pharmaceutical Research* **2016**, *33* (10), 2373–2387.
(85) Nanospectra Biosciences Inc. *MRI/US Fusion Imaging and Biopsy in Combination With Nanoparticle Directed Focal Therapy for Ablation of Prostate Tissue*; 2016; p ClinicalTrials.gov Identifier: NCT02680535.
(86) Kim, E. Y.; Kumar, D.; Khang, G.; Lim, D.-K. Recent Advances in Gold Nanoparticle-Based Bioengineering Applications. *J. Mater. Chem. B* **2015**, *3* (43), 8433–8444.
(87) Polte, J. Fundamental Growth Principles of Colloidal Metal Nanoparticles – a New Perspective. *CrystEngComm* **2015**, *17* (36), 6809–6830.
(88) Hu, X.; Zhang, Y.; Ding, T.; Liu, J.; Zhao, H. Multifunctional Gold Nanoparticles: A Novel Nanomaterial for Various Medical Applications and Biological Activities. *Frontiers in Bioengineering and Biotechnology* **2020**, *8*.
(89) Kvitek, L.; Prucek, R.; Panacek, A.; Soukupova, J. Physicochemical Aspects of Metal Nanoparticle Preparation. In *Engineered Nanomaterials - Health and Safety*; IntechOpen, 2020.
(90) Daniel, M. C.; Astruc, D. Gold Nanoparticles: Assembly, Supramolecular Chemistry, Quantum-Size-Related Properties, and Applications Toward Biology, Catalysis, and Nanotechnology. *Chemical Reviews* **2004**, *104* (1), 293–346.

(91) Zhao, P.; Li, N.; Astruc, D. State of the Art in Gold Nanoparticle Synthesis. *Coordination Chemistry Reviews* **2013**, *257* (3–4), 638–665.
(92) Rana, S.; Bajaj, A.; Mout, R.; Rotello, V. M. Monolayer Coated Gold Nanoparticles for Delivery Applications. *Advanced Drug Delivery Reviews* **2012**, *64* (2), 200–216.
(93) Pengo, P.; Şologan, M.; Pasquato, L.; Guida, F.; Pacor, S.; Tossi, A.; Stellacci, F.; Marson, D.; Boccardo, S.; Pricl, S.; Posocco, P. Gold Nanoparticles with Patterned Surface Monolayers for Nanomedicine: Current Perspectives. *European Biophysics Journal* **2017**, *46* (8), 749–771.
(94) Yeh, Y.-C.; Creran, B.; Rotello, V. M. Gold Nanoparticles: Preparation, Properties, and Applications in Bionanotechnology. *Nanoscale* **2012**, *4* (6), 1871–1880.
(95) Turkevich, J.; Stevenson, P. C.; Hillier, J. A Study of the Nucleation and Growth Processes in the Synthesis of Colloidal Gold. *Discussions of the Faraday Society* **1951**, *11*, 55.
(96) FRENS, G. Controlled Nucleation for the Regulation of the Particle Size in Monodisperse Gold Suspensions. *Nature Physical Science* **1973**, *241* (105), 20–22.
(97) Brust, M.; Walker, M.; Bethell, D.; Schiffrin, D. J.; Whyman, R. Synthesis of Thiol-Derivatised Gold Nanoparticles in a Two-Phase Liquid–Liquid System. *J. Chem. Soc., Chem. Commun.* **1994**, *0* (7), 801–802.
(98) Brust, M.; Fink, J.; Bethell, D.; Schiffrin, D. J.; Kiely, C. Synthesis and Reactions of Functionalised Gold Nanoparticles. *Journal of the Chemical Society, Chemical Communications* **1995**, No. 16, 1655.
(99) Poirier, G. E.; Pylant, E. D. The Self-Assembly Mechanism of Alkanethiols on Au(111). *Science* **1996**, *272* (5265), 1145–1148.
(100) Hostetler, M. J.; Wingate, J. E.; Zhong, C.-J.; Harris, J. E.; Vachet, R. W.; Clark, M. R.; Londono, J. D.; Green, S. J.; Stokes, J. J.; Wignall, G. D.; Glish, G. L.; Porter, M. D.; Evans, N. D.; Murray, R. W. Alkanethiolate Gold Cluster Molecules with Core Diameters from 1.5 to 5.2 Nm: Core and Monolayer Properties as a Function of Core Size. *Langmuir* **1998**, *14* (1), 17–30.
(101) Templeton, A. C.; Wuelfing, W. P.; Murray, R. W. Monolayer-Protected Cluster Molecules. *Accounts of Chemical Research* **2000**, *33* (1), 27–36.
(102) Choo, H.; Cutler, E.; Shon, Y. S. Synthesis of Mixed Monolayer-Protected Gold Clusters from Thiol Mixtures: Variation in the Tail Group, Chain Length, and Solvent. *Langmuir* **2003**, *19* (20), 8555–8559.
(103) Hostetler, M. J.; Templeton, A. C.; Murray, R. W. Dynamics of Place-Exchange Reactions on Monolayer-Protected Gold Cluster Molecules. *Langmuir* **1999**.
(104) Hostetler, M. J.; Green, S. J.; Stokes, J. J.; Murray, R. W. Monolayers in Three Dimensions: Synthesis and Electrochemistry of ω-Functionalized Alkanethiolate-Stabilized Gold Cluster Compounds. *Journal of the American Chemical Society* **1996**, *118* (17), 4212–4213.
(105) Briñas, R. P.; Maetani, M.; Barchi, J. J. A Survey of Place-Exchange Reaction for the Preparation of Water-Soluble Gold Nanoparticles. *Journal of Colloid and Interface Science* **2013**, *392*, 415–421.
(106) Azubel, M.; Kornberg, R. D. Synthesis of Water-Soluble, Thiolate-Protected

Gold Nanoparticles Uniform in Size. *Nano Letters* **2016**, *16* (5), 3348–3351.
(107) Bürgi, T. Properties of the Gold–Sulphur Interface: From Self-Assembled Monolayers to Clusters. *Nanoscale* **2015**, *7* (38), 15553–15567.
(108) Häkkinen, H. The Gold–Sulfur Interface at the Nanoscale. *Nature Chemistry* **2012**, *4* (6), 443–455.
(109) Luo, Z.; Hou, J.; Menin, L.; Ong, Q. K.; Stellacci, F. Evolution of the Ligand Shell Morphology during Ligand Exchange Reactions on Gold Nanoparticles. *Angewandte Chemie - International Edition* **2017**, *56* (43), 13521–13525.
(110) Montalti L.; Zaccheroni, N.; Baxter, R.; Teobaldi, G.; Zerbetto, M. . P. Kinetics of Place Exchange Reactions of Thiols on Gold Nanoparticles. *Langmuir* **2003**, *19* (5), 5172.
(111) Hong, R.; Fernández, J. M.; Nakade, H.; Arvizo, R.; Emrick, T.; Rotello, V. M. In Situ Observation of Place Exchange Reactions of Gold Nanoparticles. Correlation of Monolayer Structure and Stability. *Chemical communications (Cambridge, England)* **2006**, No. 22, 2347–2349.
(112) Locardi, F.; Canepa, E.; Villa, S.; Nelli, I.; Lambruschini, C.; Ferretti, M.; Canepa, F. Thermogravimetry and Evolved Gas Analysis for the Investigation of Ligand-Exchange Reaction in Thiol-Functionalized Gold Nanoparticles. *Journal of Analytical and Applied Pyrolysis* **2018**, *132*.
(113) Gifford, J. C.; Bresee, J.; Carter, C. J.; Wang, G.; Melander, R. J.; Melander, C.; Feldheim, D. L. Thiol-Modified Gold Nanoparticles for the Inhibition of Mycobacterium Smegmatis. *Chem. Commun.* **2014**, *50* (100), 15860–15863.
(114) Kitaoka, T.; Yokota, S.; Opietnik, M.; Rosenau, T. Synthesis and Bio-Applications of Carbohydrate–Gold Nanoconjugates with Nanoparticle and Nanolayer Forms. *Materials Science and Engineering: C* **2011**, *31* (6), 1221–1229.
(115) Lin, J.; Alexander-Katz, A. Cell Membranes Open "Doors" for Cationic Nanoparticles/Biomolecules: Insights into Uptake Kinetics. *ACS Nano* **2013**, *7* (12), 10799–10808.
(116) Porret, E.; Sancey, L.; Martín-Serrano, A.; Montañez, M. I.; Seeman, R.; Yahia-Ammar, A.; Okuno, H.; Gomez, F.; Ariza, A.; Hildebrandt, N.; Fleury, J.-B.; Coll, J.-L.; Le Guével, X. Hydrophobicity of Gold Nanoclusters Influences Their Interactions with Biological Barriers. *Chemistry of Materials* **2017**, *29* (17), 7497–7506.
(117) Sun, S.; Huang, Y.; Zhou, C.; Chen, S.; Yu, M.; Liu, J.; Zheng, J. Effect of Hydrophobicity on Nano-Bio Interactions of Zwitterionic Luminescent Gold Nanoparticles at the Cellular Level. *Bioconjugate Chemistry* **2018**, *29* (6), 1841–1846.
(118) Schaeublin, N. M.; Braydich-Stolle, L. K.; Schrand, A. M.; Miller, J. M.; Hutchison, J.; Schlager, J. J.; Hussain, S. M. Surface Charge of Gold Nanoparticles Mediates Mechanism of Toxicity. *Nanoscale* **2011**, *3* (2), 410.
(119) Schleh, C.; Semmler-Behnke, M.; Lipka, J.; Wenk, A.; Hirn, S.; Schäffler, M.; Schmid, G.; Simon, U.; Kreyling, W. G. Size and Surface Charge of Gold Nanoparticles Determine Absorption across Intestinal Barriers and Accumulation in Secondary Target Organs after Oral Administration. *Nanotoxicology* **2012**, *6* (1), 36–46.

(120) Huang, R.; Carney, R. P.; Stellacci, F.; Lau, B. L. T. Colloidal Stability of Self-Assembled Monolayer-Coated Gold Nanoparticles: The Effects of Surface Compositional and Structural Heterogeneity. *Langmuir* **2013**, *29* (37), 11560–11566.
(121) Uzun, O.; Hu, Y.; Verma, A.; Chen, S.; Centrone, A.; Stellacci, F. Water-Soluble Amphiphilic Gold Nanoparticles with Structured Ligand Shells. *Chem. Commun.* **2008**, No. 2, 196–198.
(122) White, S. H.; Wimley, W. C. MEMBRANE PROTEIN FOLDING AND STABILITY: Physical Principles. *Annual Review of Biophysics and Biomolecular Structure* **1999**, *28* (1), 319–365.
(123) Pooga, M.; Langel, Ü. Classes of Cell-Penetrating Peptides; Humana Press, New York, NY, 2015; pp 3–28.
(124) Ruseska, I.; Zimmer, A. Internalization Mechanisms of Cell-Penetrating Peptides. *Beilstein Journal of Nanotechnology* **2020**, *11*, 101–123.
(125) Thorén, P. E. G.; Persson, D.; Esbjörner, E. K.; Goksör, M.; Lincoln, P.; Nordén, B. Membrane Binding and Translocation of Cell-Penetrating Peptides †. *Biochemistry* **2004**, *43* (12), 3471–3489.
(126) Patel, L. N.; Zaro, J. L.; Shen, W.-C. Cell Penetrating Peptides: Intracellular Pathways and Pharmaceutical Perspectives. *Pharmaceutical Research* **2007**, *24* (11), 1977–1992.
(127) Van Lehn, R. C.; Ricci, M.; Silva, P. H. J.; Andreozzi, P.; Reguera, J.; Voïtchovsky, K.; Stellacci, F.; Alexander-Katz, A. Lipid Tail Protrusions Mediate the Insertion of Nanoparticles into Model Cell Membranes. *Nature Communications* **2014**, *5*, 4482.
(128) Torchi, A.; Simonelli, F.; Ferrando, R.; Rossi, G. Local Enhancement of Lipid Membrane Permeability Induced by Irradiated Gold Nanoparticles. *ACS Nano* **2017**, *11* (12), 12553–12561.
(129) Simonelli, F.; Bochicchio, D.; Ferrando, R.; Rossi, G. Monolayer-Protected Anionic Au Nanoparticles Walk into Lipid Membranes Step by Step. *The Journal of Physical Chemistry Letters* **2015**, *6* (16), 3175–3179.
(130) Tatur, S.; Maccarini, M.; Barker, R.; Nelson, A.; Fragneto, G. Effect of Functionalized Gold Nanoparticles on Floating Lipid Bilayers. *Langmuir* **2013**, *29*, 6606–6614.
(131) Pfeiffer, T.; De Nicola, A.; Montis, C.; Carlà, F.; Van Der Vegt, N. F. A.; Berti, D.; Milano, G. Nanoparticles at Biomimetic Interfaces: Combined Experimental and Simulation Study on Charged Gold Nanoparticles/Lipid Bilayer Interfaces. *Journal of Physical Chemistry Letters* **2019**, *10* (2), 129–137.
(132) Lolicato, F.; Joly, L.; Martinez-Seara, H.; Fragneto, G.; Scoppola, E.; Baldelli Bombelli, F.; Vattulainen, I.; Akola, J.; Maccarini, M. The Role of Temperature and Lipid Charge on Intake/Uptake of Cationic Gold Nanoparticles into Lipid Bilayers. *Small* **2019**, *15* (23), 1805046.
(133) Verma, A.; Uzun, O.; Hu, Y.; Hu, Y.; Han, H.-S.; Watson, N.; Chen, S.; Irvine, D. J.; Stellacci, F. Surface Structure-Regulated Cell Membrane Penetration by Monolayer Protected Nanoparticles. *Nature materials* **2008**, *7* (7), 588–595.
(134) Jewell, C. M.; Jung, J.-M.; Atukorale, P. U.; Carney, R. P.; Stellacci, F.; Irvine,

D. J. Oligonucleotide Delivery by Cell-Penetrating "Striped" Nanoparticles. *Angewandte Chemie International Edition* **2011**, *50* (51), 12312–12315.

(135) Carney, R. P.; Carney, T. M.; Mueller, M.; Stellacci, F. Dynamic Cellular Uptake of Mixed-Monolayer Protected Nanoparticles. *Biointerphases* **2012**, *7* (1–4), 3–11.

(136) Leduc, C.; Jung, J. M.; Carney, R. R.; Stellacci, F.; Lounis, B. Direct Investigation of Intracellular Presence of Gold Nanoparticles via Photothermal Heterodyne Imaging. *ACS Nano* **2011**, *5* (4), 2587–2592.

(137) Atukorale, P. U.; Yang, Y.-S.; Bekdemir, A.; Carney, R. P.; Silva, P. J.; Watson, N.; Stellacci, F.; Irvine, D. J. Influence of the Glycocalyx and Plasma Membrane Composition on Amphiphilic Gold Nanoparticle Association with Erythrocytes. *Nanoscale* **2015**, *7* (26), 11420–11432.

(138) Sabella, S.; Carney, R. P.; Brunetti, V.; Malvindi, M. A.; Al-Juffali, N.; Vecchio, G.; Janes, S. M.; Bakr, O. M.; Cingolani, R.; Stellacci, F.; Pompa, P. P. A General Mechanism for Intracellular Toxicity of Metal-Containing Nanoparticles. *Nanoscale* **2014**.

(139) Yang, Y.-S. S.; Atukorale, P. U.; Moynihan, K. D.; Bekdemir, A.; Rakhra, K.; Tang, L.; Stellacci, F.; Irvine, D. J. High-Throughput Quantitation of Inorganic Nanoparticle Biodistribution at the Single-Cell Level Using Mass Cytometry. *Nature Communications* **2017**, *8* (1), 14069.

(140) Carney, R. P.; Astier, Y.; Carney, T. M.; Voïtchovsky, K.; Jacob Silva, P. H.; Stellacci, F. Electrical Method to Quantify Nanoparticle Interaction with Lipid Bilayers. *ACS Nano* **2013**, *7* (2), 932–942.

(141) Van Lehn, R. C.; Atukorale, P. U.; Carney, R. P.; Yang, Y. S.; Stellacci, F.; Irvine, D. J.; Alexander-Katz, A. Effect of Particle Diameter and Surface Composition on the Spontaneous Fusion of Monolayer-Protected Gold Nanoparticles with Lipid Bilayers. *Nano Letters* **2013**, *13* (9), 4060–4067.

(142) Atukorale, P. U.; Guven, Z. P.; Bekdemir, A.; Carney, R. P.; Van Lehn, R. C.; Yun, D. S.; Jacob Silva, P. H.; Demurtas, D.; Yang, Y. S.; Alexander-Katz, A.; Stellacci, F.; Irvine, D. J. Structure-Property Relationships of Amphiphilic Nanoparticles That Penetrate or Fuse Lipid Membranes. *Bioconjugate Chemistry* **2018**, *29* (4), 1131–1140.

(143) Tahir, M. A.; Guven, Z. P.; Arriaga, L. R.; Tinao, B.; Yang, Y. S. S.; Bekdemir, A.; Martin, J. T.; Bhanji, A. N.; Irvine, D.; Stellacci, F.; Alexander-Katz, A. Calcium-Triggered Fusion of Lipid Membranes Is Enabled by Amphiphilic Nanoparticles. *Proceedings of the National Academy of Sciences of the United States of America* **2020**, *117* (31), 18470–18746.

(144) Cagno, V.; Andreozzi, P.; D'Alicarnasso, M.; Silva, P. J.; Mueller, M.; Galloux, M.; Goffic, R. Le; Jones, S. T.; Vallino, M.; Hodek, J.; Weber, J.; Sen, S.; Janecek, E. R.; Bekdemir, A.; Sanavio, B.; Martinelli, C.; Donalisio, M.; Welti, M. A. R.; Eleouet, J. F.; Han, Y.; Kaiser, L.; Vukovic, L.; Tapparel, C.; Král, P.; Krol, S.; Lembo, D.; Stellacci, F. Broad-Spectrum Non-Toxic Antiviral Nanoparticles with a Virucidal Inhibition Mechanism. *Nature Materials* **2018**, *17* (2), 195–203.

(145) Van Lehn, R. C.; Alexander-Katz, A. Free Energy Change for Insertion of Charged, Monolayer-Protected Nanoparticles into Lipid Bilayers. *Soft Matter*

2014, *10* (4), 648–658.
(146) Salassi, S.; Simonelli, F.; Bochicchio, D.; Ferrando, R.; Rossi, G. Au Nanoparticles in Lipid Bilayers: A Comparison between Atomistic and Coarse-Grained Models. *Journal of Physical Chemistry C* **2017**, *121* (20), 10927–10935.
(147) Van Lehn, R. C.; Alexander-Katz, A. Energy Landscape for the Insertion of Amphiphilic Nanoparticles into Lipid Membranes: A Computational Study. *PLOS ONE* **2019**, *14* (1), e0209492.
(148) Lane, J. M. D.; Grest, G. S. Spontaneous Asymmetry of Coated Spherical Nanoparticles in Solution and at Liquid-Vapor Interfaces. *Physical Review Letters* **2010**, *104* (23), 235501.
(149) Deol, S. S.; Bond, P. J.; Domene, C.; Sansom, M. S. P. Lipid-Protein Interactions of Integral Membrane Proteins: A Comparative Simulation Study. *Biophysical Journal* **2004**, *87* (6), 3737–3749.
(150) Strandberg, E.; Killian, J. A. Snorkeling of Lysine Side Chains in Transmembrane Helices: How Easy Can It Get? *FEBS Letters* **2003**, *544* (1–3), 69–73.
(151) Leroueil, P. R.; Hong, S.; Mecke, A.; Baker, J. R.; Orr, B. G.; Banaszak Holl, M. M. Nanoparticle Interaction with Biological Membranes: Does Nanotechnology Present a Janus Face? *Accounts of Chemical Research* **2007**, *40* (5), 335–342.
(152) Lovrić, J.; Bazzi, H. S.; Cuie, Y.; Fortin, G. R. A.; Winnik, F. M.; Maysinger, D. Differences in Subcellular Distribution and Toxicity of Green and Red Emitting CdTe Quantum Dots. *Journal of Molecular Medicine* **2005**, *83* (5), 377–385.
(153) Montis, C.; Generini, V.; Boccalini, G.; Bergese, P.; Bani, D.; Berti, D. Model Lipid Bilayers Mimic Non-Specific Interactions of Gold Nanoparticles with Macrophage Plasma Membranes. *Journal of Colloid and Interface Science* **2018**, *516*, 284–294.
(154) Herbig, M. E.; Assi, F.; Textor, M.; Merkle, H. P. The Cell Penetrating Peptides PVEC and W2-PVEC Induce Transformation of Gel Phase Domains in Phospholipid Bilayers without Affecting Their Integrity †. *Biochemistry* **2006**, *45* (11), 3598–3609.
(155) Sandhu, K. K.; McIntosh, C. M.; Simard, J. M.; Smith, S. W.; Rotello, V. M. Gold Nanoparticle-Mediated Transfection of Mammalian Cells. *Bioconjugate Chemistry* **2002**, *13* (1), 3–6.
(156) Sheavly, J. K.; Pedersen, J. A.; Van Lehn, R. C. Curvature-Driven Adsorption of Cationic Nanoparticles to Phase Boundaries in Multicomponent Lipid Bilayers. *Nanoscale* **2019**, *11* (6), 2767–2778.
(157) Heikkilä, E.; Martinez-Seara, H.; Gurtovenko, A. A.; Vattulainen, I.; Akola, J. Atomistic Simulations of Anionic Au144(SR)60 Nanoparticles Interacting with Asymmetric Model Lipid Membranes. *Biochimica et Biophysica Acta (BBA) - Biomembranes* **2014**, *1838* (11), 2852–2860.
(158) Heikkilä, E.; Martinez-Seara, H.; Gurtovenko, A. A.; Javanainen, M.; Häkkinen, H.; Vattulainen, I.; Akola, J. Cationic Au Nanoparticle Binding with Plasma Membrane-like Lipid Bilayers: Potential Mechanism for Spontaneous

Permeation to Cells Revealed by Atomistic Simulations. *The Journal of Physical Chemistry C* **2014**, *118* (20), 11131–11141.
(159) Singer, S. J.; Nicolson, G. L. The Fluid Mosaic Model of the Structure of Cell Membranes. *Science* **1972**, *175* (4023), 720–731.
(160) Nicolson, G. Update of the 1972 Singer-Nicolson Fluid-Mosaic Model of Membrane Structure. *Discoveries* **2013**.
(161) Van Meer, G.; Voelker, D. R.; Feigenson, G. W. Membrane Lipids: Where They Are and How They Behave. *Nature Reviews Molecular Cell Biology* **2008**, *9* (2), 112–124.
(162) Harayama, T.; Riezman, H. Understanding the Diversity of Membrane Lipid Composition. *Nature Reviews Molecular Cell Biology* **2018**, *19* (5), 281–296.
(163) T. E. Thompson and C. Huang. *Membrane Physiology, Chapter 2: Composition and Dynamics of Lipidscin Biomembranes*, 2nd ed.; Dairy Science & Technology, CRC Taylor & Francis Group, 1987.
(164) Boon, J. M.; Smith, B. D. Chemical Control of Phospholipid Distribution across Bilayer Membranes. *Medicinal Research Reviews* **2002**, *22* (3), 251–281.
(165) Carreira, A. C.; Santos, T. C.; Lone, M. A.; Zupančič, E.; Lloyd-Evans, E.; de Almeida, R. F. M.; Hornemann, T.; Silva, L. C. Mammalian Sphingoid Bases: Biophysical, Physiological and Pathological Properties. *Progress in Lipid Research* **2019**, *75*, 100988.
(166) Maula, T.; Artetxe, I.; Grandell, P.-M.; Slotte, J. P. Importance of the Sphingoid Base Length for the Membrane Properties of Ceramides. *Biophysical Journal* **2012**, *103* (9), 1870–1879.
(167) Barenholz, Y.; Thompson, T. E. Sphingomyelin: Biophysical Aspects. *Chemistry and Physics of Lipids* **1999**, *102* (1–2), 29–34.
(168) Yeagle, P. L. *The Membranes of Cells The Membranes of Cells*, 3rd ed.; Elsevier, 2016.
(169) Yu, R. K.; Tsai, Y.-T.; Ariga, T.; Yanagisawa, M. Structures, Biosynthesis, and Functions of Gangliosides-an Overview. *Journal of Oleo Science* **2011**, *60* (10), 537–544.
(170) Myant, N. B. The Distribution of Sterols and Related Steroids in Nature. In *The Biology of Cholesterol and Related Steroids*; Elsevier, 1981; pp 123–159.
(171) Huang, J.; Feigenson, G. W. A Microscopic Interaction Model of Maximum Solubility of Cholesterol in Lipid Bilayers. *Biophysical Journal* **1999**, *76* (4), 2142–2157.
(172) Pradas, I.; Huynh, K.; Cabré, R.; Ayala, V.; Meikle, P. J.; Jové, M.; Pamplona, R. Lipidomics Reveals a Tissue-Specific Fingerprint. *Frontiers in Physiology* **2018**, *9*.
(173) Hoejholt, K. L.; Mužić, T.; Jensen, S. D.; Dalgaard, L. T.; Bilgin, M.; Nylandsted, J.; Heimburg, T.; Frandsen, S. K.; Gehl, J. Calcium Electroporation and Electrochemotherapy for Cancer Treatment: Importance of Cell Membrane Composition Investigated by Lipidomics, Calorimetry and in Vitro Efficacy. *Scientific Reports* **2019**, *9* (1), 4758.
(174) Szlasa, W.; Zendran, I.; Zalesińska, A.; Tarek, M.; Kulbacka, J. Lipid Composition of the Cancer Cell Membrane. *Journal of Bioenergetics and Biomembranes* **2020**, *52* (5), 321–342.

(175) Chong, P. L. G.; Zhu, W.; Venegas, B. On the Lateral Structure of Model Membranes Containing Cholesterol. *Biochimica et Biophysica Acta - Biomembranes* **2009**, *1788* (1), 2–11.
(176) Björkhem, I.; Meaney, S. Brain Cholesterol: Long Secret Life Behind a Barrier. *Arteriosclerosis, Thrombosis, and Vascular Biology* **2004**, *24* (5), 806–815.
(177) Israelachvili, J. N.; Mitchell, D. J.; Ninham, B. W. Theory of Self-Assembly of Lipid Bilayers and Vesicles. *BBA - Biomembranes* **1977**, *470* (2), 185–201.
(178) Kühne, T. D.; Khaliullin, R. Z. Electronic Signature of the Instantaneous Asymmetry in the First Coordination Shell of Liquid Water. *Nature Communications* **2013**, *4* (1), 1450.
(179) Israelachvili, J. N.; Marčelja, S.; Horn, R. G. Physical Principles of Membrane Organization. *Quarterly Reviews of Biophysics* **1980**, *13* (2), 121–200.
(180) Lewis, B. A.; Engelman, D. M. Lipid Bilayer Thickness Varies Linearly with Acyl Chain Length in Fluid Phosphatidylcholine Vesicles. *Journal of Molecular Biology* **1983**, *166* (2), 211–217.
(181) Rawicz, W.; Olbrich, K. C.; Mcintosh, T.; Needham, D.; Evans, E. Effect of Chain Length and Unsaturation on Elasticity of Lipid Bilayers. **2000**, *79* (March), 328–339.
(182) Lorent, J. H.; Levental, K. R.; Ganesan, L.; Rivera-Longsworth, G.; Sezgin, E.; Doktorova, M.; Lyman, E.; Levental, I. Plasma Membranes Are Asymmetric in Lipid Unsaturation, Packing and Protein Shape. *Nature Chemical Biology* **2020**, *16* (6), 644–652.
(183) Gennis, R. B. *Biomembranes: Molecular Structure and Function*, 1st ed.; Charles R. Cantor, Ed.; Springer Advanced Texts in Chemistry, 1989.
(184) Simons, K.; Vaz, W. L. C. Model Systems, Lipid Rafts, and Cell Membranes. *Annual Review of Biophysics and Biomolecular Structure* **2004**, *33* (1), 269–295.
(185) Contreras, F.-X.; Sánchez-Magraner, L.; Alonso, A.; Goñi, F. M. Transbilayer (Flip-Flop) Lipid Motion and Lipid Scrambling in Membranes. *FEBS Letters* **2010**, *584* (9), 1779–1786.
(186) Marsh, D. Analysis of the Bilayer Phase Transition Temperatures of Phosphatidylcholines with Mixed Chains. *Biophysical Journal* **1992**, *61* (4), 1036–1040.
(187) Cevc, G. How Membrane Chain-Melting Phase-Transition Temperature Is Affected by the Lipid Chain Asymmetry and Degree of Unsaturation: An Effective Chain-Length Model. *Biochemistry* **1991**, *30* (29), 7186–7193.
(188) Fricke, N.; Dimova, R. GM1 Softens POPC Membranes and Induces the Formation of Micron-Sized Domains. *Biophysical Journal* **2016**, *111* (9), 1935–1945.
(189) De Meyer, F.; Smit, B. Effect of Cholesterol on the Structure of a Phospholipid Bilayer. *Proceedings of the National Academy of Sciences of the United States of America* **2009**, *106* (10), 3654–3658.
(190) Kessel, A.; Ben-Tal, N.; May, S. Interactions of Cholesterol with Lipid Bilayers: The Preferred Configuration and Fluctuations. *Biophysical Journal* **2001**, *81* (2), 643–658.
(191) Huang, J.; Buboltz, J. T.; Feigenson, G. W. Maximum Solubility of Cholesterol

in Phosphatidylcholine and Phosphatidylethanolamine Bilayers. *Biochimica et Biophysica Acta - Biomembranes* **1999**, *1417* (1), 89–100.

(192) Pike, L. J. The Challenge of Lipid Rafts. *Journal of Lipid Research* **2009**, *50* (Supplement), S323–S328.

(193) Simons, K.; Ikonen, E. Functional Rafts in Cell Membranes. *Nature* **1997**, *387* (6633), 569–572.

(194) Sezgin, E.; Levental, I.; Mayor, S.; Eggeling, C. The Mystery of Membrane Organization: Composition, Regulation and Roles of Lipid Rafts. *Nature Reviews Molecular Cell Biology* **2017**, *18* (6), 361–374.

(195) Rietveld, A.; Simons, K. The Differential Miscibility of Lipids as the Basis for the Formation of Functional Membrane Rafts. *Biochimica et Biophysica Acta (BBA) - Reviews on Biomembranes* **1998**, *1376* (3), 467–479.

(196) Korade, Z.; Kenworthy, A. K. Lipid Rafts, Cholesterol, and the Brain. *Neuropharmacology*. 2008, pp 1265–1273.

(197) Brown, D. A.; London, E. Functions of Lipid Rafts in Biological Membranes. *Annual Review of Cell and Developmental Biology* **1998**, *14* (1), 111–136.

(198) Eggeling, C.; Ringemann, C.; Medda, R.; Schwarzmann, G.; Sandhoff, K.; Polyakova, S.; Belov, V. N.; Hein, B.; Von Middendorff, C.; Schönle, A.; Hell, S. W. Direct Observation of the Nanoscale Dynamics of Membrane Lipids in a Living Cell. *Nature* **2009**, *457* (7233), 1159–1162.

(199) Raghunathan, K.; Kenworthy, A. K. Dynamic Pattern Generation in Cell Membranes: Current Insights into Membrane Organization. *Biochimica et Biophysica Acta - Biomembranes* **2018**, *1860* (10), 2018–2031.

(200) Kraft, M. L. Plasma Membrane Organization and Function: Moving Past Lipid Rafts. *Molecular Biology of the Cell* **2013**, *24* (18), 2765–2768.

(201) Lichtenberg, D.; Goñi, F. M.; Heerklotz, H. Detergent-Resistant Membranes Should Not Be Identified with Membrane Rafts. *Trends in Biochemical Sciences* **2005**, *30* (8), 430–436.

(202) Krause, M. R.; Regen, S. L. The Structural Role of Cholesterol in Cell Membranes: From Condensed Bilayers to Lipid Rafts. *Accounts of Chemical Research* **2014**, *47* (12), 3512–3521.

(203) Frisz, J. F.; Lou, K.; Klitzing, H. A.; Hanafin, W. P.; Lizunov, V.; Wilson, R. L.; Carpenter, K. J.; Kim, R.; Hutcheon, I. D.; Zimmerberg, J.; Weber, P. K.; Kraft, M. L. Direct Chemical Evidence for Sphingolipid Domains in the Plasma Membranes of Fibroblasts. *Proceedings of the National Academy of Sciences* **2013**, *110* (8), E613–E622.

(204) London, E. Insights into Lipid Raft Structure and Formation from Experiments in Model Membranes. *Current Opinion in Structural Biology* **2002**, *12* (4), 480–486.

(205) Brown, D. A.; London, E. Structure and Function of Sphingolipid- and Cholesterol-Rich Membrane Rafts. *Journal of Biological Chemistry* **2000**, *275* (23), 17221–17224.

(206) Connell, S. D.; Smith, D. A. The Atomic Force Microscope as a Tool for Studying Phase Separation in Lipid Membranes (Review). *Molecular Membrane Biology* **2006**, *23* (1), 17–28.

(207) Dietrich, C.; Bagatolli, L. A.; Volovyk, Z. N.; Thompson, N. L.; Levi, M.; Jacobson, K.; Gratton, E. Lipid Rafts Reconstituted in Model Membranes. *Biophysical Journal* **2001**, *80* (3), 1417–1428.
(208) Baumgart, T.; Hess, S. T.; Webb, W. W. Imaging Coexisting Fluid Domains in Biomembrane Models Coupling Curvature and Line Tension. *Nature* **2003**, *425* (6960), 821–824.
(209) Kuzmin, P. I.; Akimov, S. A.; Chizmadzhev, Y. A.; Zimmerberg, J.; Cohen, F. S. Line Tension and Interaction Energies of Membrane Rafts Calculated from Lipid Splay and Tilt. *Biophysical Journal* **2005**, *88* (2), 1120–1133.
(210) Maulik, P. R.; Shipley, G. G. Interactions of N-Stearoyl Sphingomyelin with Cholesterol and Dipalmitoylphosphatidylcholine in Bilayer Membranes. *Biophysical Journal* **1996**, *70* (5), 2256–2265.
(211) Levental, I.; Veatch, S. L. The Continuing Mystery of Lipid Rafts. *Journal of Molecular Biology* **2016**, *428* (24), 4749–4764.
(212) Levental, I.; Wang, H. Membrane Domains beyond the Reach of Microscopy. *Journal of Lipid Research* **2020**, jlr.C120000693.
(213) Heberle, F. A.; Doktorova, M.; Scott, H. L.; Skinkle, A.; Waxham, M. N.; Levental, I. Direct Label-Free Imaging of Nanodomains in Biomimetic and Biological Membranes by Cryogenic Electron Microscopy. *bioRxiv* **2020**, 2020.02.05.935551.
(214) Li, G.; Wang, Q.; Kakuda, S.; London, E. Nanodomains Can Persist at Physiologic Temperature in Plasma Membrane Vesicles and Be Modulated by Altering Cell Lipids. *Journal of Lipid Research* **2020**, jlr.RA119000565.
(215) Baumgart, T.; Hammond, A. T.; Sengupta, P.; Hess, S. T.; Holowka, D. A.; Baird, B. A.; Webb, W. W. Large-Scale Fluid/Fluid Phase Separation of Proteins and Lipids in Giant Plasma Membrane Vesicles. *Proceedings of the National Academy of Sciences* **2007**, *104* (9), 3165–3170.
(216) Lagny, T. J.; Bassereau, P. Bioinspired Membrane-Based Systems for a Physical Approach of Cell Organization and Dynamics: Usefulness and Limitations. *Interface Focus* **2015**, *5* (4), 20150038.
(217) Chen, K. L.; Bothun, G. D. Nanoparticles Meet Cell Membranes: Probing Nonspecific Interactions Using Model Membranes. *Environmental Science & Technology* **2014**, *48* (2), 873–880.
(218) Farnoud, A. M.; Nazemidashtarjandi, S. Emerging Investigator Series: Interactions of Engineered Nanomaterials with the Cell Plasma Membrane; What Have We Learned from Membrane Models? *Environmental Science: Nano* **2019**, *6* (1), 13–40.
(219) Rascol, E.; Devoisselle, J. M.; Chopineau, J. The Relevance of Membrane Models to Understand Nanoparticles-Cell Membrane Interactions. *Nanoscale* **2016**, *8* (9), 4780–4798.
(220) Bulbake, U.; Doppalapudi, S.; Kommineni, N.; Khan, W. Liposomal Formulations in Clinical Use: An Updated Review. *Pharmaceutics* **2017**, *9* (4), 12.
(221) Morales-Penningston, N. F.; Wu, J.; Farkas, E. R.; Goh, S. L.; Konyakhina, T. M.; Zheng, J. Y.; Webb, W. W.; Feigenson, G. W. GUV Preparation and Imaging: Minimizing Artifacts. *Biochimica et Biophysica Acta (BBA) - Biomembranes*

2010, *1798* (7), 1324–1332.
(222) Méléard, P.; Bagatolli, L. A.; Pott, T. Chapter 9 - Giant Unilamellar Vesicle Electroformation: From Lipid Mixtures to Native Membranes Under Physiological Conditions. *Methods in Enzymology* **2009**, *465*, 161–176.
(223) Montes, L.-R.; Ahyayauch, H.; Ibarguren, M.; Sot, J.; Alonso, A.; Bagatolli, L. A.; Goñi, F. M. Electroformation of Giant Unilamellar Vesicles from Native Membranes and Organic Lipid Mixtures for the Study of Lipid Domains under Physiological Ionic-Strength Conditions. *Liposomes. Methods in Molecular Biology™ (Methods and Protocols)* **2010**, *606*, 105–114.
(224) Bagatolli, L. A.; Needham, D. Quantitative Optical Microscopy and Micromanipulation Studies on the Lipid Bilayer Membranes of Giant Unilamellar Vesicles. *Chemistry and Physics of Lipids* **2014**, *181*, 99–120.
(225) Kiessling, V.; Domanska, M. K.; Murray, D.; Wan, C.; Tamm, L. K. Supported Lipid Bilayers. In *Wiley Encyclopedia of Chemical Biology*; John Wiley & Sons, Inc.: Hoboken, NJ, USA, 2008.
(226) Mingeot-Leclercq, M.-P.; Deleu, M.; Brasseur, R.; Dufrêne, Y. F. Atomic Force Microscopy of Supported Lipid Bilayers. *Nature Protocols* **2008**, *3* (10), 1654–1659.
(227) Watts, T. H.; Brian, A. A.; Kappler, J. W.; Marrack, P.; McConnell, H. M. Antigen Presentation by Supported Planar Membranes Containing Affinity-Purified I-Ad. *Proceedings of the National Academy of Sciences* **1984**, *81* (23), 7564–7568.
(228) McConnell, H. M.; Watts, T. H.; Weis, R. M.; Brian, A. A. Supported Planar Membranes in Studies of Cell-Cell Recognition in the Immune System. *Biochimica et Biophysica Acta (BBA) - Reviews on Biomembranes* **1986**, *864* (1), 95–106.
(229) Castellana, E. T.; Cremer, P. S. Solid Supported Lipid Bilayers: From Biophysical Studies to Sensor Design. *Surface Science Reports* **2006**, *61* (10), 429–444.
(230) Gunderson, R. S.; Honerkamp-Smith, A. R. Liquid-Liquid Phase Transition Temperatures Increase When Lipid Bilayers Are Supported on Glass. *Biochimica et Biophysica Acta - Biomembranes* **2018**, *1860* (10), 1965–1971.
(231) Wu, H.-L.; Chen, P.-Y.; Chi, C.-L.; Tsao, H.-K.; Sheng, Y.-J. Vesicle Deposition on Hydrophilic Solid Surfaces. *Soft Matter* **2013**, *9* (6), 1908–1919.
(232) Richter, R. P.; Brisson, A. R. Following the Formation of Supported Lipid Bilayers on Mica: A Study Combining AFM, QCM-D, and Ellipsometry. *Biophysical Journal* **2005**, *88* (5), 3422–3433.
(233) Richter, R.; Mukhopadhyay, A.; Brisson, A. Pathways of Lipid Vesicle Deposition on Solid Surfaces: A Combined QCM-D and AFM Study. *Biophysical Journal* **2003**, *85* (5), 3035–3047.
(234) Seantier, B.; Kasemo, B. Influence of Mono- And Divalent Ions on the Formation of Supported Phospholipid Bilayers via Vesicle Adsorption. *Langmuir* **2009**, *25* (10), 5767–5772.
(235) Lu, Z.; Zhang, Z.; Pang, D. *Atomic Force Microscopy in Molecular and Cell Biology*; Cai, J., Ed.; Springer Singapore: Singapore, 2018; Vol. 50.

(236) Binnig, G.; Quate, C. F.; Gerber, C. Atomic Force Microscope. *Physical Review Letters* **1986**, *56* (9), 930–933.
(237) Garcia, R. Nanomechanical Mapping of Soft Materials with the Atomic Force Microscope: Methods, Theory and Applications. *Chemical Society Reviews* **2020**, *49* (16), 5850–5884.
(238) Binnig, G.; Smith, D. P. E. Single-tube Three-dimensional Scanner for Scanning Tunneling Microscopy. *Review of Scientific Instruments* **1986**, *57* (8), 1688–1689.
(239) Taylor, M. E. Dynamics of Piezoelectric Tube Scanners for Scanning Probe Microscopy. *Review of Scientific Instruments* **1993**, *64* (1), 154–158.
(240) Meyer, G.; Amer, N. M. Novel Optical Approach to Atomic Force Microscopy. *Applied Physics Letters* **1988**, *53* (12), 1045–1047.
(241) Park, S.; Costa, K. D.; Ateshian, G. A. Microscale Frictional Response of Bovine Articular Cartilage from Atomic Force Microscopy. *Journal of Biomechanics* **2004**, *37* (11), 1679–1687.
(242) Miller, E. J.; Trewby, W.; Farokh Payam, A.; Piantanida, L.; Cafolla, C.; Voïtchovsky, K. Sub-Nanometer Resolution Imaging with Amplitude-Modulation Atomic Force Microscopy in Liquid. *Journal of Visualized Experiments* **2016**, No. 118.
(243) Stark, M.; Möller, C.; Müller, D. J.; Guckenberger, R. From Images to Interactions: High-Resolution Phase Imaging in Tapping-Mode Atomic Force Microscopy. *Biophysical Journal* **2001**, *80* (6), 3009–3018.
(244) Butt, H.-J.; Cappella, B.; Kappl, M. Force Measurements with the Atomic Force Microscope: Technique, Interpretation and Applications. *Surface Science Reports* **2005**, *59* (1–6), 1–152.
(245) Hutter, J. L.; Bechhoefer, J. Calibration of Atomic-force Microscope Tips. *Review of Scientific Instruments* **1993**, *64* (7), 1868–1873.
(246) Butt, H.-J.; Jaschke, M. Calculation of Thermal Noise in Atomic Force Microscopy. *Nanotechnology* **1995**, *6* (1), 1–7.
(247) Neumann, T. Determining the Elastic Modulus of Biological Samples Using Atomic Force Microscopy. *JPK Instrument - Application Note* 1–9.
(248) Sauerbrey, G. Verwendung von Schwingquarzen Zur Wägung Dünner Schichten Und Zur Mikrowägung. *Zeitschrift für Physik* **1959**, *155* (2), 206–222.
(249) Arnau, A.; Montagut, Y.; García, J. V; Jiménez, Y. A Different Point of View on the Sensitivity of Quartz Crystal Microbalance Sensors. *Measurement Science and Technology* **2009**, *20* (12), 124004.
(250) Mueller, R. M.; White, W. Direct Gravimetric Calibration of a Quartz Crystal Microbalance. *Review of Scientific Instruments* **1968**, *39* (3), 291–295.
(251) Lu, C.; Lewis, O. Investigation of Film-thickness Determination by Oscillating Quartz Resonators with Large Mass Load. *Journal of Applied Physics* **1972**, *43* (11), 4385–4390.
(252) Kurosawa, S.; Tawara, E.; Kamo, N.; Kobatake, Y. Oscillating Frequency of Piezoelectric Quartz Crystal in Solutions. *Analytica Chimica Acta* **1990**, *230*, 41–49.
(253) Nomura, T.; Okuhara, M. Frequency Shifts of Piezoelectric Quartz Crystals

Immersed in Organic Liquids. *Analytica Chimica Acta* **1982**, *142*, 281–284.
(254) Kanazawa, K. K.; Gordon, J. G. Frequency of a Quartz Microbalance in Contact with Liquid. *Analytical Chemistry* **1985**, *57* (8), 1770–1771.
(255) Johannsmann, D. Viscoelastic, Mechanical, and Dielectric Measurements on Complex Samples with the Quartz Crystal Microbalance. *Physical Chemistry Chemical Physics* **2008**, *10* (31), 4516.
(256) Voinova, M. V; Rodahl, M.; Jonson, M.; Kasemo, B. Viscoelastic Acoustic Response of Layered Polymer Films at Fluid-Solid Interfaces: Continuum Mechanics Approach. *Physica Scripta* **1999**, *59* (5), 391–396.
(257) Reviakine, I.; Rossetti, F. F.; Morozov, A. N.; Textor, M. Investigating the Properties of Supported Vesicular Layers on Titanium Dioxide by Quartz Crystal Microbalance with Dissipation Measurements. *The Journal of Chemical Physics* **2005**, *122* (20), 204711.
(258) Ashrafuzzaman, M.; Andersen, O. S.; McElhaney, R. N. The Antimicrobial Peptide Gramicidin S Permeabilizes Phospholipid Bilayer Membranes without Forming Discrete Ion Channels. *Biochimica et Biophysica Acta (BBA) - Biomembranes* **2008**, *1778* (12), 2814–2822.
(259) Weidema, A. F.; Kropacheva, T. N.; Raap, J.; Ypey, D. L. Membrane Permeabilization of a Mammalian Neuroendocrine Cell Type (PC12) by the Channel-Forming Peptides Zervamicin, Alamethicin, and Gramicidin. *Chemistry & Biodiversity* **2007**, *4* (6), 1347–1359.
(260) van Rooijen, B. D.; Claessens, M. M. A. E.; Subramaniam, V. Membrane Permeabilization by Oligomeric α-Synuclein: In Search of the Mechanism. *PLoS ONE* **2010**, *5* (12), e14292.
(261) Stefanovic, A. N. D.; Stöckl, M. T.; Claessens, M. M. A. E.; Subramaniam, V. α-Synuclein Oligomers Distinctively Permeabilize Complex Model Membranes. *FEBS Journal* **2014**, *281* (12), 2838–2850.
(262) Bashford, C. L. Membrane Permeabilization with Bacterial Toxins. *Biomembrane Protocols. Methods in Molecular Biology, Springer* **1994**, *27*, 295–306.
(263) Liu, J. Interfacing Zwitterionic Liposomes with Inorganic Nanomaterials: Surface Forces, Membrane Integrity, and Applications. *Langmuir* **2016**, *32* (18), 4393–4404.
(264) Moghadam, B. Y.; Hou, W. C.; Corredor, C.; Westerhoff, P.; Posner, J. D. Role of Nanoparticle Surface Functionality in the Disruption of Model Cell Membranes. *Langmuir* **2012**, *28* (47), 16318–16326.
(265) Allen, T. M.; Cleland, L. G. Serum-Induced Leakage of Liposome Contents. *BBA - Biomembranes* **1980**, *597* (2), 418–426.
(266) Dutta, S.; Watson, B.; Mattoo, S.; Rochet, J.-C. Calcein Release Assay to Measure Membrane Permeabilization by Recombinant Alpha-Synuclein. *BIO-PROTOCOL* **2020**, *10* (14).
(267) Salassi, S.; Simonelli, F.; Bartocci, A.; Rossi, G. A Martini Coarse-Grained Model of the Calcein Fluorescent Dye. *Journal of Physics D: Applied Physics* **2018**, *51* (38), 384002.
(268) Relini, A.; Cassinadri, D.; Fan, Q.; Gulik, A.; Mirghani, Z.; De Rosa, M.; Gliozzi, A. Effect of Physical Constraints on the Mechanisms of Membrane

Fusion: Bolaform Lipid Vesicles as Model Systems. *Biophysical Journal* **1996**, *71* (4), 1789–1795.

(269) Lasch, J.; Weissig, W.; Brandl, M. Preparation of Liposomes. In *Liposomes: A Practical Approach*; Torchilin, Vladimir and Weissig, V., Ed.; Oxford University Press, 2003; pp 33–104.

(270) Badley, R. A.; Martin, W. G.; Schneider, H. Dynamic Behavior of Fluorescent Probes in Lipid Bilayer Model Membranes. *Biochemistry* **1973**, *12* (2), 268–275.

(271) Kawato, S.; Kinosita, K.; Ikegami, A. Dynamic Structure of Lipid Bilayers Studied by Nanosecond Fluorescence Techniques. *Biochemistry* **1977**, *16* (11), 2319–2324.

(272) Mély-Goubert, B.; Freedman, M. H. Lipid Fluidity and Membrane Protein Monitoring Using 1,6-Diphenyl-1,3,5-Hexatriene. *Biochimica et Biophysica Acta (BBA) - Biomembranes* **1980**, *601*, 315–327.

(273) Paloncýová, M.; Ameloot, M.; Knippenberg, S. Orientational Distribution of DPH in Lipid Membranes: A Comparison of Molecular Dynamics Calculations and Experimental Time-Resolved Anisotropy Experiments. *Physical Chemistry Chemical Physics* **2019**, *21* (14), 7594–7604.

(274) Kaiser, R. D.; London, E. Location of Diphenylhexatriene (DPH) and Its Derivatives within Membranes: Comparison of Different Fluorescence Quenching Analyses of Membrane Depth. *Biochemistry* **1998**, *37* (22), 8180–8190.

(275) Lakowicz; Prendergast, F. Quantitation of Hindered Rotations of Diphenylhexatriene in Lipid Bilayers by Differential Polarized Phase Fluorometry. *Science* **1978**, *200* (4348), 1399–1401.

(276) do Canto, A. M. T. M.; Robalo, J. R.; Santos, P. D.; Carvalho, A. J. P.; Ramalho, J. P. P.; Loura, L. M. S. Diphenylhexatriene Membrane Probes DPH and TMA-DPH: A Comparative Molecular Dynamics Simulation Study. *Biochimica et Biophysica Acta - Biomembranes* **2016**, *1858* (11), 2647–2661.

(277) Lakowicz, J. R. *Principles of Fluorescence Spectroscopy*, 3rd editio.; Springer New York, 2006.

(278) Kawski, A.; Gryczyński, Z. On the Determination of Transition-Moment Directions from Emission Anisotropy Measurements. *Zeitschrift fur Naturforschung - Section A Journal of Physical Sciences* **1986**, *41* (10), 1195–1199.

(279) Kawski, A.; Gryczyński, Z. On the Determination of Transition-Moment Directions from Absorption Anisotropy Measurements. *Zeitschrift für Naturforschung A* **1987**, *42* (6), 617–621.

(280) Corry, B.; Jayatilaka, D.; Martinac, B.; Rigby, P. Determination of the Orientational Distribution and Orientation Factor for Transfer between Membrane-Bound Fluorophores Using a Confocal Microscope. *Biophysical Journal* **2006**, *91* (3), 1032–1045.

(281) Mu, T.; Chen, S.; Zhang, Y.; Guo, P.; Chen, H. Determining the Orientation of Transition Moments and Depolarization by Fluorescence Polarizing Angle Spectrum. *Optics Express* **2015**, *23* (9), 11748.

(282) Muller, J. M.; Harryvan, D. H.; Verhagen, J. C. D.; Van Ginkel, G.; Van Faassen, E. E. The Orientation of the Transition Dipole Moments of TMA-

DPH Embedded in a Poly(Vinylalcohol) Film. *Chemical Physics* **1996**, *211* (1–3), 413–420.

(283) Jabłoński, A. On the Notion of Emission Anisotropy. *Bull. Acad. Polon. Sci., Ser. sci. math. astr. phys.* **1960**, *8*, 259–264.

(284) Zheng, N.; Fan, J.; Stucky, G. D. One-Step One-Phase Synthesis of Monodisperse Noble-Metallic Nanoparticles and Their Colloidal Crystals. *Journal of the American Chemical Society* **2006**, *128* (20), 6550–6551.

(285) Guven, Z. P.; Jacob Silva, P. H.; Luo, Z.; Cendrowska, U. B.; Gasbarri, M.; Jones, S. T.; Stellacci, F. Synthesis and Characterization of Amphiphilic Gold Nanoparticles. *Journal of Visualized Experiments* **2019**, *2019* (149), 1–11.

(286) Templeton, A. C.; Hostetler, M. J.; Kraft, C. T.; Murray, R. W. Reactivity of Monolayer-Protected Gold Cluster Molecules: Steric Effects. *Journal of the American Chemical Society* **1998**, *120* (8), 1906–1911.

(287) Henrique, P.; Silva, J. Discriminative Adsorption of Amphiphilic Monolayer Protected Gold Nanoparticles on Amyloid Fibers. *EPFL Doctorate thesis* **2016**, *7037*.

(288) Bhattacharjee, S. DLS and Zeta Potential - What They Are and What They Are Not? *Journal of Controlled Release* **2016**, *235*, 337–351.

(289) Grobelny, J.; DelRio, F. W.; Pradeep, N.; Kim, D.-I.; Hackley, V. A.; Cook, R. F. Size Measurement of Nanoparticles Using Atomic Force Microscopy; 2011; pp 71–82.

(290) Amendola, V.; Meneghetti, M.; Amendola, V.; Meneghetti, M. Size Evaluation of Gold Nanoparticles by UV # Vis Spectroscopy Size Evaluation of Gold Nanoparticles by UV - Vis Spectroscopy. **2009**, *113* (February), 4277–4285.

(291) Ong, Q.; Luo, Z.; Stellacci, F. Characterization of Ligand Shell for Mixed-Ligand Coated Gold Nanoparticles. *Accounts of Chemical Research* **2017**, *50* (8), 1911–1919.

(292) Colangelo, E.; Comenge, J.; Paramelle, D.; Volk, M.; Chen, Q.; Lévy, R. Characterizing Self-Assembled Monolayers on Gold Nanoparticles. *Bioconjugate Chemistry* **2017**, *28* (1), 11–22.

(293) Mourdikoudis, S.; Liz-Marzán, L. M. Oleylamine in Nanoparticle Synthesis. *Chemistry of Materials* **2013**, *25* (9), 1465–1476.

(294) Yang, Y.; Serrano, L. A.; Guldin, S. A Versatile AuNP Synthetic Platform for Decoupled Control of Size and Surface Composition. *Langmuir* **2018**, *34* (23), 6820–6826.

(295) Peng, S.; Lee, Y.; Wang, C.; Yin, H.; Dai, S.; Sun, S. A Facile Synthesis of Monodisperse Au Nanoparticles and Their Catalysis of CO Oxidation. *Nano Research* **2008**, *1* (3), 229–234.

(296) Kluenker, M.; Mondeshki, M.; Nawaz Tahir, M.; Tremel, W. Monitoring Thiol-Ligand Exchange on Au Nanoparticle Surfaces. *Langmuir* **2018**, *34* (4), 1700–1710.

(297) Wu, B. H.; Yang, H. Y.; Huang, H. Q.; Chen, G. X.; Zheng, N. F. Solvent Effect on the Synthesis of Monodisperse Amine-Capped Au Nanoparticles. *Chinese Chemical Letters* **2013**, *24* (6), 457–462.

(298) Chen, Y.; Bothun, G. D. Cationic Gel-Phase Liposomes with "Decorated"

Anionic SPIO Nanoparticles: Morphology, Colloidal, and Bilayer Properties. *Langmuir* **2011**, *27* (14), 8645–8652.

(299) Wei, X.; Yu, J.; Ding, L.; Hu, J.; Jiang, W. Effect of Oxide Nanoparticles on the Morphology and Fluidity of Phospholipid Membranes and the Role of Hydrogen Bonds. *Journal of Environmental Sciences* **2017**, *57*, 221–230.

(300) Neal, A. L. What Can Be Inferred from Bacterium-Nanoparticle Interactions about the Potential Consequences of Environmental Exposure to Nanoparticles? *Ecotoxicology* **2008**, *17* (5), 362–371.

(301) Feng, Z. V.; Gunsolus, I. L.; Qiu, T. A.; Hurley, K. R.; Nyberg, L. H.; Frew, H.; Johnson, K. P.; Vartanian, A. M.; Jacob, L. M.; Lohse, S. E.; Torelli, M. D.; Hamers, R. J.; Murphy, C. J.; Haynes, C. L. Impacts of Gold Nanoparticle Charge and Ligand Type on Surface Binding and Toxicity to Gram-Negative and Gram-Positive Bacteria. *Chem. Sci.* **2015**, *6* (9), 5186–5196.

(302) Zhang, S.; Nelson, A.; Beales, P. A. Freezing or Wrapping: The Role of Particle Size in the Mechanism of Nanoparticle Biomembrane Interaction. *Langmuir* **2012**, *28* (35), 12831–12837.

(303) Sevink, G. J. A.; Liwo, J. A.; Asinari, P.; Mackernan, D.; Milano, G.; Pagonabarraga, I. Unfolding the Prospects of Computational (Bio) Materials Modeling. *Journal of Chemical Physics* **2020**, *153*, 100901.

(304) Smith, M. C.; Crist, R. M.; Clogston, J. D.; McNeil, S. E. Zeta Potential: A Case Study of Cationic, Anionic, and Neutral Liposomes. *Analytical and Bioanalytical Chemistry* **2017**, *409* (24), 5779–5787.

(305) Kunze, A.; Zäch, M.; Svedhem, S.; Kasemo, B. Electrodeless QCM-D for Lipid Bilayer Applications. *Biosensors and Bioelectronics* **2011**, *26* (5), 1833–1838.

(306) Salis, B.; Pugliese, G.; Pellegrino, T.; Diaspro, A.; Dante, S. Polymer Coating and Lipid Phases Regulate Semiconductor Nanorods' Interaction with Neuronal Membranes: A Modeling Approach. *ACS Chemical Neuroscience* **2019**, *10* (1), 618–627.

(307) Jyothi, G.; Mitra, C. K.; Krishnamoorthy, G. Studies on the Kinetics of Gramicidin Channels in Liposomes. Part I. *Bioelectrochemistry and Bioenergetics* **1990**, *24* (3), 297–304.

(308) Marrink, S. J.; Risselada, H. J.; Yefimov, S.; Tieleman, D. P.; de Vries, A. H. The MARTINI Force Field: Coarse Grained Model for Biomolecular Simulations. *The Journal of Physical Chemistry B* **2007**, *111* (27), 7812–7824.

(309) Yesylevskyy, S. O.; Schäfer, L. V.; Sengupta, D.; Marrink, S. J. Polarizable Water Model for the Coarse-Grained MARTINI Force Field. *PLoS Computational Biology* **2010**, *6* (6), e1000810.

(310) Laio, A.; Gervasio, F. L. Metadynamics: A Method to Simulate Rare Events and Reconstruct the Free Energy in Biophysics, Chemistry and Material Science. *Reports on Progress in Physics* **2008**, *71* (12), 126601.

(311) Gaus, K.; Gratton, E.; Kable, E. P. W.; Jones, A. S.; Gelissen, I.; Kritharides, L.; Jessup, W. Visualizing Lipid Structure and Raft Domains in Living Cells with Two-Photon Microscopy. *Proceedings of the National Academy of Sciences* **2003**, *100* (26), 15554–15559.

(312) Sahl, S. J.; Leutenegger, M.; Hilbert, M.; Hell, S. W.; Eggeling, C. Fast Molecular

Tracking Maps Nanoscale Dynamics of Plasma Membrane Lipids. *Proceedings of the National Academy of Sciences* **2010**, *107* (15), 6829–6834.

(313) Chen, X.; Tieleman, D. P.; Liang, Q. Modulating Interactions between Ligand-Coated Nanoparticles and Phase-Separated Lipid Bilayers by Varying the Ligand Density and the Surface Charge. *Nanoscale* **2018**.

(314) Lin, X.; Lin, X.; Gu, N. Optimization of Hydrophobic Nanoparticles to Better Target Lipid Rafts with Molecular Dynamics Simulations. *Nanoscale* **2020**, *12* (6), 4101–4109.

(315) Tiwari, A.; Prince, A.; Arakha, M.; Jha, S.; Saleem, M. Passive Membrane Penetration by ZnO Nanoparticles Is Driven by the Interplay of Electrostatic and Phase Boundary Conditions. *Nanoscale* **2018**, *10* (7), 3369–3384.

(316) Bhat, A.; Edwards, L. W.; Fu, X.; Badman, D. L.; Huo, S.; Jin, A. J.; Lu, Q. Effects of Gold Nanoparticles on Lipid Packing and Membrane Pore Formation. *Applied Physics Letters* **2016**, *109* (26), 263106.

(317) Melby, E. S.; Mensch, A. C.; Lohse, S. E.; Hu, D.; Orr, G.; Murphy, C. J.; Hamers, R. J.; Pedersen, J. A. Formation of Supported Lipid Bilayers Containing Phase-Segregated Domains and Their Interaction with Gold Nanoparticles. *Environmental Science: Nano* **2016**, *3* (1), 45–55.

(318) Egawa, J.; Pearn, M. L.; Lemkuil, B. P.; Patel, P. M.; Head, B. P. Membrane Lipid Rafts and Neurobiology: Age-Related Changes in Membrane Lipids and Loss of Neuronal Function. *Journal of Physiology* **2016**, *594* (16), 4565–4579.

(319) Linetti, A.; Fratangeli, A.; Taverna, E.; Valnegri, P.; Francolini, M.; Cappello, V.; Matteoli, M.; Passafaro, M.; Rosa, P. Cholesterol Reduction Impairs Exocytosis of Synaptic Vesicles. *Journal of Cell Science* **2010**, *123* (4), 595–605.

(320) Oropesa-Nuñez, R.; Seghezza, S.; Dante, S.; Diaspro, A.; Cascella, R.; Cecchi, C.; Stefani, M.; Chiti, F.; Canale, C. Interaction of Toxic and Non-Toxic HypF-N Oligomers with Lipid Bilayers Investigated at High Resolution with Atomic Force Microscopy. *Oncotarget* **2016**, *7* (29), 44991–45004.

(321) Puff, N.; Watanabe, C.; Seigneuret, M.; Angelova, M. I.; Staneva, G. Lo/Ld Phase Coexistence Modulation Induced by GM1. *Biochimica et Biophysica Acta - Biomembranes* **2014**, *1838* (8), 2105–2114.

(322) Veatch, S. L.; Keller, S. L. Separation of Liquid Phases in Giant Vesicles of Ternary Mixtures of Phospholipids and Cholesterol. *Biophysical Journal* **2003**, *85* (5), 3074–3083.

(323) Bao, R.; Li, L.; Qiu, F.; Yang, Y. Atomic Force Microscopy Study of Ganglioside GM1 Concentration Effect on Lateral Phase Separation of Sphingomyelin/Dioleoylphosphatidylcholine/ Cholesterol Bilayers. *Journal of Physical Chemistry B* **2011**, *115* (19), 5923–5929.

(324) Leri, M.; Oropesa-Nuñez, R.; Canale, C.; Raimondi, S.; Giorgetti, S.; Bruzzone, E.; Bellotti, V.; Stefani, M.; Bucciantini, M. Oleuropein Aglycone: A Polyphenol with Different Targets against Amyloid Toxicity. *Biochimica et Biophysica Acta - General Subjects* **2018**, *1862* (6), 1432–1442.

(325) Leri, M.; Bemporad, F.; Oropesa-Nuñez, R.; Canale, C.; Calamai, M.; Nosi, D.; Ramazzotti, M.; Giorgetti, S.; Pavone, F. S.; Bellotti, V.; Stefani, M.; Bucciantini, M. Molecular Insights into Cell Toxicity of a Novel Familial Amyloidogenic

Variant of B2-Microglobulin. *Journal of Cellular and Molecular Medicine* **2016**, *20* (8), 1443–1456.
(326) Samsonov, A. V.; Mihalyov, I.; Cohen, F. S. Characterization of Cholesterol-Sphingomyelin Domains and Their Dynamics in Bilayer Membranes. *Biophysical Journal* **2001**, *81* (3), 1486–1500.
(327) Frolov, V. A. J.; Chizmadzhev, Y. A.; Cohen, F. S.; Zimmerberg, J. "Entropic Traps" in the Kinetics of Phase Separation in Multicomponent Membranes Stabilize Nanodomains. *Biophysical Journal* **2006**, *91* (1), 189–205.
(328) García-Sáez, A. J.; Chiantia, S.; Schwille, P. Effect of Line Tension on the Lateral Organization of Lipid Membranes. *Journal of Biological Chemistry* **2007**, *282* (46), 33537–33544.
(329) Akimov, S. A.; Hlaponin, E. A.; Bashkirov, P. V.; Boldyrev, I. A.; Mikhalyov, I. I.; Telford, W. G.; Molotkovskaya, I. M. Ganglioside GM1 Increases Line Tension at Raft Boundary in Model Membranes. *Biochemistry (Moscow) Supplement Series A: Membrane and Cell Biology* **2009**, *3* (2), 216–222.
(330) Tahir, M. A.; Van Lehn, R. C.; Choi, S. H.; Alexander-Katz, A. Solvent-Exposed Lipid Tail Protrusions Depend on Lipid Membrane Composition and Curvature. *Biochimica et Biophysica Acta (BBA) - Biomembranes* **2016**, *1858* (6), 1207–1215.
(331) Van Lehn, R. C.; Alexander-Katz, A. Pathway for Insertion of Amphiphilic Nanoparticles into Defect-Free Lipid Bilayers from Atomistic Molecular Dynamics Simulations. *Soft Matter* **2015**, *11* (16), 3165–3175.
(332) Macháň, R.; Hof, M. Recent Developments in Fluorescence Correlation Spectroscopy for Diffusion Measurements in Planar Lipid Membranes. *International Journal of Molecular Sciences* **2010**, *11* (2), 427–457.
(333) Guo, L.; Har, J. Y.; Sankaran, J.; Hong, Y.; Kannan, B.; Wohland, T. Molecular Diffusion Measurement in Lipid Bilayers over Wide Concentration Ranges: A Comparative Study. *ChemPhysChem* **2008**, *9* (5), 721–728.
(334) Fricke, N.; Dimova, R. GM1 Softens POPC Membranes and Induces the Formation of Micron-Sized Domains. *Biophysical Journal* **2016**, *111* (9), 1935–1945.
(335) Gazit, E.; Miller, I. R.; Biggin, P. C.; Sansom, M. S. P.; Shai, Y. Structure and Orientation of the Mammalian Antibacterial Peptide Cecropin P1 within Phospholipid Membranes. *Journal of Molecular Biology* **1996**, *258* (5), 860–870.
(336) Zwang, T. J.; Fletcher, W. R.; Lane, T. J.; Johal, M. S. Quantification of the Layer of Hydration of a Supported Lipid Bilayer. *Langmuir* **2010**, *26* (7), 4598–4601.
(337) Kučerka, N.; Tristram-Nagle, S.; Nagle, J. F. Structure of Fully Hydrated Fluid Phase Lipid Bilayers with Monounsaturated Chains. *Journal of Membrane Biology* **2006**, *208* (3), 193–202.
(338) Almeida, P. F. F. Thermodynamics of Lipid Interactions in Complex Bilayers. *Biochimica et Biophysica Acta - Biomembranes* **2009**, *1788* (1), 72–85.
(339) Barnoud, J.; Rossi, G.; Monticelli, L. Lipid Membranes as Solvents for Carbon Nanoparticles. *Physical Review Letters* **2014**, *112* (6), 068102.
(340) Barnoud, J.; Rossi, G.; Marrink, S. J.; Monticelli, L. Hydrophobic Compounds

Reshape Membrane Domains. *PLoS Computational Biology* **2014**, *10* (10).
(341) Monticelli, L. On Atomistic and Coarse-Grained Models for C 60 Fullerene. *Journal of Chemical Theory and Computation* **2012**, *8* (4), 1370–1378.
(342) Ha, Y.; Katz, L. E.; Liljestrand, H. M. Distribution of Fullerene Nanoparticles between Water and Solid Supported Lipid Membranes: Thermodynamics and Effects of Membrane Composition on Distribution. *Environmental Science and Technology* **2015**, *49* (24), 14546–14553.
(343) Angelikopoulos, P.; Sarkisov, L.; Cournia, Z.; Gkeka, P. Self-Assembly of Anionic, Ligand-Coated Nanoparticles in Lipid Membranes. *Nanoscale* **2017**, *9* (3), 1040–1048.
(344) Alonso, M. A.; Millán, J. The Role of Lipid Rafts in Signalling and Membrane Trafficking in T Lymphocytes. *Journal of Cell Science* **2001**, *114* (22), 3957–3965.
(345) Ikonen, E. Roles of Lipid Rafts in Membrane Transport. *Current Opinion in Cell Biology* **2001**, *13* (4), 470–477.
(346) Liscum, L.; Munn, N. J. Intracellular Cholesterol Transport. *Biochimica et Biophysica Acta (BBA) - Molecular and Cell Biology of Lipids* **1999**, *1438* (1), 19–37.
(347) Molugu, T. R.; Brown, M. F. Cholesterol Effects on the Physical Properties of Lipid Membranes Viewed by Solid-State NMR Spectroscopy; 2019; pp 99–133.
(348) Subczynski, W. K.; Pasenkiewicz-Gierula, M.; Widomska, J.; Mainali, L.; Raguz, M. High Cholesterol/Low Cholesterol: Effects in Biological Membranes: A Review. *Cell Biochemistry and Biophysics* **2017**, *75* (3–4), 369–385.
(349) Lavie, Y.; Fiucci, G.; Czarny, M.; Liscovitch, M. Changes in Membrane Microdomains and Caveolae Constituents in Multidrug- Resistant Cancer Cells. *Lipids* **1999**, *34* (1), 57–63.
(350) Silvius, J. R.; del Giudice, D.; Lafleur, M. Cholesterol at Different Bilayer Concentrations Can Promote or Antagonize Lateral Segregation of Phospholipids of Differing Acyl Chain Length †. *Biochemistry* **1996**, *35* (48), 15198–15208.
(351) Polozov, I. V.; Gawrisch, K. Characterization of the Liquid-Ordered State by Proton MAS NMR. *Biophysical Journal* **2006**, *90* (6), 2051–2061.
(352) Biswas, A.; Kashyap, P.; Datta, S.; Sengupta, T.; Sinha, B. Cholesterol Depletion by MβCD Enhances Cell Membrane Tension and Its Variations-Reducing Integrity. *Biophysical Journal* **2019**, *116* (8), 1456–1468.
(353) Kumar, M.; Irungbam, K.; Kataria, M. Depletion of Membrane Cholesterol Compromised Caspase-8 Imparts in Autophagy Induction and Inhibition of Cell Migration in Cancer Cells. *Cancer Cell International* **2018**, *18* (1), 23.
(354) Bothun, G. D. Hydrophobic Silver Nanoparticles Trapped in Lipid Bilayers: Size Distribution, Bilayer Phase Behavior, and Optical Properties. *Journal of Nanobiotechnology* **2008**, *6*, 1–10.
(355) Park, S. H.; Oh, S. G.; Mun, J. Y.; Han, S. S. Effects of Silver Nanoparticles on the Fluidity of Bilayer in Phospholipid Liposome. *Colloids and Surfaces B: Biointerfaces* **2005**, *44* (2–3), 117–122.
(356) Park, S. H.; Oh, S. G.; Mun, J. Y.; Han, S. S. Loading of Gold Nanoparticles inside the DPPC Bilayers of Liposome and Their Effects on Membrane Fluidities. *Colloids and Surfaces B: Biointerfaces* **2006**, *48* (2), 112–118.

(357) Hoffmann, I.; Michel, R.; Sharp, M.; Holderer, O.; Appavou, M. S.; Polzer, F.; Farago, B.; Gradzielski, M. Softening of Phospholipid Membranes by the Adhesion of Silica Nanoparticles - As Seen by Neutron Spin-Echo (NSE). *Nanoscale* **2014**, *6* (12), 6945–6952.
(358) Montis, C.; Maiolo, D.; Alessandri, I.; Bergese, P.; Berti, D. Interaction of Nanoparticles with Lipid Membranes: A Multiscale Perspective. *Nanoscale* **2014**, *6* (12), 6452–6457.
(359) Wang, B.; Zhang, L.; Sung, C. B.; Granick, S. Nanoparticle-Induced Surface Reconstruction of Phospholipid Membranes. *Proceedings of the National Academy of Sciences of the United States of America* **2008**, *105* (47), 18171–18175.
(360) Wei, X.; Jiang, W.; Yu, J.; Ding, L.; Hu, J.; Jiang, G. Effects of SiO2 Nanoparticles on Phospholipid Membrane Integrity and Fluidity. *Journal of Hazardous Materials* **2015**, *287*, 217–224.
(361) Li, Y.; Gu, N. Thermodynamics of Charged Nanoparticle Adsorption on Charge-Neutral Membranes: A Simulation Study. *Journal of Physical Chemistry B* **2010**, *114* (8), 2749–2754.
(362) Gkeka, P.; Angelikopoulos, P.; Sarkisov, L.; Cournia, Z. Membrane Partitioning of Anionic, Ligand-Coated Nanoparticles Is Accompanied by Ligand Snorkeling, Local Disordering, and Cholesterol Depletion. *PLoS Computational Biology* **2014**, *10* (12).
(363) Zhao, J.; Wu, J.; Heberle, F. A.; Mills, T. T.; Klawitter, P.; Huang, G.; Costanza, G.; Feigenson, G. W. Phase Studies of Model Biomembranes: Complex Behavior of DSPC/DOPC/Cholesterol. *Biochimica et Biophysica Acta - Biomembranes* **2007**, *1768* (11), 2764–2776.
(364) Suga, K.; Umakoshi, H. Detection of Nanosized Ordered Domains in DOPC/DPPC and DOPC/CH Binary Lipid Mixture Systems of Large Unilamellar Vesicles Using a TEMPO Quenching Method. *Langmuir* **2013**, *29* (15), 4830–4838.
(365) Chakraborty, S.; Doktorova, M.; Molugu, T. R.; Heberle, F. A.; Scott, H. L.; Dzikovski, B.; Nagao, M.; Stingaciu, L. R.; Standaert, R. F.; Barrera, F. N.; Katsaras, J.; Khelashvili, G.; Brown, M. F.; Ashkar, R. How Cholesterol Stiffens Unsaturated Lipid Membranes. *Proceedings of the National Academy of Sciences of the United States of America* **2020**, *117* (36), 21896–21905.
(366) Picas, L.; Rico, F.; Scheuring, S. Direct Measurement of the Mechanical Properties of Lipid Phases in Supported Bilayers. *Biophysical Journal* **2012**, *102* (1), L01–L03.
(367) Yi, P.; Chen, K. L. Interaction of Multiwalled Carbon Nanotubes with Supported Lipid Bilayers and Vesicles as Model Biological Membranes. *Environmental science & technology* **2013**, *47* (11), 5711–5719.
(368) Zhu, B.; Wei, X.; Song, J.; Zhang, Q.; Jiang, W. Crystalline Phase and Surface Coating of Al2O3 Nanoparticles and Their Influence on the Integrity and Fluidity of Model Cell Membranes. *Chemosphere* **2020**, *247*, 125876.
(369) Jurak, M. Thermodynamic Aspects of Cholesterol Effect on Properties of Phospholipid Monolayers: Langmuir and Langmuir–Blodgett Monolayer Study. *The Journal of Physical Chemistry B* **2013**, *117* (13), 3496–3502.

(370) Pan, J.; Tristram-Nagle, S.; Nagle, J. F. Effect of Cholesterol on Structural and Mechanical Properties of Membranes Depends on Lipid Chain Saturation. *Physical Review E* **2009**, *80* (2), 021931.
(371) Liu, J. Interfacing Zwitterionic Liposomes with Inorganic Nanomaterials: Surface Forces, Membrane Integrity, and Applications. *Langmuir* **2016**, *32* (18), 4393–4404.
(372) Wang, Y.; Hu, D.; Wei, D. Transmembrane Permeation Mechanism of Charged Methyl Guanidine. *Journal of Chemical Theory and Computation* **2014**, *10* (4), 1717–1726.
(373) Van Lehn, R. C.; Alexander-Katz, A. Grafting Charged Species to Membrane-Embedded Scaffolds Dramatically Increases the Rate of Bilayer Flipping. *ACS Central Science* **2017**, acscentsci.6b00365.
(374) Vorobyov, I.; Olson, T. E.; Kim, J. H.; Koeppe, R. E.; Andersen, O. S.; Allen, T. W.; Allen, T. W. Ion-Induced Defect Permeation of Lipid Membranes. *Biophysical journal* **2014**, *106* (3), 586–597.
(375) Li, L.; Vorobyov, I.; Allen, T. W. Potential of Mean Force and PKa Profile Calculation for a Lipid Membrane-Exposed Arginine Side Chain. *Journal of Physical Chemistry B* **2008**, *112* (32), 9574–9587.
(376) MacCallum, J. L.; Bennett, W. F. D.; Tieleman, D. P. Distribution of Amino Acids in a Lipid Bilayer from Computer Simulations. *Biophysical journal* **2008**, *94* (9), 3393–3404.
(377) Khavrutskii, I. V.; Gorfe, A. A.; Lu, B.; McCammon, J. A. Free Energy for the Permeation of Na+ and CI- Ions and Their Ion-Pair through a Zwitterionic Dimyristoyl Phosphatidylcholine Lipid Bilayer by Umbrella Integration with Harmonic Fourier Beads. *Journal of the American Chemical Society* **2009**, *131* (5), 1706–1716.
(378) Zeno, W. F.; Rystov, A.; Sasaki, D. Y.; Risbud, S. H.; Longo, M. L. Crowding-Induced Mixing Behavior of Lipid Bilayers: Examination of Mixing Energy, Phase, Packing Geometry, and Reversibility. *Langmuir* **2016**, *32* (18), 4688–4697.
(379) Scheve, C. S.; Gonzales, P. A.; Momin, N.; Stachowiak, J. C. Steric Pressure between Membrane-Bound Proteins Opposes Lipid Phase Separation. *Journal of the American Chemical Society* **2013**, *135* (4), 1185–1188.
(380) Ho, C. S.; Khadka, N. K.; She, F.; Cai, J.; Pan, J. Influenza M2 Transmembrane Domain Senses Membrane Heterogeneity and Enhances Membrane Curvature. *Langmuir* **2016**, *32* (26), 6730–6738.
(381) Schäfer, L. V; de Jong, D. H.; Holt, A.; Rzepiela, A. J.; de Vries, A. H.; Poolman, B.; Killian, J. A.; Marrink, S. J. Lipid Packing Drives the Segregation of Transmembrane Helices into Disordered Lipid Domains in Model Membranes. *Proceedings of the National Academy of Sciences of the United States of America* **2011**, *108* (4), 1343–1348.
(382) Hassan-Zadeh, E.; Hussain, F.; Huang, J. Gramicidin Peptides Alter Global Lipid Compositions and Bilayer Thicknesses of Coexisting Liquid-Ordered and Liquid-Disordered Membrane Domains. *Langmuir* **2017**, *33* (13), 3324–3332.
(383) Katira, S.; Mandadapu, K. K.; Vaikuntanathan, S.; Smit, B.; Chandler, D. Pre-

Transition Effects Mediate Forces of Assembly between Transmembrane Proteins. *eLife* **2016**, *5*, e13150.

(384) Marbella, L. E.; Millstone, J. E. NMR Techniques for Noble Metal Nanoparticles. *Chemistry of Materials* **2015**, *27* (8), 2721–2739.

(385) Smith, A. M.; Marbella, L. E.; Johnston, K. A.; Hartmann, M. J.; Crawford, S. E.; Kozycz, L. M.; Seferos, D. S.; Millstone, J. E. Quantitative Analysis of Thiolated Ligand Exchange on Gold Nanoparticles Monitored by ^{1}H NMR Spectroscopy. *Analytical Chemistry* **2015**, *87* (5), 2771–2778.

(386) Hein, R.; Uzundal, C. B.; Hennig, A. Simple and Rapid Quantification of Phospholipids for Supramolecular Membrane Transport Assays. *Org. Biomol. Chem.* **2016**, *14* (7), 2182–2185.

(387) Reimhult, E.; Zäch, M.; Höök, F.; Kasemo, B. A Multitechnique Study of Liposome Adsorption on Au and Lipid Bilayer Formation on SiO2. *Langmuir* **2006**, *22* (7), 3313–3319.

(388) Eriksson, E. K.; Agmo Hernández, V.; Edwards, K. Effect of Ubiquinone-10 on the Stability of Biomimetic Membranes of Relevance for the Inner Mitochondrial Membrane. *Biochimica et Biophysica Acta - Biomembranes* **2018**, *1860* (5), 1205–1215.

(389) Jemiola-Rzeminska, M.; Kruk, J.; Skowronek, M.; Strzalka, K. Location of Ubiquinone Homologues in Liposome Membranes Studied by Fluorescence Anisotropy of Diphenyl-Hexatriene and Trimethylammonium-Diphenyl-Hexatriene. *Chemistry and Physics of Lipids* **1996**, *79* (1), 55–63.

(390) ThermoFisher Scientific. Probes for Lipids and Membranes. *Molecular Probes Handbook* **2010**, *76* (11), 547–589.

(391) Huang, Z.; Haugland, R. P. Partition Coefficients of Fluorescent Probes with Phospholipid Membranes. *Biochemical and Biophysical Research Communications* **1991**, *181* (1), 166–171.

(392) Ibarguren, M.; Alonso, A.; Tenchov, B. G.; Goñi, F. M. Quantitation of Cholesterol Incorporation into Extruded Lipid Bilayers. *Biochimica et Biophysica Acta - Biomembranes* **2010**, *1798* (9), 1735–1738.

(393) Stark, R. W.; Drobek, T.; Heckl, W. M. Thermomechanical Noise of a Free V-Shaped Cantilever for Atomic-Force Microscopy. *Ultramicroscopy* **2001**, *86* (1–2), 207–215.

(394) Kontomaris, S.-V. The Hertz Model in AFM Nanoindentation Experiments: Applications in Biological Samples and Biomaterials. *Micro and Nanosystems* **2018**, *10* (1), 11–22.

(395) Garcia-Manyes, S.; Sanz, F. Nanomechanics of Lipid Bilayers by Force Spectroscopy with AFM: A Perspective. *Biochimica et Biophysica Acta (BBA) - Biomembranes* **2010**, *1798* (4), 741–749.

(396) Lopez-Acevedo, O.; Akola, J.; Whetten, R. L.; Grönbeck, H.; Häkkinen, H. Structure and Bonding in the Ubiquitous Icosahedral Metallic Gold Cluster Au 144 (SR) 60. *The Journal of Physical Chemistry C* **2009**, *113* (13), 5035–5038.

(397) Cho, N.-J.; Jackman, J. A.; Liu, M.; Frank, C. W. PH-Driven Assembly of Various Supported Lipid Platforms: A Comparative Study on Silicon Oxide and Titanium Oxide. *Langmuir* **2011**, *27* (7), 3739–3748.

(398) Keller, C. A.; Kasemo, B. Surface Specific Kinetics of Lipid Vesicle Adsorption Measured with a Quartz Crystal Microbalance. *Biophysical Journal* **1998**, *75* (3), 1397–1402.
(399) Kankare, J. Sauerbrey Equation of Quartz Crystal Microbalance in Liquid Medium. *Langmuir* **2002**, *18* (18), 7092–7094.
(400) Cho, N.-J.; Frank, C. W.; Kasemo, B.; Höök, F. Quartz Crystal Microbalance with Dissipation Monitoring of Supported Lipid Bilayers on Various Substrates. *Nature Protocols* **2010**, *5* (6), 1096–1106.
(401) Tabaei, S. R.; Jackman, J. A.; Kim, S. O.; Liedberg, B.; Knoll, W.; Parikh, A. N.; Cho, N. J. Formation of Cholesterol-Rich Supported Membranes Using Solvent-Assisted Lipid Self-Assembly. *Langmuir* **2014**, *30* (44), 13345–13352.
(402) Eriksson, E. K.; Agmo Hernández, V. Choice of Cuvette Material Can Influence Spectroscopic Leakage and Permeability Experiments with Liposomes. *Chemistry and Physics of Lipids* **2018**, *215* (August), 63–70.
(403) Alves, A. C.; Ribeiro, D.; Horta, M.; Lima, J. L. F. C.; Nunes, C.; Reis, S. The Daunorubicin Interplay with Mimetic Model Membranes of Cancer Cells: A Biophysical Interpretation. *Biochimica et Biophysica Acta - Biomembranes* **2017**, *1859* (5), 941–948.

Acknowledgments

Here I am. Three long years have passed and this laborious thesis is finally complete. It is with genuine pride that I realize that the satisfaction given by this long-awaited moment is mainly fueled by all the valuable human contributions that have shaped me during this educational experience. At the beginning I was not sure I wanted to take this path, but then I let myself be convinced by the hope that this experience would be valuable to grow and improve myself first of all as a person, as well as a scientist. Well, after three years I can say with absolute certainty that this is one of the very few things I had planned for my PhD that has fulfilled my expectations.

First of all, none of this would have been possible without the synergistic initiative of my supervisors to convince me to pursue this path. I will be always grateful to *Prof. Annalisa Relini* and *Prof. Fabio Canepa* for that and their precious mentoring. Fabio, it was in your laboratory that I started my first steps in scientific research, and I will always cherish these precious memories. Annalisa, working with you allowed me for the first time to deal with a scientific background other than mine: this was certainly the most valuable experience in my scientific maturity.

I will always be deeply grateful to all the collaborators with whom I have worked and who have actively participated in my personal and scientific growth. *Prof. Giulia Rossi*, thank you for always supporting and guiding me, showing me trust and respect. You have been a continuous source of inspiration and an important reference point to count on: I hope you can continue to be so in the future. *Dr. Silvia Dante*, I know that your kindness, helpfulness, calmness, and complicity are invaluable qualities to encounter when working as a team. I will always treasure our work together and hope to be an equally valuable colleague to someone else in the future. *Prof. Francesco Stellacci*, your appreciation for my work will always be one of the accomplishments of my PhD that I will be most proud of. I am grateful to you for always making me feel welcome in your group and for guiding me not only on lab doubts but also on those concerning my future. *Dr. Claudio Canale*, thank you for introducing me to AFM and patiently explaining the basics; working with you has been a fundamental experience in shaping my scientific interests and making me feel capable of being an independent researcher.

I also want to thank *Prof. Luca Monticelli* and *Prof. Giovanna Fragneto* for kindly agreeing to read my thesis and evaluating my PhD work. I am very grateful for all your comments.

Surely this long experience would not have been the same without the precious contribution of all my friends and colleagues from the departments and groups in which I worked – *Stefi*, *Paolo*, *Davide*, *Virgi*, *Giulia*, *Sebastian*, *Manuela*, *Ibtissame*, *Marzia*, *Giacomo*, *Michele*, *Lorenzo*, *Matteo*, *Simone*, *Paulo*, *Francesca*, *Nicolò*, *Suiyang*, *Ula*, *Lixia*, *Vladimir*, *Anna*, *Özgün*, and *Quy*. Thank you for the continuous exchange of knowledge and advice, for the help in the lab, for the lunches together, for the coffee breaks, for the moments of listening to each other's moods and for the silly ones.

Finally, I want to thank my dearest and beloved supporter, *Stefano*. Having you by my side on this journey has given me strength, hope, and passion. This achievement would not be possible without you, without your constant listening, encouragement, and help in trying to get me to change my perspectives when necessary. I am proud of you and and I am filled with happiness when I think that we will overcome all the uncertainties of our future together. You are and will always be my happy thought.